Development of Functional Soft Matter Containing Organometallic Ionic Liquids

角谷，凌

(Degree)
博士（理学）
(Date of Degree)
2023-03-25
(Date of Publication)
2024-03-01
(Resource Type)
doctoral thesis
(Report Number)
甲第8585号
(URL)
https://hdl.handle.net/20.500.14094/0100482333

Doctoral Dissertation

Development of Functional Soft Matter Containing Organometallic Ionic Liquids

（有機金属イオン液体からなる機能性ソフトマターの開発）

January, 2023

Graduate School of Science, Kobe University

Ryo Sumitani

角谷 凌

CONTENTS

CHAPTER 1. General Introduction

CHAPTER 2. Reversible Control of Ionic Conductivity and Viscoelasticity of Ruthenium-Containing Ionic Liquids by Application of Light and Heat

CHAPTER 3. Reversible Formation of Soft Coordination Polymers from Mixtures of Ruthenium-Containing Ionic Liquid and Bridging Molecules

CHAPTER 4. Metal-Containing Poly(ionic liquid) Exhibiting Photogeneration of Coordination Network

CHAPTER 5. Switchable Ionic Conductivity and Viscoelasticity of Ruthenium Containing Ionogels

CHAPTER 6. On-Demand Gelation of Ionic Liquids Using Ruthenium-Containing Photoresponsive Gelators

CHAPTER 7. Structures, Thermal Properties, and Reactivities of Cationic Rhodium(I) complexes in Solid State

CHAPTER 1

General Introduction

1.1 Background

Ionic liquids (ILs) are salts with melting points below 100 °C consisting of cations and anions. They exhibit characteristic features such as non-volatility, flame retardancy, and high ionic conductivity. Because of these properties, they can be applied as electrolytes,[1] reaction solvents,[2] and CO_2 absorbents,[3] etc. Common ILs contain imidazolium, quaternary ammonium, pyrrolidinium, and quaternary phosphonium cations (**Fig. 1-1a**). Fluorinated anions such as PF_6^- and Tf_2N^- (bis(trifluoromethanesulfonyl)imide) are often used as their counter ions (**Fig. 1-1b**).

In order to use ILs as electrolytes, they must exhibit high ionic conductivities. Ionic conductivities of ILs at room temperature are correlated with their melting points and glass transition temperatures.[4] ILs with lower viscosities, lower melting points, and lower glass transition temperatures (T_g) typically exhibit higher ionic conductivities. In general, as the length of the alkyl chain increases, the viscosity increases while the melting point and ionic conductivity decrease (**Fig. 1-2**). However, further increase in the chain length increases the melting point.

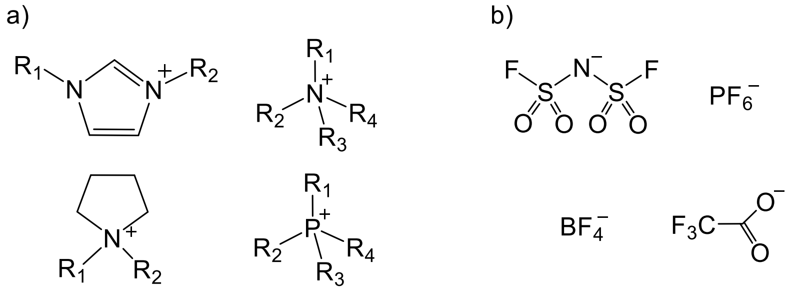

Figure 1-1. Structural formulas of (a) cations and (b) anions commonly used in ionic liquids.

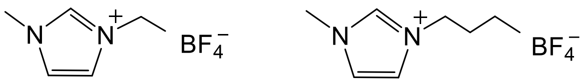

Ionic conductivity:	13.6 mS cm^{-1}	1.04 mS cm^{-1}
Melting point:	14.6 °C	–82 °C (T_g)
Viscosity:	31.8 mPa·s	223.8 mPa·s

Figure 1-2. Ionic conductivities, melting points, and viscosities of ionic liquids with different alkyl chain lengths.[5]

This thesis describes the development of Ru-containing photoreactive ionic liquids (ILs), their reversibly controlled physical properties, and their application to soft matter. This chapter provides an overview of the background of the research. ILs are salts with melting points below 100 °C, and they are useful as electrolytes and reaction media owing to their high ionic conductivity and nonvolatility.[6] Although most ILs contain onium cations, metal-containing ILs have been recently developed (**Fig. 1-3**).[7–11] One method to obtain these ILs is to introduce metal ions into the cations or anions. These ILs exhibit intriguing properties, such as catalytic[12,13] and redox activity,[14,15] magnetism,[16] and luminescence.[17]

The laboratory the author belongs to has developed various functional ILs containing cationic organometallic complexes. These ILs exhibit spin crossover,[18] thermochromism,[19] and vapochromism,[20] and other stimuli-responsive phenomena. Furthermore, photoreactive ILs containing cationic Ru complexes have also been developed in the laboratory. In acetonitrile, the cationic sandwich-type Ru complex $[\mathrm{Ru}(\mathrm{C_5H_5})(\mathrm{arene})]^+$ is known to undergo photodissociation to produce a half-sandwich complex $[\mathrm{Ru}(\mathrm{C_5H_5})(\mathrm{NCMe})_3]^+$, while the reverse reaction takes place upon heating (**Fig. 1-4**).[21,22] Based on this mechanism, Funasako *et al.* developed a Ru-containing IL that undergoes a reversible transformation between IL and coordination polymer by the application of light and heat (**Fig. 1-5a**).[23] Furthermore, Ueda *et al.* developed Ru-containing ILs that contain the $\mathrm{B(CN)_4}$ anion, which transform to porous amorphous coordination polymers upon photoirradiation (**Fig. 1-5b**).[24] The photogenerated solids exhibited gas adsorption properties owing to their microporous structures.

The investigations conducted by the author, as described in this thesis, are based on these studies. As the general background, the following sections summarize the current research on photoresponsive ILs and related photoresponsive soft matter.

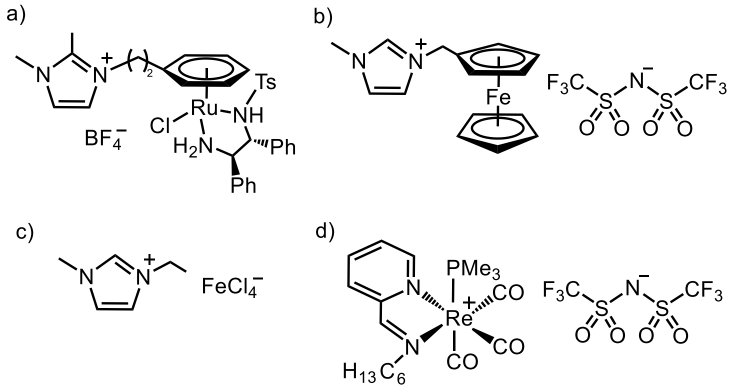

Figure 1-3. Examples of metal-containing ionic liquids exhibiting (a) catalytic activity,[13] (b) redox activity,[15] (c) magnetism,[16] and (d) luminescence.[17]

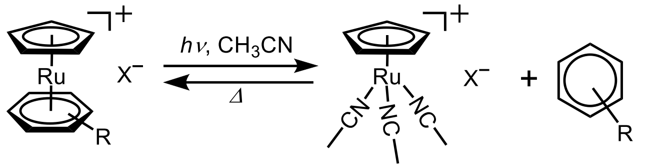

Figure 1-4. Photochemical and thermal reactions of cationic sandwich-type Ru complex $[Ru(C_5H_5)(arene)]X$ in acetonitrile solution.[21,22]

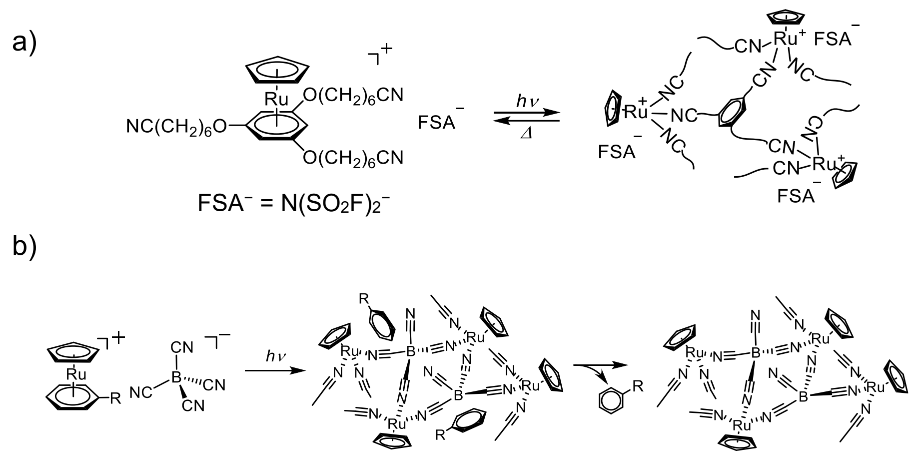

Figure 1-5. Formation of amorphous coordination polymers brought about by the photochemical reaction of Ru-containing ionic liquids.[23,24]

1.2 Photoresponsive ILs and Soft Matter

1.2.1 Photoresponsive ILs

Several photoresponsive ILs have been reported recently, whose physical properties, such as ionic conductivity, melting point, and color, undergo reversible photoinduced changes. These materials could be applied to sensors, switching devices, optical memory, etc. A majority of these ILs incorporate photoisomerizable moieties, such as azobenzene, stilbene, and cinnamate, in their cations (**Fig. 1-6**).[25–27] The changes in physical properties of these ILs have been typically investigated in dilute conditions, such as in solvents and polymers.[26,28–31] However, several ILs change their physical properties upon photoirradiation in neat conditions. The IL in **Fig. 1-7** undergoes a solid–liquid transformation owing to changes in its melting point caused by the *cis–trans* photoisomerization of azobenzene.[32] As a result of the photoisomerization, the IL's ionic conductivity reversibly switches between 4.2×10^{-10} S cm^{-1} and 1.2×10^{-7} S cm^{-1}. In addition, ILs containing spiropyran or diarylethene moieties have recently been developed, which undergo ring-opening/closing photoisomerization (**Fig. 1-8**).[33,34] Upon photoirradiation, these ILs change color, so they could be utilized for smart windows.

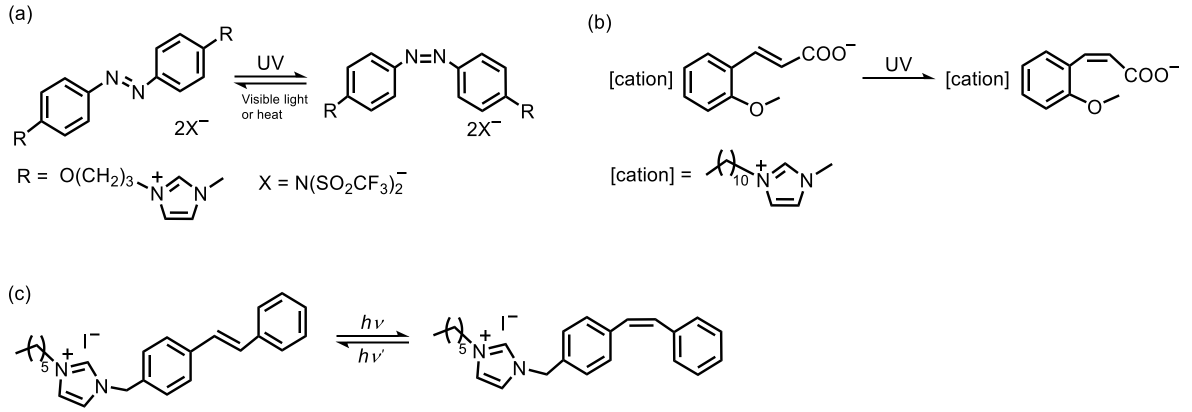

Figure 1-6. Examples of an (a) azobenzene-containing, (b) stilbene-containing, and cinnamate-containing ionic liquids.[25–27]

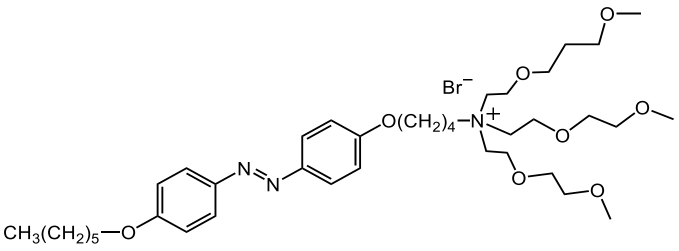

Figure 1-7. Example of an azobenzene-containing ionic liquid.[32]

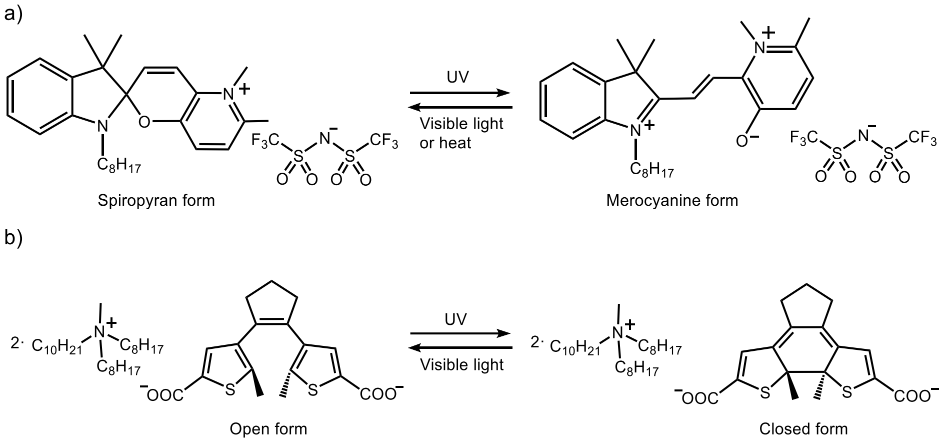

Figure 1-8. Photoisomerization of (a) spiropyran-containing[33] and (b) diarylethene-containing ionic liquids.[34]

1.2.2 Photoresponsive Soft Matter

Many types of photoresponsive soft matter have been reported, which undergo changes in physical properties, such as viscoelasticity and ionic conductivity, or are able to release small molecules. These materials have a wide range of applications in engineering, as switching devices,[35] sensors,[36] self-healing materials,[37] as well as for 3D printing[38] they are also employed in the medical field, for example as dental materials.[39] The use of light to elicit desired transformations is advantageous in that it acts as a noninvasive trigger affording the formation or cleavage of bonds, without causing the temperature to rise. In addition, light offers temporal and spatial control of the chemical process. Photoresponsive polymers and gels have been typically prepared by incorporating photoresponsive molecules that undergo isomerization, bond cleavage, radical reactions, or ligand exchange reactions upon photoirradiation.[40]

Upon photoirradiation, photorheological materials undergo viscoelasticity changes, although some of these changes are irreversible.[41–43] These materials have been utilized as actuators[44] and drug delivery systems[45] as well as means to realize microemulsion phase separation.[46] Photorheological polymers typically contain photofunctional moieties such as azobenzene, stilbene, silicic acid, spiropyran, and diarylethene. For example, upon photoirradiation, the polymers shown in **Fig. 1-9** undergo a sol–gel transition brought about by the isomerization of the azobenzene moiety.[47] Furthermore, photoresponsive polymers and gels based on photoinduced ligand exchange reactions of organometallic complexes have been reported. Many of these systems include Ru complexes in the polymer chain (**Fig. 1-10**),[48,49] and they undergo changes in viscoelasticity of about two orders of magnitude.

Physical gels are typically formed with low-molecular-weight gelators (LMWGs).[50] Liquid media such as water, organic solvents, and ILs can be gelated with LMWGs; moreover, gelation control can be achieved by changing the temperature or pH of the liquid media. The formation of gels is ascribed to the self-assembly of LMWGs to form network structures based on intermolecular interactions such as hydrogen bonding and π-stacking. Several photoresponsive gels have been reported that are based on photoresponsive LMWGs, such as those containing azobenzene moieties.[51] Photoirradiation of the gelators result in them switching between structures with gelling ability and ones without, depending on the irradiation wavelength (**Fig. 1-11**). This property facilitates the photocontrol of viscoelasticity. Furthermore, LMWGs with photocleavable gelation inhibitor sites have been reported, which gain gelling ability upon photoirradiation (**Fig. 1-12**).[52]

Different types of photoresponsive soft matter undergoing changes in ionic conductivity have been utilized as electronic materials such as sensors, switching materials, variable resistors, and gate electrodes.[53,54] Their photoresponsive mechanisms are typically based on the photoisomerizations of azobenzene,[55–57] spiropyran, or diarylethene moieties.[58–61] The isomerization of these moieties affords the means to control reversible changes in ionic conductivity, although the changes are mostly small, not exceeding two orders of magnitude.

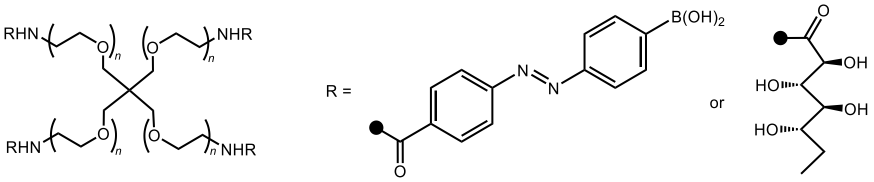

Figure 1-9. Structural formulas of azobenzene-containing polymers. These materials swell in liquid media and undergo reversible sol–gel transitions upon photoirradiation.[47]

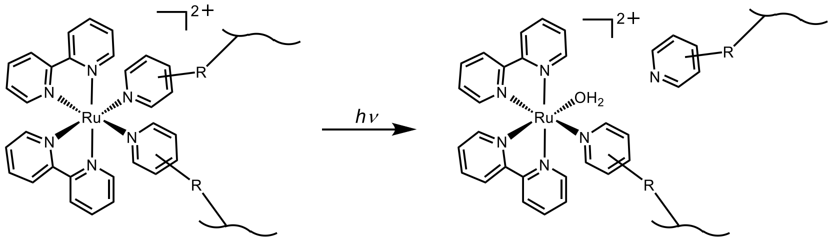

Figure 1-10. Photoinduced ligand exchange reactions of Ru-containing polymers and gels.[48,49]

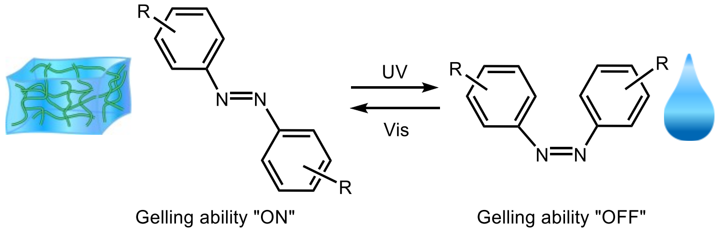

Figure 1-11. Photoswitching between the gel-forming *trans*-isomer and the non-gelling *cis*-isomer of azobenzen-containing LMWGs.[51]

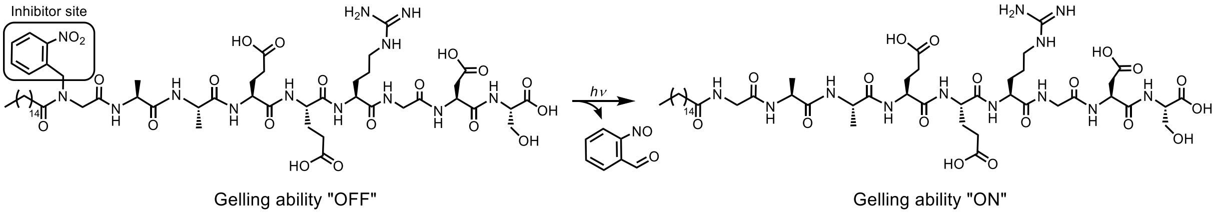

Figure 1-12 Photochemical reaction of peptide-based LMWGs containing a photocleavable gelation inhibitor site.[52]

1.2.3 Poly(ionic liquid)s and Ionogels

ILs can be immobilized via their polymerization or gelation, two processes resulting in the production of solid or semi-solid species that retain the functionality of the ILs. Poly(ionic liquid)s (PILs) are obtained as a result of the polymerization of IL monomers comprising polymerizable substituents (**Fig. 1-13a**). Notably, PILs have been utilized to manufacture gas adsorption membranes,[62] protein extraction membranes,[62] and polyelectrolytes.[63,64] Despite their high charge density, the glass transition temperature (T_g) of some PILs is as low as −60 °C.[65] On the other hand, ionogels are formed by the network structures formed by LMWGs,[66] polymers,[67] and inorganic nanoparticles[68] (**Fig. 1-13b**). Ionogels are characterized by higher ionic conductivities than PILs because of the higher mobility of the IL in the gel. Unlike hydrogels and organogels, ionogels exhibit high thermal stability because they contain non-volatile media.[69] Furthermore, high-strength and self-healing ionogels have been reported.[70]

Recently, several photoresponsive PILs have been developed, which exhibit unique features, such as ionic conductivity changes and selective absorption of dyes triggered by light irradiation.[71–73] For example, diarylethene-containing PILs exhibit photocontrollable ionic conductivity (**Fig. 1-14**).[71] Indeed, photoirradiation of these PILs results in the reduction of the ionic conductivity by about 30% via changes in cation–anion interactions due to photoisomerization.

Photoresponsive ionogels can be used in microfluidic devices and solid electrolytes, because their viscoelasticity and ionic conductivity can be photocontrolled. These gels can be prepared either by incorporating a photoresponsive moiety into the gel framework or by conducting a gelation of photoresponsive ILs. The former approach relies on various mechanisms to achieve the photocontrol of physical properties like host–guest interactions[74] and polarity,[75] as well as of processes like dimerization reactions[76] and upper critical solution temperature (UCST)-type phase transitions.[77] By contrast, only few examples currently exist of the implementation of the latter approach, probably because most photoresponsive ILs reported to date have rather high melting points. An example is a gel of an azobenzene-based IL containing a temperature-responsive polymer, which undergoes a reversible sol–gel transition upon photoirradiation (**Fig. 1-15**).[78,79] This phenomenon is based on the change in the temperature of the their lower critical solution temperature (LCST)-type phase transition resulting from photoirradiation. Another example is a gel of a spiropyran-containing IL, which undergoes a reversible color change upon photoirradiation (**Fig. 1-16**).[80] The development of photoresponsive ionogels via this approach is promising in terms of the variety and magnitude of properties that can be achieved.

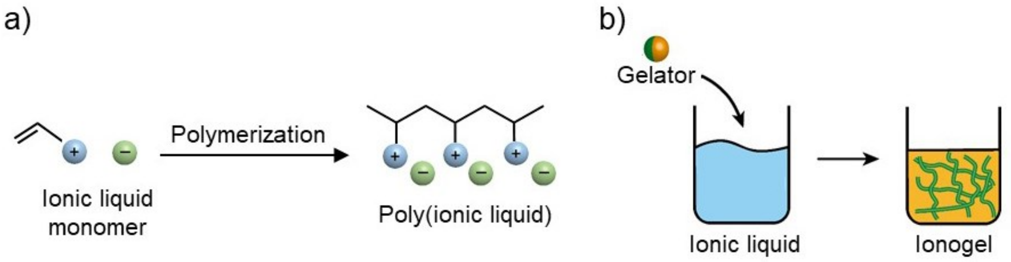

Figure 1-13. Schematic of (a) poly(ionic liquid)s and (b) ionogels.

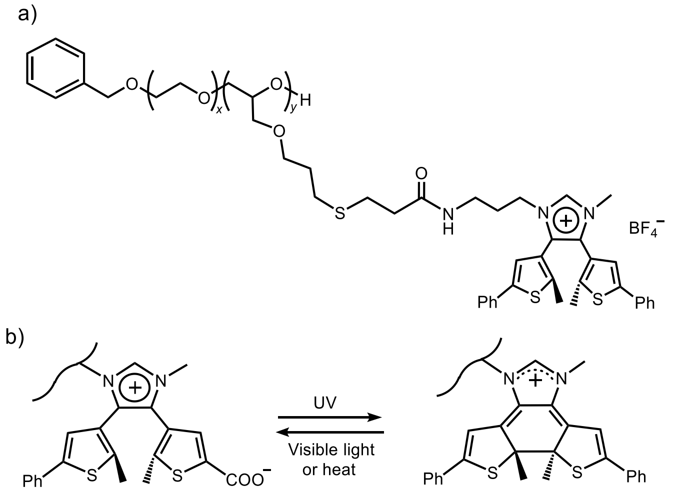

Figure 1-14. (a) Structural formula and (b) photoisomerization of diarylethene-conataining poly(ionic liquid).[71]

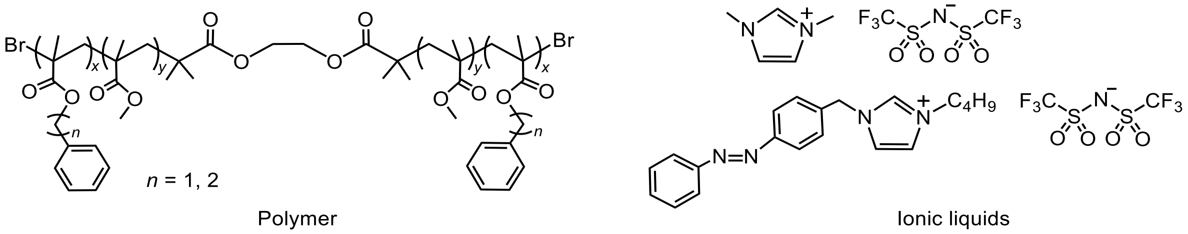

Figure 1-15. Structural formulas of photoresponsive ionogels composed of triblock copolymers and azobenzene-containing ILs.[78,79]

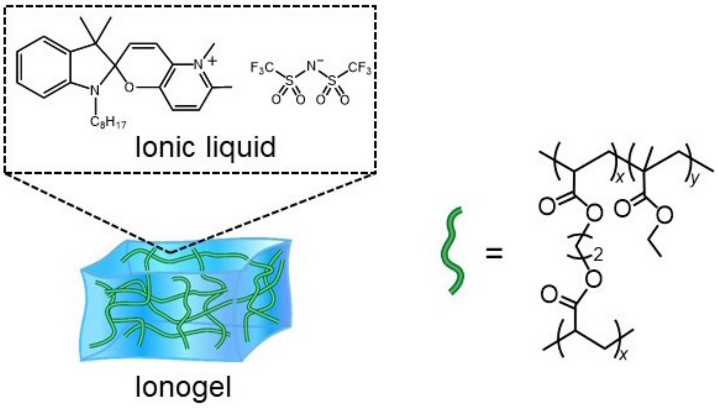

Figure 1-16. Schematic of photoresponsive ionogel composed of spiropyran-containing IL.[80]

1.3 Scope of this Thesis

The purpose of this research is to develop stimuli-responsive functional ILs and soft matter from organometallic complexes. Although many photoresponsive polymers and gels have been reported to date, their mechanisms are mostly based on the photoisomerization of organic molecules. The author hypothesized that soft matter containing photoreactive organometallic complexes would undergo various changes in their physical properties. Based on the studies on photoreactive Ru-containing ILs conducted in the laboratory to which the author belongs, the author investigated the functionalization of Ru-containing ILs and their application to soft matter. In addition, the solid-state properties of some ionic compounds containing Rh complexes were investigated. The contents of the subsequent chapters, as schematically shown in **Fig. 1-17**, are as follows:

Chapter 2 describes research conducted to explore the stimuli-responsive functions of the Ru-containing ILs and the control of their physical properties through the application of light and heat. First, the photochemical reaction of an IL bearing a cyanoalkoxy substituent was examined. Upon irradiation with UV light, this IL was transformed into a highly viscous liquid, and the process was reversed upon heating. The ionic conductivity and viscoelasticity of the ILs with one or three cyanoalkoxy substituents were then investigated, which were controlled reversibly. Secondly, in order to elucidate the correlation between the melting points and structures, ILs with three short cyanoalkoxy substituents or one thiobutyl substituent were synthesized, and their structures and reactivities were investigated. Although most of them were solid, a liquid salt was obtained in the case of the thiobutyl derivative when an asymmetric anion was used. Upon UV light irradiation, the liquid salt was transformed into a highly viscous liquid containing an anion-coordinated complex. The photoreaction rate and conversion of this IL were lower than those of ILs with cyanoalkoxy substituents.

Chapter 3 describes the development of photoreactive liquid mixtures of a Ru-containing IL and a tridentate or a bidentate bridging ligand comprising cyano groups that was carried out with the goal of extending the methodology for the fabrication of photochemical coordination polymers. Upon UV light irradiation, these liquids were transformed into elastomers of amorphous coordination polymers and one-dimensional liquid oligomers, respectively; notably, heating the photoproducts afforded the recovery of the original liquids. The topology and rheology of the photoproducts differed based on the bridging ligand utilized.

In Chapter 4, a Ru-containing PIL was developed to extend the concept of photoreactive liquids to polymers. A PIL comprising a cation with three cyanoalkoxy substituents and a polymeric anion was prepared. Upon UV light irradiation, the highly viscous liquid turned into a rubber-like elastomer, which is a unique hybrid polymer containing both coordination networks and covalent chains, and the reverse reaction occurred upon heating. Furthermore, upon photoirradiation, the precursor of this PIL, which was an IL with a vinyl-substituted anion, was transformed into a viscous elastomer containing coordination networks. Heating the photoproduct produced the PIL, since polymerization of the anion occurred owing to the catalytic activity of the cation.

Chapter 5 describes the fabrication of photoresponsive gels using photoresponsive ILs. The addition of an LMWG to Ru-containing ILs produced ionogels, whose ionic conductivity decreased and viscoelastic modulus increased upon UV photoirradiation. The IL with one cyanoalkoxy substituent remained in a gel state after photoirradiation, whereas the IL with three substituents turned into a rubbery solid. They returned to their original gel state upon heating, demonstrating the reversibility of the reaction.

Chapter 6 describes the development of photoresponsive gelators that reversibly form ionogels. Gelator-coordinated Ru complexes were synthesized and they were added to onium-type ILs. Upon UV light irradiation, the ILs transformed into ionogels, and the ionogel liquefied again upon heating, owing to the thermal reverse reaction. The photogelation conditions could be modified by the choice of the ligands and anions. In addition, several organic solvents were also photogelated. Thus, a unique and versatile method for the on-demand photogelation of liquids was developed.

Chapter 7 describes the synthesis of a series of ionic crystals containing cationic Rh, which was performed to develop reactive organometallic crystals. Cations containing cyclic ligands such as 1,5-cyclooctadiene (cod) and arenes were used. Most salts exhibited order–disorder phase transitions, and one of them exhibited a rotator phase at room temperature. The structures and reactivities of the prepared salts strongly depended on the anions. The arene-coordinated complexes underwent ligand exchange reactions in ether while maintaining in the solid phase. The results thus obtained are useful for the exploration of solid-state reactions of organometallic solids.

The author believes that these investigations provide useful knowledge for the exploration and application of soft matter based on the use of reactive organometallic cations.

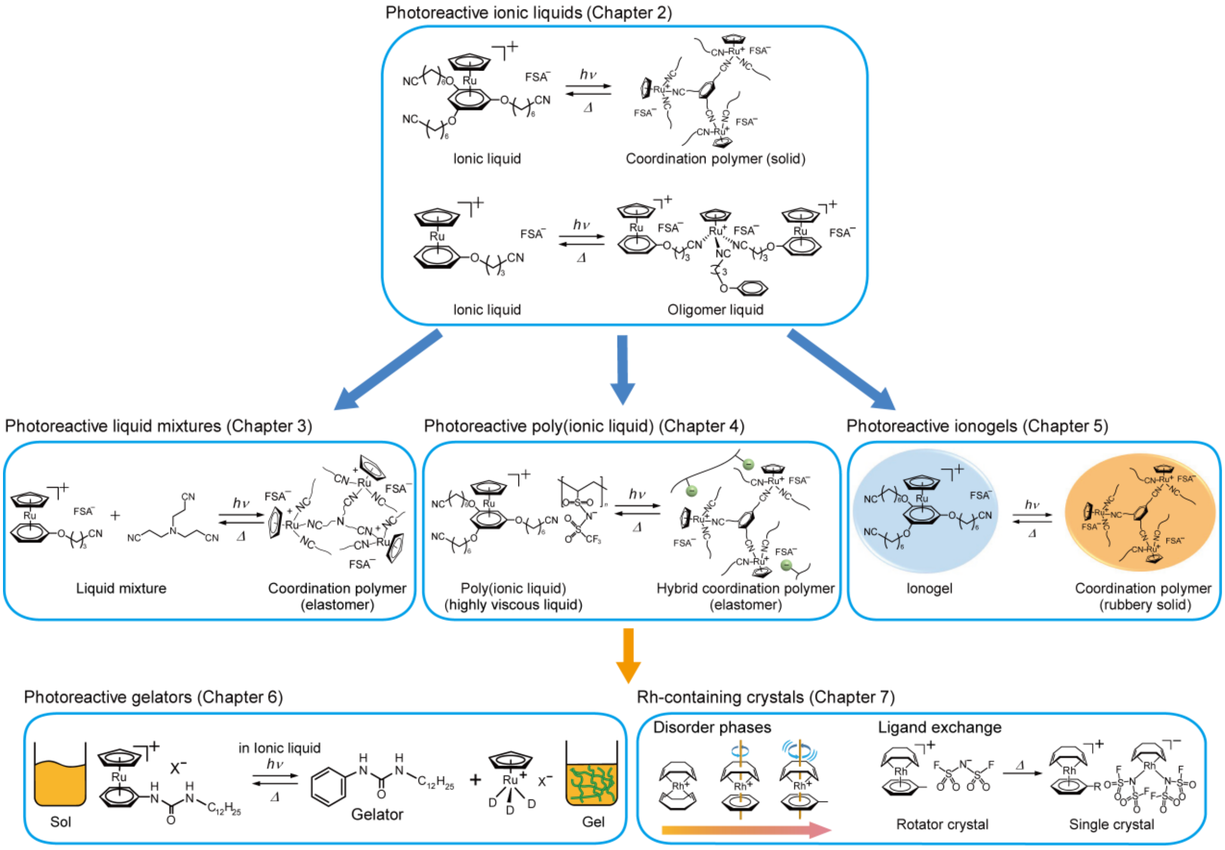

Figure 1-17. Contents of this thesis.

CHAPTER 2

Reversible Control of Ionic Conductivity and Viscoelasticity of Ruthenium-Containing Ionic Liquids by Application of Light and Heat

2.1 Introduction

Ionically conducting materials, including superionic conducting solids,[81] polymers,[82] and ILs,[1] have been used for a wide range of electronic applications such as capacitors and chemical sensors. The addition of photocontrollability to their ionic conductivity should greatly enhance their utility. Currently, however, there are very few examples of photocontrollable ionically conductive coordination polymer. A photoswitchable ionic conductor with a photoisomerizable ligand was recently reported.[83] Polymers containing photochromic moieties can reversibly change their ionic conductivity upon photoirradiation, albeit with small ionic conductivity change.[56,71,74,84] ILs containing azobenzene units exhibit reversible ionic conductivity changes owing to solid-liquid transformations based on photoisomerization.[32] Such a photoisomerization mechanism is a useful strategy for controlling ionic conductivity. However, the photochemical immobilization of ions should enable a more straightforward and flexible control of ionic conductivity, if the process is thermally or photochemically reversible.

The purpose of this study is to demonstrate the photochemical control of ionic conductivity based on a mechanism of bond transformation in ILs. As described in chapter 1, as part of the studies of our laboratory on functional ILs containing organometallic cations,[19,24,85] Funasako et al. previously reported Ru-containing organometallic IL ***tri*-1** ($[Ru(C_5H_5)\{C_6H_3(OC_6H_{12}CN)_3\}]FSA$, **Fig. 2-1a**), which reversibly transforms to an amorphous coordination polymer by the application of UV light and heat (**Fig. 2-2**).[23] Photoirradiation of ***tri*-1** causes dissociation of the arene ligand, followed by the coordination of the three cyano groups to the Ru ion, which leads to gradual solidification owing to the formation of a three-dimensionally cross-linked structure. Furthermore, the reaction can be reversed by heating. Since this transformation involves reversible fixation of the constituent ions, we hypothesized that the mechanism could be used for the control of ionic conductivity. In addition, in order to design Ru-containing ILs with higher reactivity, it is important to elucidate the molecular structure and intermolecular interactions and to investigate the effect of the substiuents. This chapter describes the results of such experiments. This chapter consists of the following three parts.

First, we investigated the reversible control of the viscoelasticity and ionic conductivity of Ru-containing ILs ***tri*-1** and **1** ($[Ru(C_5H_5)\{Ph(OC_3H_6CN)\}]FSA$) (**Fig. 2-1a**) by the application of light and heat. In the second part, the thermal properties and crystal structures of ILs **2-X** ($[Ru(C_5H_5)\{C_6H_3(OC_3H_6CN)_3\}]X$, X = FSA and Tf_2N, **Fig. 2-1**) were investigated. These salts had higher melting points because they had shorter substituents than that of ***tri*-1**. Crystal structure analysis revealed information about molecular structure and intermolecular interactions. In the last part, we synthesized ILs **3-X** ($[Ru(C_5H_5)(PhSBu)]X$, X = PF_6, FSA, and FTA ($(SO_2F)(SO_2CF_3)N^-$) to investigate the effect of a sulfur-containing substituent in the cation on the photochemical reaction of ILs. The effects of the anions on the melting point and crystal structure were discussed. The physical properties of these were compared with those of photochemically inert **4-X** (X = PF_6 and FSA, **Fig. 2-1**).[86] Furthermore, we investigated the photochemical reaction of liquid **3-FTA**.

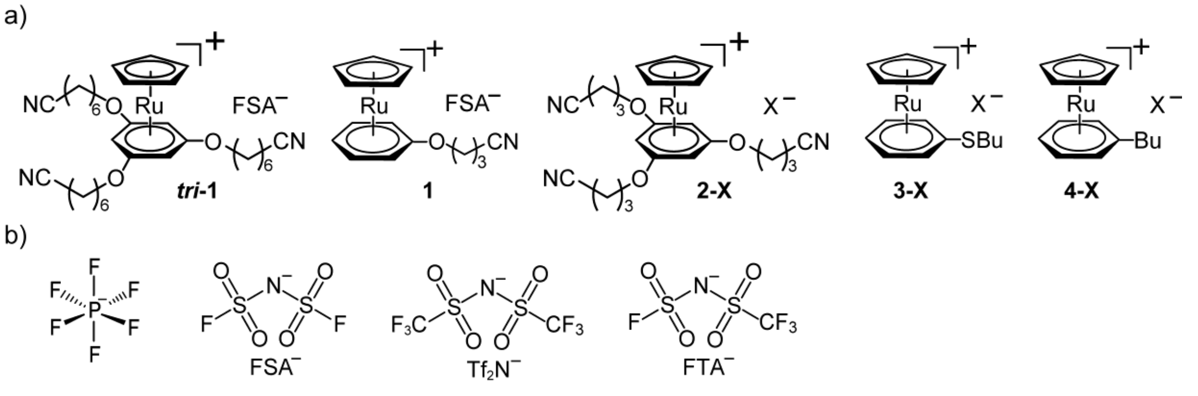

Figure 2-1. Structural formulae of ionic liquids (a) ***tri*-1**, **1**, **2-X**, **3-X**, **4-X** (X = anion) and (b) the anions used in this study.

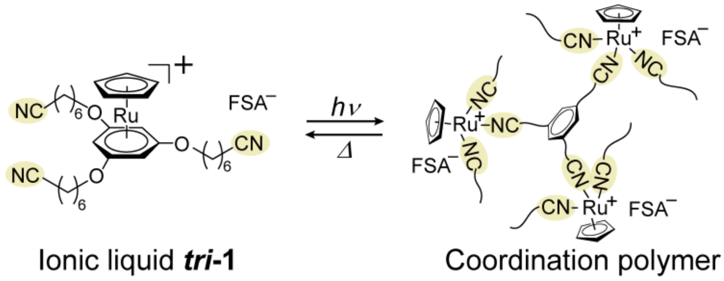

Figure 2-2. Reversible transformation between ionic liquid ***tri*-1** and amorphous coordination polymer by application of light and heat.

2.2 Results and Discussion

2.2.1 Reversible Control of Physical Properties of Ru-Containing ILs

In this section, we investigated reversible control of ionic conductivity and viscoelasticity of Ru-containing ILs ***tri*-1** and **1** by the application of light and heat. These ILs were synthesized according to the procedure in the literature.[23,86] These ILs, having different numbers of substituents, exhibit glass transitions at −53 °C[23] and −60 °C,[86] respectively.

Photoreactivity of *tri*-1 and 1. As described in the introduction section, the pale yellow liquid ***tri*-1** changes into a yellow elastomer upon UV photoirradiation (365 nm, LED) in approximately 4 to 6 h.[23] In contrast, **1** exhibited no solidification upon UV photoirradiation; this liquid changed from a pale yellow liquid to a highly viscous yellow liquid in 15 min, when the reaction rate was saturated at approximately 93%. The time course of the reaction is shown in **Fig. 2-3**, together with that of ***tri*-1**. The reaction speed of **1** was considerably faster than that of ***tri*-1** partly because of its low viscosity. Since three cyano groups are coordinated to the Ru ion, this photoreaction produces a complex in which an arene ligand and two cations are coordinated to the dissociated Ru complex (**Fig. 2-4**). The observed ratio of the photodissociated cation in the product was nearly one-third (28%), which is consistent with the reaction mechanism. The ^{1}H, ^{13}C NMR (**Figs. 2-5** and **2-6**), and ESI-MS spectra in dichloromethane are consistent with the structure, though complexes with different combinations of ligands may also be present in the product. Heating the photoproduct at 120 °C quantitatively recovered **1** within 10 min, similarly to the case of ***tri*-1**. The changes in the ^{1}H NMR and UV-Vis spectra associated with this reversible transformation are shown in **Fig. 2-7**.

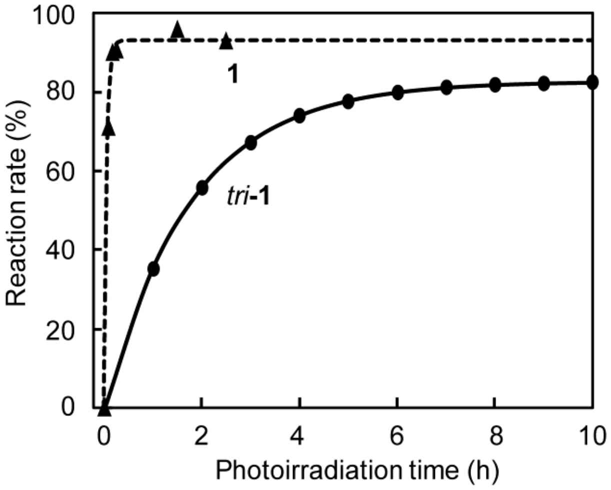

Figure 2-3. Time course of the reaction, where the reaction rate is given by the molar ratio of the photoreacted species in the products generated by photoirradiation of ***tri*-1** (—)[23] and **1** (----) as determined from the UV-Vis spectral absorbance at 370 nm and ^{1}H NMR spectra.

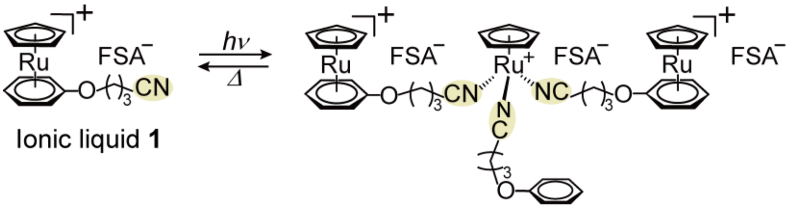

Figure 2-4. Reversible transformation between ionic liquid **1** and its oligomer by application of light and heat.

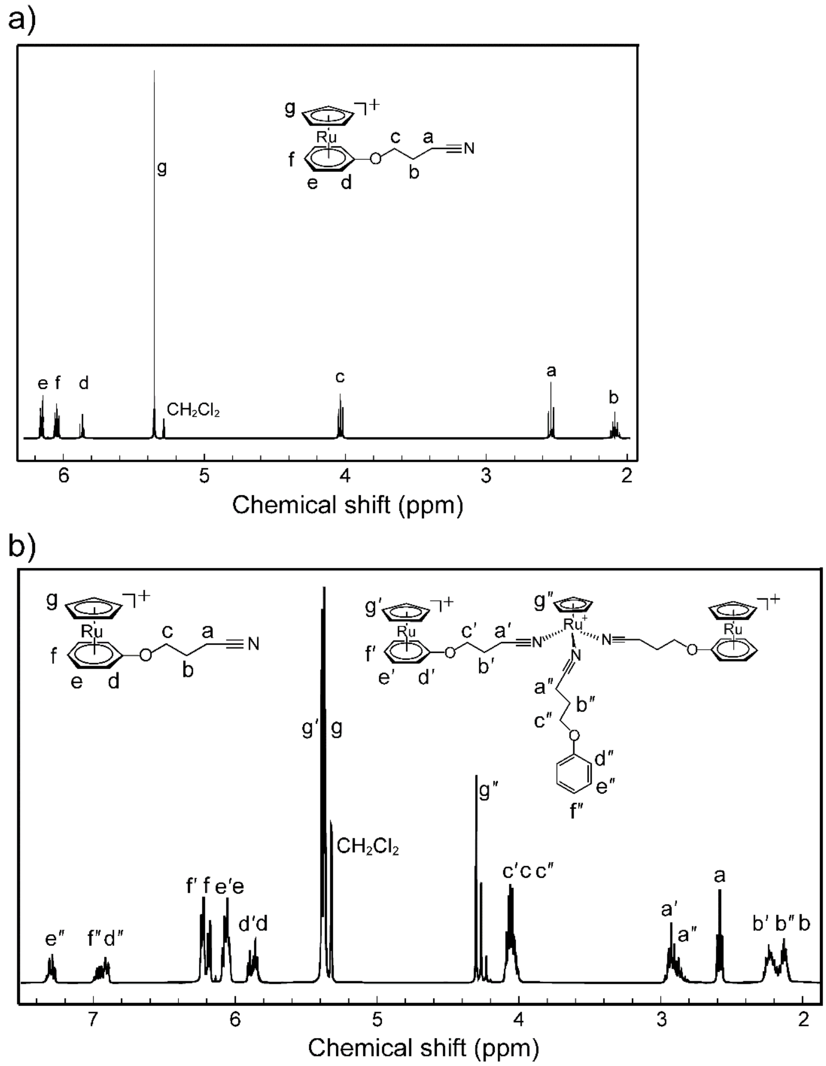

Figure 2-5. ^{1}H NMR spectra of (a) **1** and (b) its photoproduct in CD_2Cl_2. The photoproduct contains unreacted **1**.

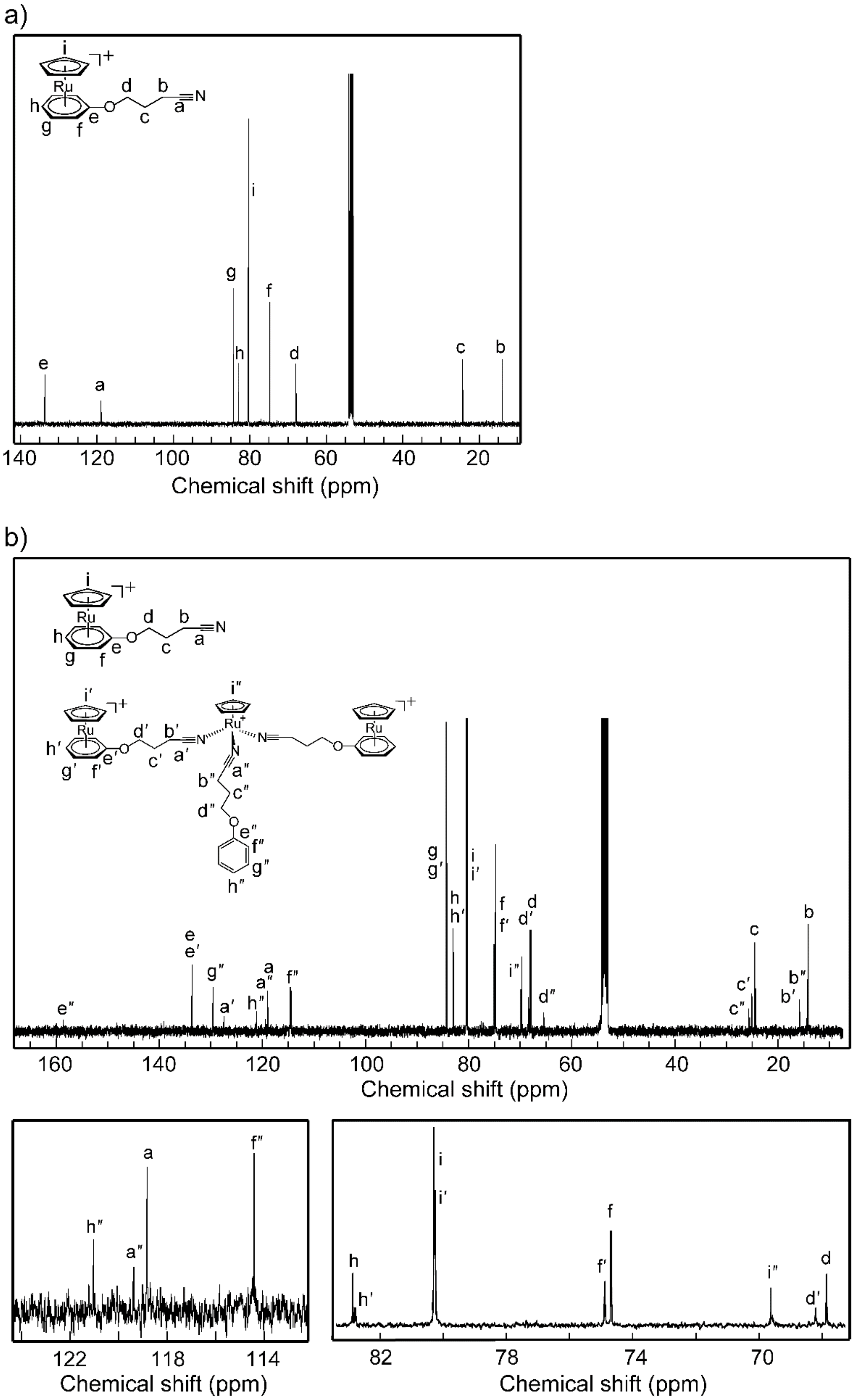

Figure 2-6. ^{13}C NMR spectra of (a) **1** and (b) its photoproduct in CD_2Cl_2. The photoproduct contains unreacted **1**.

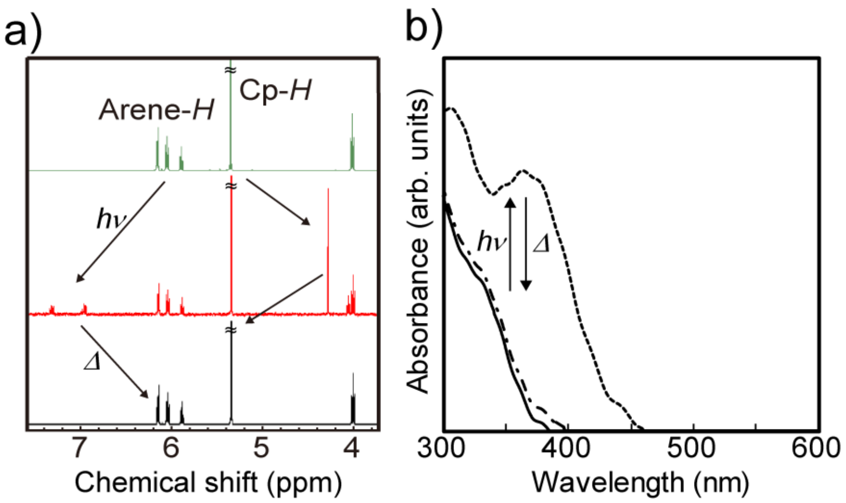

Figure 2-7. (a) ^{1}H NMR spectra (400 MHz, CD_3CN) and (b) UV-Vis spectra of **1** before (—) and after photoirradiation for 2.5 h (----), and after subsequently heating at 120 °C for 10 min (-·-·-). In the ^{1}H NMR spectra, the photodissociated cation is observed as $[Ru(C_5H_5)(NCCD_3)_3]^+$ owing to ligand exchange by the solvent.

Viscoelasticity of *tri*-1 and 1. The viscoelastic changes of ***tri*-1** and **1** upon photoirradiation were investigated. The viscosity of ***tri*-1** was 2.6 Pa·s (shear rate, 1 s^{-1}; 25 °C). The frequency dependence of the storage modulus (G') and loss modulus (G'') of ***tri*-1** is shown in **Fig. 2-8a**. The modulus values at low frequency were approximately 10^1 Pa before photoirradiation, but increased by four orders of magnitude after 8 h photoirradiation, when the reaction rate was 55%. The photoreaction speed was slower than that shown in **Fig. 2-3** because of sample thickness. Before photoirradiation, G'' exceeded G' over the entire measurement range (1–100 rad s^{-1}), indicating viscous behavior ($\tan \delta = G''/G' > 1$). However, after 4 and 8 h photoirradiation, G' exceeded G'' ($\tan \delta < 1$) in the range above 6 and 4 rad s^{-1}, respectively, thereby indicating the change to an elastomer. The complex viscosity increased greatly from 4.0 Pa·s to 1.2×10^5 Pa·s (at 2.5 rad s^{-1}) after 8 h photoirradiation (**Fig. 2-8b**). Longer photoirradiation may increase the reaction rate and viscosity even further.

In contrast, the viscosity of **1** at 25 °C was 0.9 Pa·s. This liquid was less viscous than ***tri*-1**

(2.6 Pa·s at 1 s^{-1}) owing to the lower number of substituents, which is consistent with the lower glass transition temperature of **1** than ***tri*-1**. The viscosity after photoirradiation for 8 h (reaction rate 84%) was 5.2 Pa·s, which is an increase of approximately 6 times (**Fig. 2-9**). The increase is much smaller than that observed in ***tri*-1** because the photoproduct is also a liquid in this case. Liquid **1** is a Newtonian fluid both before and after the photoreaction.

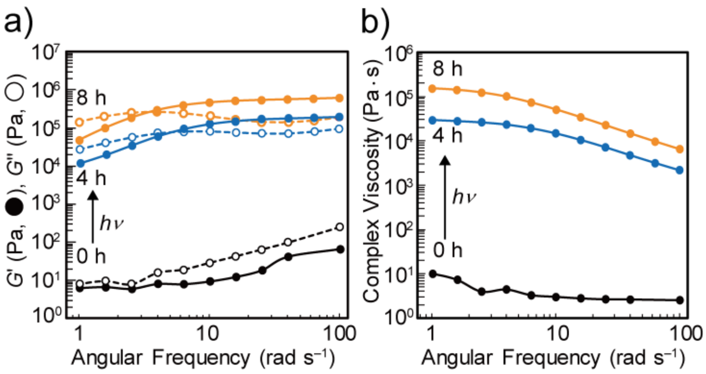

Figure 2-8. (a) Frequency dependence of the storage modulus G' (●) and loss modulus G'' (○) of ***tri*-1** before and after 4 and 8 h UV photoirradiation. (b) Frequency dependence of the complex viscosity of ***tri*-1** before and after photoirradiation (25 °C, strain 1%).

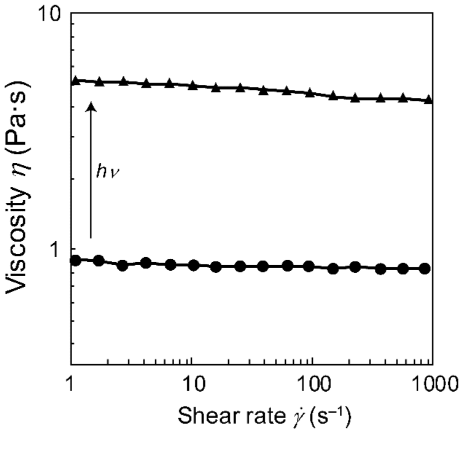

Figure 2-9. Viscosity of ionic liquid **1** before and after photoirradiation (8 h) measured at 25 °C.

Ionic conductivities of *tri*-1 and 1. Based on the results described in the previous section, the control of the ionic conductivities of ***tri*-1** and **1** by the application of light and heat was investigated. **Table 2-1** summarizes the ionic conductivity, viscosity, and Walden product values of ***tri*-1** and **1** at 25 °C. Their ionic conductivities were 3.1×10^{-5} and 4.0×10^{-4} S cm^{-1}, respectively, and the higher ionic conductivity of the latter is consistent with its lower viscosity. These cation and anion are responsible for the ionic conductivity, and the Walden products, i.e., the product of ionic conductivity and solution viscosity, are comparable to those of other ILs.[87,88] The smaller Walden product of ***tri*-1** than **1** is ascribed to its larger cation volume.

Photoirradiation of these liquids resulted in the decrease of ionic conductivity owing to bond formation between the cations, which reduces their mobility. Irradiation of ***tri*-1** reduced its ionic conductivity by two orders of magnitude in 2 h (**Fig. 2-10**). Subsequent heating of the sample at 120 °C for 10 min recovered the conductivity through the reverse reaction, as expected. Changes in ionic conductivity caused by alternate hourly cycles of photoirradiation and heating are shown in **Fig. 2-10b** (dashed line). The changes were smaller for a 10-min cycle (**Fig. 2-10b**, solid line). Photoirradiation of **1** decreased its ionic conductivity by one order of magnitude in 15 min (**Fig. 2-11a**), and heating at 120 °C recovered the initial value. Thus, its photoresponse was considerably faster than that of ***tri*-1**. The change in ionic conductivity was larger than that in ***tri*-1** for the 10-min cycle (**Fig. 2-11b**).

There are various organic polymers that exhibit viscoelastic changes or reversible bond formation by the application of light and heat,[47,49,89–92] but few exhibit changes in ionic conductivity.[74] There are several ionic[27,32,93] and molecular[42,94] materials that display solid-liquid changes by the application of light and heat. Among them, azobenzene-containing ILs exhibit on-off control of the ionic conductivity based on the phase change.[32] The current system, however, exhibits continuous structural changes from an IL to a networked or oligomeric structure, thereby enabling flexible control of the ionic conductivity. The reactivities of Ru complexes is versatile to fabricate such stimuli-responsive materials. Several Ru-containing polymers that exhibit intriguing redox- and photo-responsivity are reported recently.[48]

Table 2-1. Ionic conductivity (25 °C), viscosity, Walden product, and glass transition temperature of ionic liquids ***tri*-1** and **1** before and after UV photoirradiation

Compound	Ionic conductivity (S cm^{-1})		Viscosity (mPa s)		Walden product	T_g
	Before	After	Before	After	(mPa s mS cm^{-1})^a	(°C)^a
***tri*-1**	3.1×10^{-5}	$4.8 \times 10^{-7\,b}$	2.6×10^{3}	$1.2 \times 10^{8\,d}$	81	-53^{f}
1	4.0×10^{-4}	$3.7 \times 10^{-5\,c}$	9.2×10^{2}	$5.2 \times 10^{3\,d}$	370	-60^{g}

[a] Before photoirradiation. [b] After 2 h photoirradiation. [c] After 10 min photoirradiation. [d] After 8 h photoirradiation. [e] After 70 min photoirradiation. [f] Ref. 23. [g] Ref. 86.

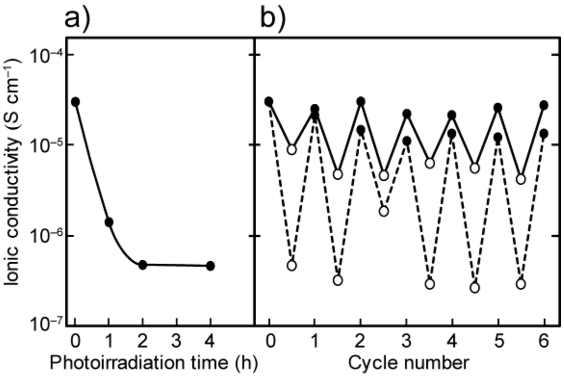

Figure 2-10. (a) Time course of ionic conductivity (25 °C) of ***tri*-1** upon UV irradiation. (b) Ionic conductivity changes of ***tri*-1** for alternating hourly (---) or 10 min (—) cycles of UV photoirradiation (open circles) and 120 °C heating (filled circles).

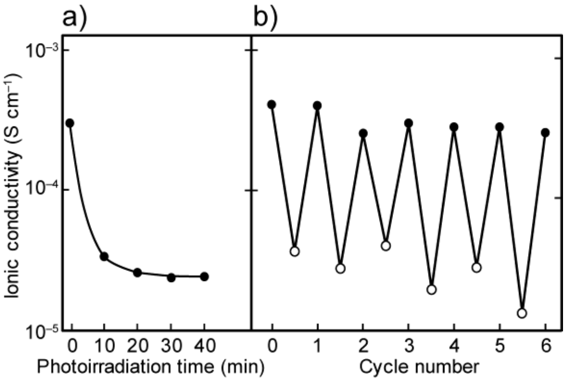

Figure 2-11. (a) Time course of ionic conductivity of **1** upon UV irradiation (25 °C). (b) Ionic conductivity changes of **1** for alternating 10 min (—) cycles of UV photoirradiation (open circles) and heating at 120 °C (filled circles).

2.2.2 Properties and Structures of Ru-Containing ILs with Short Substituents

In the previous section, we demonstrated the control of physical properties using photoreactivity of Ru-containing ILs. To develop ILs with higher reactivity, it is important to clarify the correlation between physical properties and molecular structures. In this section, the thermal properties, photoreactivities, and crystal structures of Ru-containing ILs **2-FSA** and **2-Tf$_2$N** with substituents shorter than that of ***tri*-1** are discussed. **2-FSA** and **2-Tf$_2$N** were synthesized in the similar procedure as ***tri*-1**.[23] These ILs exhibited higher crystallinity and were suitable for the crystal structure analysis, which provided information about their molecular structures and intermolecular interactions.

Thermal properties. Differential scanning calorimetry (DSC) measurements of **2-FSA** and **2-Tf$_2$N** were performed. Both salts were obtained as crystals with melting points of ~80 °C. Upon cooling from the melt, they both underwent a glass transition, at low temperatures.

The DSC trace for **2-FSA** is shown in **Fig. 2-12a**. A solid-phase transition ($\Delta H = 0.3$ kJ mol^{-1}, $\Delta S = 2$ J K^{-1} mol^{-1}) was observed at –155.0 °C (**Fig. 2-13**), which was found to be an order–disorder transition (see below). This salt melted at 86.9 °C ($\Delta H_\mathrm{m} = 48.1$ kJ mol^{-1}, $\Delta S_\mathrm{m} = 133$ J K^{-1} mol^{-1}) and did not crystallize upon cooling from the melt, thus showing a glass transition at –26 °C. The DSC trace for **2-Tf$_2$N** is shown in **Fig. 2-12b**. This salt underwent a phase transition in the solid state at 75.0 °C, which was immediately followed by melting at 78.9 °C ($\Delta H_\mathrm{m} = 46.6$ kJ mol^{-1}, $\Delta S_\mathrm{m} = 132$ J K^{-1} mol^{-1}). Upon cooling from the melt, this salt underwent a glass transition at –26 °C, and during reheating, partial cold crystallization occurred at 29 °C, which was followed by melting. The ratios of the glass transition temperature to the melting points of **2-FSA** and **2-Tf$_2$N** are 0.68 and 0.70, respectively, which agree with the empirical relationship ($T_\mathrm{g}/T_\mathrm{m} = 2/3$) for molecular compounds.[95]

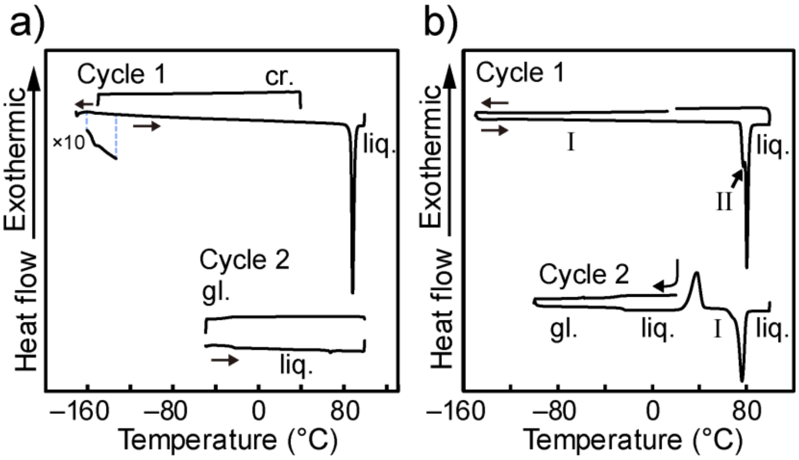

Figure 2-12. DSC traces of (a) **2-FSA** and (b) **2-Tf₂N**, where cr., liq., and gl. are the crystal, liquid, and glassy phases, respectively (scan rate of 10 °C min^{-1}).

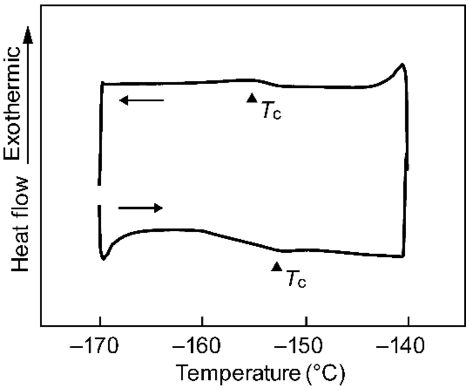

Figure 2-13. DSC traces of **2-FSA**, where T_c is order–disorder transition temperature (scan rate of 5 °C min^{-1}).

Photoreactivity of 2-FSA. The time course of the photoreactivity of **2-FSA** in the liquid state was investigated (**Fig. 2-14**). The supercooled liquid of **2-FSA** at 20 °C gradually transformed to an amorphous coordination polymer upon UV photoirradiation (365 nm, deep UV lamp), similarly to ***tri*-1**.[23] However, the reaction rate was considerably lower (~50% conversion in 7 h). This tendency is consistent with the higher glass transition temperature of **2-FSA** (T_g = –26 °C) than that of ***tri*-1** (T_g = –53 °C [23]), which leads to the higher viscosity of **2-FSA**.

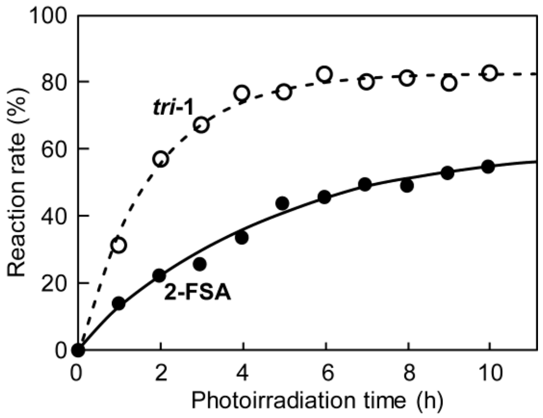

Figure 2-14. Time course of the reaction, where the reaction rate is given by the molar ratio of the photoreacted species in the products generated by photoirradiation of **2-FSA** (—) and ***tri*-1**[23] (----).

Crystal structures of 2-FSA. The crystal structures of **2-FSA** were determined at −173 and 0 °C, which are below and above the solid phase transition temperature ($T_c = -155.0$ °C). The analysis revealed that the phase transition accompanied order–disorder of the anion.

The packing diagrams determined at −173 and 0 °C are shown in **Figs. 2-15a** and **2-15b**, respectively. The space group was $P2_1/n$ at both temperatures. The cations and anions were arranged alternately in the crystal, and there was no π–π interactions between the cations. There were two pairs of crystallographically independent cations and anions at −173 °C ($Z = 8$, **Fig. 2-15a**), whereas an independent pair existed at 0 °C ($Z = 4$, **Fig. 2-15b**). The *a*-axis was halved in the high-temperature phase as compared to that in the low-temperature phase, accompanied by disordering of the anion. However, the molecular arrangements were almost the same in both phases.

The molecular structures at these temperatures are shown in **Fig. 2-16**. The structures of cation A and anion A are shown in **Fig. 2-16a**, while those of cation B and anion B were almost the same (**Fig. 2-17**). Moreover, the molecular structures of the cations were almost the same at both temperatures, with larger thermal ellipsoids at 0 °C than at −173 °C. The three substituents in the cation adopted twisted conformations, two of which were outwardly oriented.

The coordination structures of the cations were almost identical to those of other Ru sandwich complexes.[96–98] The anions were ordered at −173 °C and adopted a *transoid* conformation (**Fig. 2-16a**). At 0 °C, however, the N atom and the SO_2F moieties exhibited two-fold rotational disorders (occupancy ratios = 0.5:0.5, **Fig. 2-16b**). This kind of order–disorder phenomenon of the FSA anion is often observed in the solid state.[99–103]

There were weak intermolecular hydrogen-bond-like interactions between the cyano group of the cation and the arene–H (CH···N = 2.46 and 2.55 Å, at −173 °C; 2.56 Å, at 0 °C), as indicated by dotted lines in **Fig. 2-15a**, which were 0.2–0.3 Å shorter than the van der Waals (vdW) distance. Similar CN···H interactions have been observed in the crystals of imidazolium ILs containing cyanoalkyl substituents.[104,105] There were hydrogen-bond-like interactions between the cation and anion, Cp–H···O, and arene–H···O, which were shorter than the vdW distance by > 0.2 Å. Cp stands for the cyclopentadienyl ring. These interactions may raise the melting point of this salt.

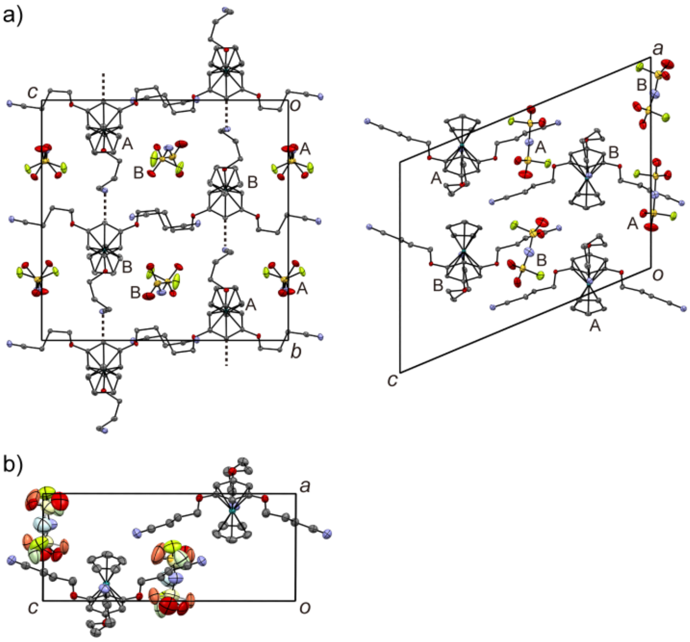

Figure 2-15. Packing diagrams of **2-FSA** at (a) −173 and (b) 0 °C. The dotted lines in (a) represent the CN···H interactions.

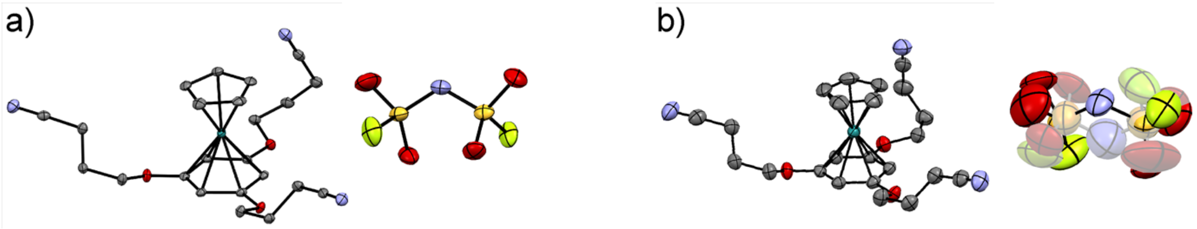

Figure 2-16. Molecular structures of **2-FSA** at (a) −173 and (b) 0 °C. The gray part in (b) represents the disordered moieties with smaller occupancy.

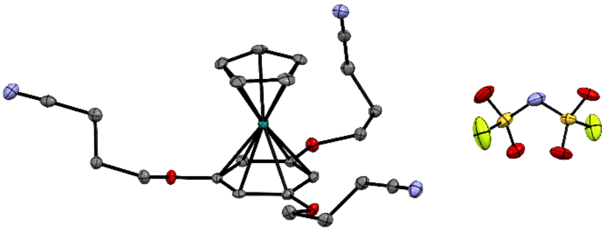

Figure 2-17. Molecular structures of cation B and anion B in **2-FSA** at −173 °C. The hydrogen atoms were omitted for clarity.

Crystal structure of 2-Tf$_2$N. The packing diagram of **2-Tf$_2$N** at –173 °C is shown in **Fig. 2-18a**. The space group was *Pca*2$_1$, and there were two pairs of crystallographically independent cations and anions ($Z = 8$). The cations formed a columnar arrangement through π–π interactions. The anions were not ordered even at this temperature, thus showing severe disorder. The crystal structure was the same at 0 °C.

The structures of cation A and anion A are shown in **Fig. 2-18b**. Cation B and anion B possessed almost the same structures as cation A and anion A (**Fig. 2-19**), respectively. The substituents in the cation adopted twisted conformations and surrounded the sandwich complex moiety. The Cp ring exhibited a rotational two-fold disorder with occupancy ratios of 0.70:0.30 (cation A) and 0.58:0.42 (cation B). The coordination structures of the cations were almost identical to those of other Ru sandwich complexes.[96–98] The cation in **2-Tf$_2$N** displayed a more compact substituent arrangement as compared to that in **2-FSA**.

The cations exhibited a columnar arrangement along the *b*-axis, through π–π interactions.

The column composed of cation A is shown in **Fig. 2-18c**. Cation B also formed a similar column. In the columns, there were two intermolecular C···C contacts between the Cp and arene rings, which were 0.13 Å shorter than the vdW distance (C···C = 3.23, 3.24 Å between cation A and 3.27, 3.26 Å between cation B). The centroid-centroid distances between these rings were 3.77 Å (cation A) and 3.74 Å (cation B). There is a complex with a 1,3,5-substituted arene ligand that shows stronger π–π interactions (Cp–arene centroid-centroid distances: 3.37. 3.43 Å [98]) than this salt. There were weak hydrogen-bond-like interactions between the columns, as indicated by dotted lines in **Fig. 2-18a**. They are between one of the three cyano groups in cation A and the arene–H of cation B in the adjacent column with a distance 0.3 Å shorter than that of vdW (CH···N = 2.48 Å between cations A, and 2.47 Å between cations B). These interactions may raise the melting point of this salt.

The anion was located between the columns of the cations (**Fig. 2-18a**). Between the cation and anion, there were contacts such as $\mathrm{Cp}_{\text{(cation A)}}$–H···$\mathrm{O}_{\text{(anion B)}}$ and $\mathrm{arene}_{\text{(cation B)}}$–H···$\mathrm{O}_{\text{(anion A)}}$, which were more than 0.2 Å shorter than the vdW distance. The anion adopting the *transoid* conformation exhibited severe disorder, where displacements of the atoms by 0.5 Å (anion A) and 1 Å (anion B) occurred, with occupancy ratios of 0.61:0.39 (anion A) and 0.67:0.33 (anion B). The *transoid* conformation is more stable than the *cisoid* one.[106] Disorder of the $\mathrm{Tf_2N}$ anion, which is ordered at low temperatures, is often observed in the solid state.[99–103] The severe disorder of the current salt even at −173 °C is probably due to the large space in which the anions are located. The extensive anion disorder may lower the melting point of this salt.

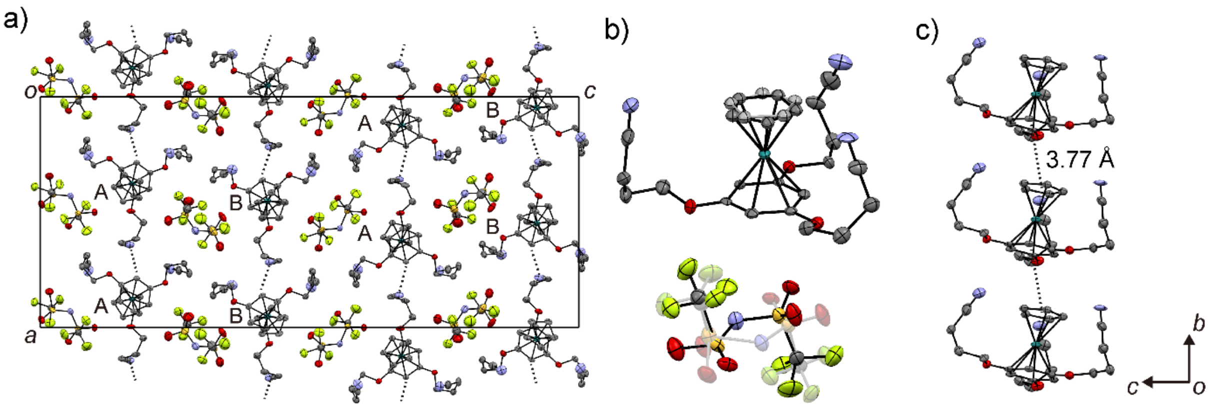

Figure 2-18. Crystal structure of **2-Tf₂N** at −173 °C. (a) Packing diagram (*b*-axis projection); (b) molecular structures of cation A and anion A, where the part displayed in gray shows the disordered moieties; and (c) stacking of the cations (cation A). The dotted lines in (a) represent the CN···H interactions. The dotted lines in (c) represent the centroid-centroid distances.

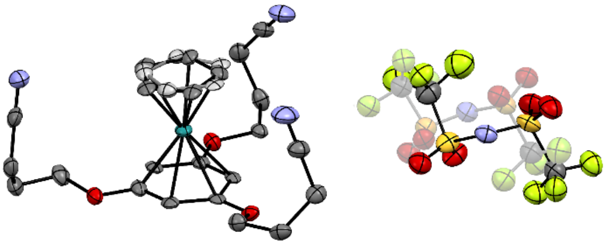

Figure 2-19. Molecular structures of cation B and anion B in **2-Tf₂N** at −173 °C. The hydrogen atoms were omitted for clarity. The part displayed in gray represents the disordered moieties.

2.2.3 Properties and Structures of Ru-Containing ILs with Butylthio Substituents

Although cyano substituents are effective for the photochemical reactions described in the previous sections, the investigation of other substituents is significant. In this section, the thermal properties, photoreactivities, and crystal structures of Ru-containing ILs **3-X** (X = PF_6, FSA, and FTA) with thiobutyl groups were investigated. **3-PF_6** was synthesized by the reaction of $[Ru(C_5H_5)(NCCH_3)_3]PF_6$ with butylthiobenzene, whereas **3-FSA** and **3-FTA** were obtained by anion exchange from the PF_6 salt.

Thermal properties. The results of the DSC of the salts are summarized in **Table 2-2**. **3-PF_6** and **3-FSA** were colorless crystals, whereas **3-FTA** was a pale orange liquid; all these salts were regarded as ILs with melting points below 100 °C.

3-PF_6 melted at 74.0 °C, and no crystallization occurred upon cooling from the melt, exhibiting a glass transition at −45 °C (**Fig. 2-20a**). Upon heating from the glassy state, it changed to a liquid, and then cold crystallization occurred over a temperature range of −10–35 °C. The ratios of the glass transition temperature to the melting points of **3-PF_6** is 0.66, which agree with the empirical relationship ($T_g/T_m = 2/3$) for molecular compounds.[95]

3-FSA melted at 64.4 °C. Unlike **3-PF_6**, this salt crystallized at approximately −20 °C upon cooling from the melt. This behavior was in contrast with that of **1** and **4-FSA**, which exhibit only glass transition (at −60 and −82 °C, respectively).[86,96] In addition, **3-FSA** exhibited a phase transition at −96.7 °C (ΔS = 2.9 J K^{-1} mol^{-1}, **Fig. 2-20b**), which was analyzed by X-ray crystallography to be an order–disorder phase transition (see below).

3-FTA was a liquid at ambient temperature, and no crystallization occurred upon cooling. The liquid exhibited glass transition at −79 °C. This indicates that the FTA anion is effective in producing a Ru-containing organometallic IL with a low melting point.

To investigate the thermal stability of the cation, TG-DTA measurement of **3-FSA** was performed (**Fig. 2-21**). The decomposition temperature of this salt was 234 °C (at 3% weight loss, 10 K min^{-1}), which was 20–30 K lower than those of **1** (253 °C [86]) and **4-FSA** (265 °C [96]).

3-FSA exhibited a weight loss of ~30 wt% at 210–280 °C, which corresponds to the loss of the arene ligand (calculated value: 32 wt%). Therefore, the introduction of the butylthio substituent decreased the thermal stability of the cation.

Table 2-2. Glass transition temperatures (T_g), melting points (T_m), melting enthalpies (ΔH_m), and melting entropies (ΔS_m) of **3-X** (X = PF_6, FSA, and FTA)

	T_g (°C)	T_m (°C)	ΔH_m (kJ mol^{-1})	ΔS_m (J K^{-1} mol^{-1})
3-PF$_6$	–45	74.0	32.1	92.4
3-FSA		64.4	11.7	34.6
3-FTA	–79			

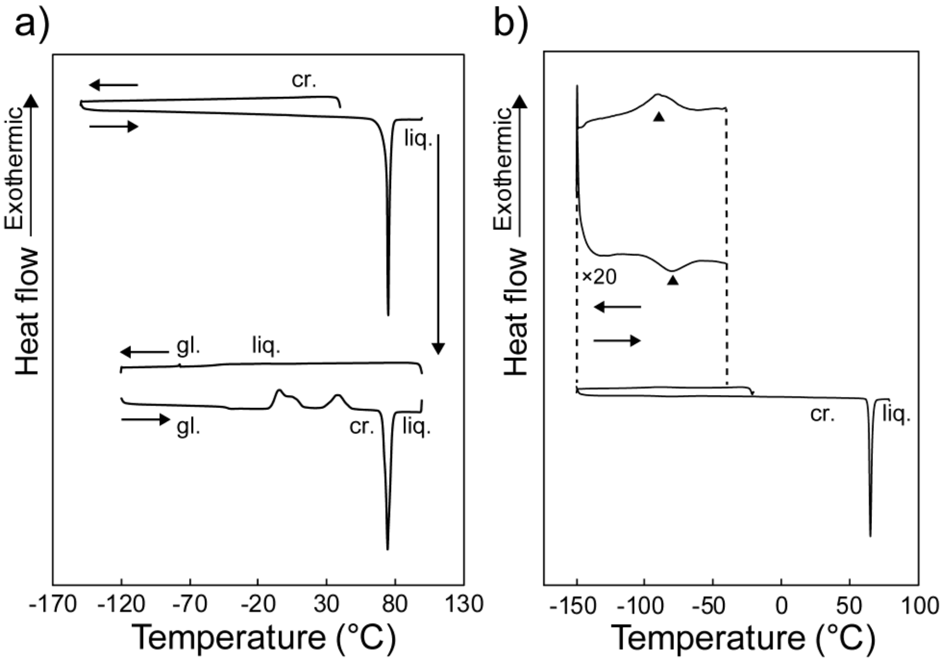

Figure 2-20. DSC traces of (a) **3-PF$_6$** and (b) **3-FSA**, where cr., liq., and gl. are the crystal, liquid, and glassy phases, respectively (scan rate of 10 °C min^{-1}).

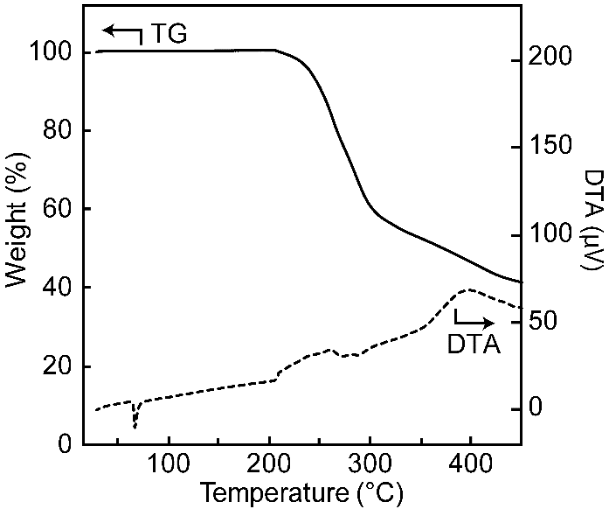

Figure 2-21. TG–DTA traces of **3-FSA** measured under a nitrogen atmosphere at 10 K min^{-1}. The TG and DTA curves are represented by solid and dashed lines, respectively.

Melting points vs. packing efficiency. FSA salts typically exhibit significantly lower melting points than the corresponding PF_6 salts. However, the melting point of **3-FSA** (T_m = 64.4 °C) was closer to that of **3-PF$_6$** (T_m = 74.0 °C) than expected. To investigate the reason, we examined the packing efficiency of the salts in the solid state.

The crystal structures of **3-PF$_6$** and **3-FSA** were determined at −183 °C through X-ray crystallography (see below), and their packing indices were calculated using the Platon software (**Table 2-3**). The packing indices of other Ru-containing complexes calculated from their structural data are summarized in **Table 2-3**. The FSA salts exhibited lower packing indices than the PF_6 salts owing to the asymmetry of the PF_6 anion, which was consistent with their low melting points. However, the comparison is vague as only a few PF_6 and FSA salts have been structurally characterized. The packing index of **3-FSA** (73.6%) was significantly higher than those of the other FSA salts (69–71%), which could be accountable for its relatively high melting point (compared to [Ru(C_5H_5)(PhR)]FSA: T_m = 33.5 °C (R = OCH_2OMe [86]), T_m = 16.9 °C (R = Et [96]), and the salts listed in **Table 2-3**) and tendency to readily crystallize when cooled from the melt. In addition, the lower packing index of **3-PF$_6$** (71.3%) than that of structurally similar PF_6 salts (**Table 2-3**) could be accountable for its lower melting point.

Table 2-3. Packing indices and melting points (T_m) of **3-PF₆**, **3-FSA**, and related salts

Salts		Packing index (%)[a]	T_m (°C)	Reference
PF_6 salts	**3-PF₆**	71.3	74.0	this study
	4-PF₆	74.8	87.0	86
	$[Ru(C_5H_5)(PhOCH_2OMe)]PF_6$	74.1	109.1	86
FSA salts	**3-FSA**	73.6	64.4	this study
	$[Ru(C_5H_5)(PhOC_9H_{19})]FSA$	69.5	57.9	107
	$[Ru(C_5H_5)\{1,2,3\text{-}C_6H_3(OEt)_3\}]FSA$	68.6	59.8	97
	2-FSA	71.4	86.9	this study

[a] Calculated for the structures at −183 °C (**3-PF₆** and **3-FSA**) and at −173 °C (other salts).

Crystal structures of 3-PF₆ and 3-FSA. X-ray crystallography of **3-PF₆** and **3-FSA** indicated significantly similar packing to each other. The low-temperature phase transition of **3-FSA** was an order–disorder phase transition of the cations and anions.

X-ray crystallography of **3-PF₆** was performed at −183 °C; the packing diagram is shown in **Fig. 2-22a**. The compound crystallized in the space group $P\overline{1}$ ($Z = 2$), and the asymmetric unit contained a pair of cation and anion. The cations and anions were arranged alternately, and every cation was surrounded by six anions. The PhSBu moieties were adjacent to each other between the cations although no π–π interactions were discerned.

X-ray crystallography of **3-FSA** was performed at −183 °C and 0 °C to investigate the nature of the phase transition at −97 °C. The packing diagrams at both temperatures are shown in **Fig. 2-22b**, which closely resembled that of **3-PF₆**. The space group was the same in both phases ($P\overline{1}$, $Z = 2$), and the asymmetric unit contained a pair of cation and anion. The molecular arrangements were almost identical at both temperatures, with larger thermal ellipsoids at 0 °C than at −183 °C. No disorder was discerned at −183 °C, whereas the cations and anions exhibited disorder at 0 °C. The Cp ring of the cation exhibited a two-fold rotational disorder at

0 °C with an occupancy ratio of 0.38:0.62. The anion adopted an ordered *transoid* structure at −183 °C, and the environments around the two SO$_2$F groups were different; there were short O···HC contacts between one of the SO$_2$F groups and the arene moieties of the neighboring cations, which were 0.2–0.4 Å shorter than the van der Waals distance. At 0 °C, the N atom and SO$_2$F moieties of the anion exhibited an extensive three-fold rotational disorder with an occupancy ratio of 0.53:0.27:0.20 (**Fig. 2-23**). FSA anions typically exhibit an order–disorder phase transition in the crystal[100,102,108] although the disorder is generally two-fold; hence, the observed three-fold disorder was distinctive.

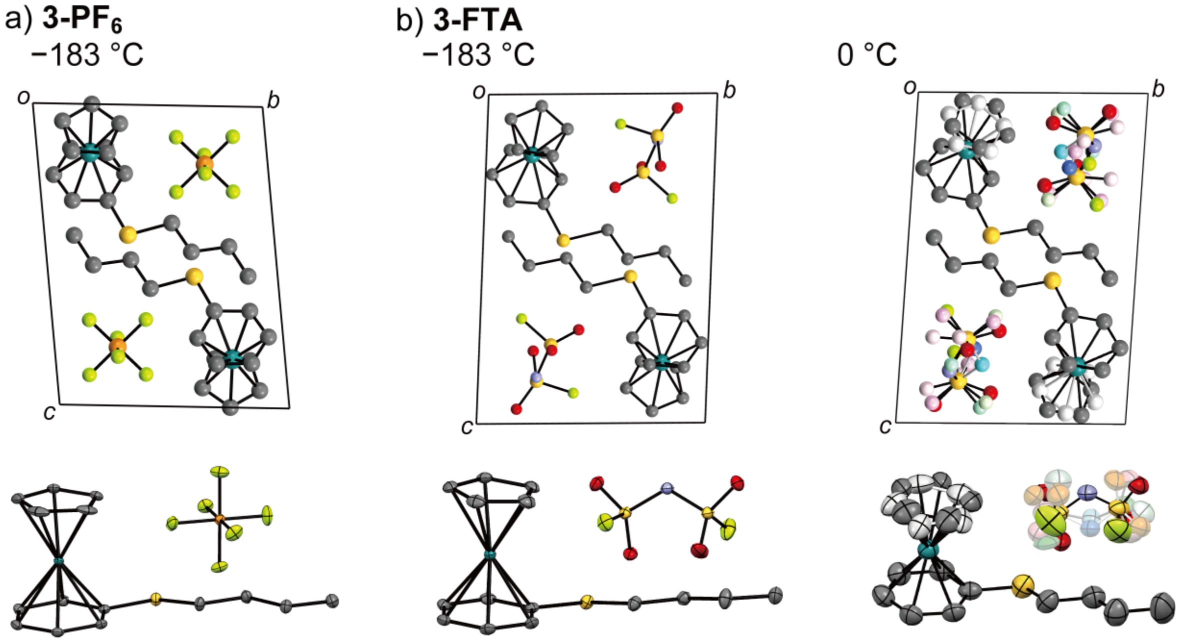

Figure 2-22. Packing diagrams of (a) **3-PF$_6$** (−183 °C) and (b) **3-FSA** (−183 and 0 °C). The ORTEP diagrams of the molecular structures are shown below each figure. The disordered moieties are displayed in gray.

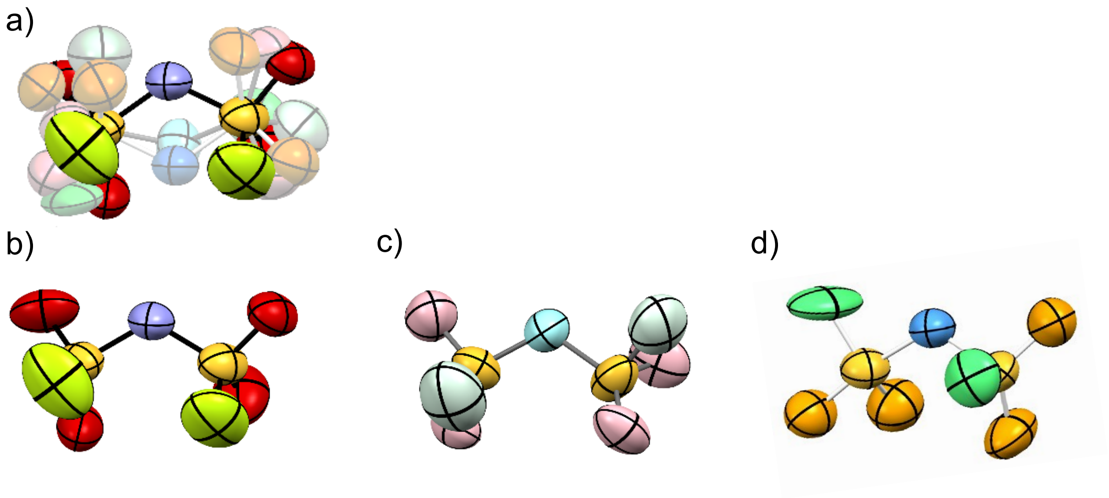

Figure 2-23. Structure of the anion in the **3-FSA** crystal at 0 °C. (a) Disorder structure and (b–d) three components of the disorder, whose occupancies are 0.53, 0.27, and 0.20, respectively.

Photoreactivity of 3-FTA. The UV photoirradiation (365 nm, LED) of **3-FTA** for 30 min resulted in a mixture of photoproducts and unreacted species, and the pale orange liquid transformed to a yellow and more viscous liquid. The change in the UV-vis spectra due to photoirradiation can be observed in **Fig. 2-24a**, which shows a new absorption peak at approximately 410 nm. This observation, along with the changes in the ^{1}H NMR and FT-IR spectra (**Figs. 2-25** and **2-26**), indicated that the sandwich structure transformed to a half-sandwich structure.[23] A plausible structure of the dominant photoproduct, which is a dinuclear complex, is shown in **Fig. 2-27** (product A). After photodissociation, the Ru ion accepts three donor atoms, namely, the dissociated ligand (PhSBu) and the undissociated cation and anion. Density functional theory (DFT) calculations indicated that the suggested structure was the most stable among plausible structures (**Fig. 2-28**). However, the structure could not be confirmed through ^{1}H NMR spectroscopy because of dissociation.

The amount (%) of photodissociated cations as a function of photoirradiation time was determined from the ^{1}H NMR spectra; the plot is shown in **Fig. 2-29a**. The amount was 22% in 45 min, which corresponded to a 43% yield of product A. This result indicates that the reaction is considerably less efficient than that of **1** (93% in 15 min). The low efficiency could be attributed to the UV-vis absorption of the photoproduct, which made the photoirradiation at 365 nm less effective, and a likely thermal reverse reaction during photoirradiation.

As the coordination ability of the sandwich complex ligand in product A is weak owing to its cationic nature, it could dissociate to produce product B, as shown in **Fig. 2-27**. The dissolution of the yellow photoproduct in dichloromethane produced a yellow–green solution, which exhibited a UV-vis absorption peak at approximately 427 nm (**Fig. 2-30**). Furthermore, after removal of free ligands from product A through gel permeation chromatography (GPC), a peak was observed in the ESI-MS spectrum at *m*/*z* = 585.2495 (Na^+ adduct) that corresponded to product B. DFT calculations predicted that the structure of product B (**Fig. 2-28**) is similar to those of other Ru complexes with the *N*,*O*-chelate coordination of FSA.[109] However, we were unable to isolate the compound; thus, the peaks of the ^1H NMR and ESI-MS spectra could not be completely assigned.

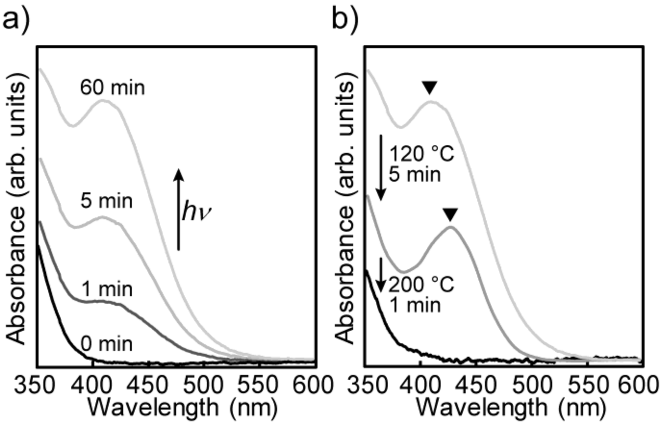

Figure 2-24. UV-vis spectral changes upon (a) photoirradiation of **3-FTA** and (b) heating the photoproduct of **3-FTA**. The sample was sandwiched between two quartz plates to perform the measurements.

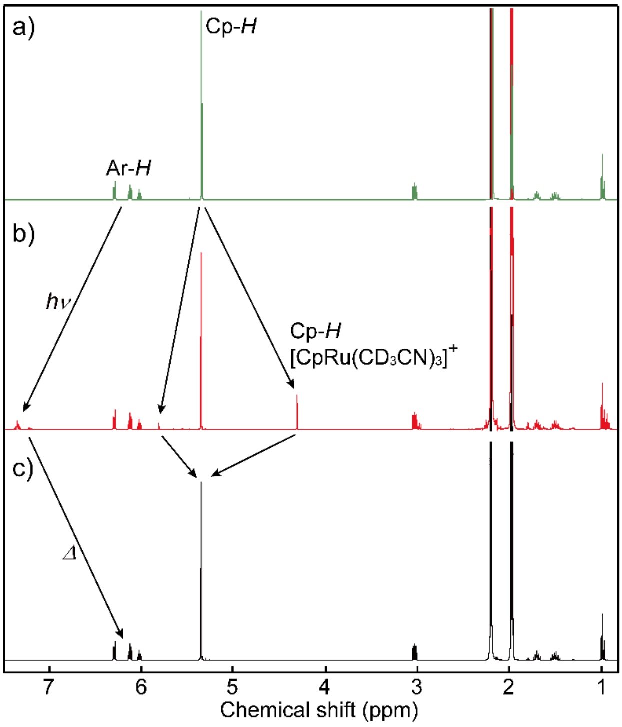

Figure 2-25. ^{1}H NMR spectra (in CD_3CN) of **3-FTA** (a) before and (b) after photoirradiation for 90 min and (c) after heating the photoproduct at 200 °C for 1 min. In CD_3CN, weakly coordinated ligands dissociate from the half-sandwich complexes to produce solvent-coordinated complexes such as $[Ru(C_5H_5)(NCCD_3)_3]^+$ and $[Ru(C_5H_5)(PhSBu)(NCCD_3)_2]^+$.

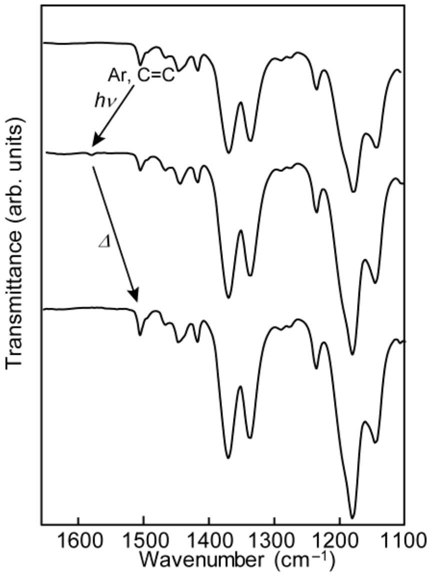

Figure 2-26. Changes in FT-IR spectra observed upon photoirradiation of **3-FTA** for 90 min and after successive heating of the photoproduct at 200 °C for 1 min.

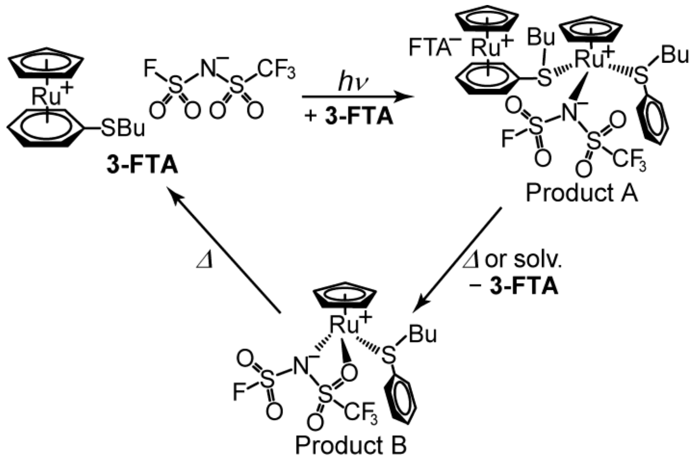

Figure 2-27. Putative photochemical and thermal reactions of **3-FTA**.

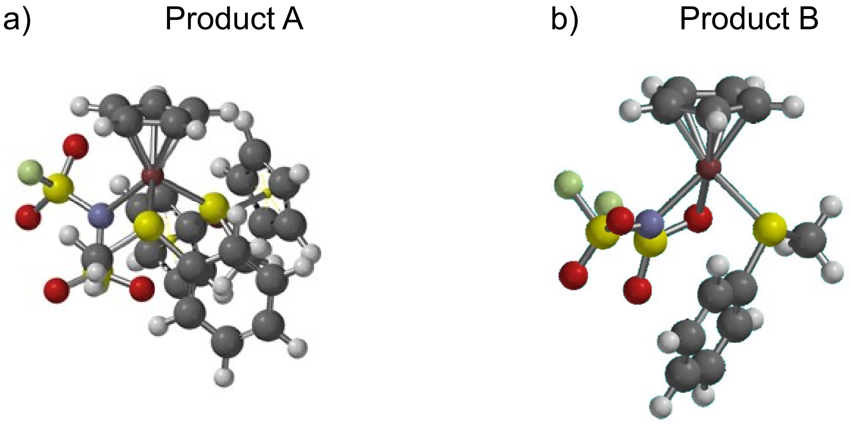
a) Product A

b) Product B

Figure 2-28. Optimized geometries of products A and B obtained using DFT calculations (B97-D/LanL2DZ). The butyl group of the cation was replaced with a methyl group for the calculations.

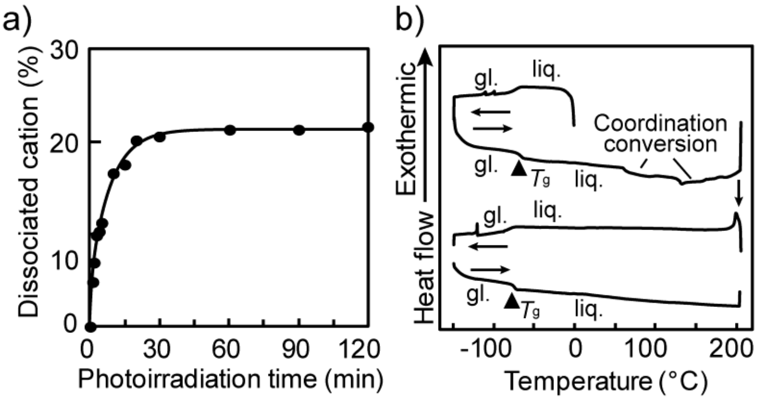

Figure 2-29. (a) Amount (%) of the photodissociated cations observed for the photoreaction of **3-FTA** plotted as a function of photoirradiation time. (b) DSC traces (first and second cycles) of the photoproduct of **3-FTA**.

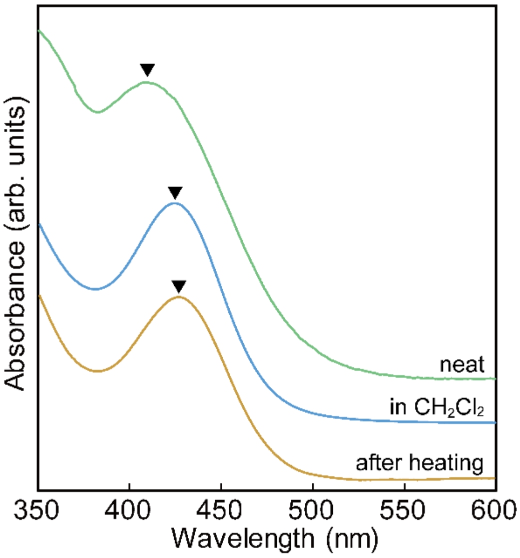

Figure 2-30. UV-vis spectra of the photoproduct of **3-FTA** in the neat state (top), in CH_2Cl_2 solution (middle), and in the neat state after heating at 120 °C for 5 min (bottom).

Thermal reaction of the photoproduct of 3-FTA. The photoproduct of **3-FTA** transformed back to **3-FTA** via an intermediate state upon heating. After heating the photoproduct (λ_{max} = 410 nm) at 120 °C for 5 min, the UV–vis absorption peak shifted to 427 nm (**Fig. 2-24b**). Based on the results discussed in the previous section, we deduced that the intermediate contained cation-dissociated product B. After further heating at 200 °C for 1 min (or 120 °C for 1 h), **3-**

FTA was completely recovered, and no UV-vis absorption peak was observed in the visible region. The recovery was further confirmed by the changes in the ^{1}H NMR spectrum (**Fig. 2-25**).

The thermal reaction of the photoproduct was analyzed by DSC (scan rate: 10 °C min^{-1}, **Fig. 2-29b**). During the first heating cycle, the photoproduct exhibited a glass transition at −72 °C and significantly broad endothermic peaks from 60–180 °C, which were attributed to the coordination transformation of the cation.[23] The results were similar at a scan rate of 5 °C min^{-1}. Considering the reactivity of the photoproduct, we speculated that the broad peaks at approximately 80 and 140 °C corresponded to the transformation of product A to B and then to the original IL. The onset of decomposition at >180 °C was indicated by the occurrence of an exotherm. In the second cycle, a glass transition was observed at −77 °C, and the broad endothermic peaks at high temperatures were absent, which is consistent with the recovery of **3-FTA**. The thermal reverse reaction occurred at a higher temperature range than that for the photoproduct of ***tri*-1** (50–120 °C [23]), which is attributed to the stronger S–Ru bond than the CN–Ru bond.

These results indicated that the photoreaction of the sulfur-containing IL was significantly different from those of the ILs containing cyano substituents. The photoreactivity and conversion of the sulfur-containing IL were low, and the photoproducts were likely dinuclear or mononuclear complexes and not oligomers owing to the low coordination ability of the cationic ligand. Sulfide sulfur generally has a stronger coordination ability to Ru ions than the cyano group. Therefore, ILs with dialkylsulfide substituents may produce bridged structures with higher thermal stability upon photoirradiation. However, their products might be susceptible to C–S bond cleavage.

Ionic conductivities of 3-FTA. The ionic conductivity of **3-FTA** decreased after UV photoirradiation owing to the photochemical reaction. The ionic conductivity of **3-FTA** was 8.8

× 10^{-4} S cm^{-1} at 25 °C, which was lower than those of typical imidazolium ILs (e.g., 4.1 × 10^{-3} S cm^{-1} for [Bmim]Tf_2N [110]) but higher than those of Ru-containing organometallic ILs with other anions (e.g., 4.0 × 10^{-4} S cm^{-1} for **1**) owing to its low viscosity. Upon UV irradiation for 70 min, the ionic conductivity of the IL decreased to 8.7 × 10^{-5} S cm^{-1} (**Fig. 2-31a**). This is consistent with the formation of product A, which is accompanied by a decrease in the number of carrier ions and an increase in viscosity. As seen in **Fig. 2-31a**, the photoreaction was slower than that of **1**. The magnitude of the conductivity change of **3-FTA** was similar to that of **1** (4.0 × 10^{-4} S cm^{-1} to 3.7 × 10^{-5} S cm^{-1}) despite the lower reaction rate of **3-FTA** (suggested 43% yield of product A) than that of **1** (93%). This is probably because the anion in **3-FTA** is bound to the photoproduct, whereas the anion in **1** is free after the photoreaction.

The intermediate formed after heating the photoproduct at 120 °C for 1 h exhibited an ionic conductivity of 1.7 × 10^{-4} S cm^{-1}. This value was between those before and after photoirradiation, which is coherent considering the dissociation of product A. Further heating of the photoproduct at 200 °C for 3 min increased its ionic conductivity to 2.1 × 10^{-4} S cm^{-1}. This value was slightly lower than the initial value, which might be owing to slight decomposition.

The temperature dependence of the ionic conductivity of **3-FTA** before and after photoirradiation was measured (**Fig. 2-31b**). The data before photoirradiation were fitted using the Vogel–Fulcher–Tamman (VFT) equation[111–113]:

$$\sigma(T) = \frac{\mathrm{A}}{\sqrt{T}}\exp\left(\frac{-E_a}{k_B(T-T_0)}\right),$$

where A is proportional to the number of carrier ions in the matrix, and E_a and T_0 are the activation energy for ion transport and the ideal glass transition temperature, respectively. The obtained values of these parameters were E_a = 162(19) meV, A = 623(319) S $K^{1/2}$ cm^{-1}, and T_0 = 122(12) K, where the values in parentheses are the standard deviations. The data after photoirradiation were fitted using the Arrhenius equation $\sigma(T) = \sigma_\infty \exp(-E_\mathrm{a}/k_\mathrm{B}T)$[114,115] ($E_\mathrm{a}$ =

730(12) meV and $\sigma_\infty = 2.2(0.9) \times 10^8$ S cm^{-1}) and indicated a linear relationship. However, the plot deviated from the straight line above 60 °C owing to the thermal reaction. The larger activation energy after photoirradiation was consistent with the higher viscosity and larger molecules of product A.

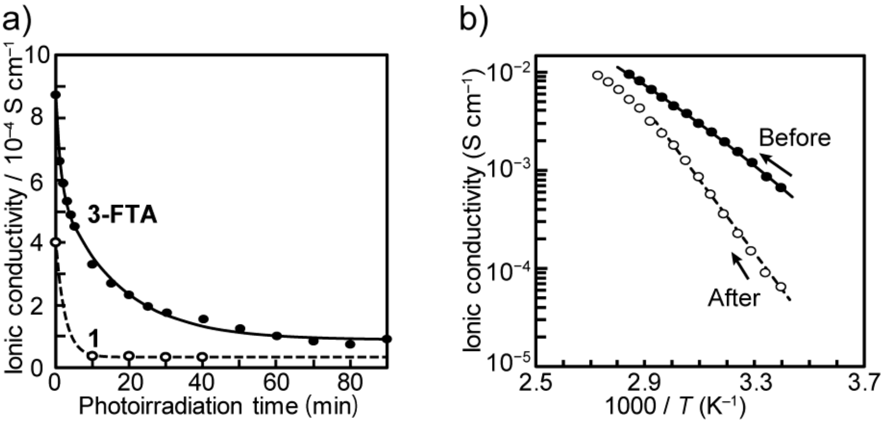

Figure 2-31. (a) Change in ionic conductivities of **3-FTA** (solid line) and **1** (dashed line) as a function of photoirradiation time. (b) Temperature dependence of ionic conductivity of **3-FTA** before (●) and after (○) photoirradiation. The solid and dashed lines in (b) indicate the fitting with the VFT and Arrhenius equations, respectively.

2.3 Conclusion

This study demonstrated reversible control of ionic conductivity and viscoelasticity of Ru-containing ILs via photochemical and thermal reactions. In addition, the molecular design strategies for these photoreactive ILs were derived. The photoreactivity and melting point of these ILs varied with the number and species of substituents. The crystal structure analysis revealed that the melting point is higher for salts with dense packing.

The ionic conductivity and viscoelasticity of Ru-containing ILs ***tri*-1** and **1** could be reversibly controlled by the application of light and heat. The physical property changes are based on the reversible formation of intermolecular bonds. It is noteworthy that the numbers of substituents caused striking changes in the photoproducts, i.e., a three-dimensional coordination polymer solid or an oligomeric liquid. Therefore, the viscoelasticity changes, reaction rates, and physical properties of the materials were tunable by their substituents. Their IL characteristics, such as nonvolatility, are advantageous for applications such as photocontrollable capacitors, sensors, and other electronic devices.

Furthermore, Ru-containing organometallic ILs bearing cyanopropyloxy substituents **2-FSA** and **2-Tf$_2$N** were synthesized. The substituents were shorter than those in ***tri*-1**. Accordingly, the synthesized ILs had high melting points (but lower than 100 °C), enabling crystal structure analysis. The supercooled liquid of **2-FSA** exhibited a photochemical transformation into an amorphous coordination polymer, though the reaction rate was considerably low owing to its high viscosity. The crystal structure analysis revealed the characteristic features of the ILs, which may affect the physical properties of organometallic ILs and may be partly responsible for their high glass transition temperatures and high melting points.

In addition, Ru-containing organometallic ILs with sulfur-containing substituents **3-X** (X = PF$_6$, FSA, and FTA) were synthesized. **3-FSA** and **3-PF$_6$** exhibited relatively high melting points, and the high melting point of the former was attributed to its dense crystal packing. **3-FSA** underwent an order–disorder phase transition of the anions and cations at low temperatures.

3-FTA was in the liquid state, which indicated that the unsymmetric anion is effective for obtaining Ru-containing organometallic ILs with low melting points. The results of this study are beneficial for the design of photofunctional materials based on Ru-containing organometallic ILs.

2.4 Experimental Section

General. [Ru(C_5H_5)($NCCH_3$)$_3$]PF_6, ***tri*-1**, and **1** were synthesized according to the procedure in the literature.[21–23,86] Butylthiobenzene was synthesized by the reaction of thiophenol and 1-bromobutane in methanol (yield 89%).[116] Other reagents were purchased from TCI Co. (Tokyo, Japan). ^{1}H, ^{13}C, and ^{19}F NMR spectra were recorded using Bruker Avance 400 instruments (400 MHz). FT-IR spectroscopy were carried using a Thermo Nicolet iS5 spectrometer equipped with an attenuated total reflectance unit (ATR, diamond). UV-vis absorption spectroscopy was conducted using a JASCO V-570 UV/VIS/NIR spectrophotometer. DSC measurements were performed using a TA Instruments Q100 differential scanning calorimeter at scan rates of 10 and 5 °C min^{-1} using aluminum hermetic pans as sample containers. TG-DTA measurements were performed using a Rigaku TG8120 thermal analyzer at a scan rate of 10 K min^{-1} under a nitrogen atmosphere. GPC was performed using a Recycling Preparative HPLC system (LC908, Japan Analytical Industry) equipped with JAIGEL-2HR (eluent: chloroform). Dynamic viscoelasticity was measured using a TA Instruments DHR-1 rheometer equipped with a ϕ 8 mm parallel plate. The frequency dependence of the dynamic viscoelasticity (1–100 rad s^{-1}) was measured at 25 °C under an application of 1% strain. Ionic conductivity was measured using a Solartron 1260 impedance analyzer. Gold interdigitated electrodes with gap dimensions of 200 μm were used; the cell constant was determined by measuring the conductivity of 0.01 M KCl aqueous solution at 25 °C. The sample was sandwiched between an electrode and a quartz plate and sealed with epoxy resin. A Japan High Tech 10013 L heating/cooling stage was used for temperature control. Electrospray ionization–mass spectrometry (ESI-MS) was performed using a Thermo Fisher Scientific LTQ-Orbitrap Discovery instrument.

Photochemical reactions. Photoirradiation was carried out with a deep UV lamp (250 W) using USHIO SP-9 SPOT CURE for **2-FSA**, and LED light source (Hamamatsu Photonics LC-L1V3, 0.6 W cm^{-2}) for other salts. The photoirradiation was conducted at 20 °C for **2-FSA** and 10 °C for other salts on samples sandwiched between two quartz plates or sealed in the electrode cells for conductivity measurements. The reaction rates were determined from the UV–Vis spectral absorbance (365 or 370 nm), and ^{1}H NMR spectra.[23] The samples used for the viscoelasticity measurements were thicker than those used in other experiments; hence, the photoreaction speed was considerably slower. The ESI-MS spectrum (solvent: CH_2Cl_2) of the photoreaction product of **1** was measured, and its peak appeared at the same position as that of **1** because it is trivalent. ESI-MS: m/z calcd. for $[Ru_3(C_5H_5)_3(C_6H_5OC_3H_6CN)_3]^{3+}$ 328.0275, found 328.0280.

Synthesis of $[Ru(C_5H_5)\{1,3,5\text{-}C_6H_3(OC_3H_6CN)_3\}]$FSA (2-FSA). 2-FSA was synthesized by the same method that was employed for the synthesis of the cyanohexyloxy derivative,[23] except that 1,3,5-$C_6H_3(OC_3H_6CN)_3$ was utilized as the arene ligand (white solid, yield 35%). The single crystals were prepared by the slow diffusion of diethyl ether into a dichloromethane (DCM) solution of the salt. ^{1}H NMR (400 MHz, $CDCl_3$, TMS): δ = 2.15 (m, 6H, -$OCH_2CH_2CH_2CN$), 2.60 (t, J = 6.7 Hz, 6H, -$OCH_2CH_2CH_2CN$), 4.14 (t, J = 5.5 Hz, 6H, -$OCH_2CH_2CH_2CN$), 5.39 (s, 5H, Cp), 6.11 (s, 3H, ArH). FT-IR (ATR, cm^{-1}): 569 (s), 740 (m), 825 (m), 1046 (m), 1104 (m), 1174 (vs), 1362 (m), 1379 (m), 1537 (m), 2247 (w). ESI-MS: m/z calcd. for $[C_{23}H_{26}N_3O_3Ru]^+$ 494.1018, found 494.1034. Anal. calcd. for $C_{23}H_{26}F_2N_4O_7RuS_2$: C, 41.01; H, 3.89; N, 8.32. Found: C, 41.14; H, 3.88; N, 8.14.

Synthesis of $[Ru(C_5H_5)\{1,3,5\text{-}C_6H_3(OC_3H_6CN)_3\}]Tf_2N$ (2-Tf_2N). 2-Tf_2N was synthesized by the same method, except that $LiTf_2N$ was utilized instead of KFSA for the anion exchange. The product was recrystallized from ethyl acetate–diethyl ether (white solid, yield 46%). The single crystals utilized for the structural analysis were prepared by the slow diffusion of diethyl ether into a DCM solution of the salt. ^{1}H NMR (400 MHz, $CDCl_3$, TMS): δ= 2.15 (m, 6H, -$OCH_2CH_2CH_2CN$), 2.59 (t, J = 6.7 Hz, 6H, -$OCH_2CH_2CH_2CN$), 4.16 (t, J = 5.7 Hz, 6H, -$OCH_2CH_2CH_2CN$), 5.41 (s, 5H, Cp), 6.13 (s, 3H, ArH). FT-IR (ATR, cm^{-1}): 569 (s), 609 (s), 739 (m), 795 (m), 852 (m), 894 (m), 1046 (s), 1173 (vs), 1350 (m), 1391 (m), 1425 (m), 1537 (s), 2240 (w). Anal. calcd. for $C_{25}H_{26}F_6N_4O_7RuS_2$: C, 38.81; H, 3.39; N, 7.24. Found: C, 38.83;

H, 3.34; N, 7.36.

Synthesis of [Ru(C_5H_5)(PhSBu)]PF_6 (3-PF_6). [Ru(C_5H_5)($NCCH_3$)$_3$]PF_6 (303 mg, 0.70 mmol) was dissolved in acetonitrile (10 mL) in a nitrogen atmosphere. Then, butylthiobenzene (162 mg, 0.97 mmol) was added to the solution and stirred at 90 °C for 24 h. The resultant solution was evaporated under reduced pressure, and the residue was dissolved in a small amount of acetonitrile. The solution was charged to an alumina column, and unreacted ligand was eluted with hexane. Then the desired compound was eluted with acetonitrile. The solvent was evaporated and the residue dried under vacuum. The residue was recrystallized from acetone–diethyl ether by slow cooling to −60 °C and then collected by filtration. A few black and solid impurities were observed using a microscope and were subsequently removed. The desired product was obtained as a white needle-shaped crystal (131 mg, 39%). ^{1}H NMR (400 MHz, $CDCl_3$): δ = 0.97 (t, 3H, CH_3, J = 7.32 Hz), 1.49 (sext, 2H, $SCH_2CH_2CH_2$, J = 7.68 Hz), 1.69 (quint, 2H, $SCH_2CH_2CH_2$, J = 7.64 Hz), 3.00 (t, 2H, $SCH_2CH_2CH_2$, J = 7.36 Hz), 5.39 (s, 5H, Cp-H_5), 6.11 (t, 1H, Ar-H_1, J = 5.68 Hz), 6.21 (t, 2H, Ar-H_2, J = 6.32 Hz), 6.27 (d, 2H, Ar-H_2, J = 5.88 Hz). FT-IR (ATR, cm^{-1}): 567, 728 (S–F), 824, 1088 (C–C), 1179 (S=O), 1363 (S=O), 1418 (Cp, C–H), 1503 (C=C), 2871, 2932, 2954, 3092 (C–H). Anal. calcd. for $C_{15}H_{19}F_6PRuS$: C, 37.7, H, 4.01, N, 0.00. Found: C, 37.8, H, 4.17, N, 0.03.

Synthesis of [Ru(C_5H_5)(PhSBu)]FSA (3-FSA). An aqueous solution of K[FSA] (178 mg, 0.812 mmol) was added to a solution of [Ru(C_5H_5)(PhSBu)]PF_6 (128 mg, 0.268 mmol) in acetone and stirred for 20 min. Then, acetone was evaporated under reduced pressure, followed by the addition of water and dichloromethane to the residue. The residue was extracted five times using dichloromethane, and the obtained combined organic layer was dried using anhydrous magnesium sulfate. The anion exchange procedure was repeated and the complete exchange of PF_6 was confirmed by the absence of the PF_6 peak (δ = −73.83, −71.92) in the ^{19}F NMR spectrum (solvent: CD_3CN). Subsequently, the residue was recrystallized from acetone–diethyl ether by slow cooling to −60 °C. The desired product was obtained as white needle-shaped crystals (88 mg, 64%).^{1}H NMR (400 MHz, CD_3CN): $\delta = 0.98$ (t, 3H, CH_3, $J = 7.36$ Hz), 1.49 (sext, 2H, $SCH_2CH_2CH_2$, $J = 7.68$ Hz), 1.70 (quint, 2H, $SCH_2CH_2CH_2$, $J = 7.52$ Hz), 3.02 (t, 2H, $SCH_2CH_2CH_2$, $J = 7.48$ Hz), 5.34 (s, 5H, Cp-H_5), 6.01 (t, 1H, Ar-H_1, $J = 5.72$ Hz), 6.11 (t, 2H, Ar-H_2, $J = 6.4$ Hz), 6.28 (d, 2H, Ar-H_2, $J = 5.92$ Hz). FT–IR (ATR, cm^{-1}): 569, 601, 721 (S–F), 759, 805, 848, 1074 (C–C), 1146 (S=O), 1181, 1337, 1370 (S=O), 1418 (Cp, C–H), 1504 (C=C), 2874, 2933, 2962, 3112 (C–H). Anal. calcd. for $C_{15}H_{19}F_2NO_4RuS_3$: C, 35.15, H, 3.74, N, 2.73. Found: C, 35.49, H, 3.47, N, 2.87.

Synthesis of [Ru(C_5H_5)(PhSBu)]FTA (3-FTA). Anion exchange was conducted as described for **3-FSA** using Li[FTA] (80 mg, 0.337 mmol) and [Ru(C_5H_5)(PhSBu)]PF_6 (70.3 mg, 0.147 mmol). The procedure was repeated three times, and the crude product was purified by passing it through a short alumina column (eluent: acetonitrile). After the solvent was evaporated, the residue was heated under vacuum at 60 °C for 15 h. The desired product was obtained as a pale orange liquid (78 mg, 94%). ^{1}H NMR (400 MHz, CD_3CN): $\delta = 0.98$ (t, 3H, CH_3, $J = 7.36$ Hz), 1.50 (sext, 2H, $SCH_2CH_2CH_2$, $J = 7.6$ Hz), 1.70 (quint, 2H, $SCH_2CH_2CH_2$, $J = 7.56$ Hz), 3.02 (t, 2H, $SCH_2CH_2CH_2$, $J = 7.48$ Hz), 5.34 (s, 5H, Cp-H_5), 6.02 (t, 1H, Ar-H_1, $J = 5.72$ Hz), 6.12 (t, 2H, Ar-H_2, $J = 6.32$ Hz), 6.29 (d, 2H, Ar-H_2, $J = 5.88$ Hz). ^{19}F NMR (400 MHz, CD_3CN): $\delta = -79.3, 55.6$. FT–IR (ATR, cm^{-1}): 721 (C–S), 759, 805, 848, 1074 (C–C), 1146, 1181, 1337, 1370 (S=O), 1418 (Cp, C–H), 1504 (C=C), 2874, 2933, 2962, 3112 (C–H). Anal. calcd. for $C_{16}H_{19}F_4NO_4RuS_3$: C, 34.16; H, 3.40; N, 2.49. Found: C, 34.53; H, 3.40; N, 2.10.

X-ray crystallography. Single crystal X-ray diffraction data were collected using Bruker APEX II Ultra (X-ray source: MoKα). The crystals were cooled at the rate of 2 °C min^{-1}. Calculations were performed using SHELXL[117]; the crystallographic parameters are listed in **Table 2-4** and **2-5**. Packing indices were calculated using the Platon software.[118] Because of the severe disorder, restraints were applied to the temperature factors of the anion in **2-FSA** at 0 °C, the temperature factors of anion B, the cation Cp rings and the bond lengths of anion B in **2-**

Tf_2N.

CCDC 1997224 (**2-FSA**, −173 °C), 1997223 (**2-FSA**, 0 °C), 1997222 (**2-Tf_2N**, −173 °C), 2052308 (**3-PF_6**, −183 °C), 2059258 (**3-FSA**, −183 °C), and 2063565 (**3-FSA**, 0 °C) contain the crystallographic data pertaining to this work.

Table 2-4. Crystallographic parameters for **2-FSA** and **2-Tf_2N**

	2-FSA (−173 °C)	**2-FSA** (0 °C)	**2-Tf_2N** (−173 °C)
Empirical formula	$C_{23}H_{26}F_2N_4O_7RuS_2$	$C_{23}H_{26}F_2N_4O_7RuS_2$	$C_{25}H_{26}F_6N_4O_7RuS_2$
Formula weight	673.67	673.67	773.69
Crystal system	Monoclinic	Monoclinic	Orthorhombic
Space group	$P2_1/n$	$P2_1/n$	$Pca2_1$
a [Å]	15.653(2)	7.9875(4)	19.279(4)
b [Å]	18.163(2)	18.2176(9)	7.0227(15)
c [Å]	20.218(3)	18.8031(9)	45.241(10)
α [°]	90	90	90
β [°]	112.705(2)	90.2270(10)	90
γ [°]	90	90	90
V [Å^3]	5302.6(12)	2736.1(2)	6125(2)
Z	8	4	8
ρ_{calcd} [g cm^{-3}]	1.688	1.635	1.678
μ [mm^{-1}]	0.814	0.789	0.734
Temperature [K]	100	273	100
$F(000)$	2736.0	1368.0	3120.0
Reflns collected	30745	15866	32824
R_{int}	0.0342	0.0249	0.0278
Goodness of fit	1.029	1.023	1.107
$R_1{}^a$, $R_w{}^b$ ($I > 2\sigma(I)$)	0.0402, 0.0981	0.0368, 0.0956	0.0527, 0.1218
$R_1{}^a$, $R_w{}^b$ (all data)	0.064, 0.1112	0.0488, 0.1037	0.0563, 0.1218

$^aR_1 = \Sigma||F_o| - |F_c|| / \Sigma|F_o|$. $^bR_w = [\Sigma w (F_o^2 - F_c^2)^2/\Sigma w (F_o^2)^2]^{1/2}$.

Table 2-5. Crystallographic parameters for **3-PF$_6$** and **3-FSA**

	3-PF$_6$ (−183 °C)	**3-FSA** (−183 °C)	**3-FSA** (0 °C)
Empirical formula	$C_{15}H_{19}F_6PRuS$	$C_{15}H_{19}F_2NO_4RuS_3$	$C_{15}H_{19}F_2NO_4RuS_3$
Formula weight	477.4	512.56	512.56
Crystal system	triclinic	triclinic	triclinic
Space group	$P\bar{1}$	$P\bar{1}$	$P\bar{1}$
a [Å]	7.528(3)	7.7168(19)	7.8377(9)
b [Å]	9.202(3)	9.370(2)	9.5249(11)
c [Å]	12.616(5)	13.320(3)	13.5742(16)
α [°]	84.052(4)	90.778(3)	91.711(2)
β [°]	73.771(4)	97.877(3)	98.3740(10)
γ [°]	89.723(4)	102.049(3)	102.0820(10)
V [Å^3]	834.3(5)	932.1(4)	978.4(2)
Z	2	2	2
ρ_{calcd} [g cm^{-3}]	1.9	1.826	1.740
μ [mm^{-1}]	1.217	1.217	1.160
Temperature [K]	90	90	273
F(000)	476	516	516
Reflns collected	4144	5015	9961
R (int)	0.0184	0.0106	0.0128
Goodness of fit	1.067	1.053	1.061
R_1[a], R_w[b] ($I > 2\sigma(I)$)	0.0184	0.024	0.0356
R_1[a], R_w[b] (all data)	0.0189	0.0252	0.0988

[a] $R_1 = \Sigma||F_o| - |F_c|| / \Sigma|F_o|$. [b] $R_w = [\Sigma w (F_o^2 - F_c^2)^2/\Sigma w (F_o^2)^2]^{1/2}$.

CHAPTER 3

Reversible Formation of Soft Coordination Polymers from Mixtures of Ruthenium-Containing Ionic Liquid and Bridging Molecules

3.1 Introduction

Recently, organic polymers with dynamic covalent bonds or supramolecular interactions, which reversibly dissociate by external stimuli such as heat, have attracted considerable attention because of their self-healing properties.[119–123] Some polymers exhibit reversible changes in their physical properties (such as viscoelasticity and ionic conductivity) as a result of external stimuli based on the reversible bond formation mechanisms.[71,74] These features are useful for sensors and electronic devices. Coordination bonds are also useful for bonding transformations. There are stimuli-responsive metallopolymers that exhibit reversible bond formation.[48,49,124–128] However, metallopolymers mostly have low-dimensional structures,[129] and there are very few examples of coordination polymers with this property.[130] This is partly because coordination polymers are generally crystalline, hard materials.[129,131]

To explore stimuli-responsive network coordination polymers, we designed soft coordination polymers that are produced by the photoirradiation of metal-containing ILs.[23,24,132,133] As described in the previous chapter, the Ru-containing IL (***tri*-1**) shown in **Fig. 3-1a** transforms into an amorphous coordination polymer (***tri*-2**) upon UV photoirradiation, and the reverse reaction occurs upon heating.[23] However, its photoreaction requires several hours under standard UV-LED light. To overcome this disadvantage, we further designed a photoreactive IL $[Ru(C_5H_5)(PhOC_3H_6CN)]FSA$ (**1**) with only one substituent (**Fig. 3-1b**).[132] Its photoreaction is more than 10× faster than that shown in **Fig. 3-1a** because of its low viscosity. However, the product is a liquid composed of trinuclear complexes, and no photo solidification occurs.

The purpose of this study is to design a novel type of photoreactive liquid that transforms into a solid coordination polymer upon photoirradiation, while maintaining high reactivity. The idea was to add a tridentate bridging ligand to **1**, as schematically illustrated in **Fig. 3-2a**. Photoirradiation of the liquid mixture would produce a network coordination polymer linked by the tridentate ligands, whereas the low viscosity of the liquid mixtures enables fast reactions.

By contrast, the use of a bidentate ligand instead of a tridentate ligand would produce a one-dimensional structure or oligomers (**Fig. 3-2b**), which are less likely to form a solid.

Based on this idea, in this study, we prepared liquid mixtures of IL **1** and the bridging ligands shown in **Fig. 3-3** and investigated their thermal properties and photoreactivities. The tridentate ligand tris(2-cyanoethyl)amine ($N(C_2H_4CN)_3$, **L**) and bidentate ligand 1,4-dicyanobutane ($NC(CH_2)_4CN$, **L'**) both have high boiling points and low vapor pressures. As shown below, the liquid mixture of **1** and **L** (abbreviated as **1a**, hereafter) transformed into soft amorphous coordination polymer **2a** upon UV photoirradiation, whereas the mixture of **1** and **L'** (abbreviated as **1b**) transformed into oligomer liquid **2b**. These photoreaction products reverted to the original liquids upon heating. Their ionic conductivity and viscoelasticity changes upon photoirradiation were investigated and are discussed compared with those of related Ru-containing ILs.

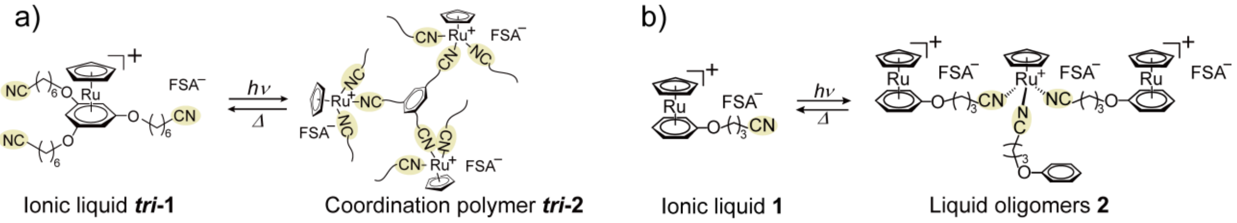

Figure 3-1. Reversible formation of (a) coordination polymer and (b) oligomer liquid from ruthenium-containing ionic liquids. FSA$^-$ stands for bis(fluorosulfonyl)amide anion.

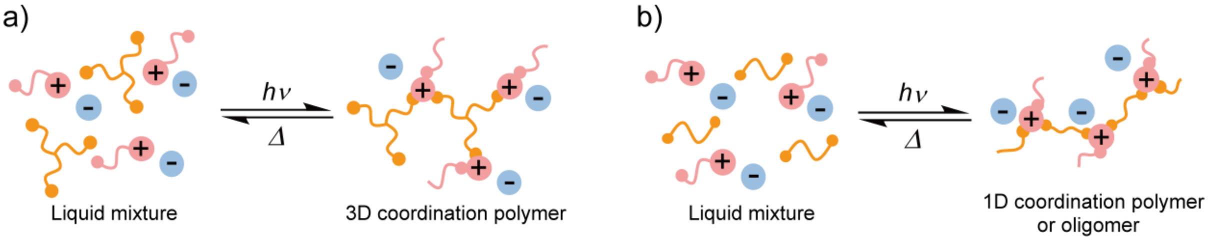

Figure 3-2. Schematic illustration of photochemical reactions of liquid mixtures comprising photoreactive ionic liquid and (a) tridentate or (b) bidentate bridging ligand.

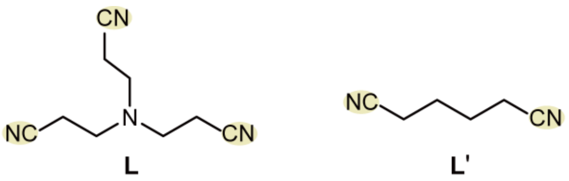

Figure 3-3. Bridging ligands used in this study.

3.2 Results and Discussion

Thermal properties and photoreactivity. For the preparation of **1a** and **1b**, **1** and the corresponding bridging ligands were mixed in molar ratios of 3:2 and 1:1, respectively. The ratios were set such that the ratio of ruthenium to cyano groups was 1:3, considering the reaction mechanism.

Upon UV photoirradiation, colorless liquids **1a** and **1b** transformed into soft yellow elastomer **2a** and yellow highly viscous liquid **2b**, respectively, after 30 min (**Figs. 3-4** and **3-5**). The products contained ~20% unreacted cations. The products reverted to the original colorless liquid mixtures upon heating, although the thermal reaction occurred slowly even at ambient temperature. Details of the reactions are described in the following sections.

The thermal properties of the liquid mixtures and photoproducts were investigated using DSC. The glass transition temperatures and melting points of the compounds are summarized in **Table 3-1**. The DSC traces are shown in **Fig. 3-6**. **1a** and **1b** did not solidify upon cooling, exhibiting glass transitions at T_g = −70 °C and −84 °C, respectively. Their glass transition temperatures are lower than that of **1** (T_g = −60 °C),[86] which is ascribed to the decrease in viscosity due to the addition of bridging ligands. The melting points of **L** and **L'** are 59 °C and 1.9 °C, respectively,[134,135] exhibiting crystallization upon cooling, whereas **L** additionally exhibits a solid phase transition. Therefore, the observation of only a glass transition in the liquid mixtures indicates their homogeneity and no phase separation. An IL with a longer substituent $[Ru(C_5H_5)(PhOC_6H_{12}CN)]FSA$ (T_m = 43.5 °C)[86] was less useful because its mixtures with the bridging ligands exhibited partial solidification at ambient temperature. The photoreaction products **2a** and **2b** exhibited glass transitions at T_g = −26 and −40 °C, respectively. These glass transition temperatures, which are considerably higher than those of **1a** and **1b,** are consistent with the formation of intermolecular coordination bonds. The thermal behaviours of the photoproducts are discussed in the following sections.

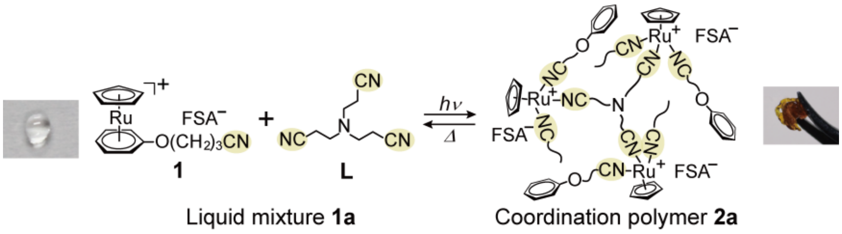

Figure 3-4. Photochemical transformation of liquid mixture **1a** into soft amorphous coordination polymer **2a**. The product contains some unreacted cations inside the solid. Reverse reaction occurs thermally. Photographs before and after UV irradiation are shown below each formula.

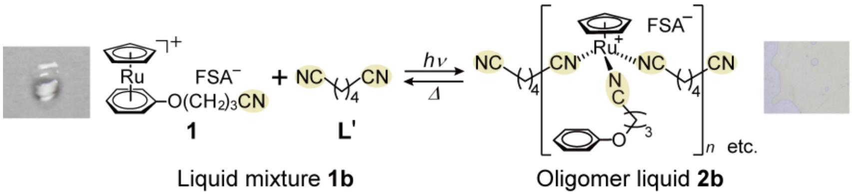

Figure 3-5. Photochemical transformation of **1b** into oligomer liquid **2b**. Product contains some unreacted cations and other oligomeric species. Reverse reaction occurs thermally. Photographs before and after UV irradiation are shown below each formula, wherein **2b** is sandwiched between two quartz plates.

Table 3-1. Glass transition temperatures (T_g) and melting points (T_m) of liquid mixtures, their photoproducts, ionic liquid, and bridging ligands

Compounds		T_g (°C)	T_m (°C)
Liquid mixture	**1a**	−70	
	1b	−80	
Photoproduct	**2a** (74%)[a]	−26	
	2b (63%)[a]	−40	
Ionic liquid	**1**	−60[b]	
Bridging ligand	**L**		59[c]
	L'		1.9[d]

[a] Reaction rate. [b] Ref. 86. [c] Ref. 134. [d] Ref. 135.

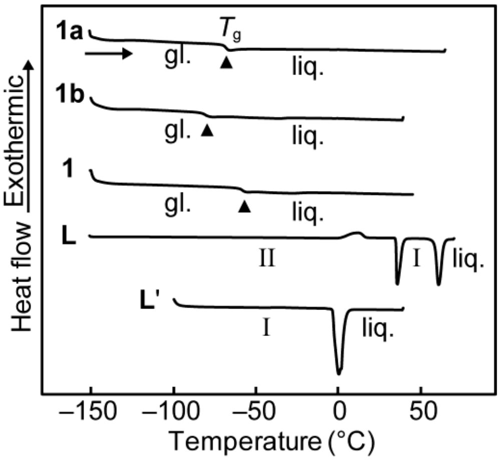

Figure 3-6. DSC traces of **1a**, **1b**, **1**, **L**, and **L'** recorded on heating runs (gl.: glassy phase, liq.: liquid phase, I, II: crystal phases, ▲: glass transition).

Investigation of photochemical reactions. The photochemical reactions and reverse reactions of **1a** and **1b** were investigated by ^{1}H NMR, UV-vis, and IR spectroscopy. Their spectral changes were similar to those of ***tri*-1** (**Fig. 3-1a**).[23] As shown in **Figs. 3-4** and **3-5**, photoirradiation of the liquids caused photodissociation of the sandwich complex, followed by coordination of the cyano groups from the bridging ligands.

The ^{1}H NMR spectra of **1a** and its photoproduct **2a,** measured in CD_3CN, are shown in **Fig. 3-7**. The coordination polymer component in **2a** dissociates in CD_3CN to yield a mixture of a solvent-coordinated complex $[Ru(C_5H_5)(CD_3CN)_3]^+$ (80%) and free ligands (**Fig. 3-7b**); the unreacted sandwich complex $[Ru(C_5H_5)(PhO(CH_2)_3CN)]^+$ (20%) was also observed. The data indicate that the reaction rate was 80%, and the presence of unreacted cations in the product may be ascribed to the incorporation of the cation into the network structure during the photoreaction, as similarly observed in the photoreaction of ***tri*-1**.[23] Another possibility is the concomitant thermal reverse reaction during photoirradiation.

Heating the coordination polymer completely recovered the original liquid (**Fig. 3-7c**). The structural change was also supported by the UV-vis and IR spectra. **1a** had no absorption bands in the visible region, but the absorption bands characteristic of the cyano coordinated complex appeared at $\lambda_{\max}$ = 310 and 370 nm after photoirradiation (**Fig. 3-8a**),[22,23] which is consistent with the color change from colorless to yellow. Similarly, the CN stretching peaks in the IR spectrum shifted from 2243 cm^{-1} to 2270 cm^{-1} after photoirradiation (**Fig. 3-8b**), which corresponds to the change from the non-coordinating to metal-coordinated cyano group.[23] The C=C stretching peaks of the arene ligand shifted from 1530 cm^{-1} to 1584 and 1599 cm^{-1}, which corresponds to the change from a coordinated to non-coordinated ligand.[23] These spectral changes were reversible by the application of light and heat. The absorbance change in the UV spectra shown in **Fig. 3-8a** is ascribed to different sample thicknesses.

The thermal behavior of **2a**, as revealed by DSC, was consistent with its thermal reactivity. The DSC traces of **2a** (reaction rate 74%) are shown in **Fig. 3-9**, which exhibits a glass transition at –26 °C (cycle 1). Upon heating in cycle 1, a very broad, small endothermic peak was observed at approximately 60 °C (not clearly visible in the figure). The peak probably corresponds to the coordination transformation, similar to the case of ***tri*-2**, which displayed a broad peak at approximately 100 °C.[23] In the second cycle, a glass transition was observed at −70 °C, which is consistent with the transformation into **1a**.

1b exhibited similar spectral changes upon photoirradiation (**Figs. 3-10–3-12**). The product contained unreacted cations of approximately 25%, as determined from the ^{1}H NMR spectrum. The presence of the unreacted cation may be due to the concomitant thermal reverse reaction during photoirradiation. The product was an equilibrium mixture of coordination-bonded oligomers, and the dominant species may be trimer or tetramer, considering the amount of unreacted cations. However, it was impossible to identify each component spectroscopically owing to the lability of the coordination bond. The thermal transformation from **2b** (T_g = –40 °C) to **1b** was also confirmed by DSC measurements, in which the glass transition of **1b** (T_g = –78 °C) was observed in the second cycle (**Fig. 3-12**). During the heating process in cycle 1, a very broad endothermic peak was observed at approximately 40 °C, which corresponds to the coordination transformation.

The contrasting photoproducts of **1a** and **1b**, which are solid and liquid, respectively, are reasonable in terms of dimensionality. One-dimensional systems are susceptible to defects to form oligomers, whereas two- and three-dimensional systems maintain their network structures, despite the defects resulting from the presence of unreacted cations.

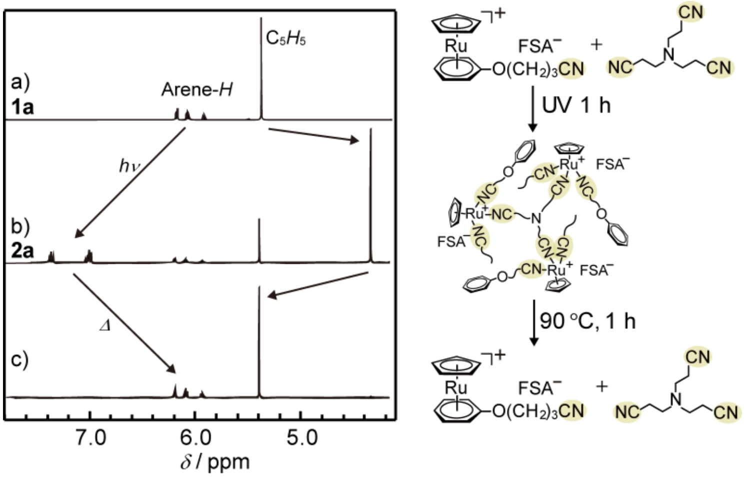

Figure 3-7. ^{1}H NMR spectra of (a) **1a**, (b) **2a**, and (c) after heating **2a** at 90 °C for 1 h (CD_3CN). Coordination polymer dissociates to yield an acetonitrile-coordinated species when dissolved in CD_3CN.

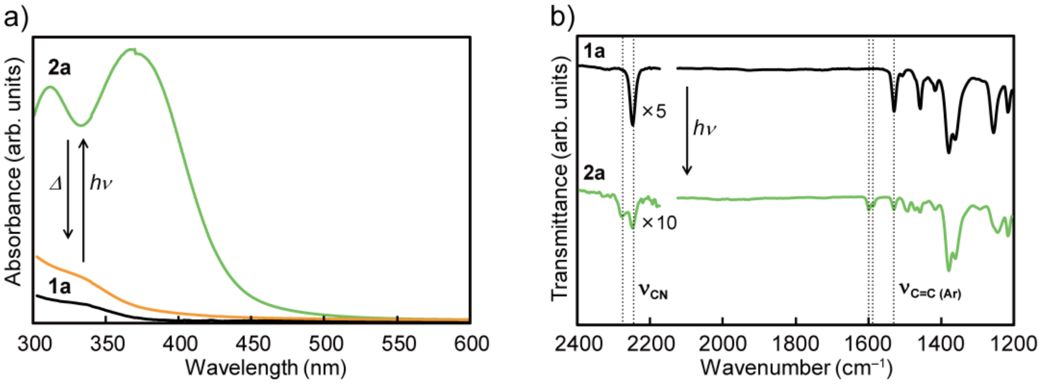

Figure 3-8. (a) UV-vis and (b) IR spectra of **1a** and **2a**.

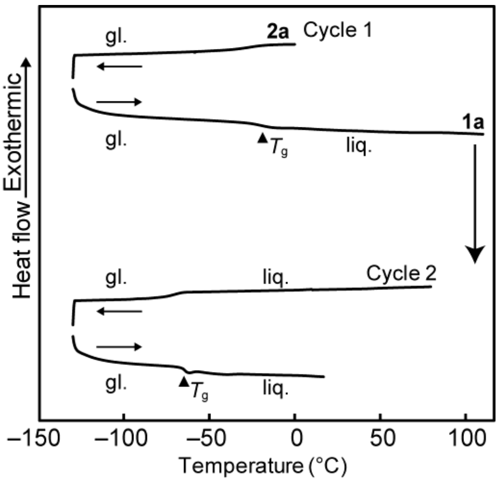

Figure 3-9. DSC traces of **2a** (gl.: glassy phase, liq.: liquid phase).

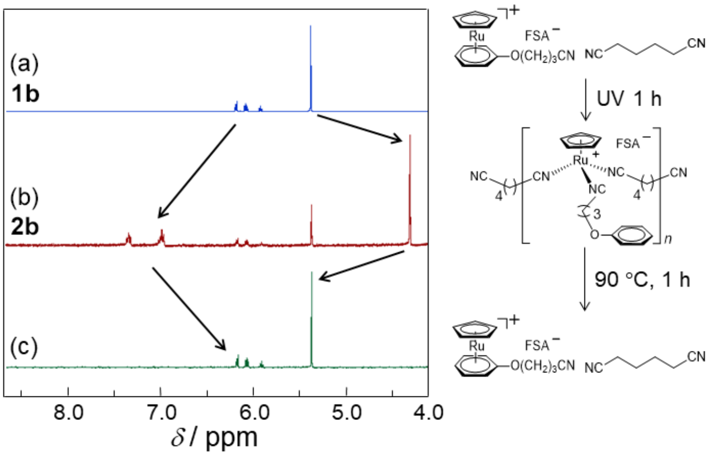

Figure 3-10. ^{1}H NMR spectra of (a) **1b**, (b) **2b** (UV photoirradiated for 1 h), and (c) after heating **2b** at 90 °C for 1 h (solvent: CD_3CN).

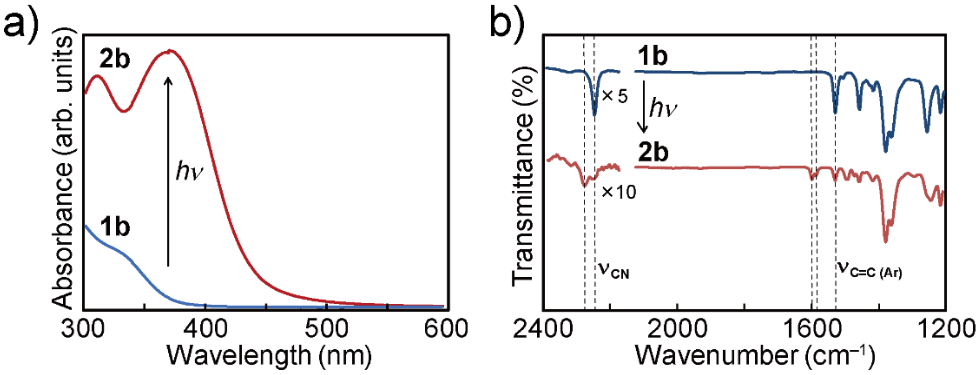

Figure 3-11. (a) UV-vis spectra and (b) FT-IR spectra of **1b** and **2b** (UV photoirradiated for 1 h) and after heating **2b** at 90 °C for 1 h.

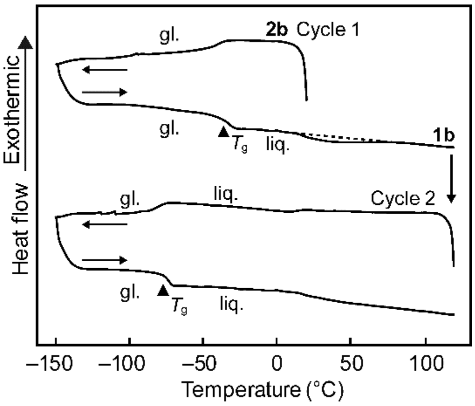

Figure 3-12. DSC traces of **2b** (gl: glassy phase, liq: liquid phase). Dotted line shows the baseline.

Rates of photochemical and thermal reactions. The photoreaction rates of **1a** and **1b** were investigated in detail. The rates of photodissociated cations in their reactions are plotted as a function of photoirradiation time in **Fig. 3-13**, together with those of **1** and ***tri*-1**.[23,132] The plots show that the reaction rates of **1a** and **1b** were almost constant over 0.5 h at 80% and 75%, respectively. The photoreactions of **1a** and **1b** were more than 10× faster than that of ***tri*-1**. The reaction rates of **1a** and **1b** reached 50% in 10 min, whereas it took 100 min for ***tri*-1**. The reactions were, however, somewhat slower than that of **1**, which reached a constant value (31%) within 15 min. It should be noted that the dissociation rate of 31% in **1** corresponds to a 93% overall reaction rate because the dominant product is a trimer containing two undissociated cations.[132] It is noteworthy that the reaction of **1a** is fast despite its transformation into a solid.

Both **2a** and **2b** underwent reverse reactions upon heating at 100 °C for a few minutes, when complete transformation into original **1a** and **1b** was observed. However, the reaction occurred slowly even at ambient temperature. This is consistent with the observation of the DSC peaks owing to the coordination transformation near room temperature. The time course of the rate of dissociated cations in **2a** and **2b** when left at 17 °C is shown in **Fig. 3-14**. The rate decreased to 44% (**2a**) and 33% (**2b**) after 5 days. This feature indicates that **2a** retains the intermolecular coordination bonds for a longer time than **2b** does, which is consistent with the results of the

DSC measurements. Their facile thermal reverse reaction is partly ascribed to the effect of entropy, which makes the original liquid mixtures more favorable energetically. The dissociation rate in **2** decreased from 33% to 2% over 5 d, whereas the dissociation was very slow in the dichloromethane solution.[132] These results are in contrast to ***tri*-2**, for which the reverse reaction was not noticeable at ambient temperature. This is consistent with the higher coordination transformation temperature of ***tri*-2** (~100 °C) than that of **2a** and **2b**.[23]

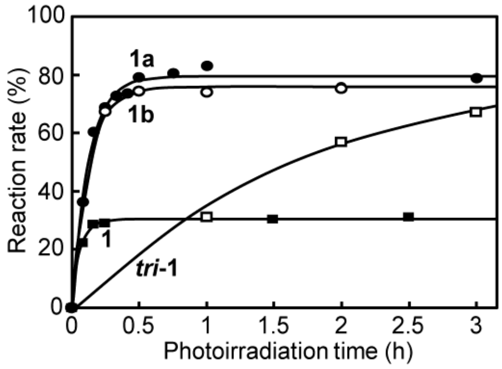

Figure 3-13. Photoreaction rates of **1a** (●) and **1b** (○) plotted versus photoirradiation time as determined from the UV-vis spectral absorbance at 370 nm and ^{1}H NMR spectra. The data for **1** (■) and ***tri*-1** (□) are also shown.

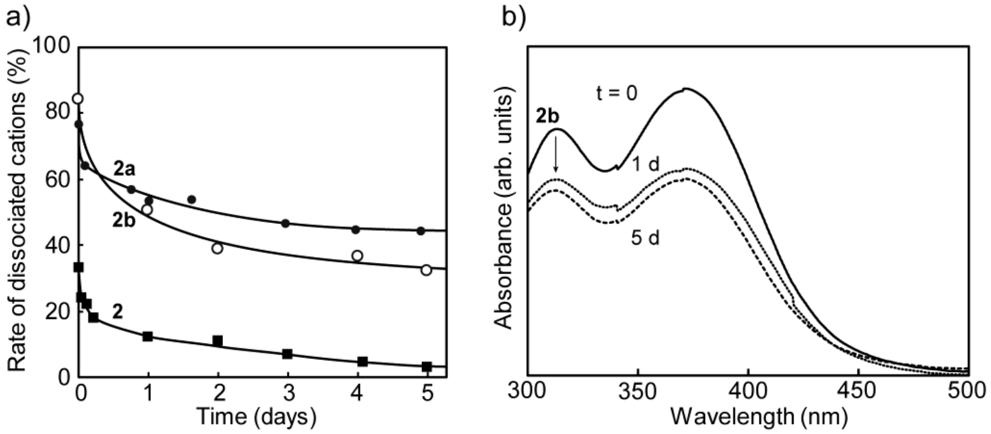

Figure 3-14. (a) Time course of rate of dissociated cations in **2a** (●), **2b** (○), and **2** (■) when left at 17 °C under dark as determined from the UV-vis spectral absorbance at 370 nm and ^{1}H NMR spectra. (b) UV-vis spectra changes of **2b** when left at 17 °C.

Viscoelasticity. Dynamic viscoelasticity measurements were taken at 25 °C to evaluate the changes in the physical properties of **1a** and **1b** upon photoirradiation. The samples after the photoirradiation of **1a** for 18 h (67% reaction rate) and **1b** for 8.3 h (61% reaction rate) are designated as **2a** and **2b**, respectively. Their reaction rates were lower than those reported in the previous sections because the samples were thicker. Photoirradiation caused a marked increase in the elastic modulus and viscosity owing to the structural transformations.

The viscosity and complex viscosity data before and after photoirradiation are summarized in **Table 3-2**. The viscosities of **1a** and **1b** were 620 mPa·s and 89 mPa·s, respectively, at a shear rate of 1 s^{-1}. Their viscosities were considerably lower than that of **1** (920 mPa·s, at 1 s^{-1}). In particular, the viscosity of **1b** is one order of magnitude smaller than that of **1a** and even closer to that of a typical IL [Emim]FSA (Emim = 1-ethyl-3-methylimidazolium cation; 19 mPa·s, at 20 °C).[136] Although Ru-containing organometallic ILs are generally highly viscous, the results demonstrate that mixing additional molecules is an effective method for reducing their viscosity.

The angular frequency (ω) dependence of the storage and loss elastic modulus of **1a** measured after photoirradiation for 0.5 h, 10 h, and 18 h (**2a**) are shown in **Fig. 3-15a**. Initially, the loss elastic modulus exceeds the storage elastic modulus in the entire frequency range. However, both the storage and loss elastic modulus increased by three to four orders of magnitude with photoirradiation time, and the storage elastic modulus exceeded the loss elastic modulus in the frequency region at $\omega > 16$ rad s^{-1} in 10 h and $\omega > 2$ rad s^{-1} in 18 h. The time course of the storage elastic modulus and loss tan δ (= G' / G'') of **1a** measured upon photoirradiation (angular frequency 10 rad s^{-1}) is shown in **Fig. 3-15b**. The loss tan δ approached 1 in 6 h, indicating a semi-solid property. However, the loss elastic modulus was still large and tan δ was not much smaller than 1 even after 18 h of photoirradiation, which is ascribed to the presence of 33% of unreacted cations. These features demonstrate the transformation from liquid into a rubbery elastomer. The complex viscosities of **1a** before and after photoirradiation are shown in **Fig. 3-15c**. The values for **1a** and **2a** were 4.8×10^2 and 6.7×10^7 mPa·s at an angular frequency of 10 rad s^{-1}, and increased by five orders of magnitude upon photoirradiation.

The viscosity of **1b** before and after photoirradiation for 0.2 h, 1.0 h, and 8.3 h (**2b**) are shown in **Fig. 3-16**. The viscosity increased with photoirradiation time, reflecting the transformation into oligomers. The viscosity of **2b** was 5.2×10^4 mPa·s at a shear rate of 1 s^{-1}, which was three orders of magnitude higher than that before photoirradiation. The loss elastic modulus exceeded the storage elastic modulus in the entire frequency range, supporting its liquid state.

Table 3-2. Viscosity, ionic conductivity, and Walden product of **1a**, **1b**, and related materials at 25 °C

Compounds	Viscosity (mPa s)[a]		Ionic conductivity (S cm^{-1})		Walden product[d]
	Before[b]	After	Before	After[c]	(mPa s mS cm^{-1})
1a	6.2×10^2	6.7×10^7 [f] (67%)[g]	2.7×10^{-4}	8.7×10^{-6}	160
1b	8.9×10^1	5.2×10^4 [b] (61%)[g]	9.8×10^{-4}	2.0×10^{-5}	87
1[e]	9.2×10^2	5.2×10^3 [b] (28%)[g]	4.0×10^{-4}	3.2×10^{-5}	370
***tri*-1**[e]	2.6×10^3	1.2×10^8 [f] (84%)[g]	3.1×10^{-5}	3.2×10^{-6}	81

[a] 1 mPa s = 1 cP. [b] Value at a shear rate of 1 s^{-1}. [c] After 30 min photoirradiation. [d] Value before photoirradiation. [e] Ref. 132. [f] Complex viscosity at 10 rad s^{-1}. [g] Rate of dissociated cations.

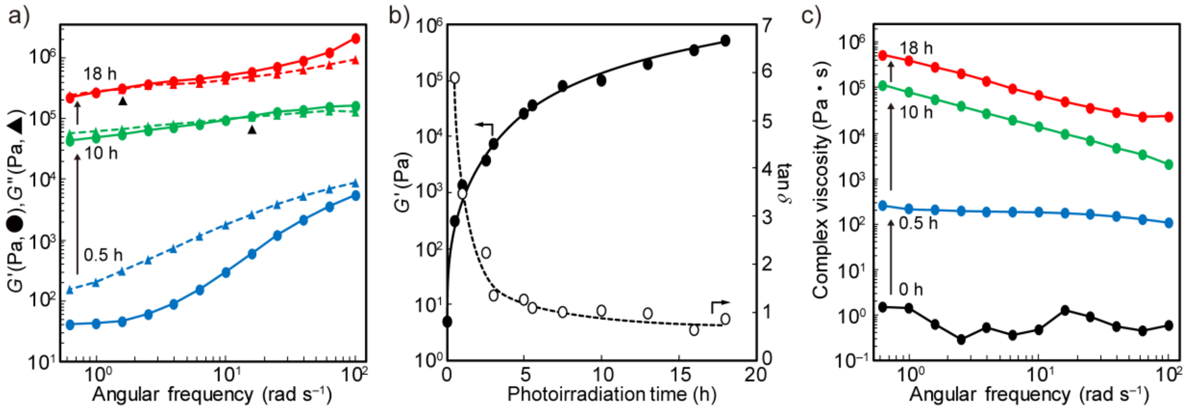

Figure 3-15. (a) Storage elastic modulus (G', solid lines) and loss elastic modulus (G'', dashed lines) of **1a** after photoirradiation plotted as function of angular frequency. Data after photoirradiation for 0.5 h (blue), 10 h (green), and 18 h (red) are shown. Triangles indicate crossover points. (b) Storage elastic modulus (G', ●) and loss tan δ (○) of **1a** plotted versus photoirradiation time (25 °C, angular frequency 10 rad s^{-1}). (c) Complex viscosity of **1a** plotted as function of angular frequency measured before and after photoirradiation for 0.5 h, 10 h, and 18 h (1% strain).

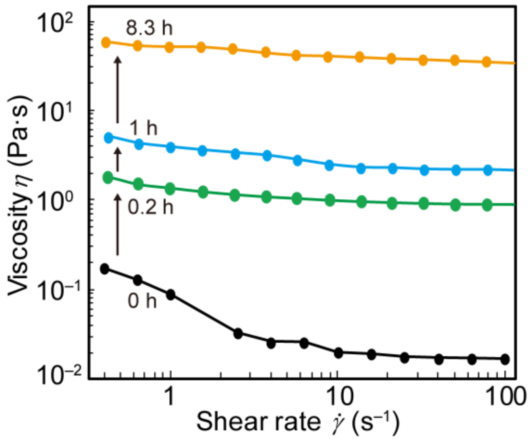

Figure 3-16. Viscosity of **1b** plotted as function of shear rate at 25 °C measured before and after photoirradiation for 0.2 h, 1.0 h, and 8.3 h.

Ionic conductivities. The photoreaction of these liquid mixtures accompanies the formation of intermolecular coordination bonds, making the cation less mobile. Based on this mechanism, their ionic conductivities were reversibly controlled by the application of light and heat.

The ionic conductivities of **1a** and **1b** before and after photoirradiation for 30 min are summarized in **Table 3-2**, together with those of **1** and ***tri*-1**. The ionic conductivities of **1a** and **1b** before photoirradiation were 2.7×10^{-4} and 9.8×10^{-4} S cm^{-1}, respectively, which are similar to that of **1** (4.0×10^{-4} S cm^{-1}). The addition of bridging ligands lowers the ionic concentration, although it is compensated for by the decrease in viscosity. The Walden products, the products of ionic conductivity and solution viscosity, of these liquids were 160 and 87 mPa s mS cm^{-1}, respectively, which are considerably smaller than that of **1** (370 mPa s mS cm^{-1}).

The UV photoirradiation of **1a** reduced the ionic conductivity from 2.7×10^{-4} S cm^{-1} to 8.7×10^{-6} S cm^{-1} in 30 min owing to the transformation into a coordination polymer (**Fig. 3-17a**). The different photoreaction rates for the ionic conductivity and viscoelasticity measurements of **1a** are ascribed to different sample thicknesses. The similarity of their trends (**Figs. 3-15b** and **3-17**) indicates that they are both resulting from the network formation reaction. Subsequent heating at 120 °C for 20 min increased the value to 9.6×10^{-5} S cm^{-1} owing to the recovery of the liquid state. The ionic conductivity response of **1b** was similar to that of **1**,[132] exhibiting a smaller change than **1a** (**Fig. 3-17a**). The conductivity decreased upon UV photoirradiation from 9.8×10^{-4} S cm^{-1} to 2.0×10^{-5} in 30 min. Subsequent heating at 120 °C for 10 min increased the value to 9.1×10^{-4} S cm^{-1}.

The reversible cycles of ionic conductivity in **1a** and **1b** are shown in **Fig. 3-17b**. These figures show the plot for alternating 10 min cycles of UV photoirradiation and 120 °C heating. For **1a**, the conductivity for alternating hourly cycles is also shown, which exhibits a larger change (**Fig. 3-17b** left, dotted line). Repeating the cycle of photo and thermal reactions of **1a** and **1b** resulted in a very slight decrease in ionic conductivity, which could be due to slight oxidation of the sample or contamination by epoxy resin from the sample holder. It is noteworthy that the current liquids exhibit a fast response comparable to **1**, and in particular, **1a** exhibits a large ionic conductivity change upon photoirradiation, as seen in **Fig. 3-17a**. These features are potentially useful for device applications.

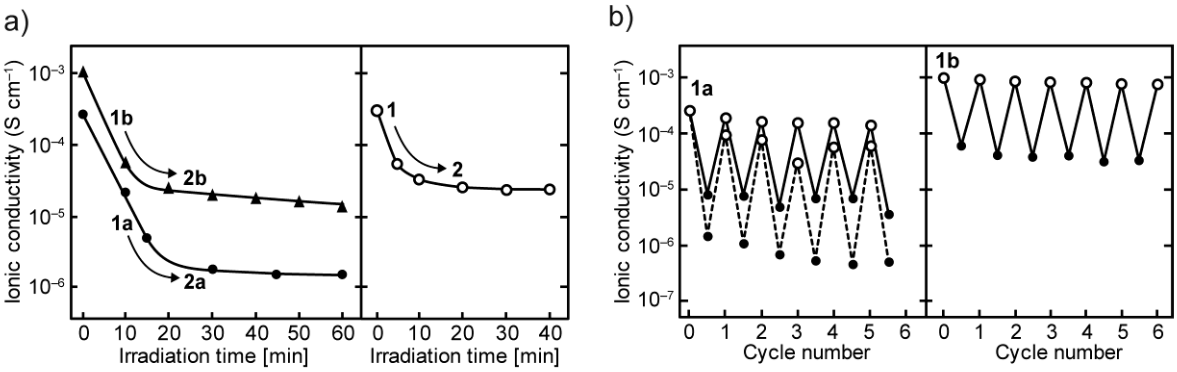

Figure 3-17. (a) Time course of ionic conductivity of **1a** (●), **1b** (▲) and **1** (○) measured upon photoirradiation at 25 °C. (b) Ionic conductivity changes of **1a** and **1b** for alternating 10 min (—) or hourly (---) cycles of UV photoirradiation (filled circles) and 120 °C heating (open circles).

Correlation of viscosity, glass transition temperature, and ionic conductivity. In this section, we discuss physical property changes before and after the photoreaction of the current and related materials that have the same bond-switching mechanism. The viscosities of **1**, **1a**, **1b**, ***tri*-1**, and related materials ($[Ru(C_5H_5)\{C_6H_3(OC_6H_{12}CN)_3\}]H_2C{=}CSO_2NSO_2CF_3$ (**1d**) and the corresponding PIL (**1c**)[133]) are plotted versus their glass transition temperatures in **Fig. 3-18a**. The viscosity increases with the increase in the glass transition temperature, including data for **1a**, **1b**, and **1c**, which are not genuine ILs. The ionic conductivities before and after UV photoirradiation are plotted against the viscosity and complex viscosity in **Fig. 3-18b**. The values of viscosities and complex viscosities are plotted for liquids and elastomers, respectively, which are nearly equivalent according to the empirical Cox–Merz rule.[137] Before photoirradiation, the ionic conductivities of liquids with lower viscosity tend to be larger (**1b** > **1a** ≈ **1** > ***tri*-1** > **1d** > **1c**), as is generally observed in ILs.[138,139] The changes in viscosity and ionic conductivity before and after the photoreaction are small during the transformation into oligomer liquids (**2** and **2b**), whereas the changes are generally large during the transformation into three-dimensional coordination polymers. This figure also shows that Ru-containing ILs can be used to create materials with a wide range of ionic conductivities and viscoelastic properties.

These studies demonstrate the versatility of the coordination-bond switching mechanism of external stimuli in controlling their physical properties. Ru-containing organometallic complexes will have versatile applications in the further development of functional soft coordination compounds, since they are also useful for the controlled construction of dendrimers.[140]

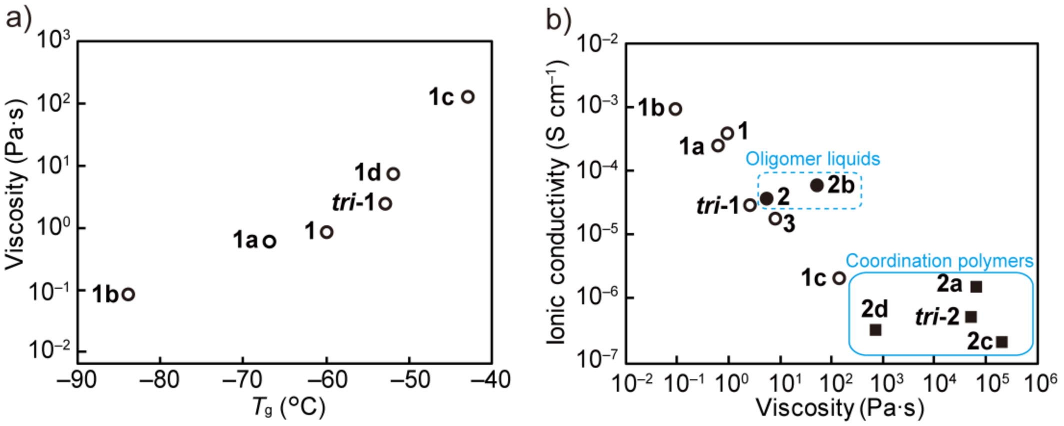

Figure 3-18. (a) Correlation between glass transition temperature (T_g) and viscosity of liquid mixtures (**1a**, **1b**), ionic liquids[86,132] (**1**, **tri-1**, **1d**), and poly(ionic liquid)[133] (**1c**). (b) Correlation between viscosity and ionic conductivity. Values of viscosities and complex viscosities are plotted for liquids (○: before photoreaction, ●: oligomer liquids) and coordination polymers (■), respectively. Data for $[Ru(C_5H_5)\{C_6H_3(OC_6H_{12}CN)_3\}]H_2C{=}CHSO_2NSO_2CF_3$ (**1d**), its polymer (**1c**), and their photoproducts (**2d** and **2c**) are also shown.

3.3 Conclusion

In this study, as a novel approach to fabricating soft coordination polymers from liquids, we designed photoreactive liquid mixtures comprising a Ru-containing IL and a bridging molecule. The liquid mixtures produced an amorphous network coordination polymer or oligomer liquid upon photoirradiation. The use of different bridging ligands, either tridentate or bidentate, changed the topology and fluidity of the products. In addition, the liquid mixtures had lower viscosity than the IL component, enabling rapid photoreaction. The liquid design is advantageous for materials variation. Furthermore, based on the reversible coordination transformation by the application of light and heat, their ionic conductivities and viscoelastic properties were reversibly controlled. The comparison of the current and related materials proved the coordination-bond switching mechanism useful for controlling their physical properties over a wide range. Their tunable ionic conductivity and viscoelastic properties may be useful for future device applications. The mechanical and self-healing properties of these materials are worthy of future investigation.

3.4 Experimental Section

General. IL **1** was synthesized according to the method in the literature.[86] ^{1}H and ^{19}F NMR spectra were recorded using a Bruker Avance 400 spectrometer. The FT-IR spectra were recorded using a Thermo Nicolet iS5 instrument with an attenuated total reflection attachment. The UV–vis spectra were measured using a JASCO V-570 UV/VIS/NIR spectrophotometer. Differential scanning calorimetry (DSC) measurements were performed using a TA Instruments Q100 differential scanning calorimeter with a sweep rate of 10 K min^{-1}. ESI-MS spectra were measured using a Thermo Fisher Scientific LTQ-Orbitrap Discovery. The viscosity of the liquids was measured using a TA Instruments Discovery HR-1. The ionic conductivities were measured using a Solartron 1260 impedance analyzer and gold interdigitated electrodes with gap dimensions of 200 μm. Since repeated photo and thermal reactions in air cause gradual oxidation of the ruthenium complex,[133] the samples were sandwiched between the electrode and a quartz glass plate and further coated with epoxy resin.

Photoreaction. To prepare **1a** and **1b**, IL **1** and the corresponding bridging ligand were mixed at a molar ratio of 3:2 and 1:1, respectively, in dichloromethane. After irradiation with ultrasonic waves for 5 min, the solvent was evaporated under reduced pressure, and the residue was vacuum dried at ambient temperature for 1 h. The compositions of the resultant liquids were checked by ^{1}H NMR spectroscopy in CD_3CN. To investigate the photoreaction, UV light was irradiated into the liquids sandwiched between two quartz plates at 10 °C. A Lightningcure UV-LED spotlight source (LC-L1V5, Hamamatsu Photonics; 365 nm, 600 mW cm^{-2}) was used as the light source. For the viscoelastic measurements, the photoreaction was slower owing to the increased sample thickness (15–35 μm).

CHAPTER 4

Metal-Containing Poly(ionic liquid) Exhibiting Photogeneration of Coordination Network

4.1 Introduction

PILs are ionically conductive polymers synthesized by the polymerization of ILs with polymerizable substituents.[141–144] They are versatile because they display both the characteristics of ILs and polymers, though the development of stimuli-responsive PILs is limited. In addition, bonding transformation or reorganization of polymers by external stimuli attracted much attention recently, as documented by self-healing polymers,[122] Ru-containing polymers,[48,49] photoresponsive polymers,[123,145] and high-strength gels.[146] Furthermore, the development of photocontrollable soft ionic conductors is an important topic of investigation. There are currently only a few examples of such materials,[32,56,71,74,84] most of which contain photochromic moieties. In this study, therefore, we introduced a polymeric anion into the photoreactive IL ***tri*-1** to develop photoresponsive PILs. We hypothesized that its photoreaction would produce a novel hybrid CP containing both covalent chains and coordination networks.

This chapter describes the synthesis, properties, and reactivities of PIL **1c** and its precursor IL **1d** (**Fig. 4-1**), which have the same cations as ***tri*-1**. UV photoirradiation transformed PIL **1c** into a unique amorphous hybrid CP via the formation of a coordination network between the cations, and the reaction was reversed by heating. Similarly, UV photoirradiation transformed IL **1d** into an amorphous CP but heating the product unexpectedly produced PIL **1c** via polymerization of the anion. The physical properties of these materials were investigated by differential scanning calorimetry (DSC) and dynamic rheological measurements. Furthermore, we demonstrate that their ionic conductivities are controlled by the application of light and heat based on the bonding transformation mechanism.

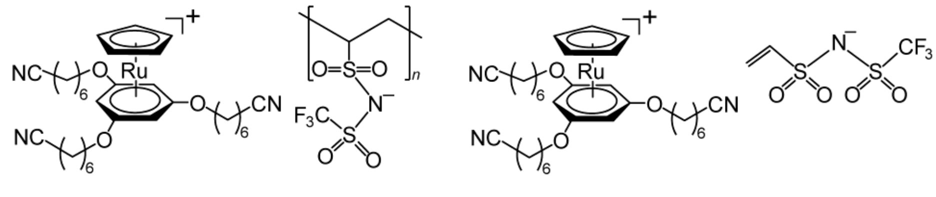

Figure 4-1. Structural formulae of (a) poly(ionic liquid) **1c** and (b) polymerizable ionic liquid **1d**.

4.2 Results and Discussion

Synthesis and reactivities of PIL 1c and IL 1d. PIL **1c** is an orange-yellow highly viscous liquid, which was synthesized by bulk polymerization of IL **1d** in the presence of azobisisobutyronitrile (AIBN) in 88% yield. IL **1d** is a pale yellow liquid, synthesized by the anion exchange of the corresponding chloride salt (yield 74%). The thermal decomposition temperature of IL **1d** as determined by thermogravimetric analysis was 201 °C (−3wt% weight loss temperature, **Fig. 4-2**). PIL **1c** and IL **1d** exhibited glass transitions at −43 and −52 °C, respectively, as determined by DSC (**Table 4-1**). It is reasonable that the PIL exhibits a higher glass transition temperature than the IL.[63] The comparable glass transition temperature of ILs **1d** and ***tri*-1** ($T_g = -53$ °C [23]) seems reasonable considering their similar molecular structures.

An overview of the photochemical and thermal reactivities of these materials is shown in **Fig. 4-3**. PIL **1c** formed a cationic network upon UV photoirradiation, transforming into an amorphous hybrid CP **2c** in a few hours. Similarly, IL **1d** transformed into an amorphous CP **2d** upon photoirradiation. In these reactions, some unreacted cations remained in the resultant solids. CPs **2c** and **2d** exhibited glass transitions at −8 °C and −21 °C, respectively, temperatures that are higher than those of **1c** and **1d**. The higher glass transition temperature of CP **2c** compared to that of CP **2d** is ascribed to the anionic polymer chains in **2c**. CP **2c** changed back to PIL **1c** upon heating. However, CP **2d** did not form IL **1d** but was transformed into PIL **1c** upon heating via polymerization of the anion’s functional group. The details of each reaction are discussed in the following sections.

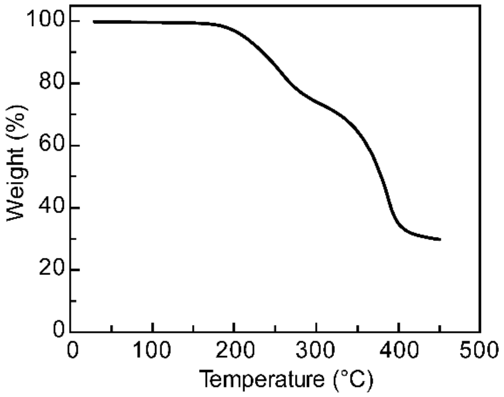

Figure 4-2. Thermogravimetric (TG) trace of IL **1d** (heating rate: 5 °C min^{-1}).

Table 4-1. Glass transition temperatures of PILs, IL, and CPs

compound	T_g (°C)
1c (PIL)	–43
1d (IL)	–52
***tri*-1**[a] (IL)	–53
2c (CP, 69%)[b]	–8
2d (CP, 92%)[b]	–21
***tri*-2**[a] (CP, 100%)[b]	0

[a]Ref. 23. [b]Reaction rates are shown in parenthesis.

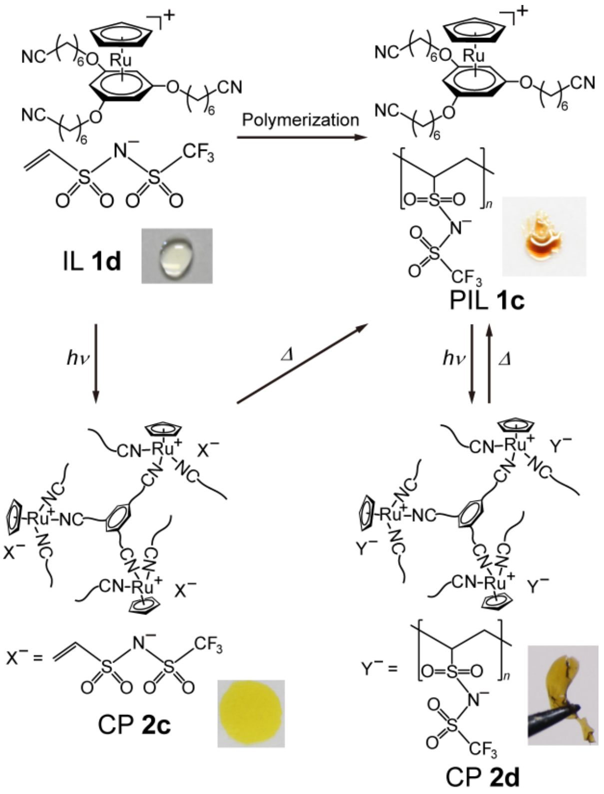

Figure 4-3. Photochemical and thermal reactions of PIL **1c** and IL **1d**. Anions X⁻ and Y⁻ are polymeric and polymerizable anions, respectively. The methylene chains of the coordination polymer have been omitted for simplicity. The photograph of CP **2d** is of the sample sandwiched between quartz plates.

Photochemical reactivity of PIL 1c. Upon UV photoirradiation, the orange-yellow highly viscous liquid PIL **1c** gradually transformed into the orange rubbery elastomer **2c** (**Fig. 4-3**, left), via the formation of a cationic network structure. Heating the elastomer caused a reverse reaction to generate liquid **1c**. This transformation was reversibly repeated in an Ar atmosphere but became gradually irreversible in air owing to oxidation.

The elastomer **2c** generated by photoirradiation of PIL **1c** is an amorphous hybrid CP, comprising of anionic covalent chains and a cationic coordination network. Consistently, this photochemical reaction was accompanied by shifts in C=C stretching vibrations from 1532 to 1593 cm^{-1} and CN stretching vibrations from 2245 to 2272 cm^{-1} in the FT-IR spectrum and an increase in absorption around 310 and 370 nm in the UV–Vis spectrum (**Figs. 4-4** and **4-5**).

They correspond to the structural transformation from the sandwich complex to the cyano-coordinated complex.[22,23] The reaction rate, or cation dissociation rate after photoirradiation for 4 h was 75% as determined from ^{1}H NMR spectra in CD_3CN (**Fig. 4-6**). Prolonged photoirradiation did not increase the reaction rate. Therefore, 25% of the Ru complexes remained in the product as the sandwich complex, which percentage did not decrease upon further photoirradiation. The presence of residual sandwich complexes (~20%) is also observed in the photoreaction product of ***tri*-1**, which is ascribed to the incorporation of unreacted molecules into the network during photoreaction.[23]

CP **2c** returned to PIL **1c** upon heating at 90 °C for 2h. However, the reaction rate was 95%, and 5% of the cyano-coordinated complex remained in the liquid. The thermal reaction was further investigated by DSC (**Fig. 4-7**). In the heating process, CP **2c** showed a glass transition at −8 °C and a very broad endothermic peak at 70–140 °C ($\Delta H = 4$ kJ mol^{-1}, peak top 105 °C), which relates to the conversion to PIL **1c**. This is consistent with ***tri*-2** showing a broad endothermic peak ($\Delta H = 5.2$ kJ mol^{-1}) at 50–120 °C upon transformation to ***tri*-1**.[23] The reaction enthalpy of CP **2c** corresponds to approximately 70% of that of ***tri*-2**, which is consistent with the reaction rate of the cation (75%). In the second cycle, a glass transition was observed at −39 °C, which also indicates the formation of PIL **1c**. The slightly higher glass transition temperature than that of the original **1c** ($T_g = -43$ °C) resulted from the low reaction rate of the cation (85%) owing to the shorter heating time.

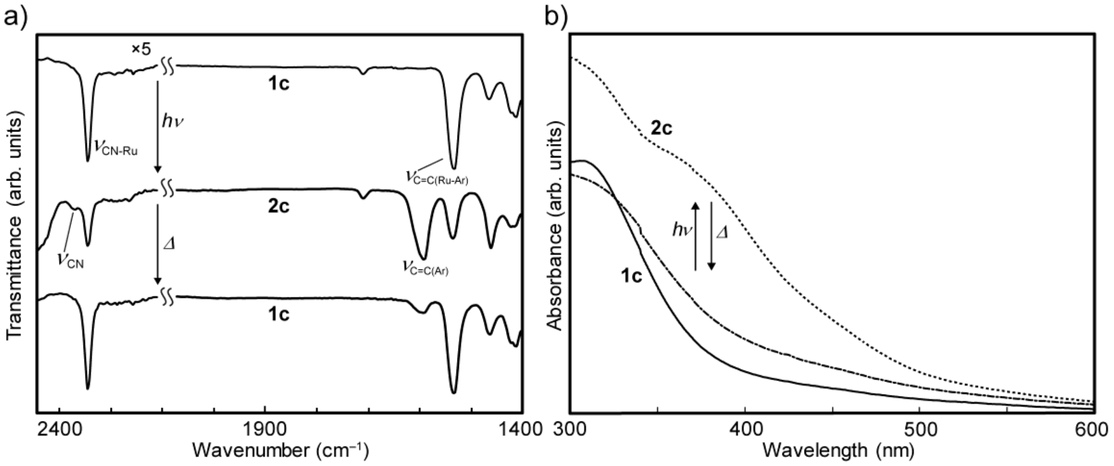

Figure 4-4. (a) FT-IR spectra and (b) UV–vis spectra of PIL **1c**, CP **2c**, and after heating **2c** at 90 °C for 2 h.

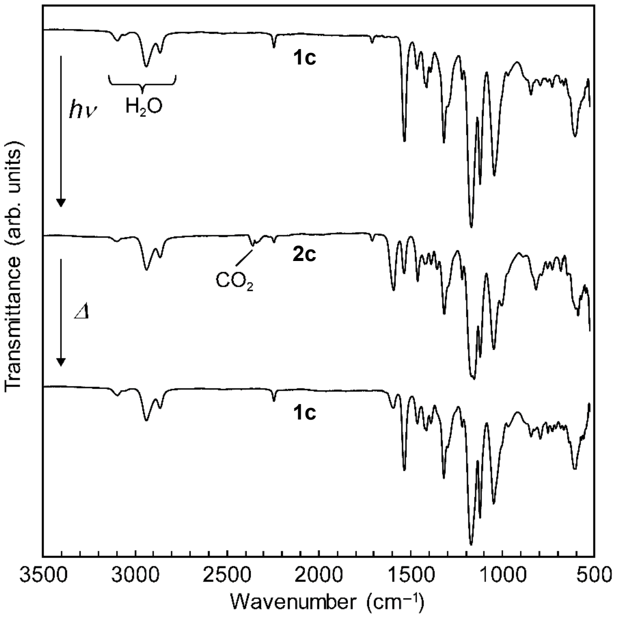

Figure 4-5. FT-IR spectra of (a) PIL **1c**, (b) CP **2c**, and (c) after heating **2c** at 90 °C for 2h.

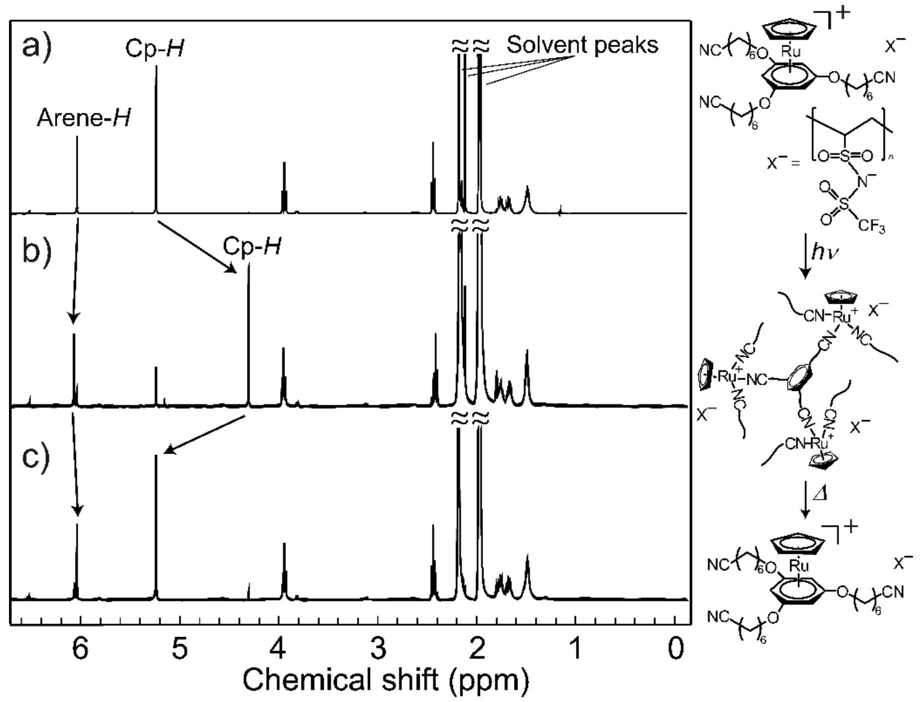

Figure 4-6. ^{1}H NMR spectra (400 MHz, CD_3CN) of (a) PIL **1c**, (b) CP **2c**, and (c) after heating **2c** at 90 °C for 2h.

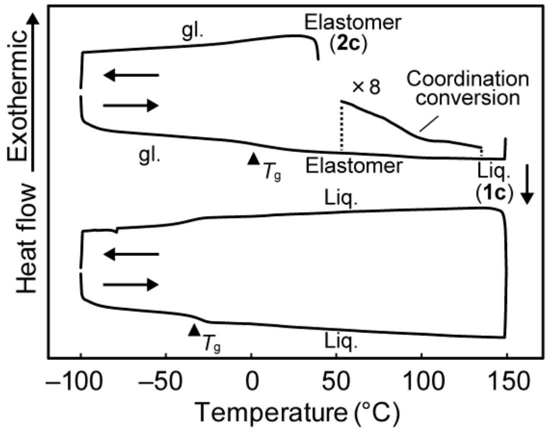

Figure 4-7. DSC traces of CP **2c**, where liq. and gl. are the liquid and glassy states, respectively.

Photochemical reactivity of IL 1d. Upon UV photoirradiation, the pale yellow liquid **1d** converted into the amorphous CP **2d**, which was an orange viscous elastomer. The product was not changed back to **1d** upon heating but transformed into PIL **1c** (**Fig. 4-3**) via polymerization of the anion. Therefore, a reversible transformation between PIL **1c** and CP **2c** was observed in the subsequent alternate cycles of photoirradiation and heating.

The elastomer **2d** generated by UV photoirradiation of IL **1d** is an amorphous CP with a cationic network structure (**Fig. 4-3**, right). The formation of the cyano-coordinated structure was also confirmed by UV–vis and FT-IR spectra (**Fig. 4-8**). The reaction rate was 95% after UV photoirradiation for 4 h, and 5% of the sandwich complex remained in the product (**Fig. 4-9**). Further photoirradiation did not increase the reaction rate.

CP **2d** transformed into PIL **1c** upon heating, not shifting back to IL **1d**. Heating caused polymerization of the anion concomitant with the structural transformation of the cations. The cations switched back to the sandwich complex almost quantitatively (98%) upon heating at 120 °C for 12 h, whereas 92% of anions were polymerized. At a milder condition of heating at 90 °C for 2 h, 91% of the cations changed back to the sandwich complex and 57% of anions polymerized. The uncommon anion polymerization is owing to the catalytic activity of the Ru half-sandwich complex. This was proven by heating the mixture of **1d** and a half-sandwich complex $[Ru(Cp)(NCCH_3)_3]PF_6$ at 90 °C, which produced the polymerized anion in 7 mol% in 2 h, whereas heating **1d** alone did not cause any reactions. It is noteworthy that the constituent of the CP itself acted as a catalyst.

The thermal reaction of CP **2d** to PIL **1c** was investigated by DSC (**Fig. 4-10**). Upon heating, **2d** exhibited a glass transition at −21 °C, and a very broad endothermic peak was observed at 40–100 °C owing to the coordination transformation of the cation, overlapped with subsequent exothermic polymerization of the anion. In the second cycle, a glass transition was observed at −43 °C, which is consistent with T_g of **1c**. After the DSC measurement, the cations in the sample changed back to the sandwich complex almost quantitatively (97%) and 66% of the anions were polymerized.

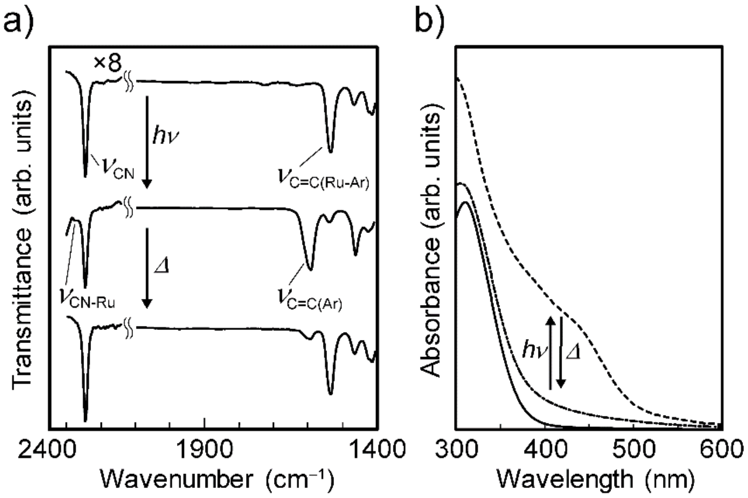

Figure 4-8. (a) FT-IR and (b) UV–Vis spectra of IL **1d**, CP **2d**, and after heating **2d** at 90 °C for 2 h.

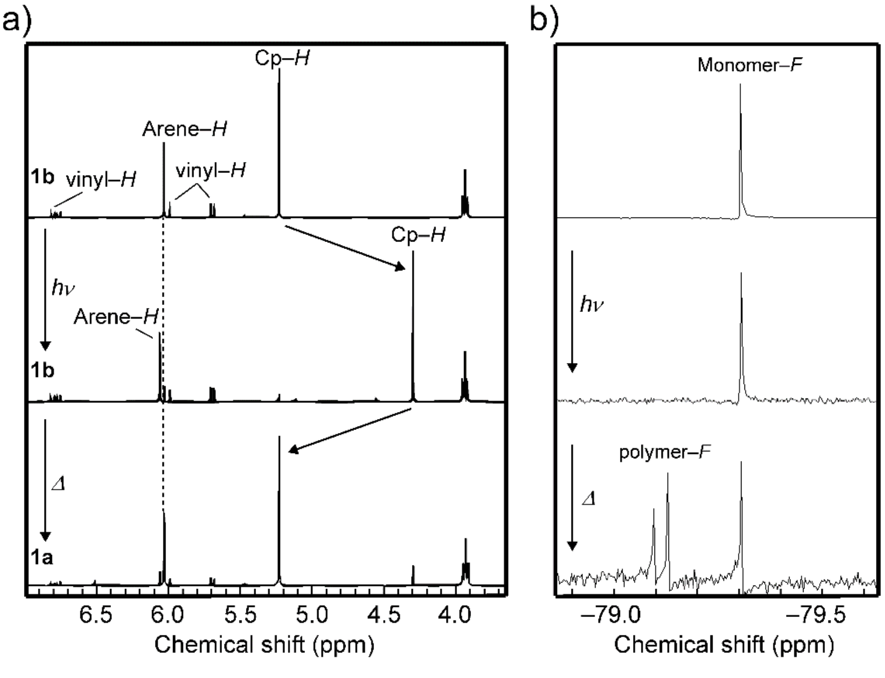

Figure 4-9. (a) ^{1}H NMR and (b) ^{19}F NMR spectra (400 MHz, CD_3CN) of IL **1d**, CP **2d**, and after heating **2d** at 120 °C for 12 h.

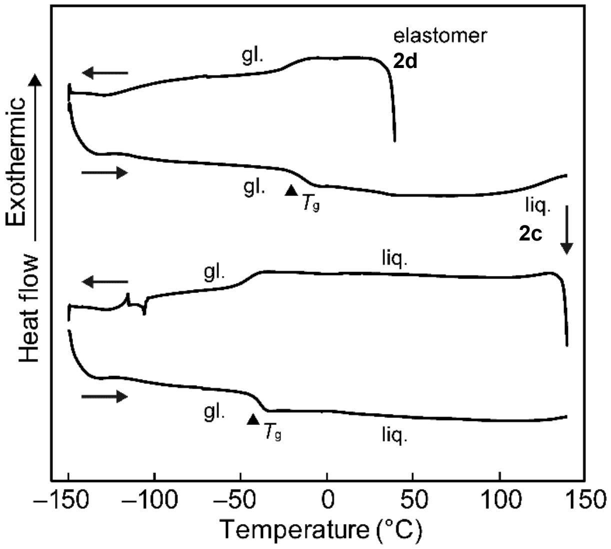

Figure 4-10. DSC traces of CP **2d** (10 °C min^{-1}) where liq. and gl. are the liquid and glassy states, respectively.

Dynamic viscoelasticity. Dynamic viscoelasticity measurements were performed at 25 °C to evaluate the changes in mechanical properties of PIL **1c** and IL **1d** upon photoirradiation. Photoirradiation caused a marked increase in viscoelasticity owing to the transformation to CP. The samples after photoirradiation of **1c** for 20 h (65% reaction rate) and that of **1d** for 8 h (77%) are designated in this section as **2c** and **2d**, respectively. Their reaction rates were lower than those reported in the previous sections because the samples were thicker.

The elastic moduli and complex viscosities of these materials at an angular frequency of 10 rad s^{-1} are summarized in **Table 4-2** together with those of ***tri*-1** and ***tri*-2**. The viscosities at a shear rate of 1 s^{-1} are also shown in the table. The viscosities of **1c**, **1d**, and ***tri*-1** were 1.3 × 10^2 Pa s (1.3 × 10^5 cP), 7.7 Pa s (7.7 × 10^3 cP), and 2.6 Pa s (2.6 × 10^3 cP), respectively. Therefore, PIL **1c** was much more viscous than ILs **1d** and ***tri*-1**. Similarly, the storage modulus of **1c** (1.9 × 10^2 Pa) was much larger than those of **1d** (11.1 Pa) and ***tri*-1** (9.4 Pa). The higher values for the PIL compared to ILs and comparable values for ILs **1d** and ***tri*-1** are reasonable considering their similar molecular structures. All the values increased markedly after photoirradiation. The storage modulus of **2c** and ***tri*-2** increased compared to those of **1c** and ***tri*-1** by orders of 10^4

and 10^5, respectively, whereas the increase from **1d** to **2d** was smaller in the order of 10^2. The loss modulus and complex viscosity of each liquid increased similarly. The elastic moduli of the photoproducts decreased in the order of **2c** (~10^6 Pa) > ***tri*-2** (~10^5 Pa) > **2d** (~10^3 Pa). This trend is consistent with their physical appearance as rubbery, soft, and viscous elastomers, respectively. Furthermore, there was a correlation between the complex viscosities and glass transition temperatures (**Table 4-1**), both decreased in the order of **1c** > **1d** > ***tri*-1**.

The angular frequency dependence of the storage modulus G' and loss modulus G'' of PIL **1c** measured at 1% strain before and after UV photoirradiation is shown in **Fig. 4-11**. In **1c**, G'' exceeds G' in the entire frequency range, indicating viscous behavior ($\tan\delta > 1$). The slopes of G' and G'' of PIL **1c** in the range of 10^2–10^3 rad s^{-1} were 2 and 1, respectively, which is a typical behavior in the terminal region.[147] However, the slope of G' was smaller below 10^2 rad s^{-1}, which is probably ascribed to the formation of domains owing to the interactions between constituent ions.[148,149] Both G'' and G' improved upon photoirradiation and increased by more than three orders of magnitude in 20 h. In CP **2c**, G' exceeded G'' ($\tan\delta < 1$) at around 400 rad s^{-1}, indicating elastic behavior. The oscillation strain dependence of viscoelasticity at this angular frequency confirmed the elastic behavior, though structural failure occurred at 2% strain (**Fig. 4-12**). The region below 400 rad s^{-1} corresponds to the glass–rubber transition region for this material.[147] The angular frequency dependence of the complex viscosity of **1c** before and after photoirradiation is shown in **Fig. 4-13**. The complex viscosities increased by three orders of magnitude upon photoirradiation. The shear rate dependence of the viscosities of **1c** and **2c** are shown in the inset of **Fig. 4-13**. **2c** exhibited a sharp decrease in viscosity at a shear rate above 10 s^{-1}, which indicates a structural failure.

Similar to PIL **1c**, the elastic moduli of IL **1d** increased upon photoirradiation (**Fig. 4-11b**). The loss modulus (G'') exceeds the storage modulus (G') before photoirradiation, showing viscous behavior. After photoirradiation for 4 and 8 h, G' exceeded G'' in the angular frequency range below 10 and 3 rad s^{-1}, respectively, indicating elastic behavior in these regions. The low-frequency shift of the intersection of G' and G'' ($\tan \delta = 1$) with increasing photoirradiation period is ascribed to the shift of the glass–rubber transition region owing to the increase of the glass transition temperature.[147] The viscosity of the liquid also exhibited a large increase upon photoirradiation (**Fig. 4-14**). Both IL **1d** and CP **2d** displayed Newtonian behavior. It is noteworthy that, though **1d** and **2d** are structurally similar to ***tri*-1** and ***tri*-2**, significant differences were observed in their viscoelasticities. The viscosity of **1d** was similar to that of ***tri*-1**, but the storage modulus of **1d** revealed a more significant angular frequency dependence than ***tri*-1**. The storage modulus of **2d** (~10^3 Pa) was much smaller than that of ***tri*-2** (~10^5 Pa, **Table 4-2**).

As shown, the investigation of the viscoelastic changes of PIL **1c** and IL **1d** upon photoirradiation demonstrated their transformation to elastomers. In particular, the presence of anionic polymer chains considerably enhance the elastic modulus and viscosity, and the different molecular structures resulted in a significant variance in their viscoelastic properties.

Table 4-2. Storage and loss modulus, complex viscosity, and viscosity of the samples at 25 °C

Compound	Storage modulus (Pa)[c]	Loss modulus (Pa)[c]	Complex viscosity (Pa s)[c]	Viscosity (Pa s)[d,e]
1c (PIL)	1.9×10^2	1.3×10^3	1.3×10^2	1.3×10^2
1d (IL)	1.1×10^1	1.1×10^2	6.5	7.7
***tri*-1**[a] (IL)	9.4	2.9×10^1	3.0	2.6
2c (CP, 65%)[b]	1.3×10^6	1.7×10^6	2.1×10^5	1.0×10^5
2d (CP, 77%)[b]	2.5×10^3	8.2×10^3	8.6×10^2	7.3×10^2
***tri*-2** [a] (CP, 55%)[b]	4.7×10^5	2.0×10^5	5.1×10^4	

[a] Ref 132. [b] Reaction rate is shown in parenthesis. [c] Value at an augular frequency of 10 rad s^{-1}.
[d] Value at a shear rate of 1 s^{-1}. [e] 1 Pa·s = 10^3 cP.

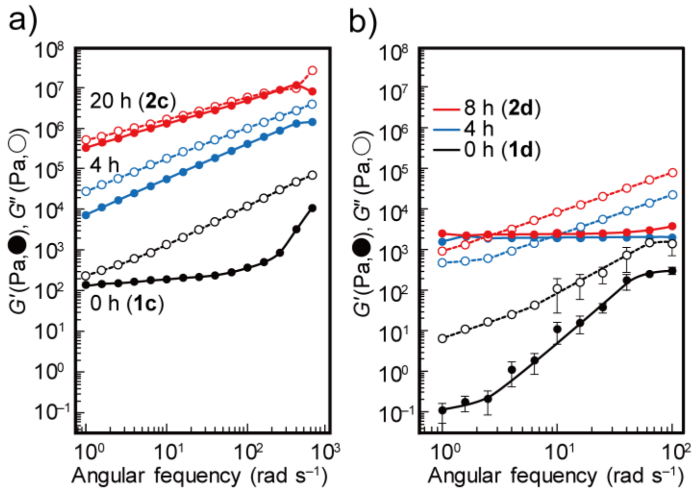

Figure 4-11. Angular frequency dependence of storage moduli (●) and loss moduli (○) of (a) PIL **1c** and (b) IL **1d** before and after photoirradiation (1% strain).

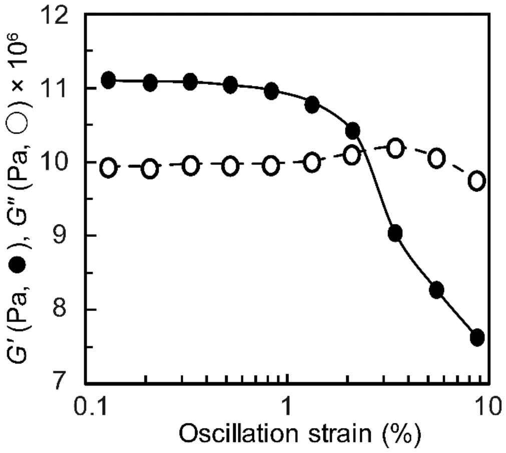

Figure 4-12. Oscillation strain dependence of the storage modulus (●) and loss modulus (○) of IL **1d** (angular frequency: 400 rad s^{-1}).

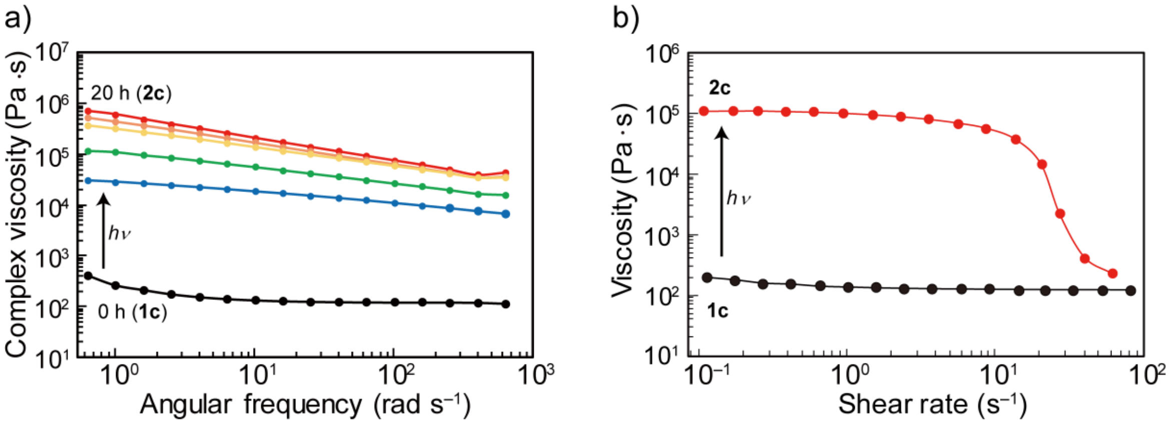

Figure 4-13. (a) Complex viscosity of PIL **1c** before and after UV photoirradiation determined at 4 h intervals (1% strain). (b) The shear rate dependence of the viscosities of PIL **1c** and CP **2c**.

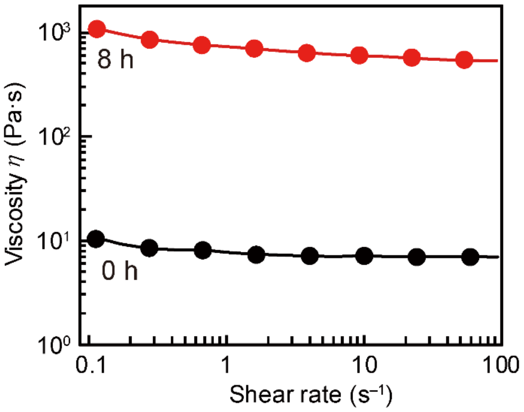

Figure 4-14. Shear rate dependence of viscosities for IL **1d** and CP **2d** (after 8 h photoirradiation).

Ionic conductivity. The ionic conductivities of PIL **1c** and IL **1d** before and after photoirradiation were measured at 25 °C (**Table 4-3**). The ionic conductivity markedly decreased upon photoirradiation, a result of the decreased mobility of the cations. The ionic conductivity was controllable by the application of light and heat.

The ionic conductivities of **1c** and **1d** were 2.2×10^{-6} and 1.9×10^{-5} S cm^{-1}, respectively. The lower value of **1c** is due to the polymeric anion, whereas the ionic conductivity of **1d** is comparable to that of ***tri*-1** (3.1×10^{-5} S cm^{-1}). These ionic conductivities are considerably lower than those of common ILs ([Bmim]Tf$_2$N: 4.1×10^{-3} S cm^{-1} at 25 °C [110]) with respect to their high viscosity. However, the value of the ionic conductivity of **1c**, which contains a small amount of monomer **1d** (< 3 mol%), should be taken with care, because the presence of 3wt% of residual ionic monomer may double the conductivity of the resultant polymer.[150] The Walden product, the product of ionic conductivity and solution viscosity, of **1d** is approximately 10^{-1} mPa s S cm^{-1}, which is comparable to those of common ILs.[87,88]

The ionic conductivity of **1c** gradually decreased upon photoirradiation, decreasing by one order of magnitude in 1 h (**Fig. 4-15a**). Heating the photoirradiated sample at 120 °C for 20 min increased the conductivity, hence the ionic conductivity was reversibly controlled by the alternate application of light and heat (**Fig. 4-15b**, left). Photoirradiation for more than 1 h decreased the ionic conductivity further, but a precise value could not be determined because of instrumental limitations. On the other hand, **1d** has a higher ionic conductivity than **1c** and photoirradiation for 1 h decreased its ionic conductivity by 2 orders of magnitude (**Fig. 4-15a**, dotted curve). Heating the photoproduct at 120 °C for 1 h increased the conductivity by 1 order of magnitude (**Fig. 4-15b**, right). The initial value was not obtained because the product was **1c**, as shown in the previous section. Hence, the subsequent alternate application of light and heat caused a reversible transformation between **1c** and its photoproduct, which resulted in the reversible ionic conductivity change (**Fig. 4-15b**, right). The better repeatability of the ionic conductivity variation starting from **1d** (**Fig. 4-15b**, right) than **1c** (**Fig. 4-15b**, left) may be ascribed to the lower viscosity of **1d**, providing better contact with the electrodes.

These results demonstrated that the ionic conductivities of these materials can be controlled by the application of light and heat. Several polymers,[56,74,84] ILs,[32,132] and PILs[71] exist that exhibit reversible control of ionic conductivity by photoirradiation, though most of them are based on photochromic molecules and few involved in bonding transformation.[74,84,132] As demonstrated in the present and previous studies,[132] the photochemical immobilization of ions enables a direct and flexible control of the ionic conductivity, which should be beneficial for various applications.

Table 4-3. Ionic conductivity (25 °C) and Walden product of **1c**, **1d**, and ***tri*-1**

	Ionic conductivity (S cm^{-1})		Walden product
Compound	Before	After 1h irradiation	(mPa s S cm^{-1})
1c	2.2×10^{-6}	2.0×10^{-7}	–
1d (1st cycle)	1.9×10^{-5}	3.2×10^{-7}	1.5×10^{-1}
(2nd cycle)[a]	3.1×10^{-6}	3.0×10^{-7}	–
***tri*-1**[b]	3.1×10^{-5}	4.8×10^{-7} [c]	8.1×10^{-2}

[a] Transformed to **1c**. [b] Ref. 132. [c] After 2 h of photoirradiation.

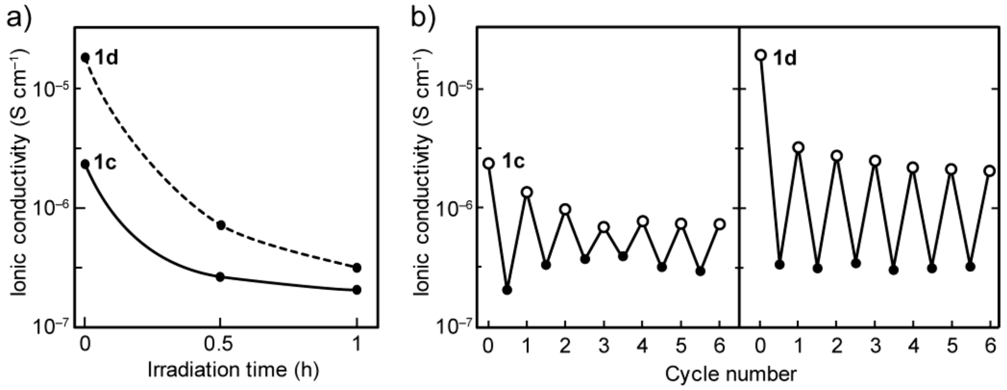

Figure 4-15. Ionic conductivities of PIL **1c** and IL **1d** at 25 °C. (a) Time course of ionic conductivities upon UV photoirradiation. (b) Ionic conductivity changes for alternating cycles of UV photoirradiation for 1 h (filled circles) and heating at 120 °C for 20 min (open circles). The heating period was 1 h only in the first cycle of **1d**.

4.3 Conclusion

In this study, we developed a Ru-containing PIL whose viscoelasticity and ionic conductivity can be reversibly controlled by photochemical and thermal reactions. This PIL transformed to an amorphous hybrid CP upon UV photoirradiation, and a reverse reaction occurred upon heating. Furthermore, the precursor IL of this PIL similarly transformed to an amorphous CP upon photoirradiation. Heating the elastomer produced the PIL, owing to the catalytic activity of the cation. The resulting elastomer from the PIL is a hybrid CP comprising anionic covalent chains and a cationic coordination network. The mechanical properties of the unique polymer warrant further investigation.

In these materials, the ionic conductivity can be controlled by the application of light and heat, the result of the reversible immobilization of the cations. The nonvolatility and high ionic conductivity of PILs and ILs are advantageous properties for photocontrollable electronic and photoresist materials. The strategy followed in this study can be extended to the design of photoresponsive gels and membranes.

4.4 Experimental Section

General. $[Ru(C_5H_5)\{1,3,5\text{-}C_6H_3(OC_6H_{12}CN)_3\}]PF_6$ was synthesized according to a literature method.[23] $KH_2C{=}CHSO_2NSO_2CF_3$ was synthesized by the method found in the literature but slightly modified.[151] Water was used instead of saturated $NaHCO_3$ aq. to wash the dichloromethane solution of the precursor $NHEt_3$ salt. ^1H and ^{19}F NMR spectra were recorded on a Bruker Avance 400 MHz spectrometer. FT-IR spectra were acquired via attenuated total reflectance (ATR) using a Thermo Scientific Nicolet iS5 spectrometer. UV–Vis spectra were obtained with a JASCO V-570 UV/VIS/NIR spectrophotometer. DSC measurements were performed using a TA Instrument Q100 differential scanning calorimeter at a scan rate of 10 °C min^{-1}. Thermogravimetric analyses were performed under a nitrogen atmosphere at a heating rate of 5 °C min^{-1} on a Rigaku TG8120 thermogravimetric analyzer. Dynamic viscoelasticities were measured using a TA Instruments DHR-2 rheometer equipped with an 8 mm parallel plate. The frequency dependence of the dynamic viscoelasticities was established at 25 °C under an application of 1% strain. Ionic conductivities were determined using a Solartron 1260 impedance analyzer. Gold interdigitated electrodes with gap dimensions of 200 μm were used, and the cell constant assessed by measuring the conductivity of 0.01 M KCl aqueous solution at 25 °C. The molecular weight and molecular weight distribution (M_w/M_n) were determined by gel permeation chromatography/size exclusion chromatography (GPC/SEC) on a TOSOH HLC-8320GPC system. Two TSKgel SuperAWM-H (6.0 mm I.D. × 15 cm) columns were used and *N*, *N*-dimethylformamide (DMF) containing 10 mM LiBr was used as the eluent (flow rate 0.6 mL/min, 40 °C). Linear polystyrene standards (Tosoh) in the range of 5.89×10^2 to 5.48×10^6 g mol^{-1} were used for calibration.

Synthesis of IL 1d. A solution of $[Ru(C_5H_5)\{1,3,5\text{-}C_6H_3(OC_6H_{12}CN)_3\}]PF_6$ (168 mg, 0.22 mmol) in a mixture of acetonitrile (1 mL) and methanol (10 mL) was charged to an anion exchange column (Dowex 1X8-100, chloride form, 7 g), and eluted with methanol (100 mL). The eluent was concentrated using a rotary evaporator, and the anion exchange performed again.

The solvent was evaporated under reduced pressure at room temperature to quantitatively obtain $[Ru(C_5H_5)\{1,3,5\text{-}C_6H_3(OC_6H_{12}CN)_3\}]Cl$ as a colorless liquid. $KH_2C{=}CHSO_2NSO_2CF_3$ (181 mg, 0.65 mmol) was added to a dichloromethane dispersion (15 mL) of $[Ru(C_5H_5)\{1,3,5\text{-}C_6H_3(OC_6H_{12}CN)_3\}]Cl$ (143 mg, 0.22 mmol) and stirred for 1 h. An excess amount of the potassium salt was used because the anion exchange was carried out in the dispersion state. To this solution, water (10 mL) was added and the solution further stirred for 1 h. The water layer was removed with a pipette, and the organic layer was washed five times with water and dried over anhydrous magnesium sulfate. The solvent was separated using a rotary evaporator at room temperature, and the residue was dissolved in dichloromethane and charged to a short plug of alumina placed in a chromatography column. After eluting impurities (R_f = 1.0) with dichloromethane/acetonitrile (4:1 v/v), acetonitrile was used to elute the desired product. The solvent was evaporated at room temperature to give the product as a pale yellow liquid, which was further dried under vacuum at ambient temperature for 1 day (yield 138 mg, 74%). An aqueous solution of silver nitrate (0.01 M, 5 mL) was used to check the absence of chloride ions. The presence of chloride ions would make the solution opaque as silver chloride precipitates. ^{1}H NMR (400 MHz, $(CD_3)_2CO$): δ= 1.52 (m, 12H, CH_2), 1.68 (m, 6H, CH_2), 1.82 (m, 6H, CH_2), 2.49 (t, 6H, CH_2, J = 6.9 Hz), 4.15 (t, 6H, CH_2, J = 6.3 Hz), 5.46 (s, 5H, Cp-H_5), 5.57 (dd, 1H, *cis*-CH, J = 0.76, 10.0 Hz), 5.94 (dd, 1H, *trans*-CH, J = 0.7, 16.7 Hz), 6.38 (s, 3H, Ar-H_3), 6.80 (dd, 1H, CHSO$_2$, J = 9.9, 16.6 Hz). ^{19}F NMR (400 MHz, $(CD_3)_2CO$): δ = –78.79 (s, 3F, CF_3). Anal. calcd. for $C_{35}H_{47}F_3N_4O_7RuS_2$: C, 49.00; H, 5.52; N, 6.53. Found: C, 48.85; H, 5.46; N, 6.39. FT-IR (ATR, cm^{-1}): 605, 794, 966 (C=C), 1049 (S=O), 1124, 1172 (S=O), 1321 (S=O), 1414, 1465, 1533 (Ar, C–C), 1632 (C=C), 2244 (CN), 2865 (C–H), 2938 (C–H).

Synthesis of PIL 1c. The mixture of **1d** (65 mg, 7.6×10^{-2} mmol) and AIBN (0.6 mg, 3.7×10^{-3} mmol) was heated at 100 °C for 4 days in the dark under a nitrogen atmosphere. The resulting black viscous liquid was dissolved in a small amount of dichloromethane. The desired product was precipitated by adding a large amount of diethyl ether, and the supernatant removed with a pipette. This procedure was repeated three times to produce an orange yellow highly viscous liquid (yield 57 mg, 88%). ^{1}H NMR spectra ($(CD_3)_2SO$) confirmed that the monomer content was less than 3%. The polymerization reaction hardly proceeded when performed in methanol or DMF, hence we adopted the bulk polymerization. However, the bulk polymerization at 70°C for 3 days left 20% of the monomer unreacted. ^{1}H NMR (400 MHz, $(CD_3)_2SO$): δ= 1.42 (m, 12H, CH_2), 1.59 (m, 6H, CH_2), 1.68 (m, 6H, CH_2), 2.33 (br, 6H, CH_2), 3.97 (t, 6H, CH_2, J = 5.9 Hz), 5.13 (s, 5H, Cp-H_5), 6.34 (s, 3H, Ar-H_3). ^{19}F NMR (400 MHz, $(CD_3)_2SO$): δ= –77.55 (s, 3F, CF_3, head to head), –77.53 (s, 3F, CF_3, head to tail). FT-IR (ATR, cm^{-1}): 605, 794, 1048 (S=O), 1123, 1171 (S=O), 1320 (S=O), 1414, 1465, 1533 (Ar, C–C), 2244 (CN), 2865 (C–H), 2938 (C–H). The molecular weights of PIL **1c** relative to polystyrene standards as determined by GPC/SEC with DMF containing LiBr as the eluent were $M_w = 4.85 \times 10^3$ g mol^{-1}, $M_n = 4.2 \times 10^3$ g mol^{-1}, and $M_w/M_n = 1.16$ (**Fig. 4-16**).

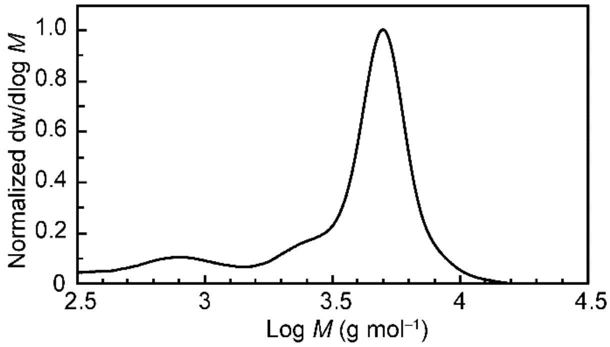

Figure 4-16. Molecular weight distribution curve of PIL **1c** relative to polystyrene standards as determined by GPC/SEC (eluent: DMF containing 10 mM LiBr).

Investigations of reactivities. The UV photoirradiation of the liquids was performed at 10 °C using a Lightningcure UV-LED spotlight source LC-L1V5 (365 nm, 600 mW cm^{-2}). The liquid samples were sandwiched between two quartz plates. The photoirradiation of the samples to measure the ionic conductivity was conducted using sealed electrodes. Thermal reactions were performed using a preheated oven at 120 °C. The dissociation rates of the cation in the photoproducts were determined from the ratio of $[Ru(C_5H_5)(NCCD_3)_3]^+$ and the remaining sandwich complex in the ^1H NMR spectra in CD_3CN.

CHAPTER 5

Switchable Ionic Conductivity and Viscoelasticity of Ruthenium Containing Ionogels

5.1 Introduction

Recently, a number of studies have been conducted on IL-based solid electrolytes, which are generally fabricated by gelation[67,68,152,153] or polymerization[141–144] of ILs. Ionic liquid gels (ionogels) have typically been prepared by incorporating low-molecular-weight gelators,[66,154–158] silica nanoparticles,[159,160] supermolecular polymers,[161,162] or covalently bonded polymers[163,164] into ILs. Furthermore, stimuli-responsive ionogels have been designed to respond to temperature changes,[165–169] pH changes,[170,171] ionic species,[172] light,[75,76,78–80,173–177] electric fields,[178] and magnetic fields.[179] They exhibit interesting switching phenomena, such as ionic conductivity alteration, structural transformation, gel–sol transition, and volume phase transition in response to external stimuli.

Controlling the electronic properties of ionogels via external stimuli, particularly via photoirradiation, is useful for novel switchable electronic devices. However, there are very few examples of ionogels that exhibit photocontrollable conductivity. The ionic conductivity of photoisomerizable ionogels varies upon photoirradiation,[175] although the variation is small. A photo-triggered gel–sol transition accompanies a larger variation,[176] although the sol state is less favorable for electronic devices. Most of the photoresponsive ionogels reported so far contain photochromic molecules such as azobenzene in the gelator or polymer framework, which facilitate the viscoelastic changes or gel–sol transitions by photoisomerization.[76,77,176] Additionally, photoresponsive gels can be synthesized from ILs containing photoresponsive moieties, although very few examples are available because of their high melting points.[80]

This study aims to develop ionogels whose ionic conductivity and viscoelasticity can be reversibly controlled by the application of light and heat. As described in the previous chapters, the ILs shown in **Fig. 5-1**, **1** and ***tri*-1**, transformed into a highly viscous oligomer-containing liquid and an amorphous solid coordination polymer, respectively, upon UV photoirradiation.[23,132] In these reactions, the photodissociation of the arene ligand is followed by the coordination of three CN groups to each Ru ion to form intermolecular bonds between the cations. The reactions were reversed upon heating. These ILs are suitable for producing the desired ionogels because these reactions are accompanied by reversible changes in the ionic conductivity caused by the application of light and heat.[23,132]

This chapter describes the syntheses and properties of ionogels **Gel-1** and **Gel-2**, which are physical gels formed from **1** and ***tri*-1**, respectively. 12-hydroxystearic acid (12-HSA, **Fig. 5-2a**), which is a typical low-molecular-weight gelator used for gelation of edible oils and ILs,[180,181] was used as the gelator in this work. Upon UV photoirradiation, the viscoelasticity of **Gel-1** increased, whereas **Gel-2** turned into a rubber-like solid, and the ionic conductivities of the two gels were reversibly controllable by the application of light and heat (**Fig. 5-2b**). The changes in the physical properties associated with these reactions were evaluated by DSC, dynamic rheology, and ionic conductivity measurements, and are described in the following sections.

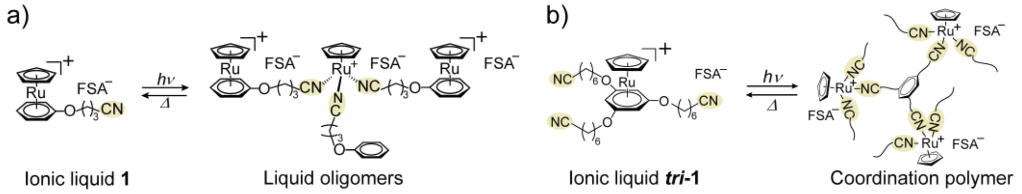

Figure 5-1. Reversible formation of (a) liquid oligomers and (b) coordination polymer from ruthenium-containing ionic liquids **1**[86] and ***tri*-1**.[23] The product of the reaction in a) is a mixture of oligomers.

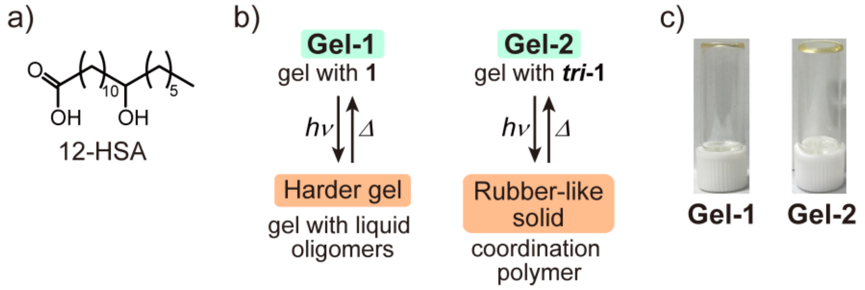

Figure 5-2. (a) Structural formula of the gelator used in this study. (b) The reactivities of **Gel-1** and **Gel-2**. (c) Photographs of the ionogels.

5.2 Results and Discussion

Synthesis and properties of the ionogels. Gel-1 and **Gel-2** were formed by adding 12-HSA (5 wt%) to **1** or ***tri*-1**, followed by heating to 120 °C and subsequent cooling to ambient temperature (**Fig. 5-2c**). They were pale yellow soft gels, exhibiting glass transitions at –60 and –54 °C, respectively, as revealed by DSC (**Fig. 5-3**). These temperatures are identical to the glass transition temperatures of the constituent ILs.[23,86] In both cases, gel–sol transitions were observed in the DSC traces at 73 °C and 66 °C upon heating and cooling, respectively. The gel–sol transition behavior was similar to that exhibited by an organogel composed of 12-HSA (7 wt%) and dodecane upon heating at 70 °C.[182]

Although pure liquid **1** does not crystallize,[86] the IL in **Gel-1** underwent cold crystallization at approximately –10 °C (**Fig. 5-3a**). This feature did not influence the characterization of the materials described below, which were conducted at ambient temperature or higher. The crystallized IL in **Gel-1** melted at 26 °C, which is consistent with its glass transition temperature (–60 °C) in terms of the empirical relationship for molecular liquids ($T_g/T_m = 2/3$).[95] **Gel-2** exhibited no crystallization.

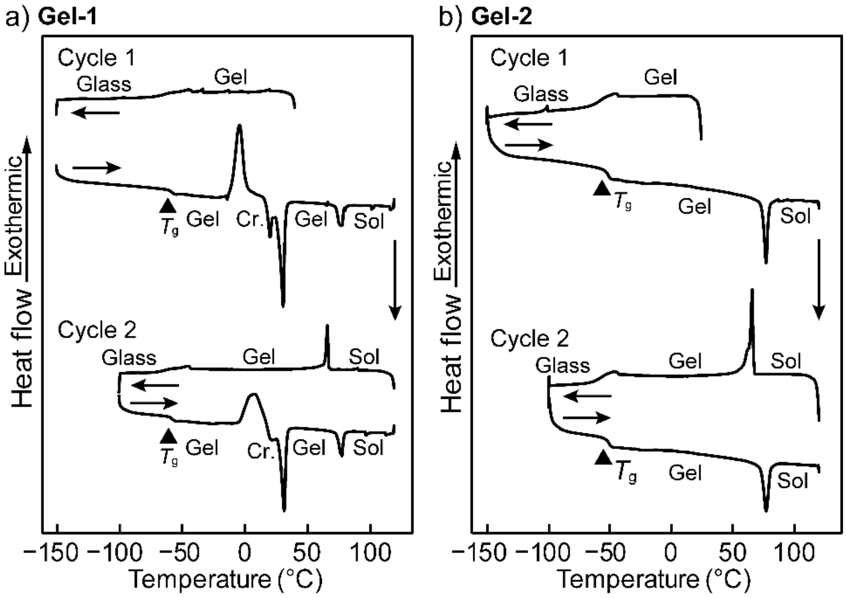

Figure 5-3. DSC traces of (a) **Gel-1** and (b) **Gel-2**.

Reactivities of Gel-1. Upon UV photoirradiation, pale yellow **Gel-1** changed to a yellow gel having a higher viscoelasticity in a few minutes. Heating the photoproduct at 120 °C for 1 min yielded the original gel. This reaction cycle was repeatable.

Upon UV photoirradiation (365 nm, LED), **Gel-1** changed to a yellow gel within a few minutes, owing to the photochemical formation of oligomer cations, as shown in **Fig. 5-1a**. The temporal evolution of the reaction determined from the UV-Vis and ^{1}H NMR spectra is shown in **Fig. 5-4a**. The reaction was 70% complete at 3 min and 90% complete at 10 min, following which it became constant. The spectral changes upon photoirradiation were identical to those observed for **1**.[132] The reaction undergone by **1** under identical conditions is shown in the figure as well. The reaction of **Gel-1** was slightly faster than that of **1**, which is probably attributable to the effect of efficient light scattering inside the gel. The photoproduct returned to its original gel state following heating at 120 °C for 1 min and subsequently cooling to ambient temperature (**Fig. 5-5a**). The photochemical and thermal reaction cycles were repeatable.

The viscoelastic changes upon photoirradiation were evaluated using dynamic rheological measurements (**Fig. 5-6a**). In the measured angular frequency range, the storage modulus (G') exceeded the loss modulus (G'') before and after photoirradiation (strain 0.1%). Both G' and G'' were nearly independent of the angular frequency, indicating a viscoelastic solid-like behavior. The viscoelastic moduli increased by two orders of magnitude following photoirradiation. The values of G' and G'' at 10 rad s^{-1} before photoirradiation were 8.6×10^2 and 1.4×10^2 Pa, respectively, whereas those after photoirradiation (90% reaction completion) were 2.3×10^4 and 3.9×10^3 Pa, respectively. Ionogels containing azobenzene moieties in their polymer backbones exhibit photo-induced changes in their viscoelastic moduli of one order of magnitude or lower,[77–79,173] whereas ionogels containing anthracene moieties in the polymer chain exhibit a larger change owing to photochemical crosslinking.[76] A significant change in the viscoelasticity was achieved in the current materials through a unique mechanism of structural transformation.

The shear-rate-dependence of the viscosities of **Gel-1** and **1**[132] before and after photoirradiation is shown in **Fig. 5-6b**. Upon photoirradiation, their viscosities increased approximately 12 and 6 times, respectively, indicating more significant changes in the gel than in the pure IL. **1** was a Newtonian fluid before and after photoirradiation, whereas **Gel-1** was a pseudoplastic fluid whose viscosity decreased at high shear rates owing to the collapse of the gel structure, approaching the value of **1**.

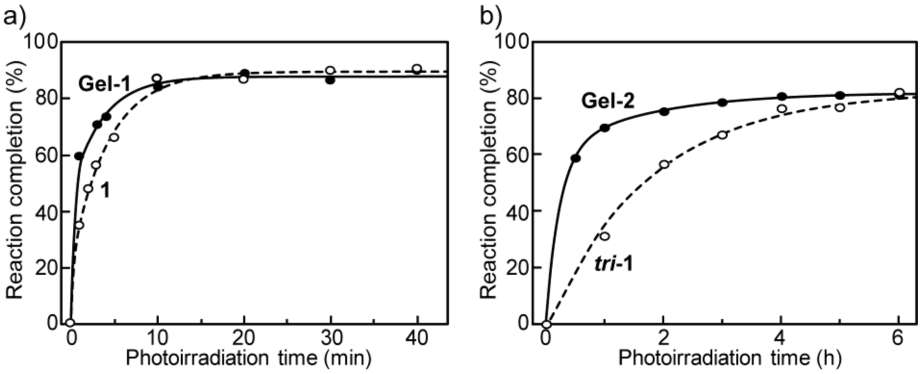

Figure 5-4. Temporal evolution of the photoreactions of (a) **Gel-1** (●) and **1** (○),[132] and (b) **Gel-2** (●) and ***tri*-1** (○).[23]

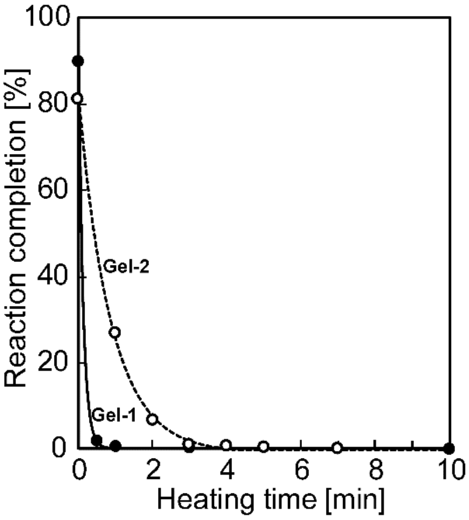

Figure 5-5. Temporal evolutions of the reactions undergone by **Gel-1** (●) and **Gel-2** (○) upon heating at 120 °C.

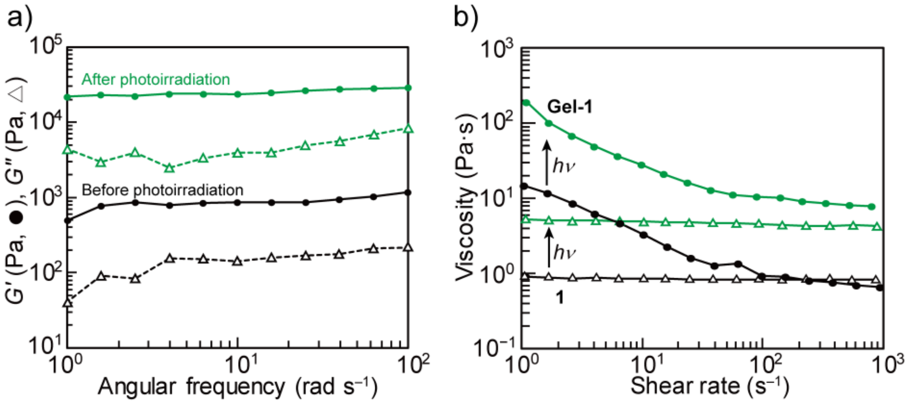

Figure 5-6. (a) Angular frequency-dependence of the viscoelastic moduli of **Gel-1** (G': ●, G'': △) measured before (black) and after (blue) photoirradiation for 1 h at 25 °C (strain 0.1%). (b) Viscosities of **Gel-1** (●) and **1** (△)[132] measured before (black) and after (blue) photoirradiation at 25 °C plotted as functions of shear rate.

Reactivities of Gel-2. Pale yellow **Gel-2** transformed into a yellow rubber-like solid upon UV photoirradiation. The photochemical reaction required several hours, exhibiting a significantly lower rate of reaction than that of **Gel-1**. Upon heating, the photoproduct returned to its original gel form within 3 min. This reaction cycle was repeatable.

Upon UV photoirradiation, **Gel-2** turned into a yellow rubber-like solid within a few hours, in which the cations formed a coordination polymer structure, as shown in **Fig. 5-1b**. **Fig. 5-4b** shows the temporal evolution of the reaction, which was 60% complete at 30 min and 80% complete at 4 h, following which it nearly became constant, because the undissociated cations (~20%) were trapped inside the solid product.[23] The photochemical reaction was much slower than that of **Gel-1**, probably owing to the higher viscosity of ***tri*-1** than **1**.[132] The evolution of the photoreaction of ***tri*-1** is shown in the figure as well. The photoreaction of **Gel-2** was much faster than that of liquid ***tri*-1**, which may be ascribed to efficient light scattering inside the gel. Heating the photoproduct at 120 °C for 3 min yielded the original ionogel. The thermal reverse reaction of the 3-D coordination polymer was slightly slower than that of **Gel-1** (**Fig. 5-5b**). The photoreaction and the thermal reaction constituted a repeatable cycle.

The viscoelastic moduli of **Gel-2** before and after photoirradiation are shown in **Fig. 5-7a**. Prior to photoirradiation, G' exceeded G'' in the measured angular frequency region (strain 0.5%), which indicates elastic behavior. Photoirradiation for 4 h increased G' and G'' by approximately one and two orders of magnitude, respectively (80% reaction completion). G' and G'' measured at 10 rad s^{-1} before photoirradiation were 1.5×10^4 and 3.7×10^3 Pa, respectively, whereas those after photoirradiation were 4.1×10^5 and 2.4×10^5 Pa, respectively. The photoproduct exhibited elastic behavior ($G' > G''$) above approximately 5 rad s^{-1}, which indicates that the material is in the glass-rubber transition region. The viscoelastic moduli of the photoproduct are comparable to those of the photoproduct of ***tri*-1** ($G' = 4.7 \times 10^5$ Pa, $G'' = 2.0 \times 10^5$ Pa, at 10 rad s^{-1}), demonstrating that the gelator has a negligible effect on the viscoelastic moduli of the coordination polymer.

Upon heating the photoproduct at 120 °C for 10 min, the reverse reaction occurred to yield the original ionogel, and the viscoelastic moduli were restored (**Fig. 5-7a**). The changes in viscoelastic moduli at 10 rad s^{-1} during and after repeated photoirradiation and heating cycles are shown in **Fig. 5-7b**, which shows that the viscoelasticity was repeatably controllable.

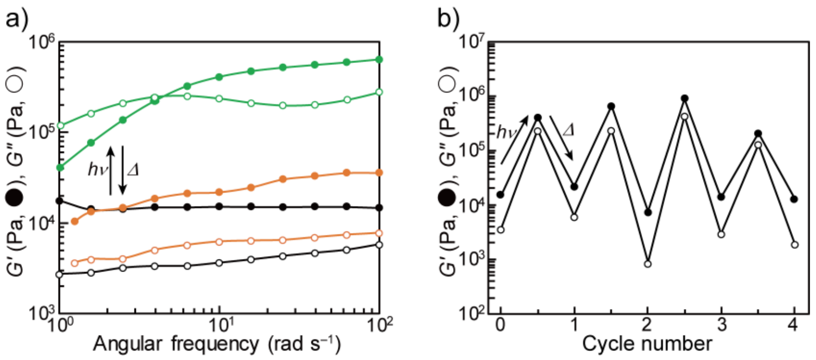

Figure 5-7. (a) Angular frequency-dependence of the viscoelastic moduli (*G*′: ●, *G*″: △) of **Gel-2** before (black) and after photoirradiation for 4 h (green), and after heating the photoproduct at 120 °C for 10 min (orange), measured at 25 °C, strain 0.5%. (b) Changes of viscoelastic moduli of **Gel-2** (*G*′: ●, *G*″: △) at 10 rad s^{-1} during repeated cycles of UV photoirradiation (4 h) and heating (120 °C for 10 min), measured at 25 °C, strain 0.5%.

Ionic conductivities of Gel-1 and Gel-2. The ionic conductivities of the gels were measured before and after UV photoirradiation. Photoirradiation of the gels leads to the formation of intermolecular coordination bonds, thereby decreasing the mobility of the cations, and the ionic conductivities of the gels are reversibly controlled by the application of light and heat.

The ionic conductivities of **Gel-1** and **Gel-2** at 25 °C were 2.6 × 10^{-4} and 2.5 × 10^{-5} S cm^{-1}, respectively (**Table 5-1**). These values are significantly lower than those of ionogels containing imidazolium ILs (*e.g.*, 4 × 10^{-1} S cm^{-1} for 1-allyl-3-butylimidazolium bis(trifluoromethanesulfonyl)amide/12-HSA)[183] because of the low ionic conductivities of the organometallic ILs (**1**: 4.0 × 10^{-4} S cm^{-1}, ***tri*-1**: 3.0 × 10^{-5} S cm^{-1}).[132] The ionic conductivities of the gels were only slightly lower than those of the pure constituent ILs, whereas their viscosities were significantly higher (**Fig. 5-8**), as typically observed in ionogels comprising low-molecular-weight gellators.[66,183]

Upon photoirradiation, the ionic conductivity of **Gel-1** decreased by one order of magnitude from 2.6 × 10^{-4} to 1.2 × 10^{-5} S cm^{-1} in 30 min (**Fig. 5-9a**). This is due to the oligomerization of the cations, which increases the viscosity of the liquid. The oligomer cations and FSA anions are the carrier ions, and the change in ionic conductivity is comparable to that of **1**. In contrast, the ionic conductivity of **Gel-2** decreased by two orders of magnitude upon photoirradiation, from 2.5×10^{-5} to 3.3×10^{-7} S cm^{-1} in 3 h (**Fig. 5-9b**). The change was larger than that of **Gel-1**, which is ascribed to the formation of the cation network, wherein the movement of the carrier ions (FSA anions and undissociated cations (~20%)) is significantly hampered in the photoproduct. Furthermore, the ionic conductivities of these gels following photoirradiation were slightly lower than those of the photoproducts of **1** (3.7×10^{-5} S cm^{-1}) and ***tri*-1** (4.8×10^{-7} S cm^{-1}). In both cases, the ionic conductivity was restored following the heating of the photoproduct at 120 °C for 10 min; hence, the cycling of the ionic conductivity was repeatably controllable. These results further demonstrate that the responsivity can be tuned by the choice of IL in the gel, which is advantageous for device applications.

Table 5-1. Ionic conductivities of **Gel-1** and **Gel-2** before and after UV photoirradiation, and the parameters for their temperature-dependence

Compounds		$\sigma_{25\ °\mathrm{C}}$ (S cm^{-1})	E_a (meV)	A (S K$^{1/2}$ cm^{-1})^a	T_0 (K)^a	σ_∞ (S cm^{-1})^b
Gel-1	before photoirradiation	2.6×10^{-4}	74.9	19.1(3.9)	186.9(6.4)	
	after photoirradiation (30 min)	1.2×10^{-5}	992			$3.2(0.4) \times 10^{11}$
Gel-2	before photoirradiation	2.5×10^{-5}	122	17.0(2.2)	166.3(3.1)	
	after photoirradiation (3 h)	3.3×10^{-7}	780			$1.4(0.5) \times 10^{7}$

^{a} Parameters for the VFT equation. ^{b} Parameters for the Arrhenius equation. Values in parentheses are standard deviations.

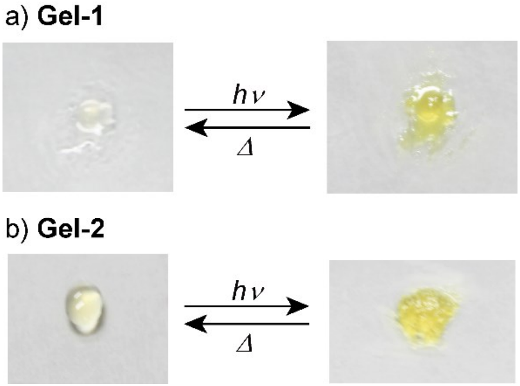

Figure 5-8. Photographs of (a) **Gel-1** and (b) **Gel-2** before and after photoirradiation.

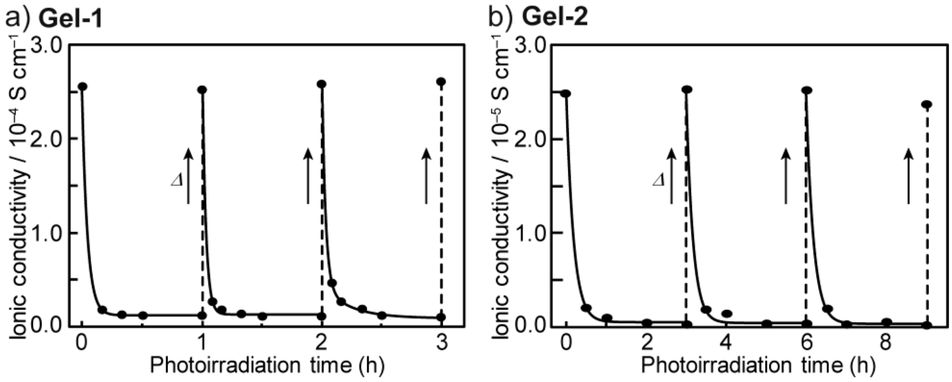

Figure 5-9. Ionic conductivity changes exhibited by (a) **Gel-1** and (b) **Gel-2**, measured at 25 °C during repeated cycles of UV photoirradiation and heating at 120 °C (10 min).

Temperature-dependence of ionic conductivity. The temperature-dependence of the ionic conductivity of the gels was measured before and after the photoreaction. The activation energies for ion transport increased following photoirradiation. The effect of the thermal reverse reaction on the conductivities was observed at elevated temperatures.

The ionic conductivities of **Gel-1** and **Gel-2** are shown in **Fig. 5-10** (left). As the temperature increased from 10 to 120 °C, their conductivities increased from 6.4×10^{-5} to 8.8×10^{-3} S cm^{-1}, and from 7.0×10^{-6} to 1.7×10^{-3} S cm^{-1}, respectively (**Fig. 5-10**, left). No change was observed at the gel–sol transition temperature (73 °C), indicating that the gelator had little effect on the ionic conductivity. The Arrhenius plots deviated from a straight line, as is typically observed in ionogels,[184] and the temperature-dependence $\sigma(T)$ obeyed the VFT (Vogel-Fulcher-

Tamman) equation,[111–113]

$$\sigma(T) = \frac{\mathrm{A}}{\sqrt{T}}\exp(\frac{-E_a}{k_B(T-T_0)}),$$

where A is proportional to the number of carrier ions in matrix, E_a and T_0 are the activation energy for ion transport and the ideal glass transition temperature, respectively.[184,185] The calculated values of the parameters are summarized in **Table 5-1**. The parameters A were similar for **Gel-1** and **Gel-2**, whereas their activation energies E_a differed at 75 and 122 meV, respectively. The higher activation energy for **Gel-2** is consistent with the higher viscosity of the IL in the gel. The activation energies were in the range typically observed from ionogels (50–150 meV).[184,186]

The temperature-dependence of the ionic conductivity of the ionogels following photoirradiation is shown in **Fig. 5-10** (right). During the heating process, the plots for the photoproducts of **Gel-1** and **Gel-2** were linear up to approximately 75 and 65 °C, respectively, and the ionic conductivities were lower than they were prior to photoirradiation. However, inflection points occurred at higher temperatures due to the thermal reverse reaction, and the ionic conductivities became identical to those prior to the photoreaction. The change was continuous in the photoproduct of **Gel-1** because the photoproduct in the gel is in liquid state, whereas the photoproduct of **Gel-2** exhibited a somewhat discontinuous change between 75–120 °C, which is the thermal reaction temperature range of the photoproduct of ***tri*-1**.[23] In both cases, the ionic conductivities measured during cooling from 120 °C were identical to those of the original ionogels.

The temperature-dependences of the ionic conductivities of the photoproducts were fitted using the Arrhenius equation $\sigma(T) = \sigma_\infty \exp(-E_a/k_B T)$.[114,115] The plots are straight lines and not well fitted using the VFT equation. The calculated values of the parameters are summarized in **Table 5-1**. The activation energies E_a for **Gel-1** and **Gel-2** after photoirradiation were 992 and 780 meV, respectively, which are much higher than the values exhibited prior to the photoreaction, reflecting the formation of intermolecular coordination bonds. The σ_∞ value of **Gel-1** (3.2×10^{11} S cm^{-1}) was much higher than that of **Gel-2** (1.4×10^{7} S cm^{-1}) after photoirradiation, because the cation oligomer can be a carrier ion, whereas the coordination polymer cation is immobile. However, these analyses are tentative because the photoproducts were in a transient thermal state, and their actual conduction mechanism is complex.

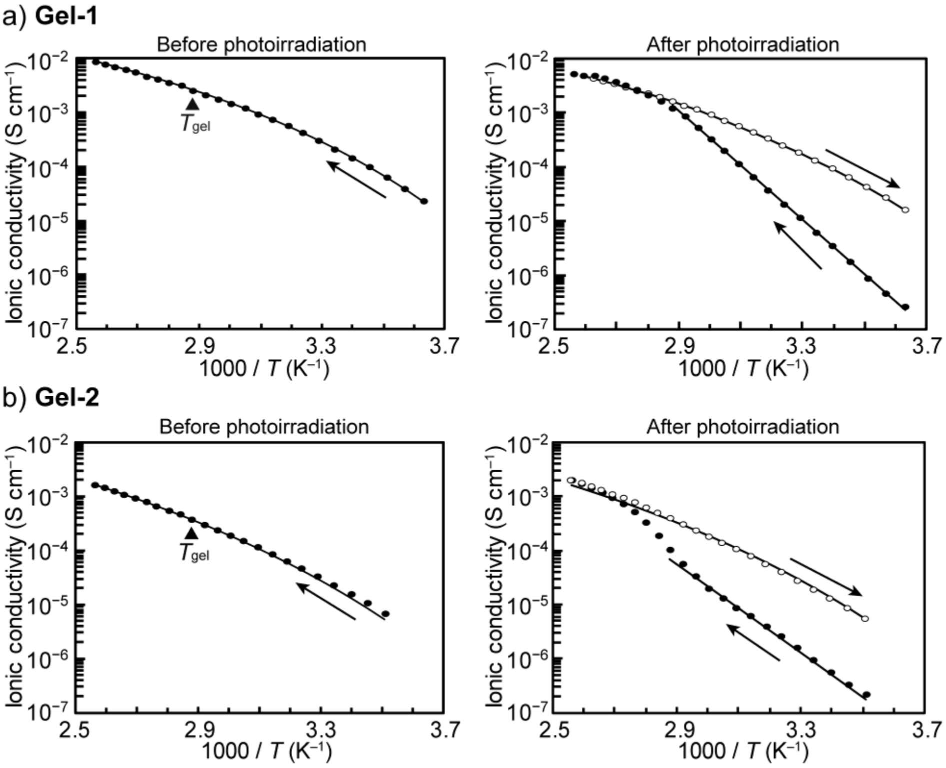

Figure 5-10. Temperature-dependence of the ionic conductivities of (a) **Gel-1**, (b) **Gel-2**, and their photoproducts (●: heating, ○: cooling). The conductivities of the photoproducts were initially measured up to 120 °C, that temperature was maintained for 10 min, and subsequent measurements were performed during cooling.

5.3 Conclusion

Photoreactive ionogels containing organometallic ILs were developed, and their ionic conductivities and viscoelasticities could be reversibly controlled by the application of UV light and heat. This controllability originates from the reversible structural transformation of the photoreactive ILs in the gel. Transformations between gels with different viscoelasticities or between gels and rubber-like solids were achieved depending on the substituents of the ILs, and the resulting change in the ionic conductivity was very large. This study demonstrated a novel strategy for fabricating stimuli-responsive ionically conducting gels. Ionogels such as the ones developed in this work can act as photoswitchable solid electrolytes, which may facilitate the development of novel electronic devices. Although a low-molecular-weight gelator was used in this study, physical gelators whose properties can be tuned in a wider range can be applied in its place.

5.4 Experimental Section

General. **1**[86] and ***tri*-1**[23] were synthesized according to previously reported methods. ^{1}H NMR spectra were recorded using a Bruker Avance 400 spectrometer. FT-IR spectra were acquired using a Thermo Nicolet iS5 spectrometer fitted with an attenuated total reflectance (ATR). UV-vis absorption spectra were recorded on a JASCO V-570 UV/VIS/NIR spectrophotometer. DSC measurements were performed using a TA Instruments Q100 differential scanning calorimeter at a sweep rate of 10 K min^{-1}. Dynamic viscoelasticities were measured using a TA Instruments DHR-1 rheometer equipped with an 8 mm parallel plate. The frequency-dependence of the dynamic viscoelasticity was measured at 25 °C. The ionic conductivities were measured using a Solartron 1260 impedance analyzer. The ionogels were sandwiched between gold interdigitated electrodes (gap dimension: 200 μm) and quartz glass plates, which were further sealed with epoxy resin. The Japan High Tech heating/cooling stage 10013L was used for temperature control.

Preparation and reaction. **Gel-1** and **Gel-2** were prepared by dissolving **1** and ***tri*-1** (20 mg), respectively, with 12-hydroxyoctadecanoic acid (1 mg) in dichloromethane (1.5 mL), followed by heating at 90 °C to evaporate the solvent. The sample was subsequently heated at 120 °C for 10 min and allowed to cool to ambient temperature. The gel obtained was dried in vacuum for 12 h. UV photoirradiation experiments were conducted on samples sandwiched between two quartz plates at 10 °C. The sealed electrodes were photoirradiated for ionic conductivity measurements. A Hamamatsu LIGHTNINGCURE LC-L1V5 UV-LED (365 nm, 600 mW cm^{-2}) was used as the light source. Thermal reactions were performed inside a preheated oven, and measurements were performed after standing the samples at room temperature for 15 h. The dissociation rates of the cations in the photoproducts were determined from the ratio of $[Ru(C_5H_5)(NCCD_3)_3]^+$ and the remaining sandwich complex in the ^{1}H NMR spectra (CD_3CN). The experimental error for the dynamic viscoelasticity measurements (**Fig. 5-7b**) was large because the sample was unloaded and reloaded after each cycle. The photoirradiation and heating cycles were performed under an argon atmosphere.

CHAPTER 6

On-Demand Gelation of Ionic Liquids Using Ruthenium-Containing Photoresponsive Gelators

6.1 Introduction

Supramolecular gels, also called physical gels, are viscoelastic materials that are typically formed by adding low-molecular-weight gelators (LMWGs) to solvents such as water, organic solvents, and ILs.[50,67,187,188] LMWGs undergo self-assembly through intermolecular interactions such as hydrogen bonding, electrostatic interactions, π–π stacking, and van der Waals interactions to form three-dimensional fibril networks, resulting in gelation.[189,190] They are versatile and can be used as separators,[191] emulsifiers,[192,193] and absorbents[194,195] and in catalytic reactions[196–198] and tissue engineering.[199,200]

In recent years, various stimuli-responsive LMWGs have been developed, which facilitate gelation of water or organic solvents by the application of light,[51] heat,[199,201,202] pH,[194,195,203] chemical stimulus,[204,205] and enzymes.[206,207] In particular, photo- induced gel formation is useful for non-contact, non-invasive gelation control. There are several examples of reversible gelation by using photoisomerizable LMWGs, polymer gelators, or metallogelators, typically containing azobenzene moieties.[51,208,209] The LMWGs with photocleavable gelation inhibitor sites, such as o-nitrophenyl and coumarin, exhibit gelation capability upon photoirradiation, though they are irreversible.[52,210,211] In addition to photo-stimuli, enzymatic reactions[212–215] and Diels-Alder reactions[201,202] have been used for gelation control via the cleavage of inhibitor sites.

Ionogels, formed by the gelation of ILs, are highly useful for applications as solid electrolytes, actuators, and gas separation membranes[67,70,152,216] owing to their high ionic conductivity and non-volatility.[6] Photogelation of ILs could extend their manipulation modes and applications, though this remains a challenge; there are only a few examples of IL photogelation, which use specially designed polymer gelators.[77,173,217–220] In comparison with polymer gelators, LMWGs are useful because only a small amount is required for gelation (favorable for ionic conductivity) and they are easily modified and manipulated. There are several LMWGs that are useful for the gelation of ILs, which are typically benzene derivatives with urea substituents.[221,222] Therefore, we aimed to develop a unique, versatile method for the on-demand photogelation of ILs using such LMWGs.

This chapter describes the development of organometallic compounds that release LMWGs upon photoirradiation in ILs. The structures of the gelator-coordinated sandwich complexes designed by us, [CpRu**L**]X (**G1-X**, X = PF_6, $B(CN)_4$; Cp = C_5H_5, **L** = $PhNHCONHC_{12}H_{25}$), and their gelator release mechanisms are shown in **Fig. 6-1a**. Note that **G1-X** are salts; thus, they are miscible in ILs. The complex releases gelator molecule **L** upon UV photoirradiation, and the reverse reaction occurs upon heating. Herein, we chose an LMWG (**L**) suitable for the gelation of ILs.[222,223] This reaction, which proceeds in the presence of coordinating molecules, is based on the reactivity of Ru sandwich complexes in coordinating solvents, as shown in **Fig. 6-1b**.[21,22] As shown in **Fig. 6-1c**, after the addition of a small amount of **G1-X**, various ILs transformed to ionogels upon UV irradiation. These gels underwent the reverse reaction and liquefied back when heated, and the photogelation was repeatable for ILs with coordinating cations. Photogelation of organic solvents was also investigated.

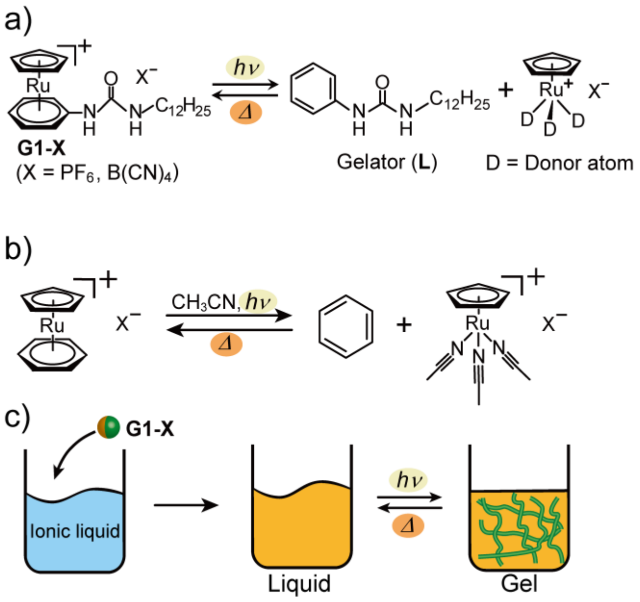

Figure 6-1. (a) Photochemical release of low-molecular-weight gelator **L** from gelator-coordinated complexes **G1-X** (X = PF_6, $B(CN)_4$) designed in this study. In the figure, D is the donor atom of the coordinating molecule in the liquid. (b) Photochemical and thermal reversible reactions of cationic sandwich-type Ru complexes in acetonitrile.[21,22] (c) Schematic representation of a reversible ionogel formation upon the application of light and heat after addition of **G1-X**.

6.2 Results and Discussion

Synthesis and properties of photoresponsive gelators. Salt **G1-PF$_6$** was obtained as a white solid with a melting point of 90 °C by the reaction of [CpRu(CH$_3$CN)$_3$]PF$_6$ with gelator **L**. Upon cooling from the melt, the salt underwent a glass transition at 8°C (**Fig. 6-2**). Salt **G1-B(CN)$_4$** was obtained as a pale-yellow liquid via anion exchange from **G1-PF$_6$**. This liquid did not crystallize upon cooling and underwent a glass transition at −36 °C. Both salts are regarded as ILs with melting points below 100 °C.

The addition of a small amount (5 wt%) of these salts to ILs **A–E**, shown in **Fig. 6-3**, resulted in the formation of homogeneous liquids except for **B**. Salt **G1-PF$_6$** was less soluble in **B** and stayed as a suspension at room temperature. However, the solubility of **G1-PF$_6$** increased at higher temperatures; it formed a homogeneous solution at 80 °C. These results show that the gelation capability of **L** is lost when it is coordinated to the CpRu unit, though **L** can gelate these ILs. The photogelation of the ILs after adding **G1-X** was then investigated, as summarized in **Table 6-1**, the details are described in the following sections.

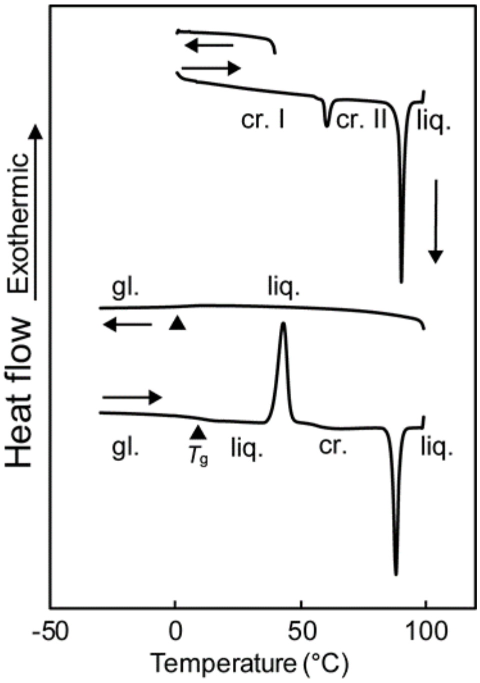

Figure 6-2. DSC curve of **G1-PF$_6$**, where cr., liq., and gl. are the crystal, liquid, and glassy states, respectively. A cold-crystallization peak is seen at 45 °C in the second cycle.

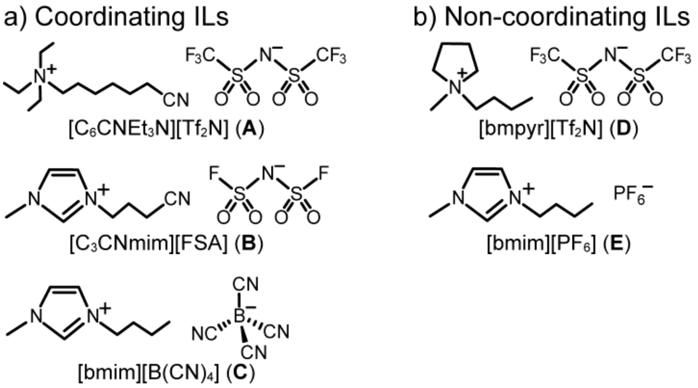

Figure 6-3. Structures of (a) coordinating and (b) non-coordinating ILs used for gelation experiments.

Table 6-1. Typical experimental conditions for photogelation and gel–sol transition temperatures of the resultant gels

				$T_{\mathrm{gel}}{}^{b}$ (°C)	
Gelator	Medium	Photoirradiation time	Heating time^{a}	Heating	Cooling
G1-PF$_6$	**A**	4 h	10 min	73	5
	B	4 h	10 min	83	55
	C	4 h	4 h^{c}	57	28
	E	No reaction			
G1-B(CN)$_4$	**D**	18 h	1 h^{c}	77	49
	E	18 h	1 h^{c}	85	55

^{a} Heated at 120 °C. ^{b} Determined by DSC (1st cycle, scan rate 10 °C min^{-1}). ^{c} Partical decomposition of the gelator occurred during heating.

Photogelation of coordinating ILs with G1-PF$_6$. After adding a small amount of **G1-PF$_6$**, the ILs containing cyano groups in the cation or anion underwent gelation upon photoirradiation, and the gels liquefied again upon heating. However, the non-coordinating ILs did not form gels under the same conditions.

[C$_6$CNEt$_3$N]Tf$_2$N (**A**) and [C$_3$CNmim]FSA (**B**), which contained 5 wt% of **G1-PF$_6$**, were a pale-yellow liquid and a white suspension, respectively. A small amount of undissolved **G1-PF$_6$** remained in the latter. The gelator was released from the complexes upon 4 h of UV photoirradiation (365 nm, LED), and the ILs transformed to yellow gels (**Fig. 6-4a**). In **B**, the undissolved complex gradually dissolved during photoirradiation. The products maintained the gel state after being maintained at room temperature for a week. Upon heating to 120 °C, the gels underwent quantitative reverse reactions within 10 min, returning to the pale-yellow liquid and suspension states. The thermal reverse reaction occurred within a short time period because the resultant cation-coordinated Ru complexes easily dissociated. The photochemical and thermal reactions were repeated at least several times.

The structural changes of the Ru complexes upon photoirradiation were confirmed by ^{1}H NMR and FT-IR spectroscopy (**Figs. 6-5–6-7**). The photorelease of the gelator in **B** was complete within 2 h, whereas the reaction rate in **A** was 84% at 2 h and ~90% at 4 and 6 h. The lower reaction rate in **A** may be ascribed to the occurrence of the concomitant thermal reverse reaction during photoirradiation, owing to the lower thermal stability of the photogenerated Ru complex (see below). In the FT-IR spectra, the peaks ascribed to the C=O stretching vibration of the gelator (1626 cm^{-1}) appeared after photoirradiation, confirming gelator release, though the change in the CN stretching vibration was not clear. Upon heating them, their spectra reverted to those before photoirradiation.

Similarly, the photogelation of [bmim]B(CN)$_4$ (**C**), containing a cyano group in the anion, was possible upon the addition of **G1-PF$_6$** (**Fig. 6-8**). Upon 4 h of photoirradiation, the gelation of the liquid occurred with quantitative gelator release. A small amount of anion-coordinated yellow Ru complexes was formed and suspended in the gel. Upon heating at 120 °C for 4 h, the resultant gel returned to a uniform liquid state, during which the gelator coordinated to the Ru complex. However, gelation did not occur upon further photoirradiation, unlike that in **A** and **B**. This is because partial decomposition (~30%) of the gelator occurred during the longer heating time. The reverse reaction for **C** took much longer than those for **A** and **B** because the anion-coordinated complex does not readily dissociate.

In the FT-IR spectrum of C after photogelation, the C=O stretching vibration peak of the released gelator (1626 cm^{-1}) and the CN stretching vibration peaks of the anion-coordinated Ru complex (2241 cm^{-1})[21,22] were observed (**Fig. 6-5b**). In **G1-PF$_6$**, the C=O stretching vibration peak of the coordinated gelator appeared at 1667 cm^{-1} (**Fig. 6-9a**), and the CN stretching vibration of the $B(CN)_4$ anion is IR silent because of its high symmetry.[24,224] Upon heating the gel, its spectrum became identical to that before its photoirradiation.

In contrast, photogelation did not occurr for [bmim]PF$_6$ (**E**) containing 5 wt% **G1-PF$_6$**, which is ascribed to the absence of coordinating substituents that stabilize the Ru complex in the reaction scheme shown in **Fig. 6-1a**. The absence of gelator release was also confirmed through ^{1}H NMR spectroscopy.

These results demonstrate that the ILs with coordinating substituents in either the cation or anion can be photogelated with **G1-PF$_6$** and the reaction can proceed even when the ILs are in a suspension state. It is convenient that the addition of only a small amount of the complex is sufficient for photogelation, and the gelation time would be shortened by the use of a high-power light source. The ILs containing cyano substituents exhibit suitable reaction solvent properties[105,225] and high CO_2 absorption capacity;[226–228] hence, the photogelation of such functional ILs would be useful for broadening their application scope.

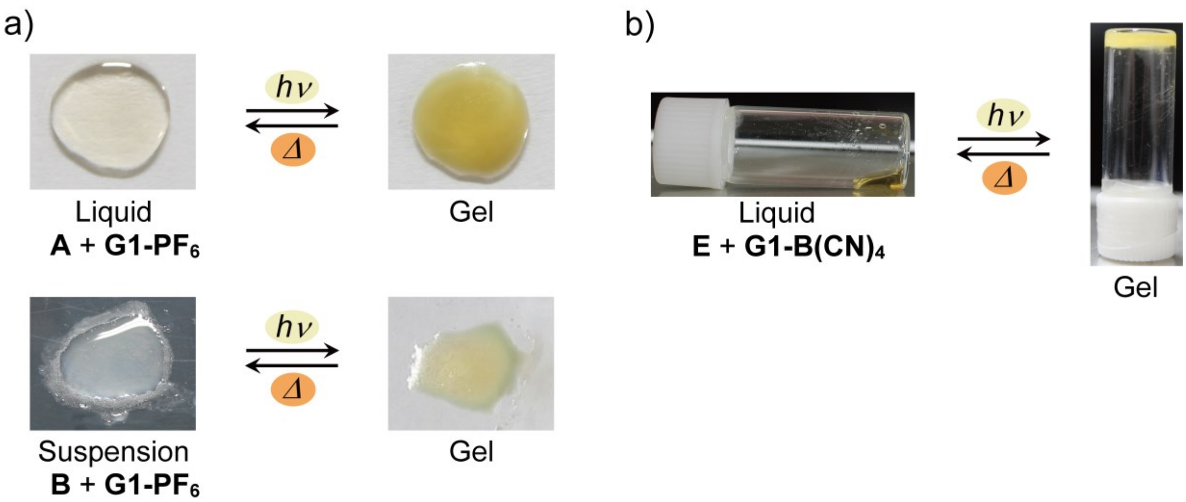

Figure 6-4. Photographs of (a) **A**, **B**, and (b) **E** (containing 5 wt% **G1-X**) before and after photoirradiation.

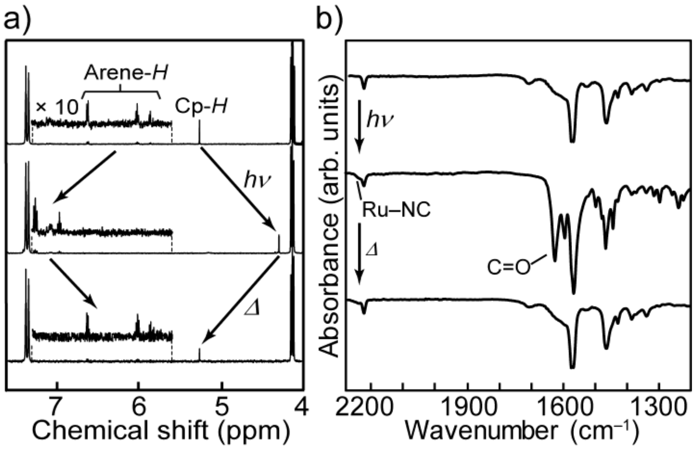

Figure 6-5. (a) ^{1}H NMR spectra (in CD_3CN) of **A** (containing 5 wt% **G1-PF$_6$**) before and after photoirradiation for 4 h and after heating at 120 °C for 10 min. The Ru complex after the photochemical reaction was observed as the solvent-coordinated complex $[CpRu(CD_3CN)_3]^+$. (b) FT-IR spectra of **C** (containing 5 wt% **G1-PF$_6$**) before and after photoirradiation for 4 h and after heating at 120 °C for 4 h.

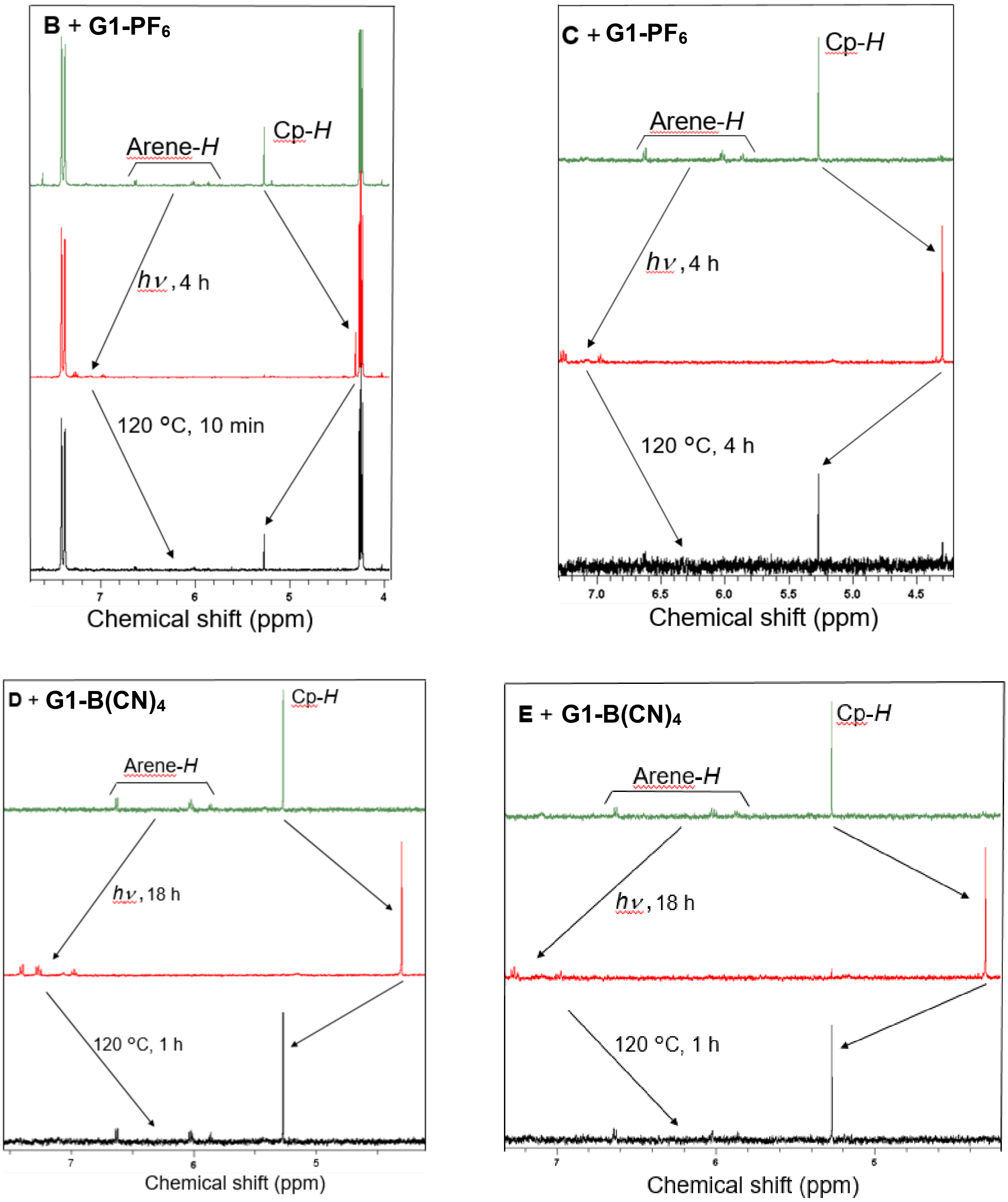

Figure 6-6. ^{1}H NMR spectra (CD$_3$CN) of **B**–**E** (containing 5 wt% **G1-X**) before and after photoirradiation and subsequent heating at 120 °C.

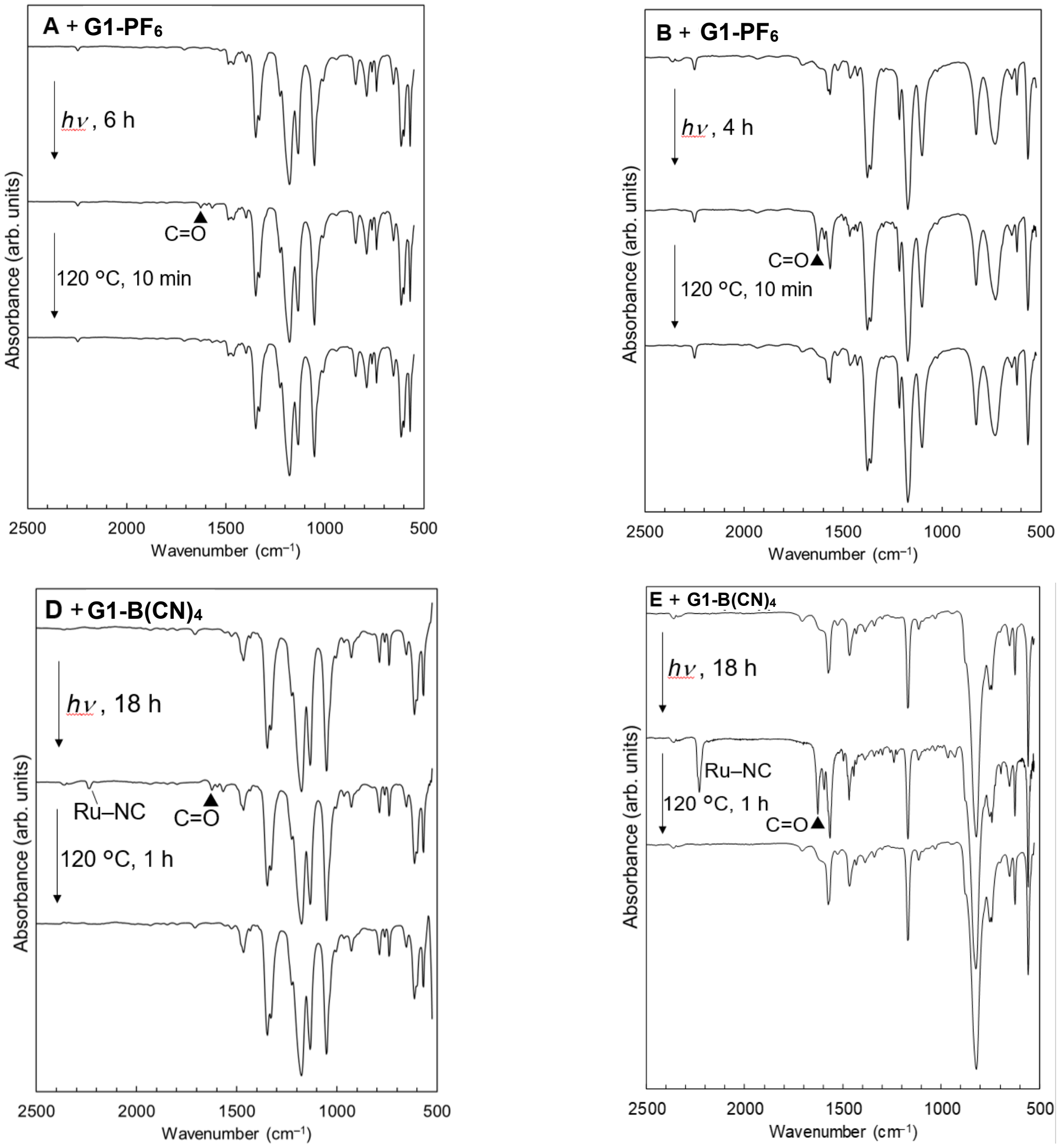

Figure 6-7. FT-IR spectra of **A**, **B**, **D**, and **E** (containing 5 wt% **G1-X**) before and after photoirradiation and after subsequent heating at 120 °C.

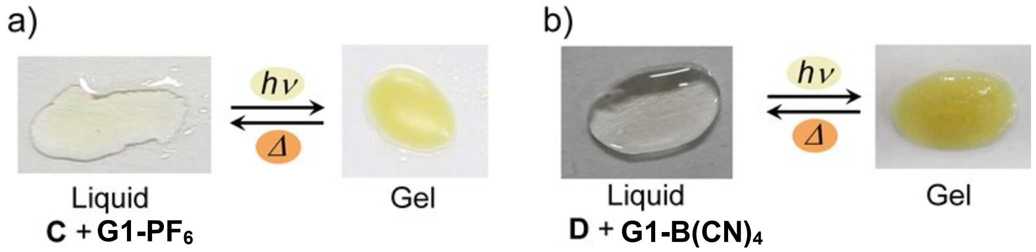

Figure 6-8. Photographs of **C** (containing 5 wt% **G1-PF$_6$**) and **D** (containing 5 wt% **G1-B(CN)$_4$**) before and after photoirradiation.

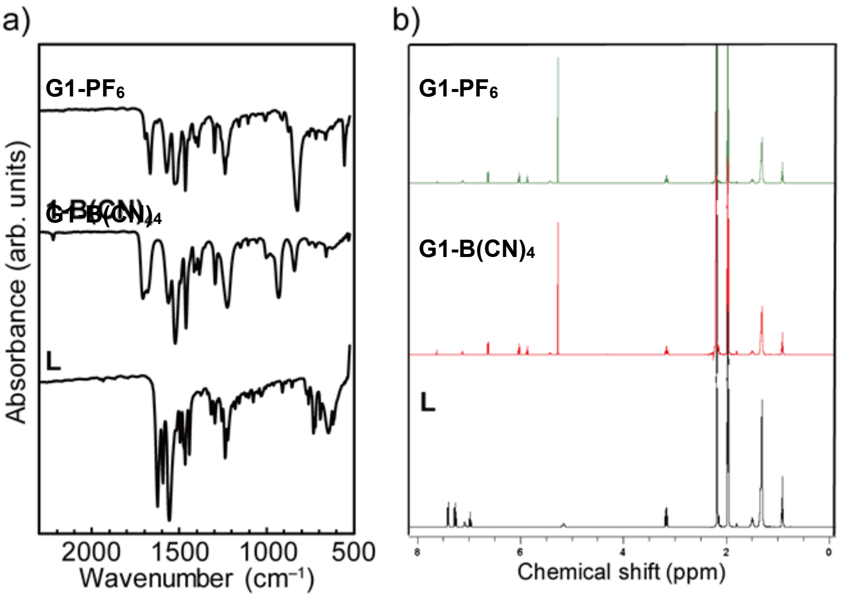

Figure 6-9. (a) FT-IR and (b) ^{1}H NMR (CD_3CN) spectra of **G1-PF$_6$**, **G1-B(CN)$_4$**, and **L**.

Photogelation of non-coordinating ILs with G1-B(CN)$_4$. The photogelation of non-coordinating ILs was achieved using **G1-B(CN)$_4$** with the coordinating anion, though the reaction took longer.

Upon UV photoirradiation (365 nm, LED) for 18 h, pale-yellow liquids of [bmPyr]Tf_2N (**D**) or [bmim]PF_6 (**E**) containing 5 wt% of **G1-B(CN)$_4$** transformed to yellow gels (**Figs. 6-4b** and **6-8**). Although the gelator release was quantitative at 18 h, the reaction rate was still 66% at 4 h for **E**, requiring a significantly longer photoirradiation time than that required by the ILs described in the previous section. This happened because the anions in the liquids are mostly PF_6^-, making the reaction of the Ru complex with $B(CN)_4^-$ substantially less efficient. The release of the gelator upon photoirradiation and the coordination of the anion to the Ru ion were confirmed spectroscopically (**Figs. 6-6** and **6-7**). The gels obtained via photoirradiation maintained their gel state even after remaining idle for a week. Upon heating at 120 °C for 1 h, the gels liquefied again owing to the reverse reaction. However, the gelation of the liquid did not occur upon further photoirradiation because the thermal reaction of the anion-coordinated complex involved partial decomposition of the gelator, similar to that in the gel containing **C**, as described in the previous section. The decomposition was facilitated at higher temperatures.

Structures and properties of ionogels prepared via photoirradiation. The structures and the thermal and mechanical properties of the ionogels were investigated by differential scanning calorimetry (DSC), scanning electron microscopy (SEM), and dynamic viscoelasticity measurements. The physical properties of the gels prepared via photoirradiation were found to be comparable to those of the ionogels prepared by the addition of the gelator to the corresponding ILs. In some cases, additional thermal treatment after photogelation was conducted to allow the formation of stronger gelator networks.

The occurrence of thermal gel–sol transitions in the ionogels prepared via photogelation was detected through DSC. The transition temperature (T_{gel}, heating) ranged between 57 and 85 °C depending on the ILs (**Table 6-1** and **Fig. 6-10**). Except for the gel prepared from **G1-PF$_6$** and **A** via photoirradiation, the sol–gel transition temperatures of the gels measured upon cooling (T_{gel}, cooling) were approximately 30 °C lower than those measured upon heating (T_{gel}, heating). Their sol–gel transition temperatures were almost the same as those of the gels prepared by the addition of gelator **L** to each IL (reference gels), showing similar hysteresis (**Table 6-2**). Thermal hysteresis is often observed in physical gels.[229]

The DSC curves of the ionogel containing **A** are shown in **Fig. 6-11**. The gel–sol transition was observed in the first cycle at 73 °C during heating, similar to the reference gel (T_{gel} = 70 °C, heating). However, the sol–gel transition was observed at 5 °C during cooling; the transition temperature was significantly lower than that of the reference gel (T_{gel} = 41 °C, cooling; **Table 6-2**). This is probably owing to the partial thermal reverse reaction that occurred during the measurement, which reduced the gelator concentration. In the second cycle, the gel–sol transition was observed at 54 °C (T_{gel}, heating), which was lower than that in the first cycle owing to the same reason. The facile thermal reverse reaction is ascribed to the intramolecular repulsion between the ammonium cations in the photogenerated complex. Upon further heating the gel, a small, very broad endothermic peak was observed at ~130 °C, which corresponds to the coordination of the gelator to the CpRu unit,[23] after which the gel–sol transition peaks disappeared (**Fig. 6-11a**). The other ionogels prepared by photogelation exhibited almost the same thermal behavior, but the gel–sol transitions were identical in the first and second cycles because the photogenerated complexes were thermally more robust. In the DSC curves of the ionogel containing **B**, small peaks corresponding to the dissolution (79 °C) and precipitation of **G1-PF$_6$** were also observed after the thermal reverse reaction, as expected for the suspension.

The SEM image of the ionogels prepared via photogelation showed fibrous microcrystalline network structures consisting of bundled nanosticks (**Fig. 6-12**). These are microcrystalline gels[229] although physical gels with LMWGs typically have linearly interconnected structures. Similar structures were observed in the gels prepared by the addition of gelator **L** to each IL (**Fig. 6-12**).

The storage modulus (G') and loss modulus (G'') of the ionogels prepared via photogelation, as investigated by dynamic viscoelasticity measurements, are listed in **Table 6-3**. In all ionogels, G' was higher than G'' within the angular frequency range of 1–100 rad s^{-1} (strain 0.1%), indicating elastic behavior (**Figs. 6-11b** and **6-13a**). The complex viscosities decreased with increasing angular frequencies, which is a typical behavior of gels.[230] These were soft gels, which yielded at 0.1–0.4% strain (**Fig. 6-13b**). These gels exhibited almost the same viscoelastic modulus as the reference gels prepared with gelator **L** (**Figs. 6-14** and **6-15**); however, the gels with **A** and **C** prepared via photogelation exhibited much lower values, which are ascribed to their higher gelator crystallinity. Thermal treatment (heated to 100 °C and subsequently cooled to ambient temperature) was effective for these gels in forming a stronger gelator network via the sol–gel transition (**Table 6-3**, **Fig. 6-16**).

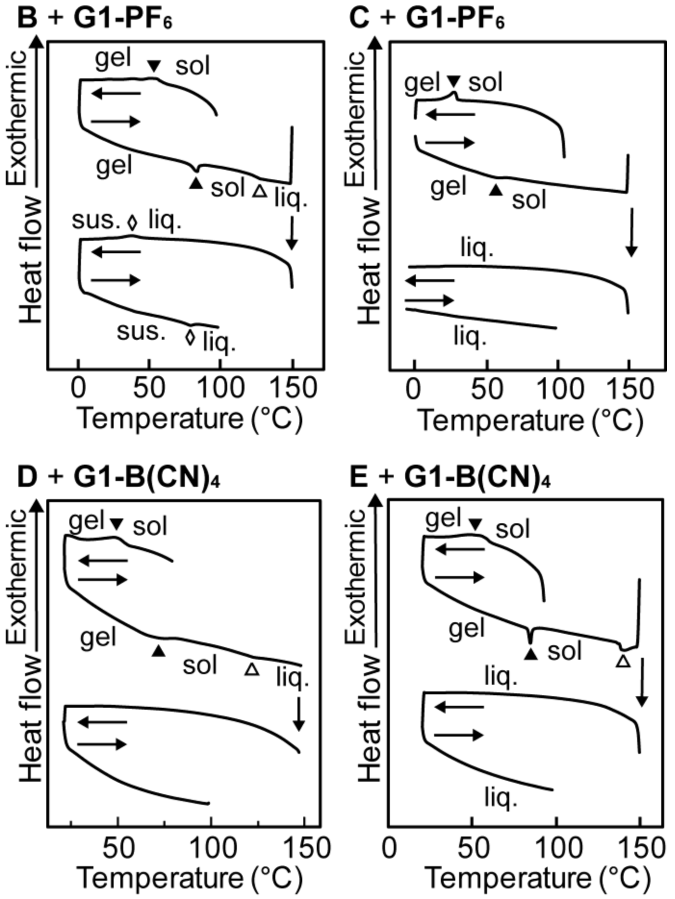

Figure 6-10. DSC curves of the ionogels prepared by photoirradiation of **B–E** (containing 5 wt% **G1-X**), where liq. and sus. are the liquid and suspension states, respectively. The peaks corresponding to the gel–sol transition, gelator coordination, and dissolution of the complex are shown by ▲, △, and ◊ symbols, respectively.

Table 6-2. Gel–sol transition temperature of the ionogels prepared by adding gelator **L**

	T_{gel} (°C)	
IL	heating	cooling
A^a	70	41
B^a	85	57
C^a	61	33
D^b	69	45
E^b	84	47

The amount of gelator added: ^{a} 2.4 wt% and ^{b} 2.5 wt%.

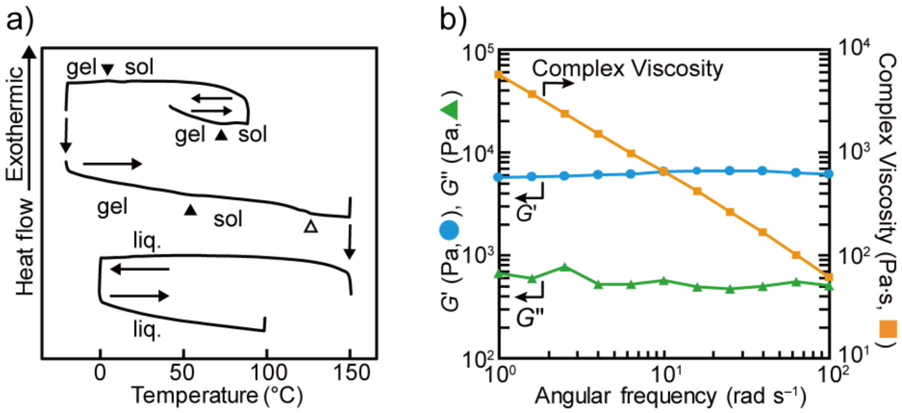

Figure 6-11. (a) DSC curves of **A** (containing 5 wt% **G1-PF$_6$**) after photogelation, where liq. is a liquid state. The peaks corresponding to the gel–sol transition and gelator coordination are designated by ▲ and △, respectively. (b) Angular frequency dependence of storage modulus (G'), loss modulus (G''), and complex viscosity of **B** (containing 5 wt% **G1-PF$_6$**) after photogelation (25 °C, strain 0.1%).

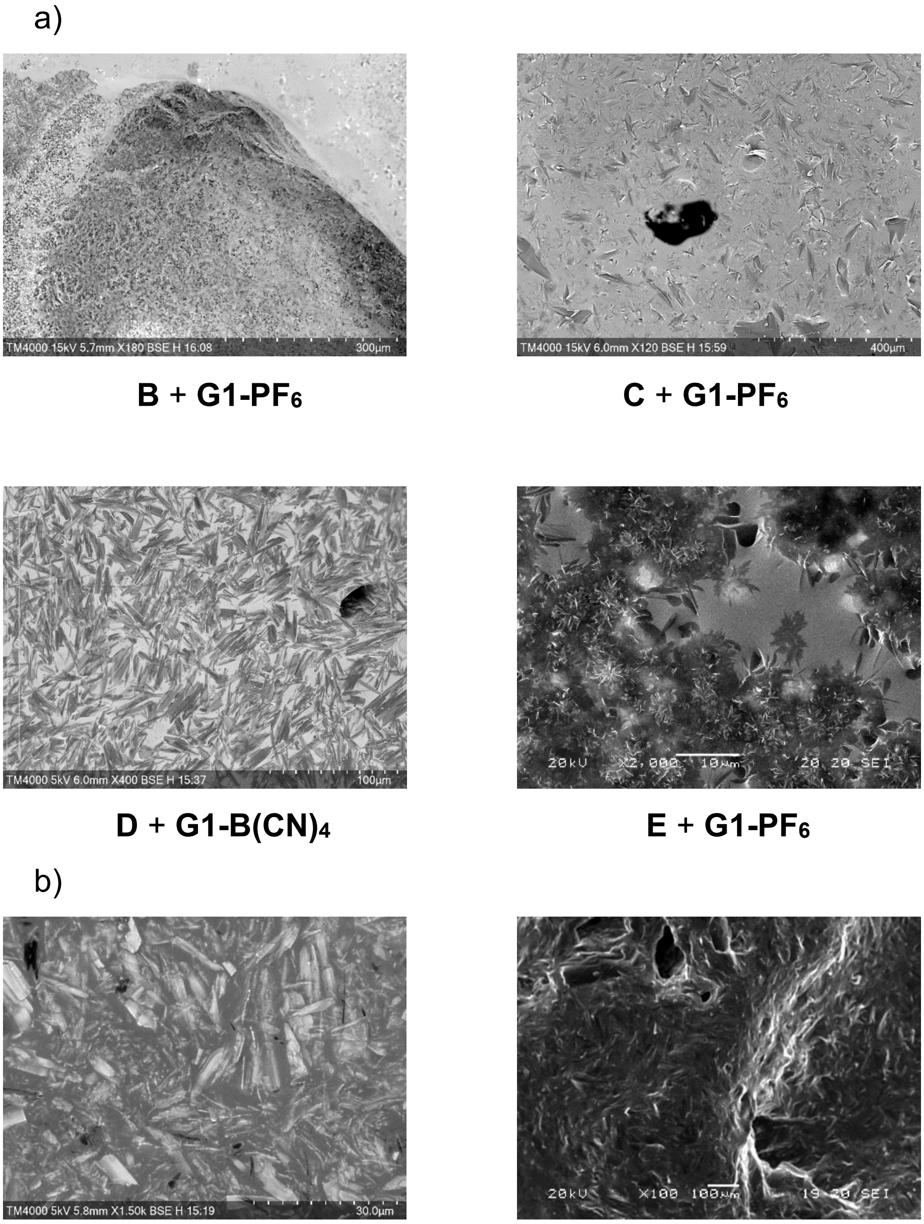

B + G1-PF$_6$ **C + G1-PF$_6$**

D + G1-B(CN)$_4$ **E + G1-PF$_6$**

D + L **E + L**

Figure 6-12. SEM images of the ionogels prepared by (a) photoirradiation of **B–E** (containing **G1-X** 5 wt%) and (b) addition of gelator **L** (2.4 wt%) to the ILs. The dark spot in the right figure in (a) is an artifact by electron beam damage.

Table 6-3. Storage modulus (*G′*), loss modulus (*G″*), and yield strain of ionogels prepared by photogelation[a] and gelator addition[b]

Medium	Gel preparation	Gelator	*G′* (Pa)[c]	*G″* (Pa)[c]	Yield strain[d] (%)
A	Photogelation	**G1-PF$_6$**	1.5×10^2	6.1×10^1	0.2
	Photogelation + heating[e]	**G1-PF$_6$**	7.3×10^3	7.0×10^2	0.4
	Gelator addition	**L**	1.1×10^4	3.7×10^3	0.1
B	Photogelation	**G1-PF$_6$**	6.5×10^3	5.7×10^2	0.4
	Gelator addition	**L**	5.7×10^3	8.7×10^2	0.1
C	Photogelation	**G1-PF$_6$**	7.6×10^3	1.1×10^3	0.4
	Photogelation + heating[e]	**G1-PF$_6$**	2.4×10^5	3.2×10^4	0.4
	Gelator addition	**L**	1.3×10^5	1.5×10^4	0.1
D	Photogelation	**G1-B(CN)$_4$**	1.3×10^4	2.0×10^3	0.1
	Gelator addition	**L**	1.5×10^4	3.6×10^3	0.1
E	Photogelation	**G1-B(CN)$_4$**	1.9×10^4	2.2×10^3	0.4
	Gelator addition	**L**	7.0×10^3	6.3×10^2	0.3

[a] Prepared upon photoirradiation after the addition of **G1-X** (5 wt%). [b] Heated to 120 °C after the addition of gelator **L** (2.4–2.5 wt%). [c] Angular frequency 10 rad s^{-1}, strain 0.1%. [d] Angular frequency 10 rad s^{-1}. [e] Heated to 100 °C after photogelation.

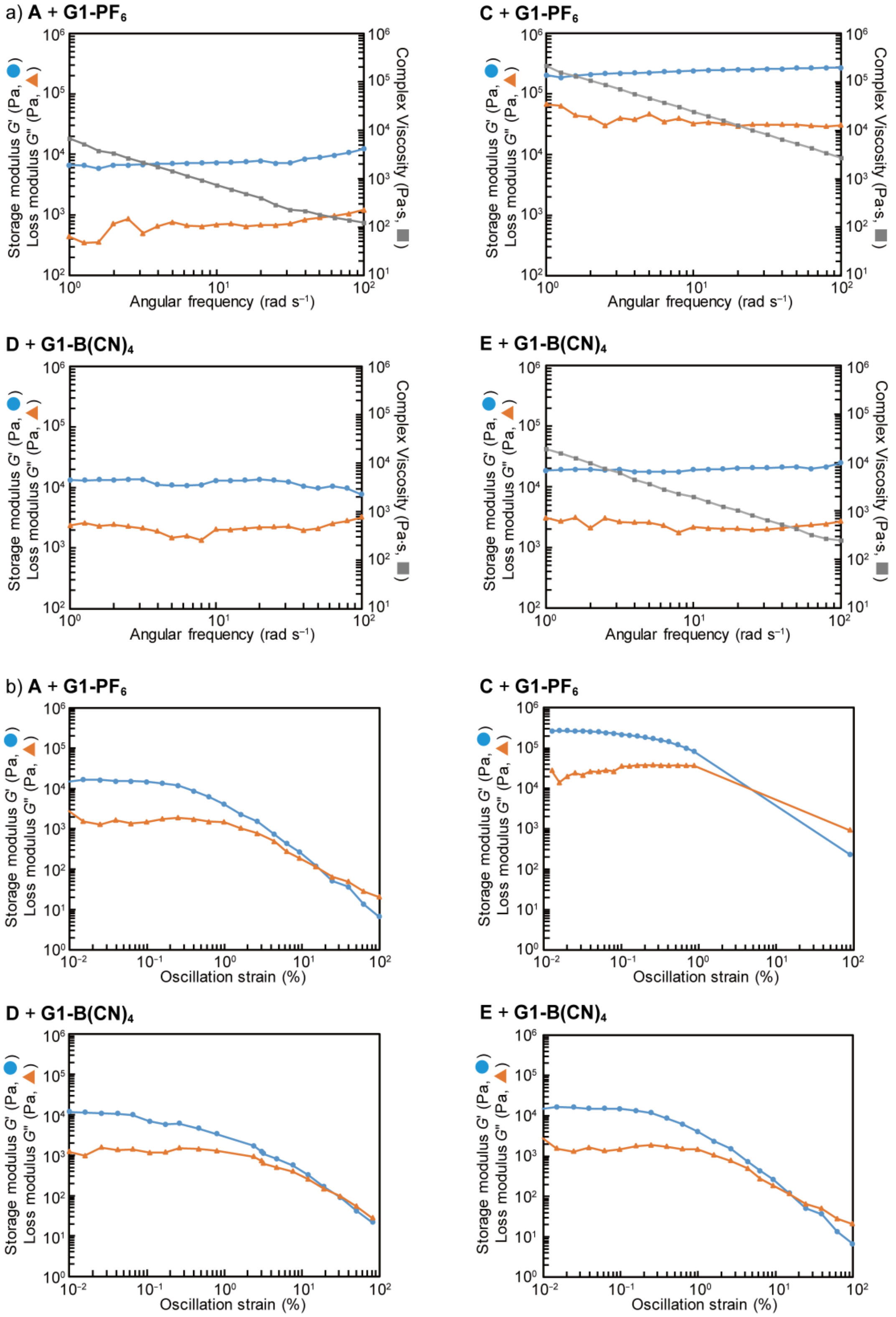

Figure 6-13. (a) Angular frequency dependence (25 °C, strain 0.1%) and (b) strain dependence (10 rad s^{-1}) of viscoelastic moduli (*G*′: △, *G*″: □) and complex viscosity (○) of the ionogels prepared by the photoirradiation of **A**, **B**, **D**, and **E** (containing 5 wt% **G1-X**). Data for **A** and **C** are acquired after thermal treatment (100 °C, 30 s).

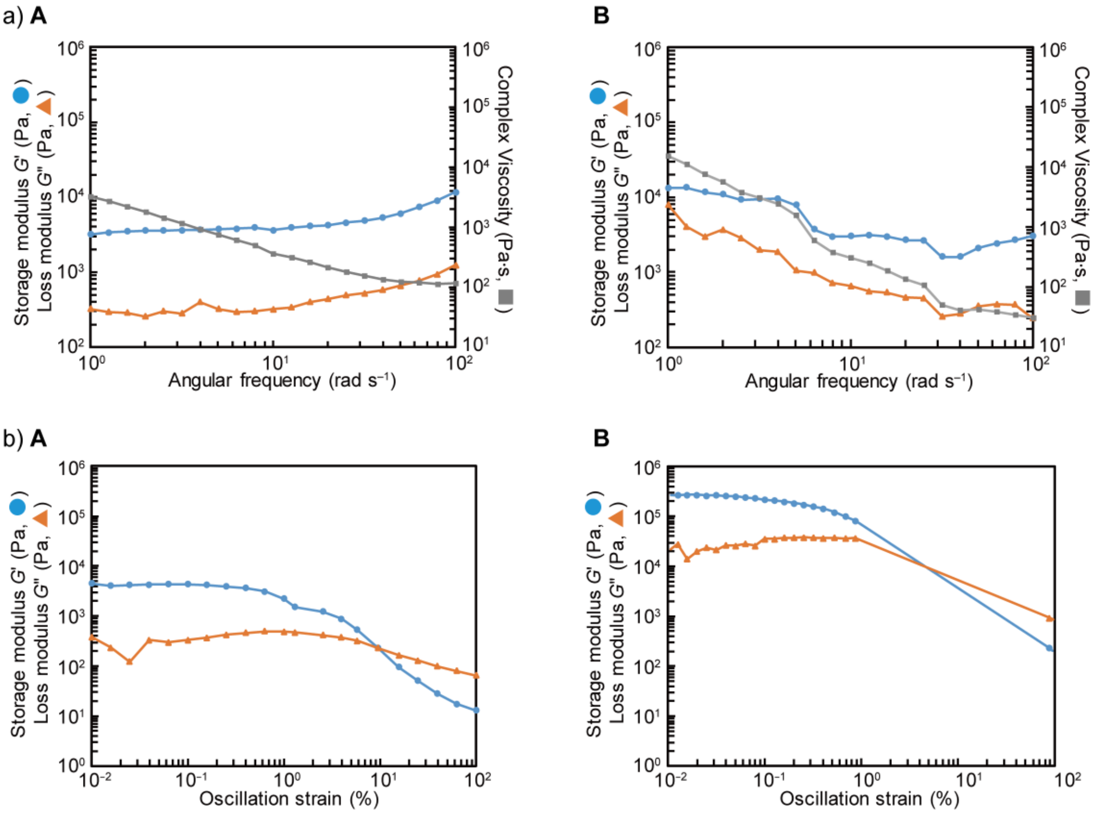

Figure 6-14. (a) Angular frequency dependence (25 °C, strain 0.1%) and (b) strain dependence (10 rad s^{-1}) of the viscoelastic moduli (*G*′: △, *G*″: □) and complex viscosity (○) of ionogels from **A** and **B** (containing 5 wt% **G1-PF$_6$**) after three cycles of photoirradiation. The data for **A** were acquired after thermal treatment (100 °C, 30 s).

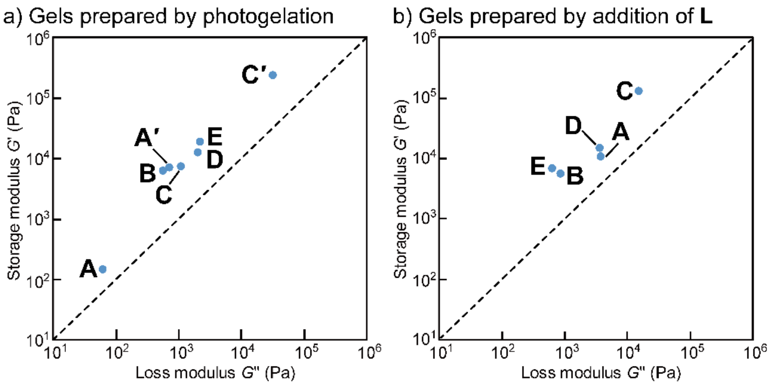

Figure 6-15. Plots of storage modulus (*G*′) and loss modulus (*G*″) of the ionogels prepared by the (a) photoirradiation of **A–E** (containing 5 wt.% **G1-X**) and (b) addition of gelator **L** (**A–C**: 2.4 wt.%, **D** and **E**: 2.5 wt%) to the ILs. For **A** and **C**, the values after thermal treatment of the gel (100 °C, 30 s) are also plotted (**A′** and **C′**).

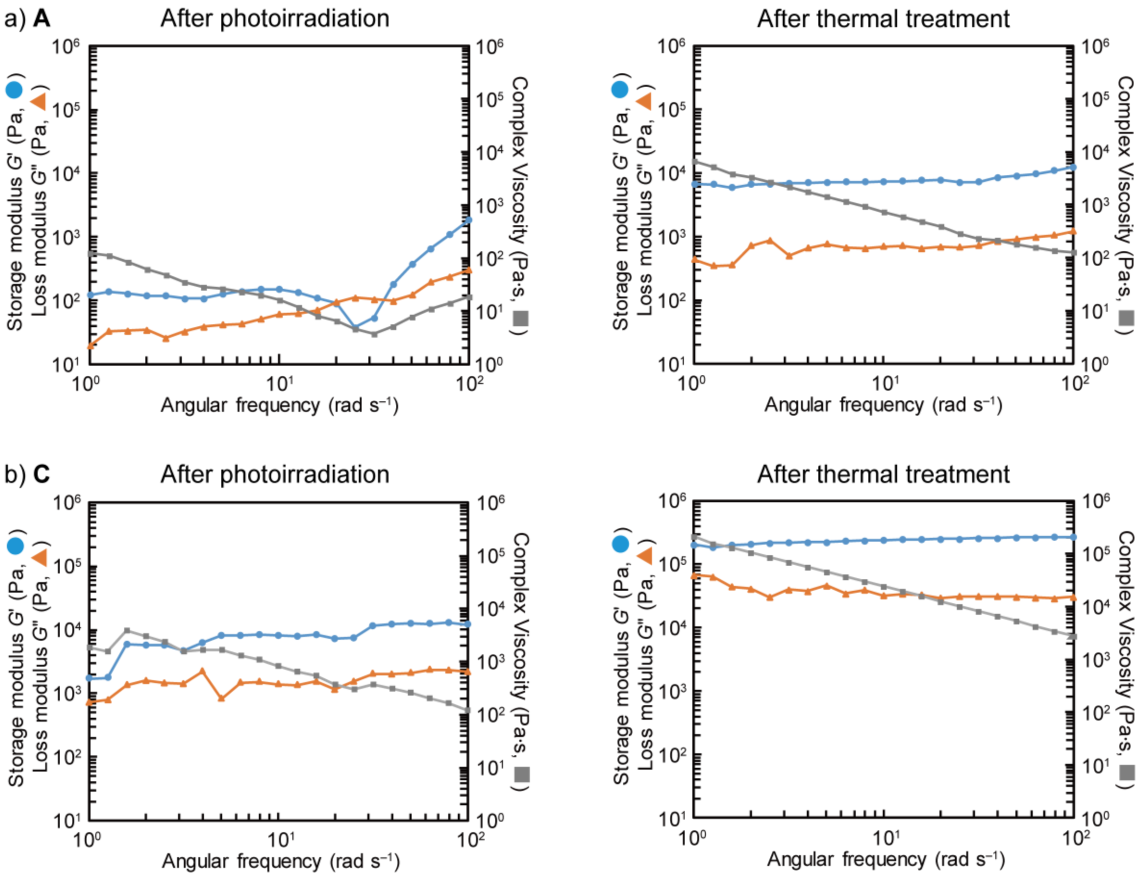

Figure 6-16. Angular frequency dependence (25 °C, strain 0.1%) of the viscoelastic moduli (G': △, G'': □) and complex viscosity (○) of gels of (a) **A** and (b) **C** (containing 5 wt% **G1-PF$_6$**) formed upon photoirradiation. Data acquired immediately after photoirradiation (left) and after subsequent thermal treatment (100 °C, 30 s; right) are shown.

Photogelation of organic solvents. Salt **G1-X** also allowed the photorelease of the gelator in organic solvents, producing gels under suitable conditions. The gelation capability could be modulated by changing the ligand species.

Upon UV photoirradiation for 1 h at 10 °C of a pale-yellow acetonitrile solution containing 5 wt% **G1-PF$_6$**, the Ru complex quantitatively released the gelator in the solution. Although no gelation occurred, given that the gelator precipitated as a white solid (**Fig. 6-17**), the gel was formed by heating the mixture to 70 °C to dissolve the solid and subsequently cooling it to 25 °C. This is because the gelator network structure is formed through sol–gel transition. Upon heating the yellow gel at 120 °C for 20 min, the complex underwent a reverse reaction to give the original liquid; hence, the photogelation was repeatable. Similarly, a benzonitrile solution containing 5 wt% **G1-PF$_6$** changed from colorless to pale yellow upon 1 h of UV photoirradiation (**Fig. 6-17b**), during which the Ru complex quantitatively released the gelator in the solution. Although the resultant solution was liquid at ambient temperature owing to its low gel–sol transition temperature, it formed a gel within 1 h when kept at 0 °C. The gel became a partial gel when warmed up to 25 °C, and upon further heating at 120 °C for 20 min, the reverse reaction occurred. Therefore, the photogelation was repeatable.

A toluene solution containing 5 wt% **G1-PF$_6$** did not release the gelator upon photoirradiation due to the absence of coordinating sites, resulting in partial deposition the gelator. In contrast, a toluene solution containing 5 wt% **G1-B(CN)$_4$** underwent gelator release after 18 h of photoirradiation, resulting in the deposition of a white solid of gelator **L** and an orange solid of the anion-coordinated Ru complex. Although it was a mixture, it transformed to a gel after heating to 70 °C and being subsequently left at 25 °C for 1 h (**Fig. 6-17c**). Upon further heating the gel at 120 °C, toluene coordinated to the Ru complex to give a sandwich complex [CpRu(toluene)]$^+$, which was soluble in toluene. The gelator did not coordinate to the complex, hence only gel–sol transitions were repeatedly observed upon temperature changes of the resultant gel. Other nonpolar liquids such as liquid paraffin can be gelated with gelator **L**, although their photogelation with **G1-B(CN)$_4$** was not possible because they were immiscible.

The gelation capability could be modulated by changing the ligand species. In addition to gelator **L**, there are many similar gelators with different gelation properties;[221] hence, appropriate gelators can be chosen. For example, gelator **L** is insoluble in a 70% ethanol aqueous solution and does not form a gel. However, gelator **L** (= *o*-$C_6H_4(CH_2Ph)(NHCONHC_{12}H_{25})$) containing a benzyl group can gelate the liquid,[221] and photogelation was possible by using an **L**-coordinated complex (**G2-B(CN)$_4$**, **Fig. 6-17d**). The complex formed a suspension in the 70% ethanol aqueous solution although it formed a gel upon photoirradiation. After photogelation, only gel–sol transitions were repeatable upon temperature changes, because the photogenerated Ru complex decomposes in the solution. The results demonstrate that the photogelation capability of the complex can be adjusted by choosing the appropriate ligand species.

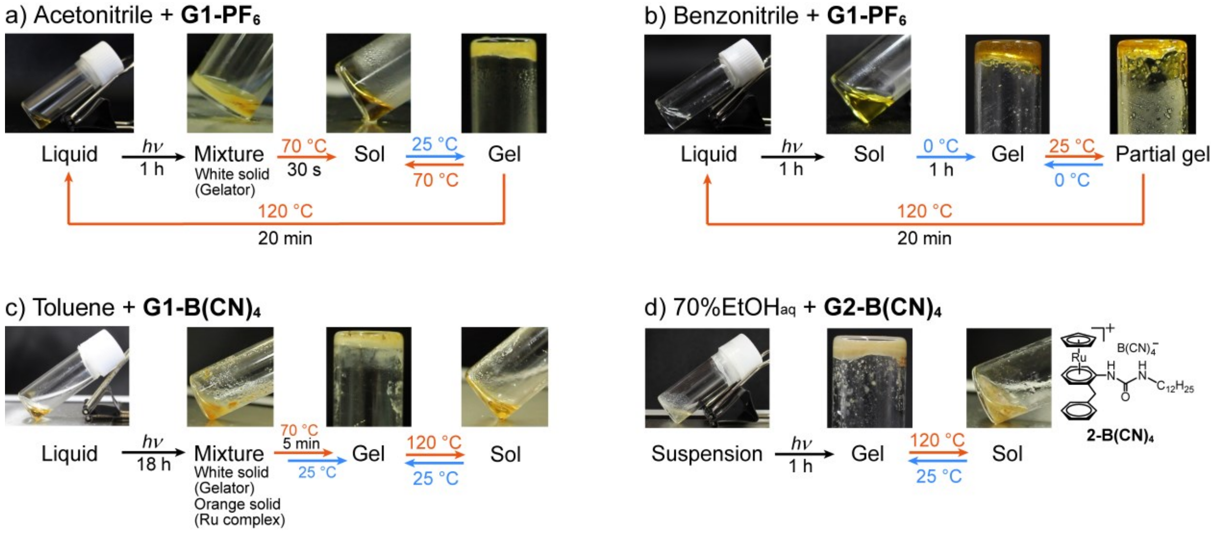

Figure 6-17. Photographs of (a) acetonitrile (containing 5 wt% **G1-PF$_6$**), (b) benzonitrile (containing 5 wt% **G1-PF$_6$**), (c) toluene (containing 5 wt% **G1-B(CN)$_4$**), and (d) 70% ethanol aqueous solution (containing 5 wt% **G2-B(CN)$_4$**) before and after photoirradiation and after heating the photoproducts. The structure of **G2-B(CN)$_4$** is also shown in (d).

Crystal structure of G1-PF$_6$. To investigate the intermolecular interactions in the gelator-coordinated complex, single-crystal X-ray analysis of **G1-PF$_6$** was performed at −183 °C. The salt crystallized in space group *P*-1 (*Z* = 4) with two cation–anion pairs per asymmetric unit (**Fig. 6-18**). The Cp ring of cation **B** exhibited a two-fold rotational disorder (occupancy 0.57:0.43). The alkyl chains of cations **A** and **B** adopted linear and bent conformations, respectively (**Fig. 6-19**), and the chains were arranged in parallel to form a layered structure. There were intermolecular hydrogen bonds (–N···O= distances: 2.91, 2.93 Å) between cations **A** and **B**, forming a one-dimensional chain. There was a π–π interaction between the Cp rings of cation **B** (interplanar distance 3.35 Å), with no other significant π–π interactions. In LMWGs with phenyl substituents, fiber structures are typically formed via π–π stacking and hydrogen bond interactions.[189,190,223] There are organometallic gelators with planar molecular structures that can gelate ILs.[155] The structural analysis results suggest that the lack of gelation capability of **G1-X** is ascribed to the presence of the bulky CpRu unit, which inhibits the π–π interaction.

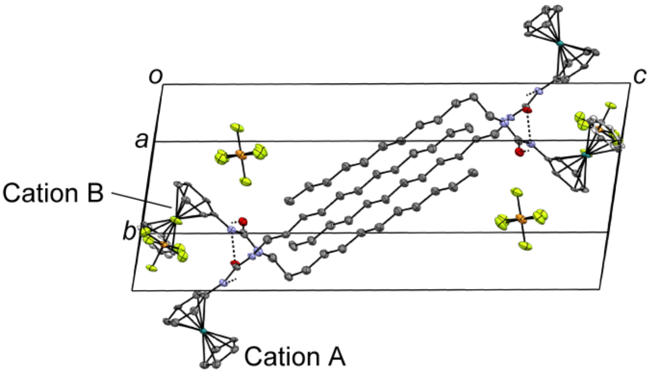

Figure 6-18. Packing diagram of **G1-PF$_6$** (−183 °C). Intermolecular -NH···O= hydrogen bonds are shown by dotted lines. Disordered parts are shown in gray.

Figure 6-19. Molecular structures of the cations of **G1-PF$_6$** in the crystal (−183 °C). The disordered moieties of cation **B** are displayed in gray.

6.3 Conclusion

We developed a simple, on-demand photogelation method for ILs using IL additives that release LMWGs upon photoirradiation. The compounds we designed are a novel class of photoresponsive gelators containing organometallic moieties, which are easy to synthesize and miscible with ILs. By adding a small amount of the compound, various ILs were transformed into ionogels upon UV photoirradiation, and the ionogel liquefied again upon heating owing to the thermal reverse reaction. The photogelation reaction was repeatable for ILs with coordinating cations. The photogelation conditions can be modified by choosing the ligands and anions, and several organic solvents were also photogelated. This is a versatile method for the preparation of stimuli-responsive ionogels, and using this method, ILs can be immobilized or patterned after coating, printing, or filling; hence, this method may be useful for electronic device fabrication and micro-engineering applications. However, the photogelation time observed in the current study was too long, and the use of a high-power light source and improved molecular design may be needed for practical applications. For example, the utilization of coordinating substituents other than the cyano group may lead to improved performance, which is worthy of future investigation. This chapter has demonstrated that the use of photoreactive organometallic compounds is an effective strategy for manipulating supramolecular gels, which may expand the scope and applications of stimuli-responsive gels.

6.4 Experimental Section

General. $C_6H_5NHCONHC_{12}H_{25}$ (**L**),[222] *o*-$C_6H_4(CH_2Ph)(NHCONHC_{12}H_{25})$ (**L'**),[221] [C_3CNmim]FSA,[231] and [bmim]$B(CN)_4$[226] were synthesized according to previously reported methods. [bmim]PF_6 was purchased from Kokusan Chemical Co., Ltd. (Japan). Other reagents were purchased from TCI Co. (Japan). ^{1}H and ^{19}F NMR spectra were recorded using a Bruker Avance 400 spectrometer. FT-IR spectra were measured using a Thermo Nicolet iS5 system with an attenuated total reflection (ATR) attachment. Elemental analyses were performed using a PerkinElmer 2400II elemental analyzer. DSC was performed using a TA Instruments Q100 differential scanning calorimeter at a sweep rate of 10 °C min^{-1}. Dynamic viscoelasticity was measured using a TA Instruments DHR-1 rheometer equipped with an 8-mm parallel plate. The frequency dependence of the dynamic viscoelasticity was determined at 25 °C. A Hamamatsu LC-L1V3 Lightning Cure UV-LED light source (LED lamp, wavelength: 365 nm, intensity: 650 mW cm^{-2}) was used for UV photoirradiation. The ratio of photodissociated cations was determined from the ^{1}H NMR spectra (CD_3CN). SEM was performed on a Hitachi High-Technologies Miniscope TM4000 or JEOL JSM-5510 system.

Synthesis of [CpRu(L)]PF_6 (G1-PF_6). Under a nitrogen atmosphere, ligand **L** (42 mg, 0.14 mmol) was added to a solution of $[CpRu(CH_3CN)_3]PF_6$ (50 mg, 0.12 mmol) in 1,2-dichloroethane (2.5 mL) and stirred at 90 °C for 21 h. The resultant solution was evaporated under reduced pressure, and the residue was purified by column chromatography (alumina, eluent: acetonitrile). The recrystallization of the product from acetone–diethyl ether (−40 °C) produced colorless needle-like crystals (37 mg, 51%). ^{1}H NMR (400 MHz, CD_3CN): $\delta = 0.91$ (t, 3H, CH_3, $J = 7.01$ Hz), 1.29–1.36 (m, 18H, $NHC_2H_4C_9H_{18}CH_3$), 1.49 (m, 2H, $NHCH_2CH_2$), 3.16 (q, 2H, $NHCH_2$, $J = 5.92$ Hz), 5.27 (s, 5H, Cp-H_5), 5.46 (m, 1H, $NHC_{12}H_{25}$), 5.86 (t, 1H, Ar-H, $J = 5.58$ Hz), 6.02 (dd, 2H, Ar-H, $J = 0.91$, 6.49 Hz), 6.63 (dd, 2H, Ar-H, $J = 5.98$, 6.29 Hz), 7.20 (m, 1H, PhNH). FT-IR (ATR, cm^{-1}):556 (P–F), 824 (P–F), 1238, 1299, 1363, 1393, 1406, 1417 (Cp, C=C), 1465, 1528, 1573 (arene, C=C), 1667 (C=O), 2849, 2918, 2956, 3125

(C–H). Anal. calcd. for $C_{24}H_{37}F_6N_2OPRu$: C, 46.83, H, 6.06, N, 4.55. Found: C, 47.14, H, 6.32, N, 4.54.

Synthesis of [CpRu(L)]B(CN)$_4$ (G1-B(CN)$_4$). A solution of **G1-PF$_6$** (46 mg, 0.073 mmol) in a mixture of acetonitrile (0.1 mL) and methanol (1 mL) was charged to an anion exchange column (Dowex 1X8-100, chloride form, 7 g) and eluted with methanol (100 mL). The eluent was concentrated under reduced pressure and the anion-exchange procedure was repeated. The complete exchange of the anion was confirmed by the absence of the PF_6 peak ($\delta = -73.83, -71.92$) in the ^{19}F NMR spectrum (solvent: CD_3CN). Chloride salt was obtained quantitatively as a pale-yellow liquid; the product was vacuum-dried at ambient temperature for 3 h. $KB(CN)_4$ (23 mg, 0.15 mmol) was added to a mixture of water (10 mL), acetone (1 mL), and chloride salt and stirred for 10 min. Acetone was then evaporated under reduced pressure; water and dichloromethane were added to the residue. The residue was extracted five times with dichloromethane, and the organic layer was combined and washed three times with water. The organic layer was then dried over anhydrous magnesium sulfate. After solvent evaporation, the residue was dried under vacuum for 5 h at 70 °C. A silver nitrate solution was used to verify the absence of chloride ions. The desired product was obtained as a pale-yellow liquid (78 mg, 94%). ^1H NMR (400 MHz, CD_3CN): $\delta = 0.91$ (t, 3H, CH_3, $J = 7.01$ Hz), 1.29–1.36 (m, 18H, $NHC_2H_4C_9H_{18}CH_3$), 1.49 (m, 2H, $NHCH_2CH_2$), 3.16 (q, 2H, $NHCH_2$, $J = 5.92$ Hz), 5.27 (s, 5H, Cp-H_5), 5.46 (m, 1H, $NHC_{12}H_{25}$), 5.86 (t, 1H, Ar-H, $J = 5.58$ Hz), 6.02 (dd, 2H, Ar-H, $J = 0.91$, 6.49 Hz), 6.63 (dd, 2H, Ar-H, $J = 5.98$, 6.29 Hz), 7.20 (m, 1H, PhNH). FT-IR (ATR, cm^{-1}): 842, 932, 1226, 1295, 1462 (Cp, C=C), 1524, 1563 (arene, C=C), 1682 (C=O), 2222 (CN). Anal. calcd. for $C_{28}H_{37}BN_6ORu$: C, 57.44, H, 6.37, N, 14.35. Found: C, 57.36, H, 6.29, N, 14.24.

Synthesis of [C$_6$CNEt$_3$N]Tf$_2$N. In a nitrogen atmosphere, an amount of 7-bromoheptanenitrile (1.84 g, 9.7 mmol) was slowly added to a solution of triethylamine (1.0 g, 9.88 mmol) in acetonitrile (2 mL). The solution was subsequently heated at 80 °C for 3 h with constant stirring. The solvent was then removed under reduced pressure. The resultant orange liquid was washed 10 times with hexane and dried under vacuum at 80 °C for 1 h to obtain $[C_6CNEt_3N]Br$ as an orange liquid (2.5 g, 90%). Potassium bis(trifluoromethanesulfonyl)imide (KTf_2N; 6.2 g, 19.4 mmol) was added to an aqueous solution (20 mL) of $[C_6CNEt_3N]Br$ (2.5 g, 8.7 mmol), and the solution was stirred vigorously for 1 h. The resultant $[C_6CNEt_3N]Tf_2N$ phase was collected and washed three times with water. The orange liquid was dried under vacuum for 3 h at 60 °C. The crude product was purified by column chromatography (alumina, eluent: dichloromethane/acetonitrile, gradient from 1:0 to 0:1). After evaporation of the solvent, the residue was dissolved in acetonitrile and heated to reflux, to which a small amount of activated carbon was added for purification. The activated carbon was then removed by filtration without cooling. After evaporation of the solvent, the residue was dried under vacuum at 130 °C for 6 h. The desired product was a pale-yellow liquid (3.4 g, 69% yield). T_g = −72 °C (DSC). ^1H NMR (400 MHz, $CDCl_3$): δ= 1.35 (t, 9H, $N(CH_2C\mathit{H_3})_3$, J= 7.22 Hz), 1.46 (m, 2H, $NC_3H_6C\mathit{H_2}$), 1.56 (m, 2H, $NC_2H_4C\mathit{H_2}$), 1.70 (m, 4H, $NCH_2C\mathit{H_2}C_2H_4C\mathit{H_2}$), 2.39 (t, 2H, $NC_5H_{10}C\mathit{H_2}$, J= 6.89 Hz), 3.16 (t, 2H, $NC\mathit{H_2}$, J= 8.51 Hz), 3.29 (q, 6H, $N(C\mathit{H_2}CH_3)_3$). FT-IR (ATR, cm^{-1}): 600, 613, 653, 739, 761, 1052 (S=O), 1134, 1177 (C–F), 1330, 1348, 1397, 1460, 1487, 2246 (CN), 2869 (C–H), 2950 (C–H). Anal. calcd. for $C_{15}H_{27}F_6N_3O_4S_2$: C, 36.66, H, 5.54, N, 8.55. Found: C, 36.48, H, 5.72, N, 8.38.

Synthesis of [CpRu(L')]B(CN)$_4$ (G2-B(CN)$_4$). [CpRu(L')]PF_6 (**G2-PF$_6$**) was synthesized using the procedure identical to that for **G1-PF$_6$** using **L'** (33 mg, 0.083 mmol) and $[CpRu(CH_3CN)_3]PF_6$ (30 mg, 0.069 mmol). The desired product was obtained as an orange viscous liquid (27 mg, 55%). ^1H NMR (400 MHz, $CDCl_3$): δ= 0.88 (t, 3H, $C\mathit{H_3}$, J= 6.89 Hz), 1.26 (m, 18H, $NHC_2H_4C_9\mathit{H_{18}}$), 1.58 (m, 2H, $NHCH_2C\mathit{H_2}$), 3.21 (m, 2H, $NHC\mathit{H_2}$), 4.00 (m, 2H, $PhC\mathit{H_2}$), 5.26 (s, 5H, Cp-*H*), 5.60–5.88 (m, 4H, Ru–Ph–*H*), 6.98 (s, 1H, $N\mathit{H}C_{12}H_{25}$), 7.22 (s, 1H, PhN*H*), 7.10–7.40 (m, 5H, CH_2Ph-*H*). FT-IR (ATR, cm^{-1}): 567 (P–F), 745, 1242, 1289, 1451 (Cp, C=C), 1465, 1482, 1563 (arene, C=C), 1632 (C=O), 2847, 2916 (C–H). **G2-B(CN)$_4$** was synthesized using the procedure identical to that for **G1-B(CN)$_4$** using **G2-PF$_6$** (21 mg, 0.030 mmol) and $KB(CN)_4$ (14 mg, 0.089 mmol). The desired product was obtained as an orange viscous liquid (13 mg, 65% yield). ^1H NMR (400 MHz, $CDCl_3$): $\delta = 0.88$ (t, 3H, CH_3, $J = 6.89$ Hz), 1.26 (m, 18H, $NHC_2H_4C_9H_{18}$), 1.58 (m, 2H, $NHCH_2CH_2$), 3.21 (m, 2H, $NHCH_2$), 4.00 (m, 2H, $PhCH_2$), 5.26 (s, 5H, Cp-*H*), 5.60–5.88 (m, 4H, Ru–Ph–*H*), 6.98 (s, 1H, $NHC_{12}H_{25}$), 7.22 (s, 1H, Ph*NH*), 7.10–7.40 (m, 5H, CH_2Ph-*H*).

Gelation experiments. A small amount (1 mg, 5 wt%) of **G1-PF₆** or **G1-B(CN)₄** was added to each IL (20 mg) on a glass plate, which was then heated at 120 °C and allowed to cool to ambient temperature. The UV photoirradiation experiments were conducted in a glove box filled with argon using samples placed on a cooling plate maintained at 10 °C. The thermal reactions of the samples were carried out at 120 °C in the glove box.

The dissociation rates of the cations in the photoproducts were determined from the ratio of $[CpRu(CD_3CN)_3]^+$ and the remaining sandwich complex in the ^1H NMR spectra (CD_3CN). Photogelation of organic solvents was investigated by adding 5 wt% of **G1-PF₆**, **G1-B(CN)₄**, or **G2-B(CN)₄** to the solvents in screw vials, which were flushed with nitrogen. The vials were placed on a cooling plate maintained at 10 °C and UV light was irradiated from outside the vials. The ionogels prepared by adding gelator **L** (2.4–2.5 wt%) to the ILs, were used as the reference gels after being heated up to 120 °C and cooled down to room temperature.

X-ray crystallography. Single crystals of **G1-PF₆**, suitable for structural analysis, were grown by recrystallization from acetone–diethyl ether by slow cooling to −40 °C. The X-ray diffraction data were collected using a Bruker APEX II Ultra diffractometer (X-ray source: MoKα) and the calculations were performed using SHELXL.[117] The crystallographic parameters are listed in **Table 6-4**. CCDC 2121035 contains the crystallographic data for this compound.

Table 6-4. Crystallographic parameters

	G1-PF$_6$
Empirical formula	$C_{24}H_{37}F_6N_2OPRu$
Formula weight	615.59
Crystal system	triclinic
Space group	$P\overline{1}$
a [Å]	9.637(4)
b [Å]	9.944(5)
c [Å]	27.528(13)
α [°]	95.325(6)
β [°]	97.691(8)
γ [°]	96.476(6)
V [Å^3]	2582(2)
Z	4
ρ_{calcd} [g cm^{-3}]	1.584
μ [mm^{-1}]	0.733
Temperature [K]	90
F(000)	1264
Reflns collected	9148
R (int)	0.0363
Goodness of fit	1.098
$R_1{}^a$, $R_w{}^b$ ($I > 2\sigma(I)$)	0.1041, 0.2448
$R_1{}^a$, $R_w{}^b$ (all data)	0.1393, 0.2643

[a] $R_1 = \Sigma||F_o| - |F_c|| / \Sigma|F_o|$. [b] $R_w = [\Sigma w (F_o^2 - F_c^2)^2 / \Sigma w (F_o^2)^2]^{1/2}$

CHAPTER 7

Structures, Thermal Properties, and Reactivities of Cationic Rhodium(I) Complexes in Solid State

7.1 Introduction

Cationic rhodium complexes with diene ligands such as 1,5-cyclooctadiene (cod) are important organometallic species that are useful for various catalytic applications, such as the hydrogenation of alkynes.[232–236] Among them, $[Rh(cod)_2]^+$ serves as a precatalyst and can be used for the in situ generation of catalysts via ligand exchange. The catalytic activities of Rh-cod complexes are affected by the thermodynamics and kinetics of their ligand exchange reactions.[237] In recent years, research on solid-state organic reactions has become increasingly important.[238] Although solid-state properties of Rh-cod complexes are important to explore solid-state organometallic reaction chemistry, this aspect has received little attention.[8] In contrast, extensive solid-state research has been conducted on the chemistry of sandwich compounds such as ferrocene, cobaltocene, and their derivatives.[239,240] Salts of cationic sandwich complexes, such as $[Fe(C_5H_5)_2]PF_6$, typically exhibit an ionic plastic crystal (IPC) phase because of the spherical shape of their cations.[96,103,241–244] The constituent molecules undergo fast reorientation or rotation in the IPC phase, resulting in high crystal symmetry and ionic conductivity.[99,245–256] Therefore, we hypothesized that salts of cationic Rh-cod complexes also exhibit an IPC or rotator phase. Molecules in the rotator phase typically rotate along the molecular long axis.[257–260] Furthermore, $[Rh(cod)_2]^+$ and its derivatives readily undergo ligand exchange reactions in solution,[261] although their solid-state reactivity has not been investigated. Crystalline phase reactions require structural flexibility or reaction cavities; hence, IPC or rotator phases may provide a suitable reaction medium for ligand-exchange reactions.

The present study reports the structures, thermal properties, and reactivities of [Rh(cod)L]X (L = cod ([**1**]X), C_6H_6 ([**2**]X), PhMe ([**3**]X); X = SbF_6, $(FSO_2)_2N$ (= FSA), CF_3BF_3, $CB_{11}H_{12}$), and $[Ir(cod)_2]SbF_6$ ([**1′**]SbF_6) in the solid state (**Fig. 7-1**). Among these, [**1**]SbF_6,[262] [**1′**]SbF_6,[263], and [**2**]SbF_6[236] are known compounds. Most of the anions are nearly spherical and are often used as components of IPCs, whereas the FSA anion (= $(FSO_2)_2N^-$) is typically used for ionic liquids.[6,264] First, we discuss the phase transitions and thermal decomposition behavior of [**1**]X, [**2**]X, and [**3**]X (X = SbF_6, FSA). [**1′**]SbF_6 and Rh-cod complexes with CF_3BF_3 and $CB_{11}H_{12}$ anions were also studied. These salts exhibit phase transitions that produce disordered structures in the solid state, of which [**3**]SbF_6 exhibits a rotator phase at room temperature. The melting behavior of the FSA salts was investigated in detail. In addition, the cation dynamics of the SbF_6 salts were investigated by solid-state NMR spectroscopy. Finally, we investigated the reactivity of SbF_6 salts with arene ligands and observed that in situ ligand exchange occurs in ether via an in-situ single-crystal-to-single-crystal (SC–SC) reaction.

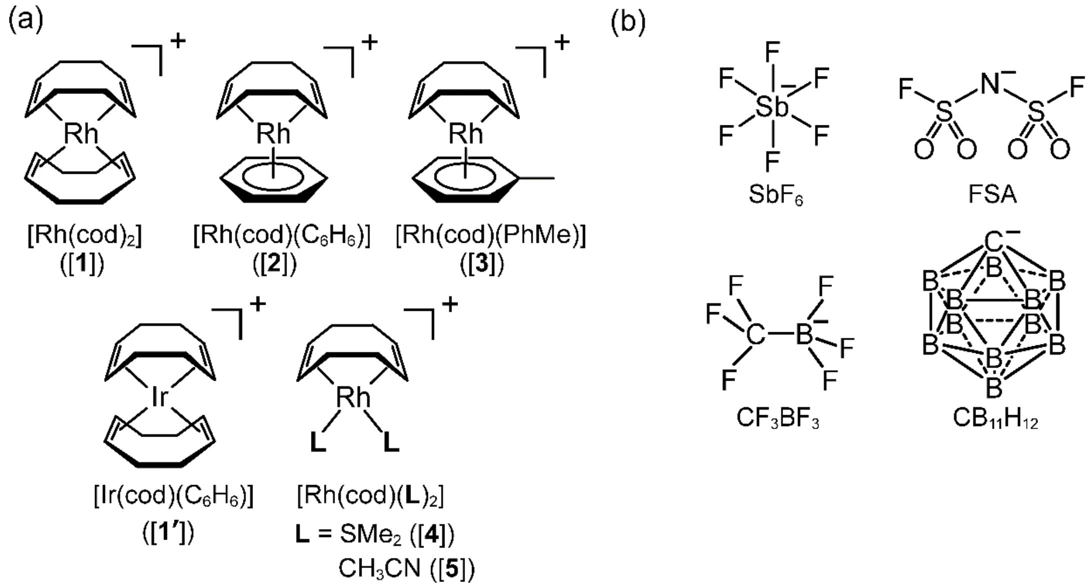

Figure 7-1. Structural formulae of (a) cations and (b) anions used in this study.

7.2 Results and Discussion

Phase behaviors. The phase behavior of [**1**]X–[**3**]X (X = SbF_6, FSA, CF_3BF_3, and $CB_{11}H_{12}$) was investigated using differential scanning calorimetry (DSC). The phase sequences and DSC curves of the salts are shown in **Figs. 7-2** and **7-3**, respectively. All the salts exhibit solid phase transitions, and the lowest temperature phase in each salt is designated as phase I. These salts decompose without melting at high temperatures, except for [**1**]FSA and [**2**]FSA, which melt at approximately 360 K.

The phase sequences of the SbF_6 salts are shown in **Fig. 7-2a**. [**1**]SbF_6 exhibits a phase transition at 329.9 K (ΔS = 19.6 J mol^{-1} K^{-1}), and the corresponding Ir complex ([**1′**]SbF_6) exhibits a phase transition at almost the same temperature (327.4 K). [**2**]SbF_6 exhibits four phase transitions, and the sum of its transition entropies (ΔS_{total} = 16.6 J mol^{-1} K^{-1}) is comparable to that of [**1**]SbF_6. [**3**]SbF_6 exhibits a phase transition from phase I to II, which is a rotator phase (see below), at 271.6 K (ΔS = 33.7 J mol^{-1} K^{-1}). This transition entropy is quite large and comparable to those of sandwich complexes from an anisotropic crystalline phase to a plastic phase (e.g., [Ru(Cp)(PhMe)]PF_6, ΔS = 29.0 J mol^{-1} K^{-1} [96,241]). The transition from phase II to III at 452.3 K (ΔS = 6.8 J mol^{-1} K^{-1}) is a transition between rotator phases; birefringence was observed in both phases under a polarizing optical microscope (POM), indicating their anisotropic crystal structures (**Fig. 7-4**).

The phase sequences of the FSA salts are shown in **Fig. 7-2b**. [**1**]FSA undergoes a phase transition at 307.4 K (ΔS = 30.6 J mol^{-1} K^{-1}). [**2**]FSA and [**3**]FSA exhibit phase transitions at 358.7 and 350.3 K, followed by melting at 369.2 and 363.3 K, respectively. The details of the melting phenomenon are discussed in the next section.

The phase sequences of salts with other anions (X = CF_3BF_3 and $CB_{11}H_{12}$) are shown in **Fig. 7-2c**. [**1**]CF_3BF_3 and [**3**]CF_3BF_3 exhibit two and six phase transitions, respectively, which occur at considerably lower temperatures than those of the other salts, probably because the CF_3BF_3 anion facilitates disorder.[244] [**1**]CF_3BF_3 undergoes a phase transition from phase I to II at 212.6

K (ΔS = 16.8 J mol^{-1} K^{-1}), whereas [**3**]CF_3BF_3 undergoes three successive phase transitions at approximately 230 K and the sum of the transition entropies (ΔS_{sum} = 15.6 J mol^{-1} K^{-1}) is comparable to that of [**1**]CF_3BF_3. [**1**]$CB_{11}H_{12}$, which contains the carborane anion, exhibits three phase transitions above 385.4 K, probably because of the large anion volume, facilitating its molecular rotation only at high temperatures. Other salts such as [**2**]CF_3BF_3, could not be synthesized because ligand exchange from [**1**]CF_3BF_3 did not occur.[261] Similarly, [**2**]$CB_{11}H_{12}$ and [**3**]$CB_{11}H_{12}$ were not obtained, probably because of anion coordination.[265]

Most salts showed successive phase transitions as a result of successive order-disorder rearrangements of cations and anions (see below), similar to the salts of sandwich complexes,[103] although none of the current salts exhibits an IPC phase; optical birefringence was observed for all phases. This is probably because of the elongated cation shapes compared to that of $[M(Cp)_2]^+$, which hinders isotropic rotation. However, the salts exhibit dynamic phases, including rotator phases, as described below.

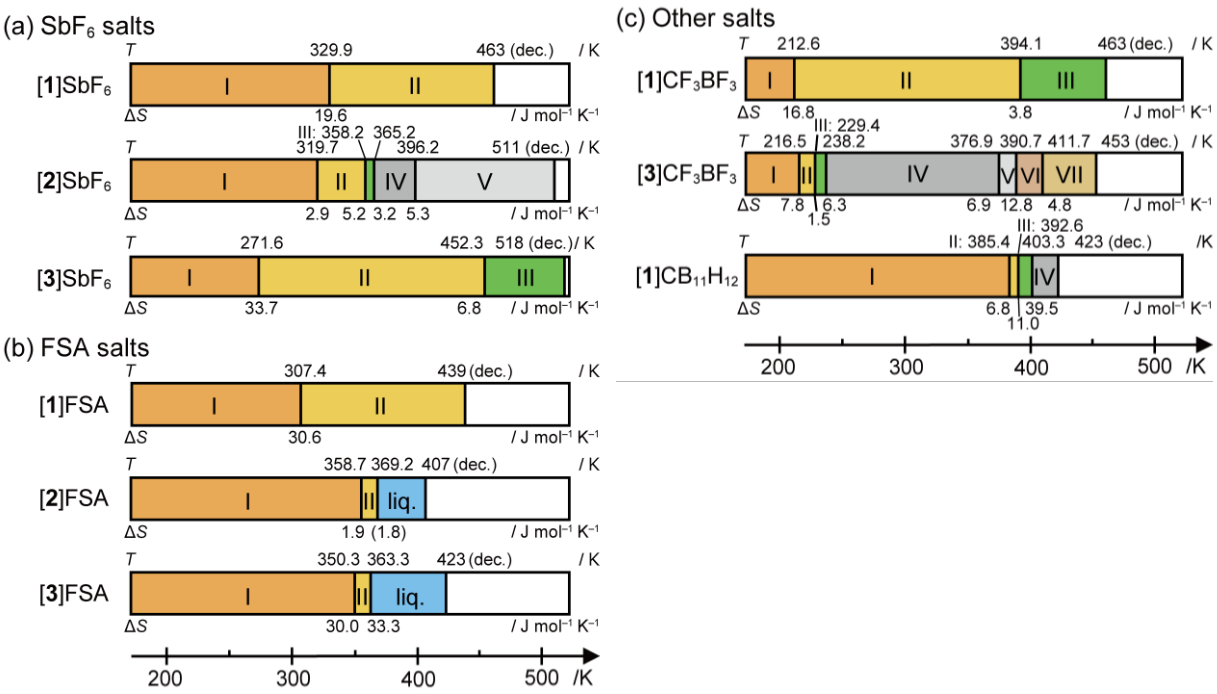

Figure 7-2. Phase sequences of [**1**]X–[**3**]X with (a) SbF_6, (b) FSA, and (c) other anions. The phase transition temperature (K) and transition entropy (J mol^{-1} K^{-1}) of each phase transition are shown above and below the bar charts, respectively. The liquid phases of [**2**]FSA and [**3**]FSA contain thermal reaction products (see text).

(a) SbF_6 salts

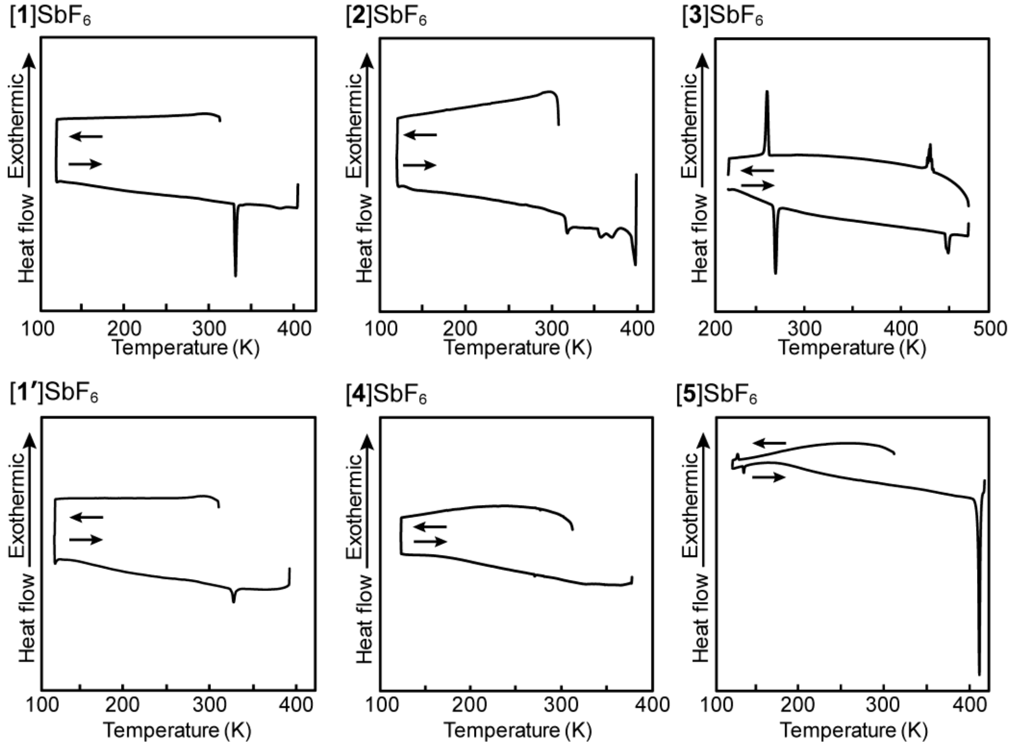

(b) FSA salts

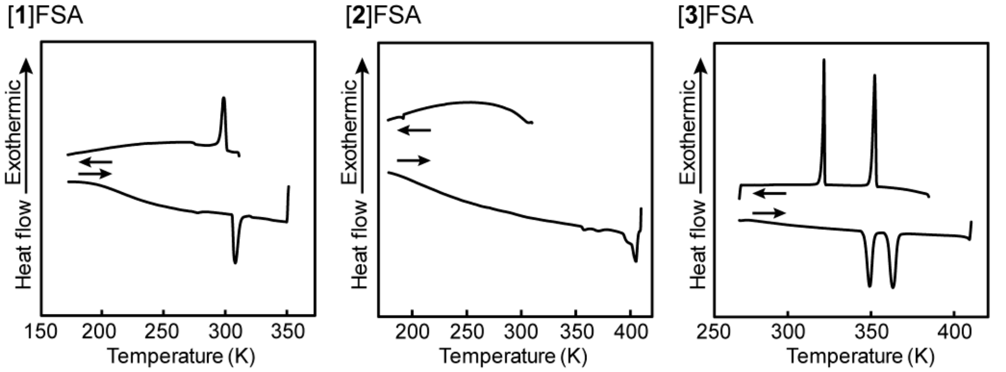

(c) other salts

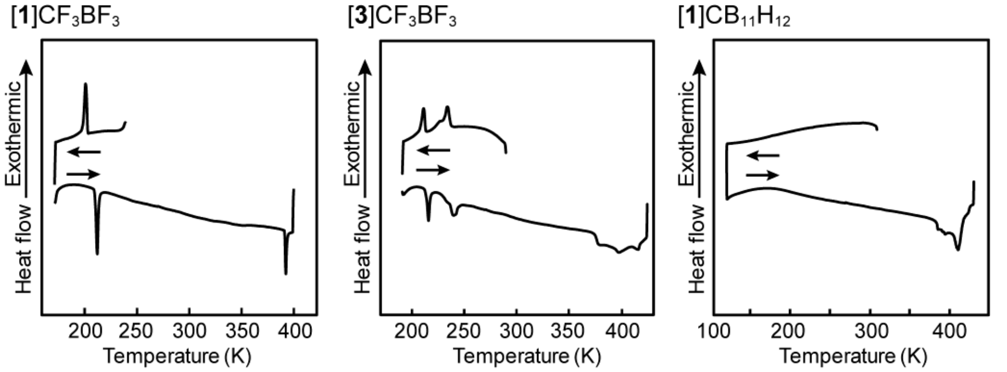

Figure 7-3. DSC thermograms (scan rate 10 K min^{-1}) of [**1**]X–[**5**]X (X = SbF_6 (a), FSA (b), and other anions (c)).

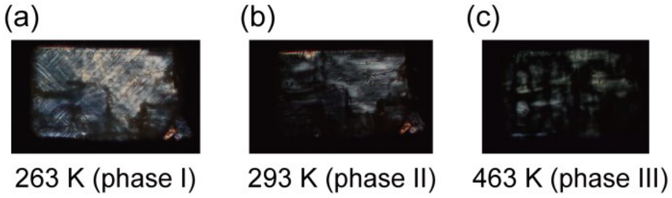

Figure 7-4. POM images in each phase of [**3**]SbF_6.

Melting behaviors of FSA salts. We investigated the melting behaviors of [**2**]FSA and [**3**]FSA in detail. Interestingly, a ligand exchange reaction occurs after melting to form anion-coordinated complexes (**Fig. 7-5a**).

Polarizing optical microscopy (POM) images of the melting behavior of [**3**]FSA are shown in **Fig. 7-5b**. This salt melts at 363 K, after which the deposition of crystals in the melt occurs within 10 min when the liquid is maintained at 383 K, and the crystals dissolve upon further heating to 409 K. [**2**]FSA exhibits similar behavior by melting at 369 K, followed by crystal deposition (**Fig. 7-6**). The entropy change observed by DSC at the melting point was small for this salt (**Fig. 7-**2) because melting overlapped with the exotherm from the ligand exchange reaction.

X-ray structural analysis of the crystal formed upon melting [**3**]FSA at 388 K showed the structure to be [**3**][Rh(cod)$(FSA)_2$]. The compound contains an anionic complex with two FSA anions coordinated to the metal center via N atoms (**Fig. 7-5a**, right), indicating that the arene ligands of every second cation are exchanged for anions. The molecular structure of this anion is shown in **Fig. 7-7**. However, we do not provide a detailed structural discussion because of its low data quality ($R_1(I > 2\sigma(I)) = 14.4\%$). Structural analysis of the reaction product of [**2**]FSA was not possible.

Although several group-11 metal complexes are known to be coordinated via the N atom of FSA or Tf_2N (= $(CF_3SO_2)_2N^-$),[266–269] very few have been studied such as platinum-group metal complexes.[270] A related phenomenon is the formation of the anion-coordinated complex

[Ir(cod)(OTf)] (OTf = $CF_3SO_3^-$) as an intermediate in the ligand exchange reaction of [Ir(cod)(*p*-xylene)]OTf in solution.[271] The formation of anion-coordinated complexes in the liquid phase observed in this study is consistent with this phenomenon.

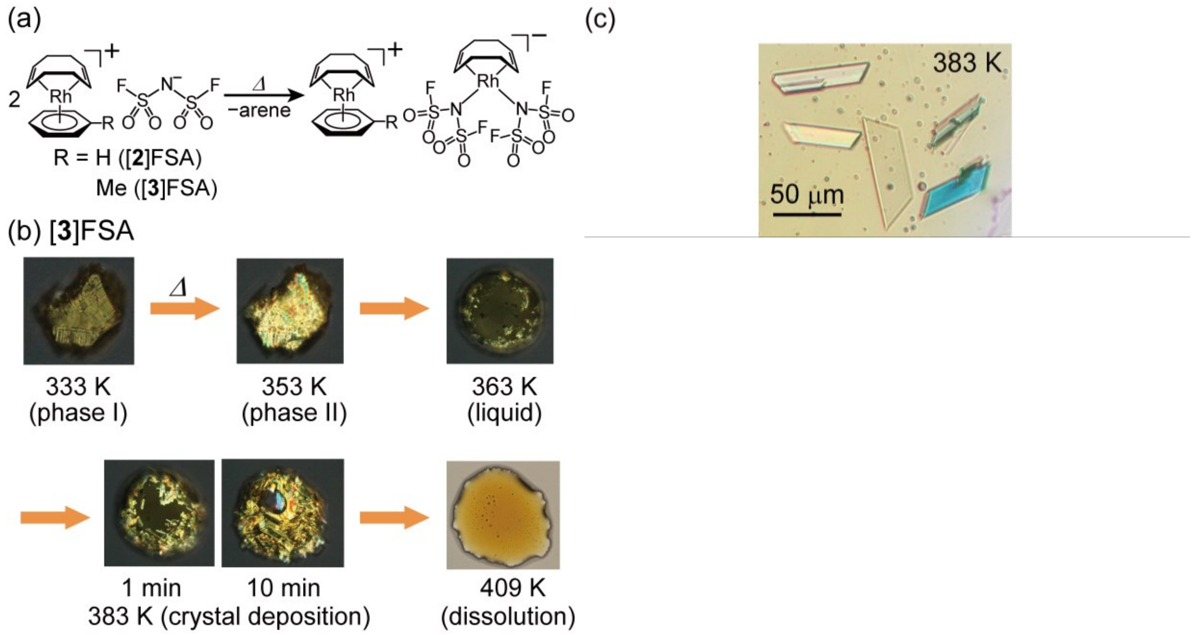

Figure 7-5. (a) Ligand exchange reaction of [**2**]FSA and [**3**]FSA that occurred upon their melting. (b) POM images of [**3**]FSA taken during heating. (c) Microscopic image of the crystals grown in the melt of [**3**]FSA taken under polarized light, after breaking up an aggregate using a needle.

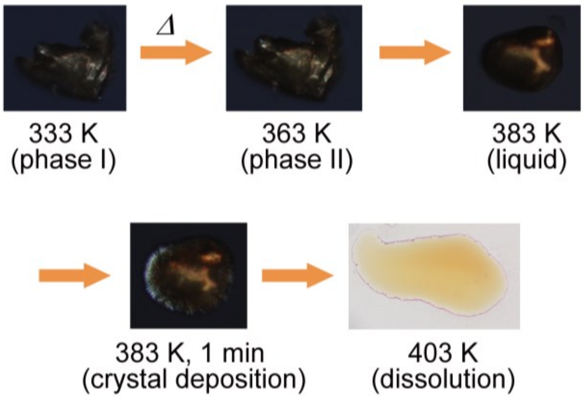

Figure 7-6. POM images of [**2**]FSA taken during melting and thermal reaction processes.

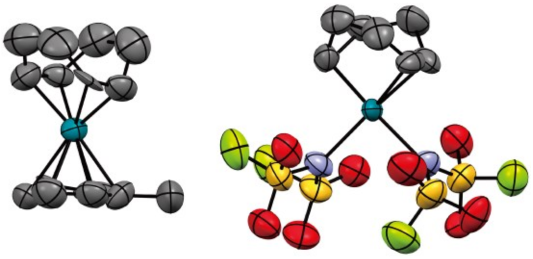

Figure 7-7. Molecular structure of [**3**][Rh(cod)(FSA)$_2$] determined by X-ray structural analysis at 388 K. The disordered part has been omitted.

Thermal decomposition behaviors. The thermal stability of [**1**]X–[**3**]X (X = SbF$_6$, FSA) was investigated by thermogravimetric (TG) measurements. FSA salts decompose at lower temperatures than SbF$_6$ salts. The TG curves were measured at a scan rate of 3 K min^{-1} under nitrogen atmosphere, as shown in **Fig. 7-8** and **7-9**. The decomposition temperatures (T_{dec} = 3 wt.% weight loss temperature) determined from the curves are listed in **Table 7-1**, together with those of the related salts.

The TG curves of the SbF$_6$ salts are shown in **Fig. 7-8a**. [**1**]SbF$_6$ decomposes at 463 K and exhibits a weight loss of approximately 36 wt.% up to 548 K owing to the loss of two cod ligands (calculated value: −39 wt.%). The decomposition temperature is similar to those of [**1**]BF$_4$ (454 K, determined by TG; **Fig. 7-9c**) and [**1**]BAr$^{\mathrm{F}}{}_4$ (T_{dec} = 437 K, BAr$^{\mathrm{F}}{}_4$ = tetrakis((3,5-trifluoromethyl)phenyl)borate)[272], indicating that the cation is responsible for the decomposition. The arene-coordinated complexes, [**2**]SbF$_6$ and [**3**]SbF$_6$, exhibit considerably higher decomposition temperatures of 511 and 518 K, respectively; [**3**]SbF$_6$ is more stable owing to the electron-donating substituent in the ligand. Each salt exhibits a weight loss of approximately 65 wt.% in one step, which may be ascribed to the loss of cod, arene ligand (calculated value: −37 wt.%), and some SbF$_5$ formed by partial decomposition of the anion.

The TG curves of the FSA salts are shown in **Fig. 7-8b**. The decomposition temperature of [**1**]FSA is 439 K, approximately 20 K lower than that of [**1**]SbF$_6$. The weight loss of approximately 34 wt.% occurs in one step owing to the loss of two cod ligands (calculated value: −37 wt.%). In contrast, the decomposition temperatures of [**2**]FSA and [**3**]FSA are 407 and 423 K, respectively, approximately 100 K lower than those of the corresponding SbF$_6$ salts owing to ligand exchange upon melting, as described above. Namely, the decomposition is ascribed to the coordination ability of the FSA anions, which leads to ligand dissociation. These salts exhibit weight losses of 18 and 12 wt.%, respectively, within a temperature range of 390–450 K, which corresponds to the loss of arene ligands (calculated values: −16 and −19 wt.%, respectively). [**1**]CB$_{11}$H$_{12}$ exhibits a similar decomposition temperature (423 K), which is consistent with the coordination ability of the carborane anion.[265]

In addition, the decomposition behavior of the Ir complex [**1′**]SbF$_6$ was investigated. The lower decomposition temperature (T_{dec} = 421 K) of this salt compared to that of [**1**]SbF$_6$ (T_{dec} = 463 K) indicates weaker coordination bonding. A similar tendency has been reported for the melting points of BF$_4$ salts ([**1′**]BF$_4$:413–418 K, [**1**]BF$_4$:479–481 K)[273], which are probably accompanied by decomposition.

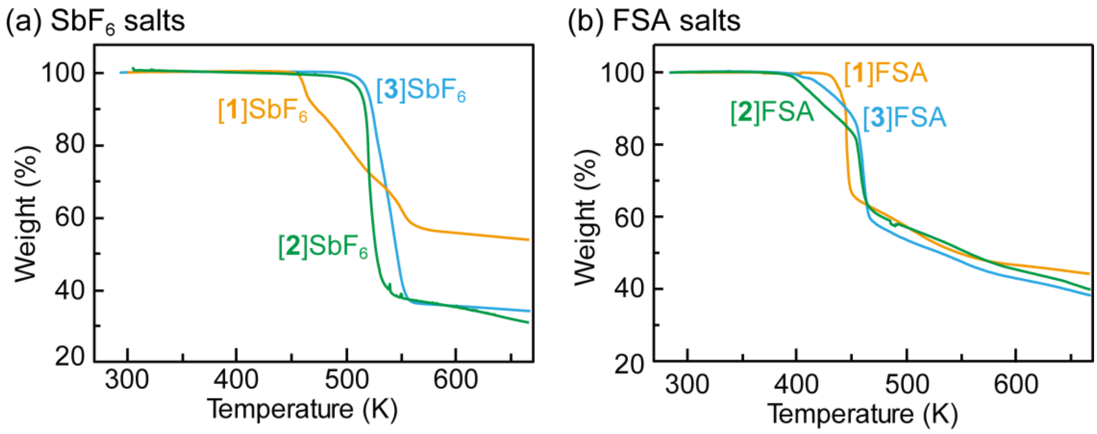

Figure 7-8. TG traces of (a) SbF$_6$ and (b) FSA salts measured at a scan rate of 3 K min^{-1} in nitrogen atmosphere.

(a) SbF$_6$ salts

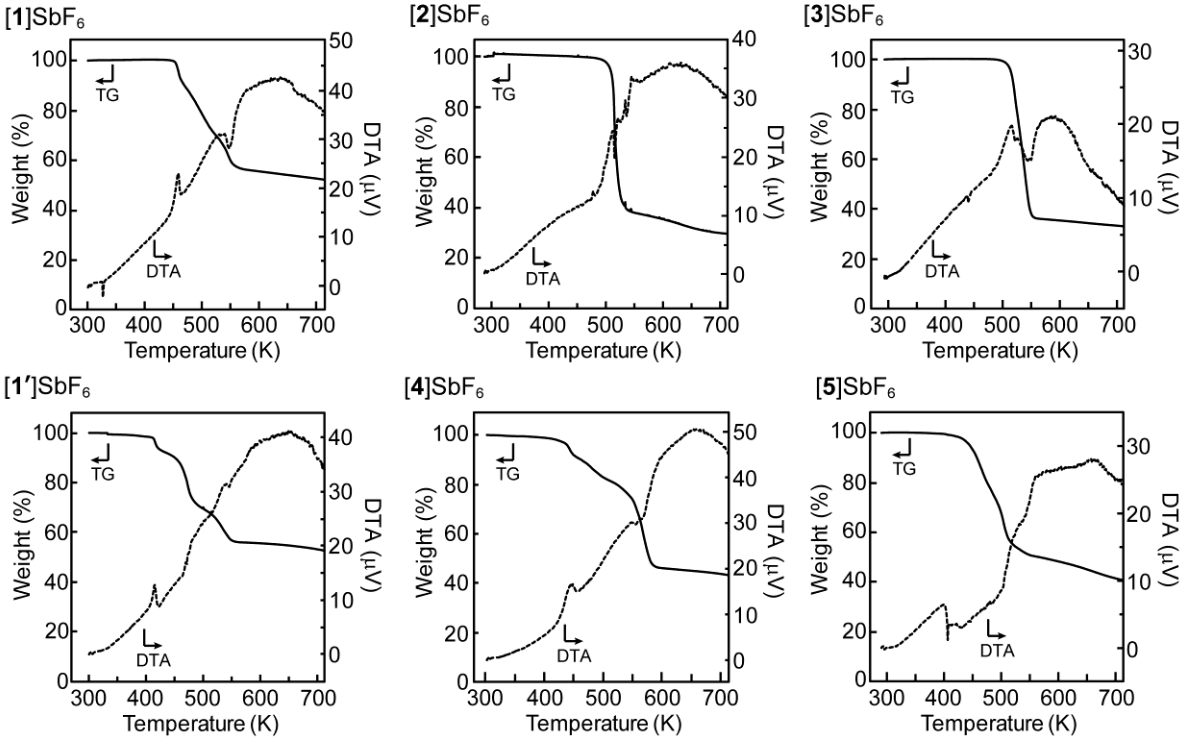

(b) FSA salts

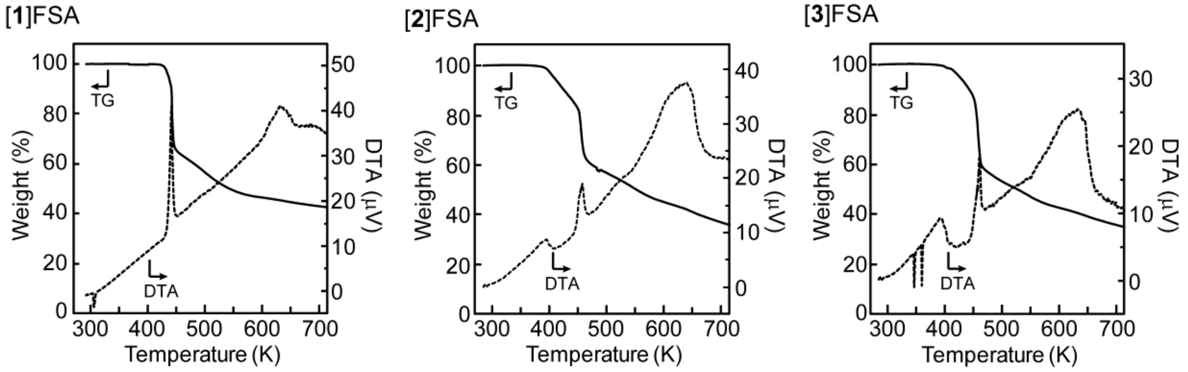

(c) Other salts

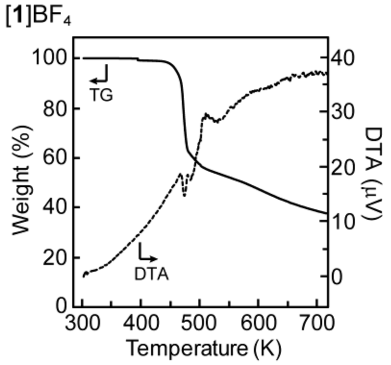

Figure 7-9. TG-DTA traces of [**1**]X–[**5**]X at a scan rate of 3 K min^{-1} under nitrogen atmosphere (X = (a) SbF$_6$, (b) FSA, and (c) other anions).

Table 7-1. Decomposition temperatures of salts containing Rh-cod complexes (K)[a]

[**1**]SbF$_6$	463	[**1**]CB$_{11}$H$_{12}$[b]	423
[**1′**]SbF$_6$	421	[**1**]CF$_3$BF$_3$[c]	463
[**2**]SbF$_6$	511	[**1**]BAr$^{\mathrm{F}}_4$[c,d]	437
[**3**]SbF$_6$	518	[**1**]BF$_4$	454
[**1**]FSA	439	[**3**]CF$_3$BF$_3$[b]	453
[**2**]FSA	407	[**3**]BF$_4$[c,e]	447
[**3**]FSA	423	[**4**]SbF$_6$	433
		[**5**]SbF$_6$	441

[a] Determined by TG measurement (−3wt.%) unless otherwise specified. [b] Determined by DSC measurement (peak-top temperature). [c] Determined by visual inspection. [d] Ref. 272. [e] Ref. 261 (described as a melting point).

General features of the crystal structures. The crystal structures of phase I of the salts were determined, except for [**3**]SbF$_6$ and [**3**]CF$_3$BF$_3$, and the structural changes from phase I to II were crystallographically elucidated for most salts (**Fig. 7-10**). Their structural features are dependent on the anion, cation, and radius ratio, as summarized in this section. In higher-temperature phases, the structural disorder is enhanced to a larger extent when the transition entropy is large.

A correlation was observed between molecular and crystal structures. In phase I, the crystal system of the FSA salts is monoclinic, reflecting low anion symmetry, whereas those of the other salts (X = SbF$_6$, CF$_3$BF$_3$, and CB$_{11}$H$_{12}$) are orthorhombic, except for [**1**]SbF$_6$. The cations and anions are arranged alternately in all the salts, where the number of cations surrounding the anions (coordination number)[274] is eight for [**1**]CB$_{11}$H$_{12}$, seven for [**2**]SbF$_6$, and six for all others in phase I. The cation-to-anion radius ratio ρ, calculated from the van der Waals volumes of the molecules, is 0.87 for CB$_{11}$H$_{12}$ salts, whereas it is 0.71, 0.68, and 0.65, for FSA, CF$_3$BF$_3$, and SbF$_6$ salts, respectively. Thus, with the exception of [**2**]SbF$_6$, the results are consistent with the radius ratio rule for ionic crystals,[275] which determines the six-coordinated ($0.41 < \rho < 0.73$) or eight-coordinated ($0.73 < \rho$) structures. Interestingly, the coordination number of [**1**]FSA, whose radius ratio is close to the boundary, changed from six in phase I to eight in phase II, owing to an increase in the effective volume caused by anion disorder in phase II.

Although phase I is an ordered phase for many salts, structural disorder increases as the cation symmetry decreases in the order [**1**]X, [**2**]X, and [**3**]X. Both cations and anions are ordered in [**1**]X (X = SbF_6, CF_3BF_3, $CB_{11}H_{12}$) with high packing coefficients (72.8%–73.2%), and both exhibit disorder in [**2**]SbF_6, and are even more extensively disordered in [**3**]X (X = SbF_6, CF_3BF_3). The FSA salts exhibit less disorder. In each salt, the structural disorder increases, and the crystal symmetry tends to be higher for higher-temperature phases.

Cation disorder is typically a two-fold rotational disorder around the long axis, as seen in [**2**]SbF_6 (phases I and II), [**1**]FSA (phase II), and [**1**]CF_3BF_3 (phase II), reflecting the elongated cation shape (**Fig. 7-10**). Cation structures in other high-temperature phases could not be determined because of extensive disorder. Ordered cations were found in phase I of [**1**]CF_3BF_3, [**1**]$CB_{11}H_{12}$, and [**1**]FSA–[**3**]FSA, with geometries almost identical to those of [Rh(cod)$_2$]X (X = BF_4, OTf)[276,277] and [Rh(cod)(arene)]SbF_6 (arene = hexamethylbenzene, 1,4-dimethylnaphthalene, etc.).[236]

The structure of each salt is discussed in detail in the following sections.

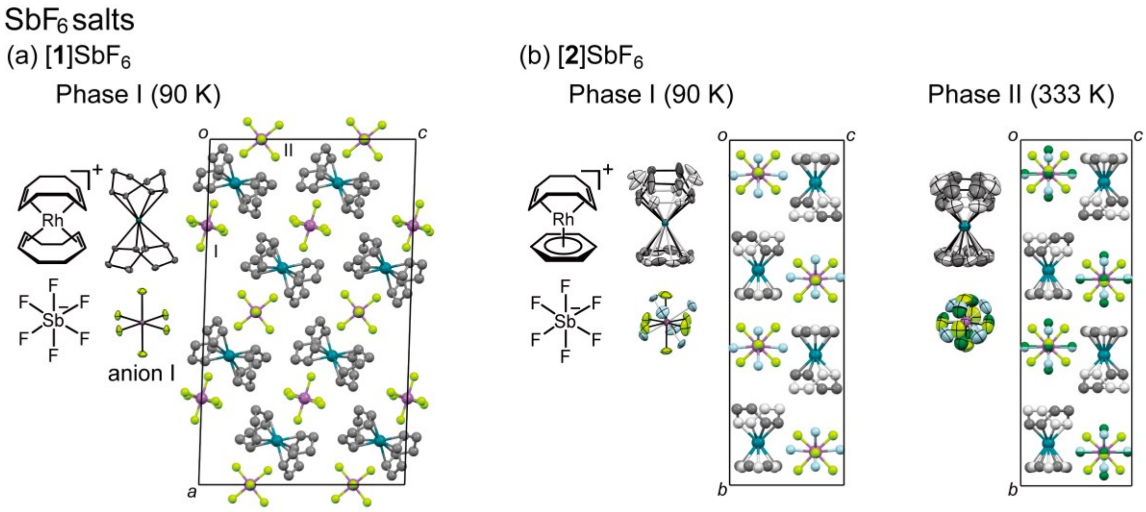
SbF$_6$ salts

(a) [**1**]SbF$_6$ Phase I (90 K)

(b) [**2**]SbF$_6$ Phase I (90 K) Phase II (333 K)

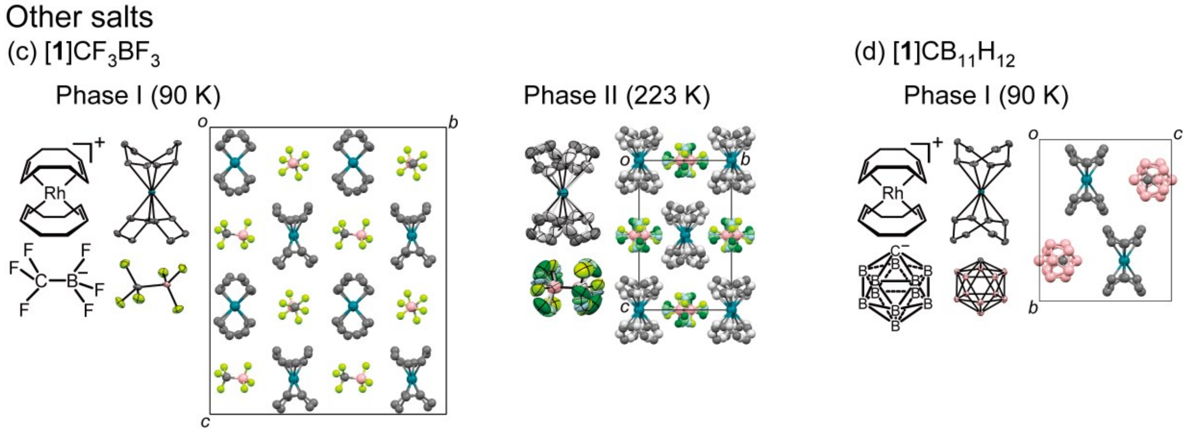
Other salts

(c) [**1**]CF$_3$BF$_3$ Phase I (90 K) Phase II (223 K)

(d) [**1**]CB$_{11}$H$_{12}$ Phase I (90 K)

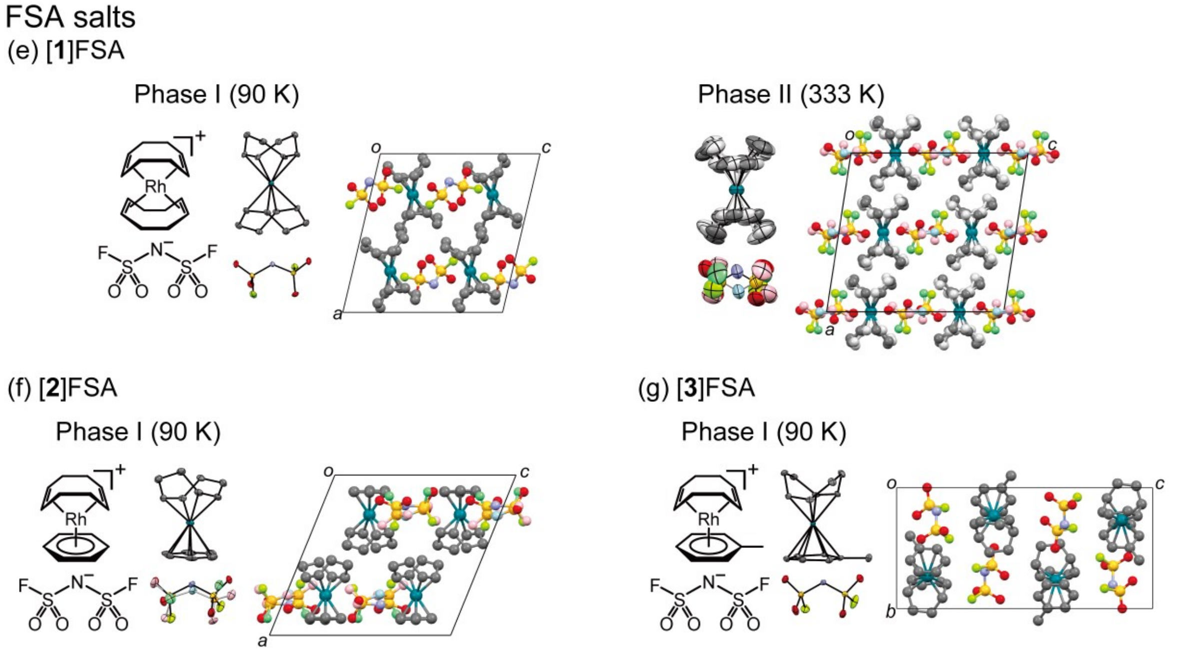
FSA salts

(e) [**1**]FSA Phase I (90 K) Phase II (333 K)

(f) [**2**]FSA Phase I (90 K)

(g) [**3**]FSA Phase I (90 K)

Figure 7-10. Molecular structures (left, ORTEP drawing, 50% probability level) and packing diagrams (right) of [**1**]X–[**3**]X. (a, b) SbF$_6$ salts, (c, d) other salts, and (e–g) FSA salts. Less occupied parts of disordered groups are shown in a lighter color.

Crystal structures of SbF_6 salts. The structural disorder becomes more extensive with a decrease in cation symmetry from **1** to **3**. The structure of [**1**]SbF_6 at 90 K (phase I), shown in **Fig. 7-10a**, has an ordered phase with a coordination number of six. The structure of phase II could not be fully refined because of extensive rotational disorder. The space groups of phases I and II are monoclinic *C*2/*c* and orthorhombic *A*, respectively, with $Z = 8$ (**Table 7-3**), where molecular rotation leads to a higher symmetry in phase II. The corresponding Ir complex [**1′**]SbF_6 is isomorphous, and its unit cell volume is identical to that of [**1**]SbF_6 within the standard deviation (**Fig. 7-11**). Their molecular structures are almost identical, with M–$C_{(cod)}$ distances of 2.220(2)–2.269(2) Å (M = Rh) and 2.196(7)–2.254(7) Å (M = Ir).

The structures of [**2**]SbF_6 at 90 K (phase I) and 333 K (phase II) are shown in **Fig. 7-10b**. The structural changes at the phase transition are small; both phases exhibit the *Cmcm* space group and a coordination number of seven, and their unit cell volumes are almost the same ($Z = 4$). The cations and anions exhibit rotational disorder in both phases. The cod, benzene ligands, and anion were refined as two-fold disordered in phase I (occupancy ratios 0.5:0.5, 0.63(2):0.37(2), and 0.654(5):0.346(5), respectively), whereas the anion required refinement of three-fold disorder in phase II, with the occupancies becoming more averaged (occupancy ratios 0.5:0.5, 0.56(3):0.44(3), and 0.402(3):0.302(3):0.296(3), respectively). These small structural changes are consistent with the small phase-transition entropy ($\Delta S = 2.9$ J mol K^{-1}). Phase IV (373 K) has the same unit cell and space group as those in phase II; the structure could not be fully refined owing to extensive disorder (**Table 7-4**).

The structure of [**3**]SbF_6 could not be determined because of the extensive rotational disorder of the cations in both phases. The powder X-ray diffraction (PXRD) patterns of [**3**]SbF_6 at 90 K (phase I) and 293 K (phase II) are shown in **Fig. 7-12a**; the pattern at 293 K is considerably simpler, with fewer peaks than that at 90 K. The crystal systems of these phases are orthorhombic *P* ($Z = 16$) and tetragonal *I* ($Z = 2$), respectively (**Table 7-9**). Molecular rotation (see below) resulted in high crystal symmetry.

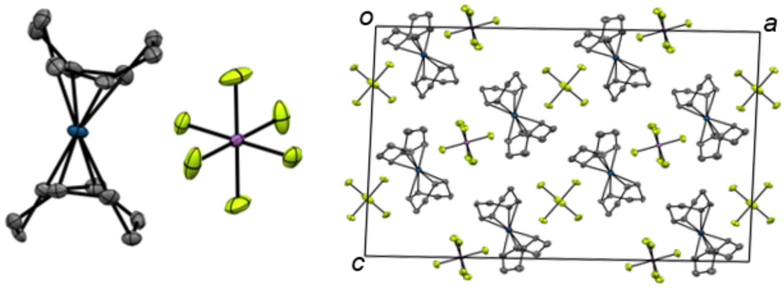

Figure 7-11. The ORTEP drawing (left) and packing diagram (right) of [**1′**]SbF_6 at 90 K.

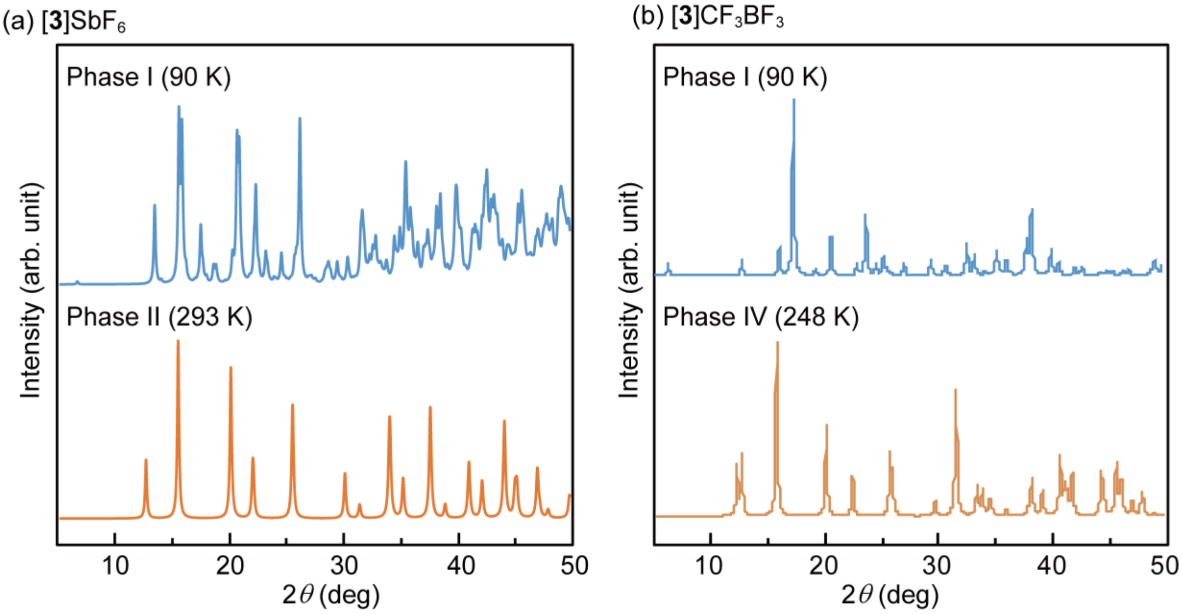

Figure 7-12. PXRD patterns of (a) [**3**]SbF_6 in phase I (90 K) and phase II (293 K) and (b) [**3**]CF_3BF_3 in phase I (90 K) and phase IV (248 K).

Cation dynamics in SbF_6 salts. The cation motion in [**1**]SbF_6–[**3**]SbF_6 was investigated using solid-state ^{1}H and ^{2}H NMR spectroscopy. As shown in the previous section, X-ray structural analysis revealed that the cation has an ordered structure in [**1**]SbF_6, rotationally disordered structure in [**2**]SbF_6, and extensive disorder in [**3**]SbF_6 at room temperature. To investigate the motion of the cod and arene ligands in the cation independently, salts with benzene-d_6 and toluene-d_8 ligands (d-[**2**]SbF_6 and d-[**3**]SbF_6, respectively) were synthesized and used for NMR measurements.

The motion of the cod ligand was investigated using ^{1}H NMR spectroscopy. The static ^{1}H NMR spectra of [**1**]SbF$_6$, *d*-[**2**]SbF$_6$, and *d*-[**3**]SbF$_6$ recorded at 299 K are shown in **Fig. 7-13a**, each displaying the proton signal of the cod ligand. The full-width-at-half-maxima of the peaks for [**1**]SbF$_6$, *d*-[**2**]SbF$_6$, and *d*-[**3**]SbF$_6$ are 54.0, 19.3, and 8.9 kHz, and the second moments (M_2) for the signals are 29.1, 3.7, and 0.8 G^2, respectively. The broad signal in [**1**]SbF$_6$ indicates that the ligand is static, which is consistent with the X-ray structure. The narrow signal in *d*-[**2**]SbF$_6$ indicates that the ligand undergoes dynamic reorientation, which demonstrates that the crystallographically observed two-fold rotational disorder of cod is dynamic in nature, with the disordered moieties not statically locked in place. A narrow signal was also obtained for *d*-[**3**]SbF$_6$ ($M_2 < 1$), indicating that the ligand undergoes extensive motion.[278]

The motions of the deuterated arene ligands in *d*-[**2**]SbF$_6$ and *d*-[**3**]SbF$_6$ were investigated using ^{2}H NMR spectroscopy. The static ^{2}H NMR spectrum of *d*-[**2**]SbF$_6$ measured at 296 K is shown in **Fig. 7-13b(i)**, in which the nuclear quadrupole coupling constant (e^2Qq/h) is 88.7 kHz (asymmetry factor $\eta = 0$). This value is half that of the static phenyl group (176 kHz),[279] indicating that the benzene ligand undergoes continuous rotational diffusion around the molecular long axis. Therefore, although benzene is rotationally disordered according to X-ray analysis, it rotates faster than the NMR time scale. This phase can also be regarded as rotational in a broader sense.

The solid-state static ^{2}H NMR spectra of *d*-[**3**]SbF$_6$ in phases II (299 K) and I (263 K) are shown in **Fig. 7-13b(ii)**, and consist of two and three components, respectively. In each spectrum, the innermost Pake doublet represents the methyl-D signal, and its small e^2Qq/h value (20.5 kHz in phase II, 20.1 kHz in phase I) indicates continuous rotational motion of the methyl group.[280] The outer Pake doublet at 299 K represents the arene-D signal, and its e^2qQ/h value (84.3 kHz, $\eta = 0$) is approximately 4 kHz smaller than that of [**2**]SbF$_6$. Line shape analysis revealed that the toluene ligand undergoes continuous rotational diffusion around the molecular long axis, accompanied by precessional motion ($\gamma = 10.4°$) of the cation along the molecular long axis, as illustrated in the figure. In contrast, two types of Pake doublets are observed for arene-D at 263 K, indicating the presence of nearly static and dynamic cations. The e^2qQ/h value of the outer signal (165.7 kHz) is approximately 10 kHz smaller than that of the static phenyl group, indicating that the ring rotation is nearly frozen, although a slight precessional motion of the cation still exists ($\gamma = 11.4°$). The small e^2qQ/h value of the inner signal (48.1 kHz) indicates extensive cation motion, which is analyzed as the continuous rotation of the phenyl ring and large precessional motion of the cation ($\gamma = 33.3°$). Alternatively, a larger precessional motion ($\gamma = 44.1°$) without molecular rotation would produce the same line shape; however, this seems less plausible.

These analyses reveal the characteristic molecular motion of the Rh-cod cations. The ^{1}H and ^{2}H NMR spectra consistently account for the X-ray structure, and the results suggest the dynamic nature of the two-fold disorder of cod observed in other salts. In addition, [**3**]SbF_6 has been demonstrated to exhibit a rotator phase in which the molecules undergo extensive but anisotropic rotation. Considering these results, the room-temperature phase of [**3**]CF_3BF_3 and the high-temperature phases of the other salts are probably rotator phases with extensive molecular motion, similar to [**3**]SbF_6. However, this could not be confirmed experimentally because of the high temperatures or narrow temperature range.

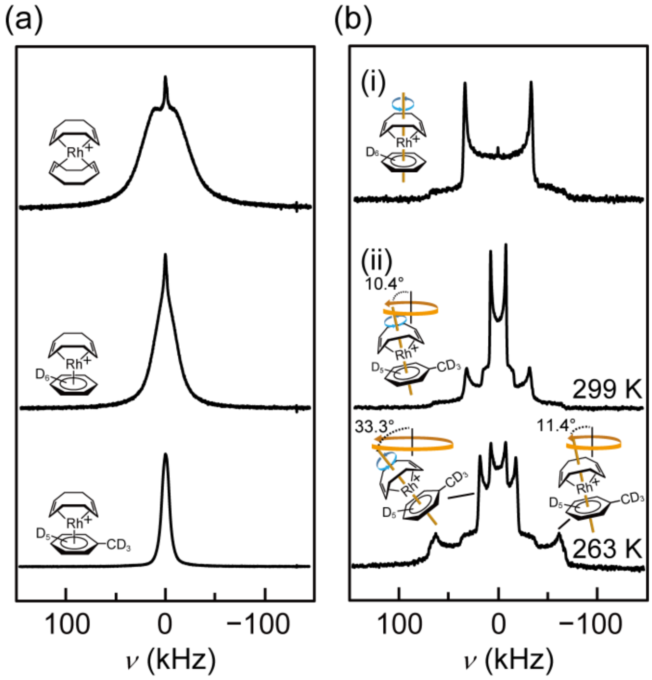

Figure 7-13. (a) Solid-state static ^{1}H NMR spectra of [**1**]SbF_6, *d*-[**2**]SbF_6, and *d*-[**3**]SbF_6 recorded at 299 K. (b) Solid-state static ^{2}H NMR spectra of (i) *d*-[**2**]SbF_6 recorded at 299 K and (ii) *d*-[**3**]SbF_6 recorded at 299 and 263 K. The molecular motions occurring in each phase are illustrated for each spectrum in (b). The frequency of the center of the resonance line of *d*-[**3**]SbF_6 was set to 0 Hz for the ^{1}H NMR spectra, whereas the center of the Pake doublet of [**1**]SbF_6 was set to 0 Hz for the ^{2}H NMR spectra.

Crystal Structures of CF_3BF_3 and $CB_{11}H_{12}$ Salts. The crystals of [**1**]CF_3BF_3, [**1**]$CB_{11}H_{12}$, and [**3**]CF_3BF_3 belong to an orthorhombic crystal system in phase I, similar to most SbF_6 salts. [**3**]CF_3BF_3 exhibits extensive structural disorder.

The structures of [**1**]CF_3BF_3 determined at 90 K (phase I) and 223 K (phase II) are shown in **Fig. 7-10c**. Phase I is an ordered phase with space group *Aba*2 ($Z = 16$). The two pairs of cations and anions are crystallographically independent, and the coordination number is six. The crystal symmetry in phase II is higher (space group *Pnnm*, $Z = 2$). Phase II is regarded as the averaged structure of phase I, having only one cation-anion pair in the asymmetric unit, with the cation best refined as two-fold rotationally disordered (occupancy ratio 0.642(15):0.358(15)). The anion occupies a special position of the two-fold rotational axis and mirror plane, with an occupancy ratio of 0.25. As a result, the carbon and boron atoms are refined as two-fold rotationally disordered (occupancy ratio 0.5:0.5), occupying almost the same position, and the fluorine atoms are refined as four-fold disordered by rotation (occupancy ratio 0.25). The molecular arrangements in phases I and II are almost identical, with slight shifts in their molecular positions (**Fig. 7-14**). This structure differs from that of [**1**]OTf (space group *C*2/*c* at room temperature, ordered structure),[276] despite the presence of structurally similar anions.

The structure of [**1**]$CB_{11}H_{12}$ at 90 K (phase I) in **Fig. 7-10d** clearly shows an ordered phase. This phase crystallizes in the space group *Pnma* ($Z = 4$), exhibiting a coordination number of eight owing to the large size of the anion. The anion geometry is almost identical to those of other reported salts.[281]

The structures of [**3**]CF_3BF_3 in both phases are extensively disordered and not satisfactorily refined, similar to those of [**3**]SbF_6. The apparent crystal systems of phases I (90 K) and IV (248 K), based on the unit cell dimensions, are orthorhombic and tetragonal, respectively ($Z = 2$). The PXRD patterns of this salt, shown in **Fig. 7-12b**, are similar to those of [**3**]SbF_6 (**Fig. 7-12a**). In particular, the patterns of the high-temperature phases are almost identical to each other, indicating that their structures are isomorphic, which is reasonable considering their similar anion volumes.

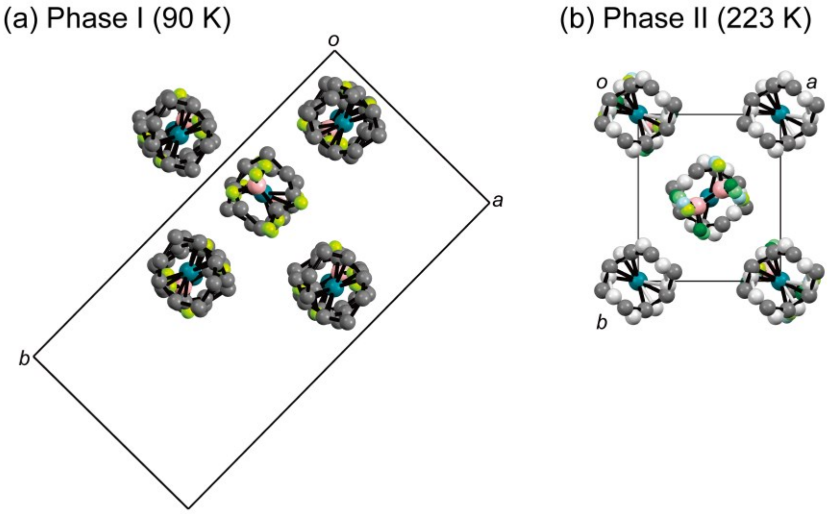

Figure 7-14. Packing diagrams of [**1**]CF_3BF_3 in (a) phase I (90 K) and (b) phase II (223 K) projected along the *c*-axis. Less occupied parts of disordered moieties in (b) are shown in a lighter color.

Crystal structure of FSA salts. The FSA salts [**1**]FSA–[**3**]FSA have a lower crystal symmetry than the other salts, reflecting their low anion symmetry.

The structures of [**1**]FSA at 90 K (phase I) and 333 K (phase II) are shown in **Fig. 7-10e**. Phase I crystallizes in space group $P2_1/c$ (Z = 4) and exhibits an ordered structure, whereas phase II crystallizes in space group $C2/c$ (Z = 4) and exhibits extensive disorder. The molecular long axes of the cations are canted with each other in phase I, but they are nearly parallel in phase II (**Fig. 7-10e**). The cation in phase II is refined as two-fold disordered by rotation (occupancy ratio 0.516(15):0.484(15)), and the anion is also refined as disordered with two equally occupied symmetry equivalent moieties. Such order–disorder in the FSA anion upon phase transition is often observed.[100,102,108,282] The coordination number change from six in phase I to eight in phase II is ascribed to an effective change in the radius ratio caused by the disorder of the anion. These large structural changes are consistent with the large transition entropy (30.6 J mol K^{-1}).

The crystal structures of [**2**]FSA and [**3**]FSA at 90 K (phase I) are shown in **Fig. 7-10f–g**.

They crystallize in the space groups $P2_1/c$ and $P2_1/n$, respectively ($Z = 4$). The cations in both structures are ordered, but the anion in [**2**]FSA exhibits two-fold disorder (occupancy ratio 0.581(5):0.419(5)). The proximity of their melting points prevented the collection of diffraction data for phase II in these salts.

Ligand exchange reactions. To explore the solid-state reactivity of Rh-cod complexes, we investigated the ligand-exchange reactions of SbF_6 salts using single crystals and found that [**3**]SbF_6 and [**2**]SbF_6 undergo an in situ SC–SC reaction.

Single crystals of [**3**]SbF_6 (0.5 mg, typical size: ~150 × 50 × 50 μm^3) were immersed in diethyl ether (5 mL), followed by the addition of a very small amount of the coordinating solvent (SMe_2 or CH_3CN, 4 μL). The sample was left to stand for three days, during which the ligand exchange reaction proceeded gradually in an SC–SC manner (**Fig. 7-15a, b** and **Table 7-2**). [**3**]SbF_6 and its products were yellow crystals insoluble in the solvent, and the structures of the SC–SC reaction products [**4**]SbF_6 and [**5**]SbF_6 were confirmed by single-crystal X-ray structural analysis (see below). The reaction occurred on the surface, which was visually observable under a POM, as thick crystals did not allow the reaction to proceed into the interior. This resulted in overall conversions of 52% and 14%, respectively, over three days, as confirmed by ^{1}H NMR spectra.

Single crystals of [**2**]SbF_6 (~50 × 50 × 20 μm^3) also exhibited SC–SC ligand exchange reactions for SMe_2 and CH_3CN under similar conditions, with overall conversions of 92% and 17%, respectively (**Table 7-2**). The higher conversion compared to that of [**3**]SbF_6 is ascribed to its smaller crystal size.

Interestingly, the addition of a large excess of SMe_2 to dissolve [**3**]SbF_6 in air resulted in the deposition of a mixture of [**4**]SbF_6 and of the new salt $[Rh(C_8H_{12}O)(SMe_2)_3]SbF_6$ ([**6**]SbF_6) over the range of two weeks. The cation of the latter consists of a ligand and central metal in the oxidized state. The structure determined by crystallographic analysis is shown in **Fig. 7-15c**.

The formation of similar compounds by the oxidation of cod complexes is known;[283,284]; hence, the reaction observed here probably also occurred by the air oxidation of the cation in solution.

In contrast, the reaction of [**1**]SbF_6 proceeded in a considerably shorter time without maintaining crystallinity. The reaction of [**1**]SbF_6 with SMe_2 and CH_3CN in diethyl ether proceeded in 76% (in a day) and 100% (in 1 h) yields, respectively, both changing from red-brown crystals to lumpy yellow amorphous solids (**Table 7-2**, **Fig. 7-16**). The reaction with SMe_2 was slower than that with CH_3CN. The faster reaction of [**1**]SbF_6 than those of [**2**]SbF_6 and [**3**]SbF_6 is probably ascribed to the easier dissociation of the cod ligand than that of the arene ligands,[261] which is also consistent with their thermal decomposition behavior (**Fig. 7-8a**).

For comparison, the direct reactions of single crystals of [**1**]SbF_6 and [**3**]SbF_6 with solvent vapors were examined. The reactions proceeded quantitatively in a considerably shorter time without maintaining crystallinity (**Fig. 7-17**). Exposure to SMe_2 vapor for 5 min produced amorphous products, even for [**3**]SbF_6, indicating that a very fast reaction results in crystallinity loss. Exposure to CH_3CN vapor resulted in the formation of yellow liquids, which is ascribed to the presence of released ligands in the products. Therefore, the use of ether as a medium is advantageous to slow down the reaction speed because of dilution, and the released ligand is efficiently removed, preventing the formation of an oily mixture.

[**2**]SbF_6 and [**3**]SbF_6 are both dynamically disordered crystals, and this feature may facilitate the SC–SC reactions. However, the correlation between reactivity and rotational phase is not clear from the current experiments. Although many examples of SC–SC reactions in coordination compounds have already been reported,[285] the current reaction is important because it involves Rh-cod precatalysts and can be potentially extended to solid-state catalytic reactions. In the current SC–SC reactions, ether may have a role in assisting molecular diffusion at the surface, similar to solvent-assisted solid-state reactions.[285] These points require further investigation.

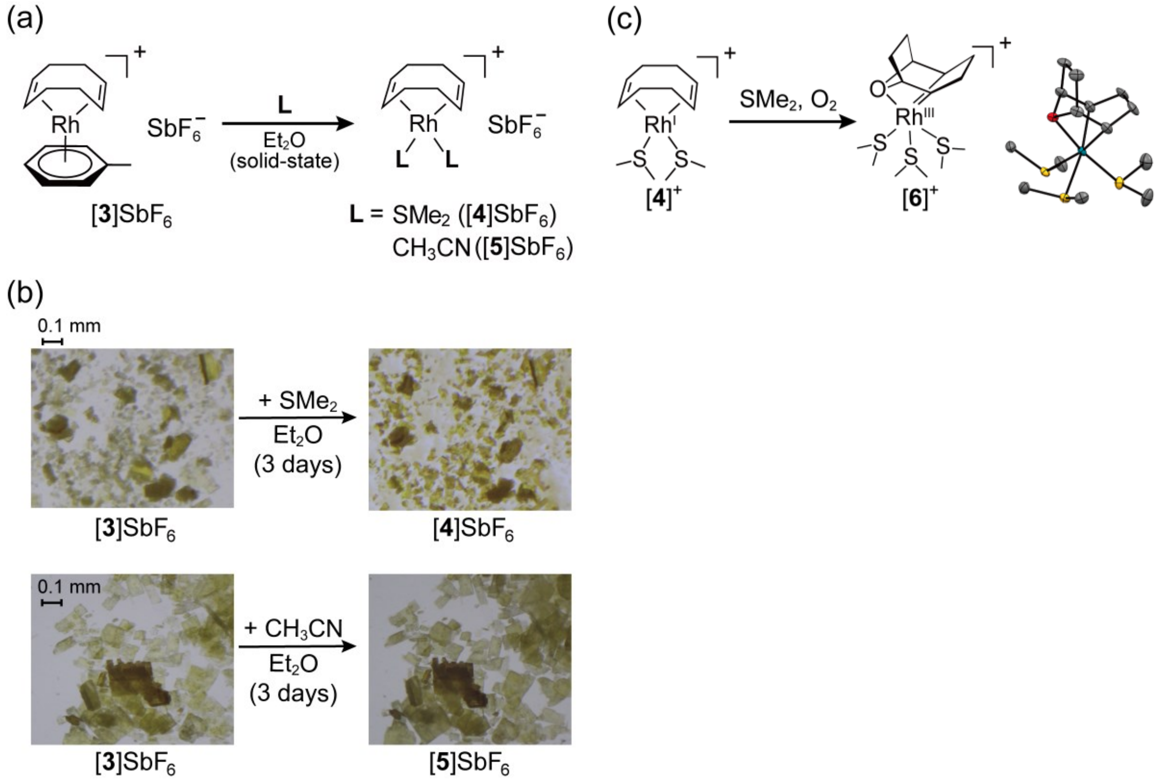

Figure 7-15. (a) Ligand exchange reaction of single crystals of [**3**]SbF_6 performed in a diethyl ether medium. (b) Conversion from [**3**]SbF_6 to [**4**]SbF_6 or [**5**]SbF_6, captured for the same samples during ligand exchange reactions in ether. (c) Oxidation reaction of $[\mathbf{4}]^+$. The X-ray structure of the cation is shown on the right.

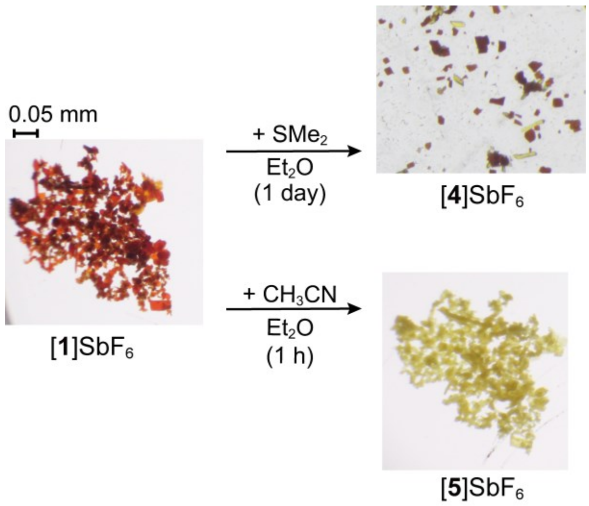

Figure 7-16. POM images taken before and after the ligand exchange reactions of the single crystals of [**1**]SbF_6 with SMe_2 or CH_3CN in ether.

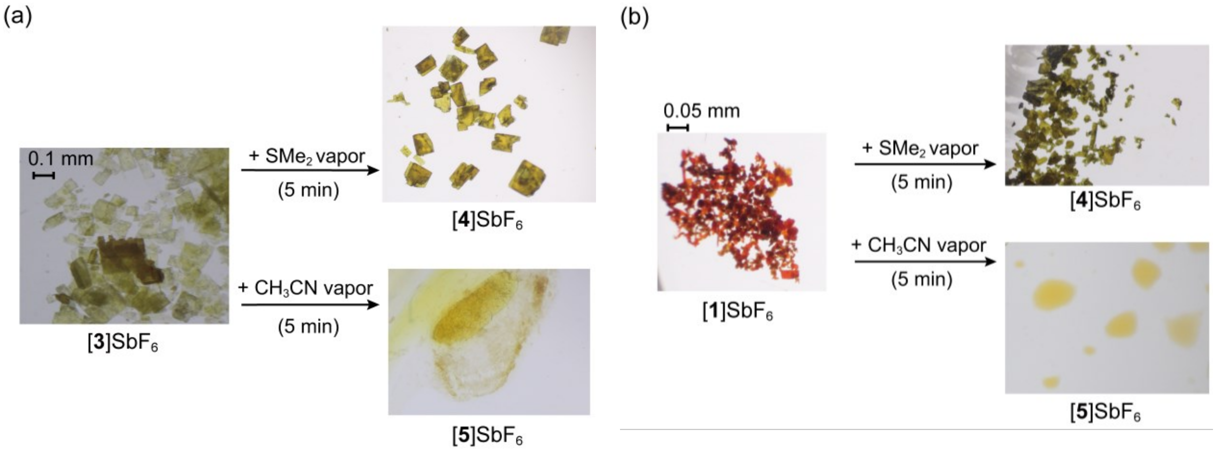

Figure 7-17. POM images taken before and after the reactions of (a) [**3**]SbF_6 and (b) [**1**]SbF_6 with the vapors of SMe_2 or CH_3CN.

Table 7-2. Morphology of products formed by reactions of [**1**]SbF_6–[**3**]SbF_6 with coordinating molecules (L′) using single crystals [SC = single crystal, A = amorphous]. Conversion and reaction time are shown in parenthesis.

	Reaction in diethyl ether			Reaction with vapor (5 min)	
L′	[**1**]SbF_6	[**2**]SbF_6	[**3**]SbF_6	[**1**]SbF_6	[**3**]SbF_6
SMe_2	A (76%, 1 d)	SC (92%, 3 d)	SC (52%, 3 d)	A (99%)	A (98%)
MeCN	A (100%, 1 h)	SC (17%, 3 d)	SC (14%, 3 d)	oil[a]	oil[a]

[a] Oil is gradually formed during reaction.

Characterization of the ligand-exchanged products. The crystal structures of the single crystals of [**4**]SbF_6 and [**5**]SbF_6 obtained via in situ SC–SC ligand exchange were determined along with their thermal properties.

The structure of the as-formed crystal of [**4**]SbF_6 determined at 90 K (phase I) is shown in **Fig. 7-18a**. This salt crystallizes in the triclinic space group *P*-1 ($Z = 2$) with a coordination number of six. One cation and two half anions are crystallographically independent, and the Rh–S bond distances are 2.370(1) and 2.3824(9) Å, respectively. The crystal structures of [**5**]SbF_6 were determined at 90 K (phase I) and 293 K (phase II) because of the phase transition at 136 K (see below). We also confirmed that the crystal structure of [**5**]SbF_6 synthesized by the SC–SC reaction is identical to that obtained by recrystallization of an authentic sample from dichloromethane-diethyl ether (**Table 7-2**). Phase I crystallizes in space group *C*2/*c* (Z = 8). Two half pairs of cations and anions are present in the asymmetric unit of the structure and are crystallographically independent, and all four ions are located on the crystallographic two-fold axes. Phase II crystallizes in space group *Fddd* (Z = 16). The crystal symmetry is higher, and the unit cell volume is twice that of phase I, but the molecular arrangements are almost identical (**Fig. 7-18b** and **7-19**). One half cation, located on a two-fold axis, and two quarters of the occupied anions, located at the intersections of two two-fold axes, are crystallographically independent. Anion I is surrounded by acetonitrile molecules and is ordered, whereas anion II is surrounded by cod and is refined as two-fold disordered by rotation (occupancy ratio 0.876(8):0.124(8)), probably because of the larger space surrounding the anion. The small transition entropy from phase I to II (4.4 J mol K^{-1}) is consistent with this rather small structural change. The cation has Rh–N bond lengths of 2.07–2.08 Å and exhibits virtually identical structure as that in [**5**]BF_4.[237]

DSC measurements revealed no phase transitions for [**4**]SbF_6 and decomposition at 433 K without melting, whereas [**5**]SbF_6 exhibited a solid phase transition at 136.0 K (ΔS = 4.4 J mol^{-1} K^{-1}), followed by melting at 410.6 K (ΔS_m = 61.7 J mol^{-1} K^{-1}, **Fig. 7-3a**). Its melting point is approximately 50 K lower than that of [**5**]BF_4 (T_m = 461–463 K[286]). Upon cooling from the melt, the salt exhibited glass transition at 279.8 K, and cold crystallization and melting occurred during its reheating.

The TG charts for these salts are shown in **Fig. 7-20**. The decomposition temperature (3 wt.%) of [**4**]SbF_6 is 433 K, and a slight weight loss starts at approximately 350 K. The loss of the two SMe_2 molecules occurs in two steps, exhibiting a weight loss of approximately 10 wt. % in each step, up to 460 and 520 K (calculated value for the loss of one SMe_2: 11 wt.%), and a weight loss of approximately 34 wt.% is observed between 520 and 600 K, which corresponds to the losses of cod and some SbF_5 formed by partial decomposition of the anion. The decomposition temperature (−3 wt. %) of [**5**]SbF_6 is 441 K, exhibiting a one-step weight loss of 36 wt.% up to 518 K. This corresponds to the loss of two acetonitrile molecules and cod (calculated value: 36 wt. %). These salts are less thermally stable than [**1**]SbF_6 and exhibit ligand desorption at lower temperatures. In particular, the slight weight loss initiated at relatively low temperatures in [**4**]SbF_6 is consistent with its tendency to gradually decompose in air. Furthermore, the slower reaction of [**1**]SbF_6 with SMe_2 than with CH_3CN in diethyl ether (**Table 7-2**) is consistent with the lower thermal stability of [**4**]SbF_6 than that of [**5**]SbF_6.

The syntheses of structurally related salts, [**5**]ClO_4,[287] [Rh(cod)(dmso)$_2$]BF_4,[288] and [Rh(cod)(H_2O)$_2$]OTf,[289] have been reported, of which [Rh(cod)(dmso)$_2$]BF_4 and [Rh(cod)(H_2O)$_2$]OTf have been structurally characterized. [Rh(cod)(H_2O)$_2$]OTf exhibits a phase transition at 215 K, where the order–disorder of the anion occurs, similar to [**4**]SbF_6.

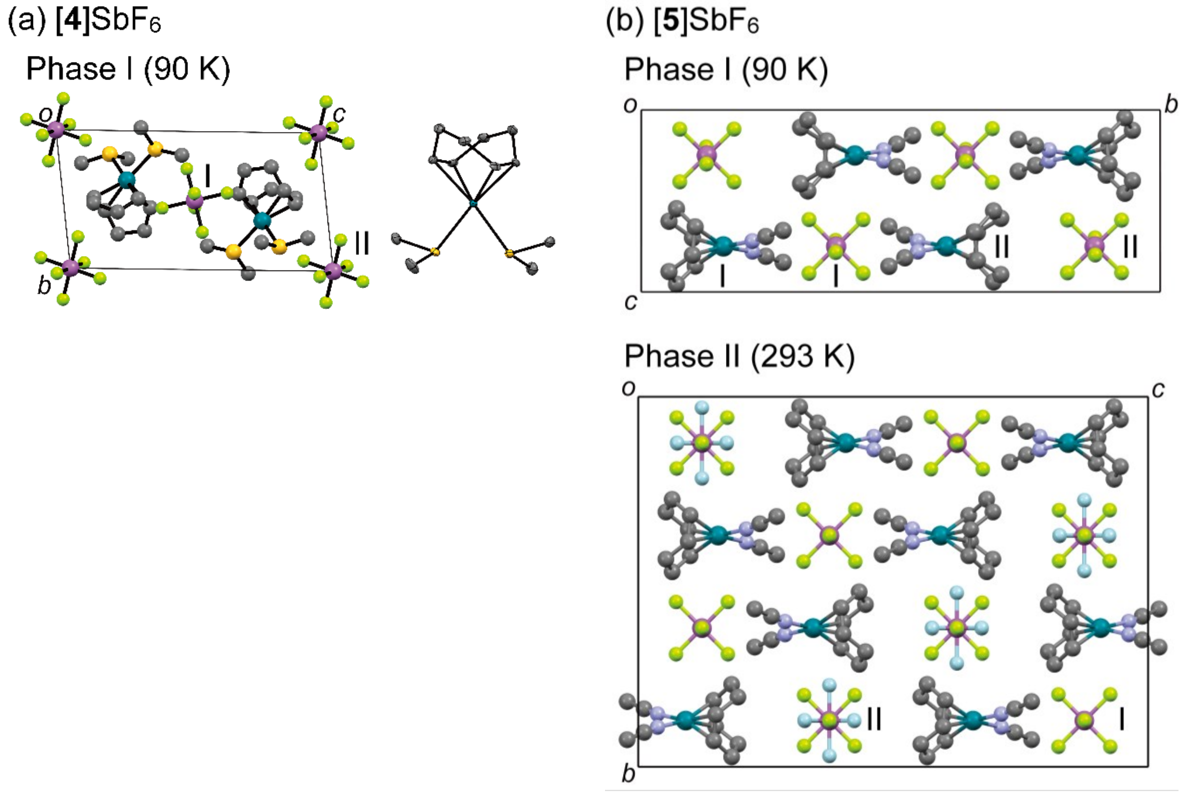

Figure 7-18. Packing diagrams of (a) [**4**]SbF$_6$ and (b) [**5**]SbF$_6$. ORTEP drawing of the cation is shown in (a). Crystallographically independent molecules are labeled as I and II.

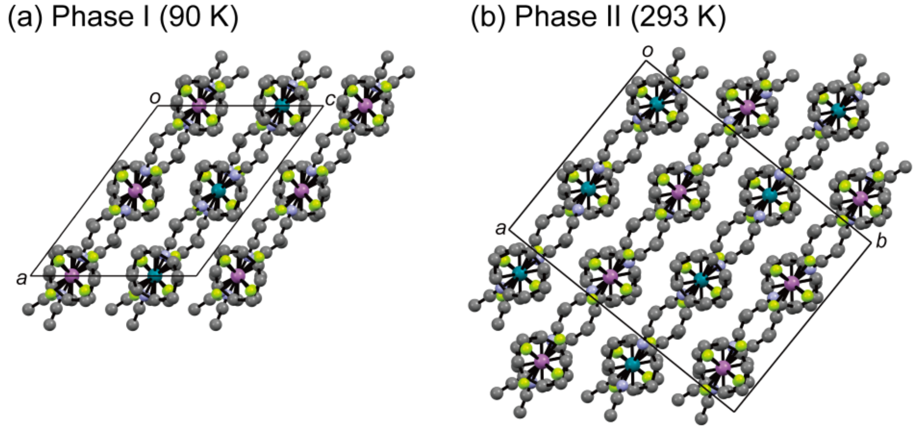

Figure 7-19. Packing diagrams of [**5**]SbF$_6$ in (a) phase I (90 K) and (b) phase II (293 K). Less occupied parts of disordered moieties in (b) are omitted for clarity.

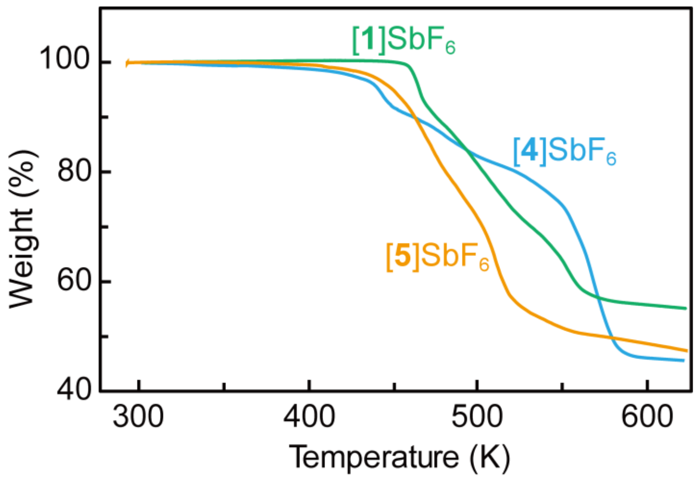

Figure 7-20. TG curves of [**1**]SbF$_6$, [**4**]SbF$_6$, and [**5**]SbF$_6$, measured at a scan rate of 3 K min^{-1} in nitrogen atmosphere.

7.3 Conclusion

In this study, the thermal properties and crystal structures of cationic Rh-cod complexes with cyclic ligands were investigated. These salts exhibit solid phase transitions, through which the disorder and crystal symmetry increase in higher-temperature phases. Crystal symmetry typically depends on the anion, whereas less symmetrical cations tend to exhibit more severely disordered phases. [Rh(cod)(PhMe)]SbF$_6$ exhibits a rotator phase at room temperature, whereas the other salts exhibit dynamically disordered phases. In contrast to the salts of sandwich complexes, no structurally isotropic IPC phase was found owing to the elongated, ellipsoidal shape of the cations. We also investigated the thermal stabilities and chemical reactivities of these salts. FSA salts with arene ligands undergo ligand-exchange reactions upon melting, leading to lower thermal stability. Salts with arene ligands undergo in situ ligand exchange in ether via an SC–SC reaction. The insights obtained in this study provide fundamental information that is useful for the development and application of organometallic reactions because the catalytic reactivities of Rh-cod complexes are based on their coordination abilities. Furthermore, this knowledge will be useful for the future exploration of organometallic solid-state reaction chemistry, including catalytic reactions.

7.4 Experimental Section

General. All reactions were performed under a nitrogen atmosphere, and dehydrated solvents were used. $[M(cod)_2]SbF_6$ (M = Rh, Ir),[262] $[Rh(cod)_2]BF_4$,[290] AgFSA,[266] and $AgCB_{11}H_{12}$[291] were synthesized according to previously reported procedures. $AgCF_3BF_3 \cdot nCH_3CN$ was obtained as a hygroscopic white powder by the reaction of KCF_3BF_3 and silver nitrate in acetonitrile. The white precipitate of potassium nitrate formed during the reaction was removed by filtration and the filtrate was concentrated, followed by the addition of diethyl ether. The desired compound precipitated after standing the solution at 233 K for a day, which was collected by filtration. Other reagents were purchased from TCI. ^1H NMR spectra were recorded on a Bruker Advance 400 spectrometer. FT-IR spectra were acquired using a Thermo Nicolet iS5 spectrometer fitted with attenuated total reflectance (ATR). DSC measurements were performed using a TA Q100 differential scanning calorimeter at a scan rate of 10 K min^{-1} using aluminum hermetic pans as sample containers. TG-DTA measurements were performed using a Rigaku TG8120 thermal analyzer at a scan rate of 3 K min^{-1} under a nitrogen atmosphere. Solid-state NMR spectra were recorded on a Tecmag Apollo spectrometer (operating at 46.045 MHz for ^2H and 299.95 2 MHz for ^1H) equipped with a Doty XC MAS 4 mm probe head. The ^1H NMR spectra were measured with a 3.9 μs π/2 pulse. The ^2H spectra were measured with a solid echo pulse sequence [$\pi/2-\tau-\pi/2-\tau-$acquisition],[292] using a 4.6 μs π/2 pulse and a delay time τ of 40 μs. The recycle delays for the ^1H and ^2H measurements were 7 s and 3 s, respectively.

Synthesis of metal complexes

$[Rh(cod)_2]X$ ([1]X; X = FSA, $CB_{11}H_{12}$, CF_3BF_3): These salts were synthesized using a method similar to that of $[Rh(cod)_2]SbF_6$.[262] The synthesis of $[Rh(cod)_2]FSA$ is described below as an example. 1,5-Cyclooctadiene (29 mg, 0.31 mmol) was added to a solution of $[Rh(cod)Cl]_2$ (50 mg, 0.10 mmol) in dichloromethane (2 mL) under stirring. An acetone solution (1 mL) of

AgFSA (79 mg, 0.23 mmol) was added, and a white precipitate was immediately formed. The suspension was stirred for 1 h and the white solid was removed by Celite filtration. The filtrate was concentrated using a rotary evaporator, to which hexane (5 mL) was added. A reddish-brown oil phase containing the desired product was separated, the hexane phase was removed with a pipette, and the remaining oil was washed twice with hexane (5 mL) and diethyl ether (5 mL × 3). The remaining solvent was removed under reduced pressure, and recrystallization of the resultant solid from dichloromethane-diethyl ether at 233 K resulted in the desired product as reddish brown crystals (78 mg, 78% yield). ^{1}H NMR (400 MHz, $CDCl_3$): δ = 2.47–2.68 (m, 16H, CH_2), 5.34 (br, 8H, CH). FTIR (ATR, cm^{-1}): 564, 736, 823, 1105, 1171, 1360, 1427, 2891. Anal. Calcd. for $C_{16}H_{24}F_2NO_4RhS_2$: C, 38.48; H, 4.84; N, 2.80. Found: C, 38.42; H, 5.02; N, 2.87. The other salts were synthesized in a similar manner using the corresponding silver salts. $[Rh(cod)_2]CB_{11}H_{12}$: reddish brown crystals (20 % yield). ^{1}H NMR (400 MHz, $CDCl_3$): δ = 0.81–0.91 (br, 11H, BH), 2.18 (s, 1H, $CHBH_{11}$) 2.35–2.54 (m, 16H, CH_2), 5.11 (br, 1H, cod–CH), 5.29 (br, 2H, cod–CH), 5.59 (br, 5H, cod–CH). FTIR (ATR, cm^{-1}): 716, 783, 860, 1001, 1023, 1065, 1426, 1472, 2509. Anal. Calcd. for $C_{17}H_{36}B_{11}Rh$: C, 44.17; H, 7.85; N, 0.00. Found: C, 43.55; H, 7.40; N, 0.12. $[Rh(cod)_2]CF_3BF_3$: reddish brown crystals (29% yield). ^{1}H NMR (400 MHz, $CDCl_3$): δ=2.46–2.69 (m, 8H, CH_2), 5.33 (br, 4H, CH). FTIR (ATR, cm^{-1}): 632, 783, 829, 862, 946, 970, 1043, 1430. Anal. Calcd. for $C_{17}H_{24}BF_6Rh$: C, 44.77; H, 5.30; N, 0.00. Found: C, 44.67; H, 5.36; N, 0.07.

[Rh(cod)L]X ([2]X: L = C_6H_6, [3]X: L = PhMe, X = SbF_6, FSA): The synthesis of $[Rh(cod)(PhMe)]SbF_6$ is described below as an example. Toluene (325 mg, 3.5 mmol) was added to a solution of $[Rh(cod)Cl]_2$ (349 mg, 0.81 mmol) in dichloromethane (5 mL) with stirring. In sequence, a solution of $AgSbF_6$ (510 mg, 1.7 mmol) in acetone (1 mL) was added to this solution to form a white precipitate. The suspension was stirred for 1 h and the solid was removed by Celite filtration. The filtrate was concentrated using a rotary evaporator, followed by addition of hexane (5 mL). A yellow oil phase containing the desired product was separated, the hexane phase was removed using a pipette, and the remaining oil was washed with hexane (5 mL × 2) and diethyl ether (5 mL × 3). The remaining solvent was removed under reduced pressure, and recrystallization of the resultant solid from dichloromethane-diethyl ether (233 K) resulted in the desired product as yellow crystals (618 mg, yield 81%). ^{1}H NMR (400 MHz, $CDCl_3$): δ = 2.08–2.17 (m, 8H, CH_2), 2.35–2.45 (m, 8H, CH_2), 2.39 (s, 3H, CH_3), 4.65 (br, 4H, CH), 6.68–6.74 (m, 3H, arene–H), 6.77–6.82 (m, 2H, arene–H). FTIR (ATR, cm^{-1}): 647, 807, 889, 990, 1165, 1452, 1549. Anal. Calcd. for $C_{15}H_{20}F_6RhSb$: C, 33.43; H, 3.74; N, 0.00. Found: C, 33.37; H, 3.77; N, 0.08. The corresponding deuterated complex $[Rh(cod)(C_6D_5CD_3)]SbF_6$ (*d*-[**3**]SbF_6) was synthesized using toluene-*d*$_8$ (84% yield). The other salts were synthesized in a similar manner using the corresponding ligands and silver salts. $[Rh(cod)(C_6H_6)]SbF_6$: Yellow crystals (19% yield). ^{1}H NMR (400 MHz, $CDCl_3$): δ = 2.11–2.19 (m, 4H, CH_2), 2.36–2.46 (m, 4H, CH_2), 4.83 (br, 4H, C*H*), 6.87 (s, 6H, C_6H_6). FTIR (ATR, cm^{-1}): 647, 785, 827, 891, 990, 1010, 1163, 1309, 1337, 1443, 1464. Anal. Calcd. for $C_{14}H_{18}F_6RhSb$: C, 32.03; H, 3.46; N, 0.00. Found: C, 31.81; H, 3.38; N, 0.08. The corresponding deuterated complex $[Rh(cod)(C_6D_6)]SbF_6$ (*d*-[**1**]SbF_6) was synthesized using benzene-*d*$_6$ and acetone as the solvents. In this case, benzene-*d*$_6$ was added to the recrystallization solvent to suppress ligand dissociation (60% yield). [Rh(cod)(PhMe)]FSA: Yellow crystals (45% yield). ^{1}H NMR (400 MHz, $CDCl_3$): δ = 2.11–2.20 (m, 4H, CH_2), 2.35–2.45 (m, 4H, CH_2), 2.42 (s, 3H, CH_3), 4.67 (br, 4H, CH), 6.72–6.78 (m, 3H, arene–H), 6.81–6.87 (m, 2H, arene–H). FTIR (ATR, cm^{-1}): 564, 727, 826, 1101, 1174, 1216, 1360, 1451, 2842. Anal. Calcd. for $C_{15}H_{20}F_2NO_4RhS_2$: C, 37.27; H, 4.17; N, 2.90. Found: C, 37.27; H, 4.19; N, 2.83. $[Rh(cod)(C_6H_6)]FSA$: Yellow crystals (19% yield). ^{1}H NMR (400 MHz, $CDCl_3$): δ = 2.11–2.19 (m, 4H, CH_2), 2.36–2.46 (m, 4H, CH_2), 4.83 (br, 4H, CH), 6.87 (s, 6H, C_6H_6). FTIR (ATR, cm^{-1}): 563, 737, 824, 1098, 1171, 1360, 1549, 1622, 2955. Anal. Calcd. for $C_{14}H_{18}F_2NO_4RhS_2$: C, 35.83; H, 3.87; N, 2.98. Found: C, 35.34; H, 3.76; N, 2.91.

[Rh(cod)(PhMe)]CF_3BF_3 ([3]CF_3BF_3): The salt was prepared using a similar method to that of [Rh(cod)(PhMe)]BF_4.[261] Toluene (1 mL) was added to a solution of $[Rh(cod)_2]CF_3BF_3$ (26 mg, 0.05 mmol) in dichloromethane (2 mL) under stirring, and the mixture was further stirred for 3 days. The solution was concentrated using a rotary evaporator, followed by addition of diethyl ether (10 mL). Subsequently, a pale orange solid precipitated and was collected by filtration. Recrystallization from dichloromethane/diethyl ether (233 K) yielded orange crystals (21 mg, 84% yield). ^{1}H NMR (400 MHz, $CDCl_3$): δ = 2.08–2.17 (m, 4H, CH_2), 2.34–2.44 (m, 4H, CH_2), 2.39 (s, 3H, CH_3), 4.65 (br, 4H, CH), 6.70–6.77 (m, 3H, arene–H), 6.79–6.84 (m, 2H, arene–H). FTIR (ATR, cm^{-1}): 631, 782, 828, 863, 947, 970, 1043, 1429, 1449. Anal. Calcd. for $C_{12}H_{18}F_6N_2RhSb$: C, 43.67; H, 4.58; N, 0.00. Found: C, 43.48; H, 4.74; N, 0.00.

[Rh(cod)(CH_3CN)$_2$]SbF_6 ([5]SbF_6): Diethyl ether (5 mL) was added to a solution of $[Rh(cod)_2]SbF_6$ (30 mg, 0.05 mmol) in acetonitrile (1 mL). A yellow solid was precipitated, which was collected by filtration, and recrystallization of the solid from dichloromethane-diethyl ether at 233 K yielded yellow crystals. The second crop was also collected and combined (76% yield). ^{1}H NMR (400 MHz, $CDCl_3$): δ = 1.86–1.96 (m, 4H, CH_2), 2.35 (s, 6H, CH_3), 2.44–2.54 (m, 4H, CH_2), 4.40 (br, 4H, CH). FT-IR (ATR, cm^{-1}): 652, 877, 981, 1005, 1027, 1082, 1166, 1228, 1314, 1337, 1409, 1437, 2284, 2311. Anal. Calcd. for $C_{12}H_{18}F_6N_2RhSb$: C, 27.75; H, 3.43; N, 5.30. Found: C, 27.40; H, 3.31; N, 5.16.

Ligand exchange reactions

In situ ligand exchange reactions using single crystals of [**2**]SbF_6 and [**3**]SbF_6 were performed in diethyl ether. The crystals (0.5 mg) were placed in diethyl ether (5 mL) under nitrogen atmosphere. These salts were insoluble in ether. A small amount of SMe_2 or acetonitrile (4 μL) was added to the solvent, which was left unperturbed, and the solids were gradually converted to $[Rh(cod)(SMe_2)_2]SbF_6$ ([**4**]SbF_6) and [**5**]SbF_6 without any change in appearance. The conversions of [**2**]SbF_6 to [**4**]SbF_6 and [**5**]SbF_6 were 92 and 17%, respectively, whereas those of [**3**]SbF_6 were 52 and 14%, respectively, as determined using ^{1}H NMR spectroscopy ($CDCl_3$). The reactions of [**1**]SbF_6 with SMe_2 or acetonitrile were performed in a similar manner. In this case, the appearance changed from reddish-brown block crystals to yellow solids, and the conversions were 76% (1 day) and 100% (after 1 h) for the reactions with SMe_2 and acetonitrile, respectively. The crystals of [**4**]SbF_6 gradually decomposed in air and turned green over a few days. To avoid possible degradation, the samples recrystallized from dichloromethane-diethyl ether (233 K) were immediately used for the TG-DTA and DSC measurements. [**4**]SbF_6: ^{1}H NMR (400 MHz, $CDCl_3$): δ = 2.06–2.18 (m, 4H, CH_2), 2.31 (s, 12H, CH_3), 2.50–2.63 (m, 4H, CH_2), 4.55 (br, 4H, CH). FT-IR (ATR, cm^{-1}): 649, 857, 980, 1031, 1306, 1335, 1430. Anal. Calcd. for $C_{12}H_{18}F_6N_2RhSb$: C, 25.24; H, 4.24; N, 0. Found: C, 24.84; H, 3.65; N, 1.17. The discrepancy in the analytical data was ascribed to slight decomposition. Upon addition of a large excess of SMe_2 (0.5 mL) to [**3**]SbF_6 (0.5 mg) in diethyl ether, part of the crystal dissolved, and upon standing the solution, a solid mixture of [**4**]SbF_6 and an oxidation product $[Rh(C_8H_{12}O)(SMe_2)_3]SbF_6$ ([**6**]SbF_6) (molar ratio ~0.8:0.2) were deposited over two weeks. The structure of the latter was determined using X-ray crystallography. [**6**]SbF_6: ^{1}H NMR (400 MHz, $CDCl_3$): δ = 2.08 (m, 4H, $RhCHCH_2$-*endo*, $OCHCH_2$-*endo*), 2.59 (m, 4H, $RhCHCH_2$-*exo*, $OCHCH_2$-*exo*), 2.63 (s, 9H, CH_3), 3.04 (m, 2H, RhCH), 5.87 (m, 2H, OCH).

The reactions with solvent vapors were performed as follows: A small vial (1 mL) containing [**1**]SbF_6 or [**3**]SbF_6 crystals (0.5 mg) was placed in a larger vial (10 mL) under a nitrogen atmosphere. A small amount of the solvent (CH_3CN or SMe_2; 0.1 mL) was placed in an outer vial, sealed, and allowed to stand at room temperature for 5 min. [**1**]SbF_6 and [**3**]SbF_6 reacted with SMe_2 vapor to form [**4**]SbF_6 as a yellow amorphous solid in almost quantitative yield. The conversion was confirmed using ^{1}H NMR spectroscopy ($CDCl_3$). The reactions with CH_3CN vapor proceeded quantitatively to result in a yellow liquid, which yielded solid [**5**]SbF_6 after vacuum-drying.

X-ray Crystallography

X-ray diffraction data were collected using a Bruker APEX II Ultra diffractometer (X-ray source: MoKα rotating anode), and calculations were performed using SHELXL[117] (software: APEX3[293]). Packing diagrams were drawn using Mercury software[294] and the packing indices were calculated using Platon.[118] [**1**]CF_3BF_3 (phase II) and [**5**]SbF_6 (phase I) were twinned; therefore, TWINABS[295] was used for scaling and empirical absorption correction, and the second component contribution was modeled using the HKLF5 refinement. PXRD patterns were calculated using XPREP[296] from the single-crystal *hkl* reflection data. The unit cell parameters were based on single-crystal unit cell determination. The crystallographic parameters are listed in **Tables 7-3–7-9**. For the structural determination of [**3**][Rh(cod)$(FSA)_2$], single crystals formed from a molten liquid of [**3**]FSA were used, and the data were collected at 388 K to prevent solidification of unreacted [**3**]FSA. The data quality was less satisfactory because of the high data-collection temperature and gradual crystal degradation. Other crystals were obtained by recrystallization from organic solvents. CSD numbers: CCDC-2183669–2183683 and 2193891 contain the crystallographic data for [**1**]SbF_6, [**1'**]SbF_6, [**2**]SbF_6, [**2**]SbF_6 (phase II), [**1**]FSA, [**1**]FSA (phase II), [**2**]FSA, [**3**]FSA, [**1**]CF_3BF_3, [**1**]CF_3BF_3 (phase II), [**1**]$CB_{11}H_{12}$, [**5**]SbF_6, [**5**]SbF_6 (phase II), [**4**]SbF_6, [**3**][Rh(cod)$(FSA)_2$], and [**6**]SbF_6.

Table 7-3. Crystallographic parameters for [**1**]SbF$_6$ and [**1′**]SbF$_6$

Compound	[**1**]SbF$_6$		[**1′**]SbF$_6$
Phase	I (90 K)	II (333 K)^c	I (90 K)
Empirical formula	$C_{16}H_{24}F_6RhSb$		$C_{16}H_{24}F_6IrSb$
Formula weight	555.01		644.3
Crystal system	monoclinic	orthorhombic *A*	monoclinic
Space group	$C2/c$		$C2/c$
a [Å]	28.523(3)	14.921(5)	28.475(8)
b [Å]	7.2771(9)	32.625(14)	7.2685(19)
c [Å]	16.991(2)	7.931(3)	17.046(5)
β [°]	91.8630(10)	90	91.888(4)
V [Å^3]	3524.9(7)	3861(2)	3526.1(16)
Z	8	8	8
ρ_{calkd} [g cm^{-3}]	2.092		2.428
μ [mm^{-1}]	2.523		9.127
$F(000)$	2160		2416
Reflns collected	9821		7029
R (int)	0.0174		0.0300
Goodness of fit	1.092		1.074
$R_1{}^a$, $R_w{}^b$ ($I > 2\sigma(I)$)	0.0154, 0.0369		0.0336, 0.0759
$R_1{}^a$, $R_w{}^b$ (all data)	0.0159, 0.0372		0.0438, 0.0813

$^aR_1 = \Sigma||F_o| - |F_c|| / \Sigma|F_o|$. $^bR_w = [\Sigma w\,(F_o{}^2 - F_c{}^2)^2/\Sigma w\,(F_o{}^2)^2]^{1/2}$. ^{c}Low data quality.

Table 7-4. Crystallographic parameters for [**2**]SbF_6

Compound	[**2**]SbF_6		
Phase	I (90 K)	II (333 K)	IV (373 K)[c]
Empirical formula	$C_{14}H_{18}F_6RhSb$		
Formula weight	524.94		
Crystal system	orthorhombic	orthorhombic	orthorhombic
Space group	*Cmcm*	*Cmcm*	*Cmcm*
a [Å]	7.0596(10)	7.351(15)	7.41(2)
b [Å]	26.014(4)	26.89(6)	27.00(8)
c [Å]	8.6274(13)	8.639(18)	8.56(2)
V [Å^3]	1584.4(4)	1708(6)	1713(8)
Z	4	4	4
ρ_{calkd} [g cm^{-3}]	2.201	2.042	2.036
μ [mm^{-1}]	2.800	2.598	2.59
F(000)	1008	1008	1008
Reflns collected	4583	4659	4760
R (int)	0.0155	0.0520	0.0669
Goodness of fit	1.043	1.013	0.959
$R_1{}^a$, $R_w{}^b$ ($I > 2\sigma(I)$)	0.0215, 0.0490	0.0397, 0.0751	0.0392, 0.0795
$R_1{}^a$, $R_w{}^b$ (all data)	0.0231, 0.0501	0.0856, 0.0893	0.127, 0.1052

[a] $R_1 = \Sigma||F_o| - |F_c|| / \Sigma|F_o|$. [b] $R_w = [\Sigma w (F_o{}^2 - F_c{}^2)^2/\Sigma w (F_o{}^2)^2]^{1/2}$. [c] Low data quality.

Table 7-5. Crystallographic parameters for [**4**]SbF_6 and [**5**]SbF_6

Compound	[**4**]SbF_6^{c}	[**5**]SbF_6		[**5**]SbF_6^{c}
Phase	I (90 K)	I (90 K)	II (293 K)	II (293 K)
Empirical formula	$C_{12}H_{24}F_6RhS_2Sb$	$C_{12}H_{18}F_6N_2RhSb$		
Formula weight	571.09	528.94		
Crystal system	triclinic	monoclinic	orthorhombic	orthorhombic
Space group	*P*–1	*C*2/*c*	*Fddd*	*Fddd*
a [Å]	7.917(2)	14.260(3)	14.0929(14)	14.0838(14)
b [Å]	8.290(2)	25.441(6)	18.7487(19)	18.7452(18)
c [Å]	15.227(4)	11.139(3)	25.831(3)	25.850(3)
α [°]	79.373(4)			
β [°]	76.425(4)	126.779(2)		
γ [°]	70.806(4)			
V [Å^3]	911.2(5)	3236.7(14)	6825.2(12)	6824.5(12)
Z	2	8	16	16
ρ_{calkd} [g cm^{-3}]	2.082	2.171	2.059	2.059
μ [mm^{-1}]	2.664	2.745	2.604	2.604
$F(000)$	556	2032	4064	4064
Reflns collected	5297	3077	9631	9755
R (int)	0.0245	0.034	0.0269	0.0235
Goodness of fit	1.043	1.151	1.019	1.014
R_1^{a}, R_w^{b} ($I > 2\sigma(I)$)	0.0287, 0.0721	0.0328, 0.0948	0.0257, 0.0623	0.0266, 0.066
R_1^{a}, R_w^{b} (all data)	0.0330, 0.0750	0.0409, 0.1080	0.0412, 0.0702	0.0411, 0.0736

$^{a}R_1 = \Sigma||F_o| - |F_c|| / \Sigma|F_o|$. $^{b}R_w = [\Sigma w (F_o^2 - F_c^2)^2/\Sigma w (F_o^2)^2]^{1/2}$. ^{c}SC–SC reaction product of [**3**]SbF_6 with dimethylsulfide or acetonitrile.

Table 7-6. Crystallographic parameters for [**6**]SbF_6

Compound	[**6**]SbF_6
Phase	I (90 K)
Empirical formula	$C_{14}H_{30}F_6ORhS_3Sb$
Formula weight	649.22
Crystal system	monoclinic
Space group	$P2_1/c$
a [Å]	10.5884(14)
b [Å]	12.5540(17)
c [Å]	16.435(2)
β [°]	90.629(2)
V [Å^3]	2184.5(5)
Z	4
ρ_{calkd} [g cm^{-3}]	1.974
μ [mm^{-1}]	2.330
$F(000)$	1280
Reflns collected	12527
R (int)	0.0427
Goodness of fit	1.027
$R_1{}^a$, $R_w{}^b$ ($I > 2\sigma(I)$)	0.0411, 0.0996
$R_1{}^a$, $R_w{}^b$ (all data)	0.0588, 0.1075

$^aR_1 = \Sigma||F_o| - |F_c|| / \Sigma|F_o|$. $^bR_w = [\Sigma w (F_o{}^2 - F_c{}^2)^2/\Sigma w (F_o{}^2)^2]^{1/2}$.

Table 7-7. Crystallographic parameters for [**1**]FSA–[**3**]FSA

Compound	[**1**]FSA		[**2**]FSA	[**3**]FSA
Phase	I (90 K)	II (333 K)	I (90 K)	I (90 K)
Empirical formula	$C_{16}H_{24}F_2NO_4RhS_2$		$C_{14}H_{18}F_2NO_4RhS_2$	$C_{15}H_{20}F_2NO_4RhS_2$
Formula weight	499.39		469.32	483.35
Crystal system	monoclinic	monoclinic	monoclinic	monoclinic
Space group	$P2_1/c$	$C2/c$	$P2_1/c$	$P2_1/n$
a [Å]	13.304(3)	13.525(9)	13.619(3)	8.8350(9)
b [Å]	10.669(2)	10.090(6)	9.1973(19)	9.5770(10)
c [Å]	13.046(3)	14.582(10)	14.268(3)	20.531(2)
β [°]	103.320(3)	98.531(10)	112.202(3)	98.0380(10)
V [Å^3]	1801.9(6)	1968(2)	1654.6(6)	1720.1(3)
Z	4	4	4	4
ρ_{calkd} [g cm^{-3}]	1.841	1.686	1.884	1.866
μ [mm^{-1}]	1.222	1.119	1.325	1.277
$F(000)$	1016	1016	944	976
Reflns collected	10099	5109	9233	9791
R (int)	0.0251	0.0349	0.0224	0.0262
Goodness of fit	1.022	1.024	1.112	1.044
$R_1{}^a$, $R_w{}^b$ ($I > 2\sigma(I)$)	0.0269, 0.0613	0.0500, 0.1308	0.0294, 0.0645	0.0217, 0.0519
$R_1{}^a$, $R_w{}^b$ (all data)	0.0357, 0.0653	0.0787, 0.1508	0.0337 0.0661	0.0240, 0.0531

$^aR_1 = \Sigma||F_o| - |F_c|| / \Sigma|F_o|$. $^bR_w = [\Sigma w (F_o{}^2 - F_c{}^2)^2/\Sigma w (F_o{}^2)^2]^{1/2}$.

Table 7-8. Crystallographic parameters for [**1**]CF_3BF_3, [**1**]$CB_{11}H_{12}$, and [**3**][Rh(cod)(FSA)$_2$]

Compound	[**1**]CF_3BF_3		[**1**]$CB_{11}H_{12}$	[**3**][Rh(cod)(FSA)$_2$]^c
Phase	I (90 K)	II (223 K)	I (90 K)	388 K
Empirical formula	$C_{17}H_{24}BF_6Rh$		$C_{17}H_{36}B_{11}Rh$	$C_{23}H_{32}F_4N_2O_8Rh_2S_4$
Formula weight	456.08		462.28	874.56
Crystal system	orthorhombic	orthorhombic	orthorhombic	triclinic
Space group	*Aba*2	*Pnnm*	*Pnma*	*P*–1
a [Å]	11.3432(14)	7.3479(7)	12.4463(13)	9.184(18)
b [Å]	22.420(3)	8.6208(8)	14.4304(15)	12.60(3)
c [Å]	27.241(3)	13.9691(13)	11.7763(12)	13.60(3)
α [°]				90.38(3)
β [°]				97.49(3)
γ [°]				100.24(3)
V [Å^3]	6927.8(14)	884.87(14)	2115.1(4)	1535(5)
Z	16	2	4	2
ρ_{calkd} [g cm^{-3}]	1.749	1.712	1.452	1.893
μ [mm^{-1}]	1.043	1.021	0.810	1.420
F(000)	3680	460	952	876
Reflns collected	16289	1024	11603	8469
R (int)	0.0185	0.020	0.0251	0.0556
Goodness of fit	1.146	1.185	1.025	1.319
$R_1{}^a$, $R_w{}^b$ ($I > 2\sigma(I)$)	0.0218, 0.0526	0.0186, 0.0537	0.0227, 0.0550	0.1444, 0.3264
$R_1{}^a$, $R_w{}^b$ (all data)	0.0232, 0.0536	0.0227, 0.0566	0.0298, 0.0585	0.2851, 0.4442

$^aR_1 = \Sigma||F_o| - |F_c|| / \Sigma|F_o|$. $^bR_w = [\Sigma w (F_o^2 - F_c^2)^2/\Sigma w (F_o^2)^2]^{1/2}$. ^{c}Low data quality.

Table 7-9. Crystallographic parameters for [**3**]SbF_6 and [**3**]CF_3BF_3[a]

Compound	[**3**]SbF_6		[**3**]CF_3BF_3		
Phase	I (90 K)	II (293 K)	I (90 K)	II (223 K)	IV (248 K)
Crystal system	Orthorhombic *P*	Tetragonal *I*	Orthorhombic *I*	Tetragonal *I*	Tetragonal *I*
a [Å]	22.354(11)	8.0673(11)	7.471(8)	7.3482(19)	7.919(7)
b [Å]	26.270(13)	8.0673(11)	8.066(9)	7.3482(19)	7.919(7)
c [Å]	11.360(6)	13.9077(19)	13.853(15)	13.973(4)	14.296(13)
V [$Å^3$]	6671(6)	905.4(3)	834.8(16)	885.9(6)	896.5(18)
Z	16	2	2	2	2

[a] Structures could not be fully refined.

REFERENCES

1 M. Armand, F. Endres, D. R. MacFarlane, H. Ohno and B. Scrosati, *Nat. Mater.*, 2009, **8**, 621–629.

2 T. Welton, *Chem. Rev.*, 1999, **99**, 2071–2084.

3 Z. Lei, C. Dai and B. Chen, *Chem. Rev.*, 2014, **114**, 1289–1326.

4 R. Hagiwara and J. S. Lee, *Electrochemistry*, 2007, **75**, 23–34.

5 H. Ohno, Ed., *Ionic Liquid II —Marvelous Developments and Colorful Near Future—*, CMC Publishing, 2006.

6 M. Kar, K. Matuszek and D. R. MacFarlane, *Ionic Liquids in Kirk-Othmer Encyclopedia of Chemical Technology*, John Wiley & Sons, Inc., Hoboken, 2019.

7 N. R. Brooks, S. Schaltin, K. Van Hecke, L. Van Meervelt, K. Binnemans and J. Fransaer, *Chem. – Eur. J.*, 2011, **17**, 5054–5059.

8 M. Iida, C. Baba, M. Inoue, H. Yoshida, E. Taguchi and H. Furusho, *Chem. – Eur. J.*, 2008, **14**, 5047–5056.

9 P. Zhang, Y. Gong, Y. Lv, Y. Guo, Y. Wang, C. Wang and H. Li, *Chem. Commun.*, 2012, **48**, 2334–2336.

10 S. A. Pierson, O. Nacham, K. D. Clark, H. Nan, Y. Mudryk and J. L. Anderson, *New J. Chem.*, 2017, **41**, 5498–5505.

11 Y. Yoshida and G. Saito, in *Ionic Liquids: Theory, Properties, New Approaches*, IntechOpen, London, England, 2011.

12 I. J. B. Lin and C. S. Vasam, *J. Organomet. Chem.*, 2005, **690**, 3498–3512.

13 T. J. Geldbach and P. J. Dyson, *J. Am. Chem. Soc.*, 2004, **126**, 8114–8115.

14 W. Wang, R. Balasubramanian and R. W. Murray, *J. Phys. Chem. C*, 2008, **112**, 18207–18216.

15 Y. Gao, B. Twamley and J. M. Shreeve, *Inorg. Chem.*, 2004, **43**, 3406–3412.

16 Y. Yoshida, A. Otsuka, G. Saito, S. Natsume, E. Nishibori, M. Takata, M. Sakata, M.

Takahashi and T. Yoko, *Bull. Chem. Soc. Jpn.*, 2005, **78**, 1921–1928.

17 S.-Y. Cho and T. Mochida, *Chem. Lett.*, 2021, **50**, 1740–1742.

18 M. Okuhata, Y. Funasako, K. Takahashi and T. Mochida, *Chem. Commun.*, 2013, **49**, 7662–7664.

19 T. Tominaga and T. Mochida, *Chem. – Eur. J.*, 2018, **24**, 6239–6247.

20 Y. Funasako, T. Mochida, K. Takahashi, T. Sakurai and H. Ohta, *Chem. – Eur. J.*, 2012, **18**, 11929–11936.

21 B. M. Trost and C. M. Older, *Organometallics*, 2002, **21**, 2544–2546.

22 T. P. Gill and K. R. Mann, *Organometallics*, 1982, **1**, 485–488.

23 Y. Funasako, S. Mori and T. Mochida, *Chem. Commun.*, 2016, **52**, 6277–6279.

24 T. Ueda, T. Tominaga, T. Mochida, K. Takahashi and S. Kimura, *Chem. – Eur. J.*, 2018, **24**, 9490–9493.

25 K. Nobuoka, S. Kitaoka, T. Yamauchi, T. Harran and Y. Ishikawa, *Chem. Lett.*, 2016, **45**, 433–435.

26 J. Yang, H. Wang, J. Wang, Y. Zhang and Z. Guo, *Chem. Commun.*, 2014, **50**, 14979–14982.

27 H. Tamura, Y. Shinohara and T. Arai, *Chem. Lett.*, 2011, **40**, 129–131.

28 L. C. Branco and F. Pina, *Chem. Commun.*, 2009, 6204–6206.

29 S. Zhang, S. Liu, Q. Zhang and Y. Deng, *Chem. Commun.*, 2011, **47**, 6641–6643.

30 Z. Li, X. Yuan, Y. Feng, Y. Chen, Y. Zhao, H. Wang, Q. Xu and J. Wang, *Phys. Chem. Chem. Phys.*, 2018, **20**, 12808–12816.

31 H. Qiu, S. Jiang, M. Takafuji and H. Ihara, *Chem. Commun.*, 2013, **49**, 2454–2456.

32 K. Ishiba, M. Morikawa, C. Chikara, T. Yamada, K. Iwase, M. Kawakita and N. Kimizuka, *Angew. Chem. Int. Ed.*, 2015, **54**, 1532–1536.

33 Y. Funasako, H. Okada and M. Inokuchi, *ChemPhotoChem*, 2019, **3**, 28–30.

34 N. Jordão, P. Ferreira, H. Cruz, A. J. Parola and L. C. Branco, *ChemPhotoChem*, 2019, **3**,

525–528.

35 A. Goulet-Hanssens, F. Eisenreich and S. Hecht, *Adv. Mater.*, 2020, **32**, 1905966.

36 D. Chen and Q. Pei, *Chem. Rev.*, 2017, **117**, 11239–11268.

37 N. Zheng, Y. Xu, Q. Zhao and T. Xie, *Chem. Rev.*, 2021, **121**, 1716–1745.

38 A. Bagheri and J. Jin, *ACS Appl. Polym. Mater.*, 2019, **1**, 593–611.

39 N. Moszner and T. Hirt, *J. Polym. Sci. A Polym. Chem.*, 2012, **50**, 4369–4402.

40 P. Strasser, U. Monkowius and I. Teasdale, *Polymer*, 2022, **246**, 124737.

41 T. Wolff and C.-S. Emming, *J. Phys. Chem.*, 1989, **93**, 4894–4898.

42 W.-C. Xu, S. Sun and S. Wu, *Angew. Chem. Int. Ed.*, 2019, **58**, 9712–9740.

43 E. Borré, S. Bellemin-Laponnaz and M. Mauro, *Chem. – Eur. J.*, 2016, **22**, 18718–18721.

44 Y. Yue, Y. Norikane, R. Azumi and E. Koyama, *Nat. Commun.*, 2018, **9**, 3234.

45 S. Mura, J. Nicolas and P. Couvreur, *Nat. Mater.*, 2013, **12**, 991–1003.

46 J. Eastoe, M. Sanchez-Dominguez, H. Cumber, G. Burnett, P. Wyatt and R. K. Heenan, *Langmuir*, 2003, **19**, 6579–6581.

47 J. V. Accardo and J. A. Kalow, *Chem. Sci.*, 2018, **9**, 5987–5993.

48 H. Zhou, M. Chen, Y. Liu and S. Wu, *Macromol. Rapid Commun.*, 2018, **39**, 1800372.

49 I. Teasdale, S. Theis, A. Iturmendi, M. Strobel, S. Hild, J. Jacak, P. Mayrhofer and U. Monkowius, *Chem. – Eur. J.*, 2019, **25**, 9851–9855.

50 E. R. Draper and D. J. Adams, *Chem. – Eur. J.*, 2017, **3**, 390–410.

51 E. R. Draper and D. J. Adams, *Chem. Commun.* , 2016, **52**, 8196–8206.

52 T. Muraoka, C.-Y. Koh, H. Cui and S. I. Stupp, *Angew. Chem. Int. Ed.*, 2009, **48**, 5946–5949.

53 Q. Shen, L. Wang, S. Liu, Y. Cao, L. Gan, X. Guo, M. L. Steigerwald, Z. Shuai, Z. Liu and C. Nuckolls, *Adv. Mater.*, 2010, **22**, 3282–3287.

54 K. Müller, J. Helfferich, F. Zhao, R. Verma, A. B. Kanj, V. Meded, D. Bléger, W. Wenzel and L. Heinke, *Adv. Mater.*, 2018, **30**, 1706551.

55 I. Decker, J.-P. Petit and D. Delabouglise, *Chem. Commun.*, 1997, 833–834.

56 H. Tokuhisa, M. Yokoyama and K. Kimura, *J. Mater. Chem.*, 1998, **8**, 889–891.

57 T.-T.-T. Nguyen, D. Türp, M. Wagner and K. Müllen, *Angew. Chem. Int. Ed.*, 2013, **52**, 669–673.

58 T. Kawai, T. Kunitake and M. Irie, *Chem. Lett.*, 1999, **28**, 905–906.

59 M. Ikeda, N. Tanifuji, H. Yamaguchi, M. Irie and K. Matsuda, *Chem. Commun.*, 2007, 1355–1357.

60 Y.-L. Lin, Y.-H. Tseng, J.-H. Ho, Y.-F. Chen and J.-T. Chen, *Chem. – Eur. J.*, 2021, **27**, 14981–14988.

61 N. Kobayashi, S. Sato, K. Takazawa, K. Ikeda and R. Hirohashi, *Electrochim. Acta*, 1995, **40**, 2309–2311.

62 Y. Kohno, D. L. Gin, R. D. Noble and H. Ohno, *Chem. Commun.*, 2016, **52**, 7497–7500.

63 H. Ohno, M. Yoshizawa and W. Ogihara, *Electrochim. Acta*, 2004, **50**, 255–261.

64 M. Yoshizawa, W. Ogihara and H. Ohno, *Polym. Adv. Technol.*, 2002, **13**, 589–594.

65 S. Washiro, M. Yoshizawa, H. Nakajima and H. Ohno, *Polymer*, 2004, **45**, 1577–1582.

66 K. Hanabusa, H. Fukui, M. Suzuki and H. Shirai, *Langmuir*, 2005, **21**, 10383–10390.

67 J. Le Bideau, L. Viau and A. Vioux, *Chem. Soc. Rev.*, 2011, **40**, 907–925.

68 N. Chen, H. Zhang, L. Li, R. Chen and S. Guo, *Adv. Energy Mater.*, 2018, **8**, 1702675.

69 K. Zhao, H. Song, X. Duan, Z. Wang, J. Liu and X. Ba, *Polymers*, 2019, **11**, 444.

70 E. Kamio, M. Minakata, Y. Iida, T. Yasui, A. Matsuoka and H. Matsuyama, *Polym. J.*, 2020, **53**, 137–147.

71 H. Nie, N. S. Schauser, N. D. Dolinski, J. Hu, C. J. Hawker, R. A. Segalman and J. Read de Alaniz, *Angew. Chem. Int. Ed.*, 2020, **59**, 5123–5128.

72 H. Nie, N. S. Schauser, N. D. Dolinski, Z. Geng, S. Oh, M. L. Chabinyc, C. J. Hawker, R. A. Segalman and J. Read de Alaniz, *Polym. Chem.*, 2021, **12**, 719–724.

73 A. Wu, F. Lu, M. Zhao, N. Sun, L. Shi and L. Zheng, *ChemistrySelect*, 2017, **2**, 1878–

1884.

74 H. Wang, C. N. Zhu, H. Zeng, X. Ji, T. Xie, X. Yan, Z. L. Wu and F. Huang, *Adv. Mater.*, 2019, **31**, 1807328.

75 F. Benito-Lopez, R. Byrne, A. M. Răduţă, N. E. Vrana, G. McGuinness and D. Diamond, *Lab Chip*, 2010, **10**, 195–201.

76 A. Saruwatari, R. Tamate, H. Kokubo and M. Watanabe, *Chem. Commun.*, 2018, **54**, 13371–13374.

77 T. Ueki, R. Usui, Y. Kitazawa, T. P. Lodge and M. Watanabe, *Macromolecules*, 2015, **48**, 5928–5933.

78 C. Wang, K. Hashimoto, R. Tamate, H. Kokubo and M. Watanabe, *Angew. Chem. Int. Ed.*, 2018, **57**, 227–230.

79 C. Wang, K. Hashimoto, R. Tamate, H. Kokubo, K. Morishima, X. Li, M. Shibayama, F. Lu, T. Nakanishi and M. Watanabe, *Chem. Commun.*, 2019, **55**, 1710–1713.

80 Z. Cao, H. Liu and L. Jiang, *ACS Appl. Polym. Mater.*, 2020, **2**, 2359–2365.

81 T. Takahashi, *High Conductivity Solid Ionic Conductors: Recent Trends and Applications*, World Scientific, Singapore, 1989.

82 V. Di Noto, S. Lavina, G. A. Giffin, E. Negro and B. Scrosati, *Electrochim. Acta*, 2011, **57**, 4–13.

83 S. Ohkoshi, K. Nakagawa, K. Imoto, H. Tokoro, Y. Shibata, K. Okamoto, Y. Miyamoto, M. Komine, M. Yoshikiyo and A. Namai, *Nat. Chem.*, 2020, **12**, 338–344.

84 H. Mochizuki, Y. Nabeshima, T. Kitsunai, A. Kanazawa, T. Shiono, T. Ikeda, T. Hiyama, T. Maruyama, T. Yamamoto and N. Koide, *J. Mater. Chem.*, 1999, **9**, 2215–2219.

85 T. Inagaki, T. Mochida, M. Takahashi, C. Kanadani, T. Saito and D. Kuwahara, *Chem. – Eur. J.*, 2012, **18**, 6795–6804.

86 A. Komurasaki, Y. Funasako and T. Mochida, *Dalton Trans.*, 2015, **44**, 7595–7605.

87 W. Xu, E. I. Cooper and C. A. Angell, *J. Phys. Chem. B*, 2003, **107**, 6170–6178.

88 D. R. MacFarlane, M. Forsyth, E. I. Izgorodina, A. P. Abbott, G. Annat and K. Fraser, *Phys. Chem. Chem. Phys.*, 2009, **11**, 4962–4967.

89 R. J. Wojtecki, M. A. Meador and S. J. Rowan, *Nat. Mater.*, 2011, **10**, 14–27.

90 J. Kida, D. Aoki and H. Otsuka, *ACS Macro Lett.*, 2019, **8**, 1–6.

91 G. Pouliquen, C. Amiel and C. Tribet, *J. Phys. Chem. B*, 2007, **111**, 5587–5595.

92 I. Tomatsu, A. Hashidzume and A. Harada, *Macromolecules*, 2005, **38**, 5223–5227.

93 S. Hisamitsu, N. Yanai, S. Fujikawa and N. Kimizuka, *Chem. Lett.*, 2015, **44**, 908–910.

94 T. Yamamoto, Y. Norikane and H. Akiyama, *Polym. J.*, 2018, **50**, 551–562.

95 O. Yamamuro, Y. Minamimoto, Y. Inamura, S. Hayashi and H. Hamaguchi, *Chem. Phys. Lett.*, 2006, **423**, 371–375.

96 T. Tominaga, T. Ueda and T. Mochida, *Phys. Chem. Chem. Phys.*, 2017, **19**, 4352–4359.

97 T. Ueda and T. Mochida, *Organometallics*, 2015, **34**, 1279–1286.

98 R. Fan, R. Sumitani and T. Mochida, *ACS Omega*, 2020, **5**, 2034–2040.

99 W. A. Henderson, M. Herstedt, V. G. Young, S. Passerini, H. C. De Long and P. C. Trulove, *Inorg. Chem.*, 2006, **45**, 1412–1414.

100 K. Matsumoto, T. Oka, T. Nohira and R. Hagiwara, *Inorg. Chem.*, 2013, **52**, 568–576.

101 I. A. Shkrob, T. W. Marin, Y. Zhu and D. P. Abraham, *J. Phys. Chem. C*, 2014, **118**, 19661–19671.

102 T. Mochida, Y. Funasako, T. Inagaki, M.-J. Li, K. Asahara and D. Kuwahara, *Chem. – Eur. J.*, 2013, **19**, 6257–6264.

103 T. Mochida, Y. Funasako, M. Ishida, S. Saruta, T. Kosone and T. Kitazawa, *Chem. – Eur. J.*, 2016, **22**, 15725–15732.

104 D. Zhao, Z. Fei, R. Scopelliti and P. J. Dyson, *Inorg. Chem.*, 2004, **43**, 2197–2205.

105 Z. Fei, D. Zhao, D. Pieraccini, W. H. Ang, T. J. Geldbach, R. Scopelliti, C. Chiappe and P. J. Dyson, *Organometallics*, 2007, **26**, 1588–1598.

106 J. Neumann, B. Golub, L.-M. Odebrecht, R. Ludwig and D. Paschek, *J. Chem. Phys.*,

2018, **148**, 193828.

107 T. Higashi, T. Ueda and T. Mochida, *Phys. Chem. Chem. Phys.*, 2016, **18**, 10041–10048.

108 R. Sumitani, Y. Funasako and T. Mochida, *J. Mol. Liq.*, 2020, **318**, 114071.

109 D. B. Williams, M. E. Stoll, B. L. Scott, D. A. Costa and W. J. Oldham Jr, *Chem. Commun.*, 2005, 1438–1440.

110 J. A. Widegren, E. M. Saurer, K. N. Marsh and J. W. Magee, *J. Chem. Thermodyn.*, 2005, **37**, 569–575.

111 H. Vogel, *Phys. Z.*, 1921, **22**, 645–646.

112 G. S. Fulcher, *J. Am. Ceram. Soc.*, 1925, **8**, 339–355.

113 G. Tammann and W. Hesse, *Z. Anorg. Chem.*, 1926, **156**, 245–257.

114 M. Petrowsky and R. Frech, *J. Phys. Chem. B*, 2010, **114**, 8600–8605.

115 H. Every, A. G. Bishop, M. Forsyth and D. R. MacFarlane, *Electrochim. Acta*, 2000, **45**, 1279–1284.

116 H. Leicht, I. Göttker-Schnetmann and S. Mecking, *J. Am. Chem. Soc.*, 2017, **139**, 6823–6826.

117 G. M. Sheldrick, *Acta Crystallogr. Sect. A*, 2008, **64**, 112–122.

118 A. L. Spek, *Acta Crystallogr. Sect. D*, 2009, **65**, 148–155.

119 N. Roy, B. Bruchmann and J.-M. Lehn, *Chem. Soc. Rev.*, 2015, **44**, 3786–3807.

120 T. Maeda, H. Otsuka and A. Takahara, *Prog. Polym. Sci.*, 2009, **34**, 581–604.

121 P. Chakma and D. Konkolewicz, *Angew. Chem. Int. Ed.*, 2019, **58**, 9682–9695.

122 A. J. R. Amaral and G. Pasparakis, *Polym. Chem.*, 2017, **8**, 6464–6484.

123 C. Zhu, C. Ninh and C. J. Bettinger, *Biomacromolecules*, 2014, **15**, 3474–3494.

124 C.-H. Li, C. Wang, C. Keplinger, J.-L. Zuo, L. Jin, Y. Sun, P. Zheng, Y. Cao, F. Lissel, C. Linder, X.-Z. You and Z. Bao, *Nat. Chem.*, 2016, **8**, 618–624.

125 S. Theis, A. Iturmendi, C. Gorsche, M. Orthofer, M. Lunzer, S. Baudis, A. Ovsianikov, R. Liska, U. Monkowius and I. Teasdale, *Angew. Chem. Int. Ed.*, 2017, **56**, 15857–15860.

126 M. Burnworth, L. Tang, J. R. Kumpfer, A. J. Duncan, F. L. Beyer, G. L. Fiore, S. J. Rowan and C. Weder, *Nature*, 2011, **472**, 334–337.

127 D. W. R. Balkenende, S. Coulibaly, S. Balog, Y. C. Simon, G. L. Fiore and C. Weder, *J. Am. Chem. Soc.*, 2014, **136**, 10493–10498.

128 Y. S. Kim, R. Tamate, A. M. Akimoto and R. Yoshida, *Mater. Horiz.*, 2017, **4**, 38–54.

129 A. Winter and U. S. Schubert, *Chem. Soc. Rev.*, 2016, **45**, 5311–5357.

130 K. Naskar, A. Dey, S. Maity, P. P. Ray, P. Ghosh and C. Sinha, *Inorg. Chem.*, 2020, **59**, 5518–5528.

131 S. R. Batten, N. R. Champness, X.-M. Chen, J. Garcia-Martinez, S. Kitagawa, L. Öhrström, M. O'Keeffe, M. P. Suh and J. Reedijk, *CrystEngComm*, 2012, **14**, 3001–3004.

132 R. Sumitani, H. Yoshikawa and T. Mochida, *Chem. Commun.*, 2020, **56**, 6189–6192.

133 R. Sumitani and T. Mochida, *Macromolecules*, 2020, **53**, 6968–6974.

134 B. Dietrich, M. W. Hosseini, J.-M. Lehn and R. B. Sessions, *Helv. Chim. Acta*, 1985, **68**, 289–299.

135 E. Badea, I. Blanco and G. Della Gatta, *J. Chem. Thermodyn.*, 2007, **39**, 1392–1398.

136 Y. Wang, K. Zaghib, A. Guerfi, F. F. C. Bazito, R. M. Torresi and J. R. Dahn, *Electrochim. Acta*, 2007, **52**, 6346–6352.

137 W. P. Cox and E. H. Merz, *J. Polym. Sci.*, 1958, **28**, 619–622.

138 M. Galiński, A. Lewandowski and I. Stępniak, *Electrochim. Acta*, 2006, **51**, 5567–5580.

139 H. Tokuda, K. Hayamizu, K. Ishii, M. A. B. H. Susan and M. Watanabe, *J. Phys. Chem. B*, 2005, **109**, 6103–6110.

140 J. Rodrigues, M. G. Jardim, J. Figueira, M. Gouveia, H. Tomás and K. Rissanen, *New J Chem*, 2011, **35**, 1938–1943.

141 A. S. Shaplov, R. Marcilla and D. Mecerreyes, *Electrochim. Acta*, 2015, **175**, 18–34.

142 J. Yuan, D. Mecerreyes and M. Antonietti, *Prog. Polym. Sci.*, 2013, **38**, 1009–1036.

143 J. Yuan and M. Antonietti, *Polymer*, 2011, **52**, 1469–1482.

144 D. Mecerreyes, *Prog. Polym. Sci.*, 2011, **36**, 1629–1648.

145 L. Brunsveld, B. J. Folmer, E. W. Meijer and R. P. Sijbesma, *Chem. Rev.*, 2001, **101**, 4071–4098.

146 M. A. Haque, T. Kurokawa and J. P. Gong, *Polymer*, 2012, **53**, 1805–1822.

147 Y. Liu, H. H. Winter and S. L. Perry, *Adv. Colloid Interface Sci.*, 2017, **239**, 46–60.

148 L.-E. Chile, P. Mehrkhodavandi and S. G. Hatzikiriakos, *J. Rheol.*, 2017, **61**, 1137–1148.

149 Q. Chen, N. Bao, J.-H. H. Wang, T. Tunic, S. Liang and R. H. Colby, *Macromolecules*, 2015, **48**, 8240–8252.

150 A. S. Shaplov, E. I. Lozinskaya, D. O. Ponkratov, I. A. Malyshkina, F. Vidal, P.-H. Aubert, O. V. Okatova, G. M. Pavlov, L. I. Komarova, C. Wandrey and Y. S. Vygodskii, *Electrochim. Acta*, 2011, **57**, 74–90.

151 H. T. Ho, M. Rollet, T. N. T. Phan and D. Gigmes, *Eur. Polym. J.*, 2018, **107**, 74–81.

152 D.-Z. Zhang, Y.-Y. Ren, Y. Hu, L. Li and F. Yan, *Chin. J. Polym. Sci.*, 2020, **38**, 506–513.

153 A. Vioux, L. Viau, S. Volland and J. Le Bideau, *C. R. Chim.*, 2010, **13**, 242–255.

154 N. Kimizuka and T. Nakashima, *Langmuir*, 2001, **17**, 6759–6761.

155 T. Tu, X. Bao, W. Assenmacher, H. Peterlik, J. Daniels and K. H. Dötz, *Chem. – Eur. J.*, 2009, **15**, 1853–1861.

156 S. Dutta, D. Das, A. Dasgupta and P. K. Das, *Chem. – Eur. J.*, 2010, **16**, 1493–1505.

157 N. Minakuchi, K. Hoe, D. Yamaki, S. Ten-no, K. Nakashima, M. Goto, M. Mizuhata and T. Maruyama, *Langmuir*, 2012, **28**, 9259–9266.

158 Y. Ishioka, N. Minakuchi, M. Mizuhata and T. Maruyama, *Soft Matter*, 2014, **10**, 965–971.

159 D. Li, F. Shi, S. Guo and Y. Deng, *Tetrahedron Lett.*, 2004, **45**, 265–268.

160 M.-A. Néouze, J. Le Bideau, P. Gaveau, S. Bellayer and A. Vioux, *Chem. Mater.*, 2006, **18**, 3931–3936.

161 A. Noro, S. Matsushima, X. He, M. Hayashi and Y. Matsushita, *Macromolecules*, 2013,

46, 8304–8310.

162 G. Sinawang, Y. Kobayashi, Y. Zheng, Y. Takashima, A. Harada and H. Yamaguchi, *Macromolecules*, 2019, **52**, 2932–2938.

163 P. Snedden, A. I. Cooper, K. Scott and N. Winterton, *Macromolecules*, 2003, **36**, 4549–4556.

164 M. A. Klingshirn, S. K. Spear, R. Subramanian, J. D. Holbrey, J. G. Huddleston and R. D. Rogers, *Chem. Mater.*, 2004, **16**, 3091–3097.

165 H. Y. Lee, Y. Cai, S. Velioglu, C. Mu, C. J. Chang, Y. L. Chen, Y. Song, J. W. Chew and X. M. Hu, *Chem. Mater.*, 2017, **29**, 6947–6955.

166 F. Benito-Lopez, M. Antoñana-Díez, V. F. Curto, D. Diamond and V. Castro-López, *Lab Chip*, 2014, **14**, 3530–3538.

167 N. Gil-González, T. Akyazi, E. Castaño, F. Benito-Lopez and M. C. Morant-Miñana, *Sens. Actuators B Chem.*, 2018, **260**, 380–387.

168 Y.-D. Zhang, X.-H. Fan, Z. Shen and Q.-F. Zhou, *Macromolecules*, 2015, **48**, 4927–4935.

169 C. C. Hall, C. Zhou, S. P. O. Danielsen and T. P. Lodge, *Macromolecules*, 2016, **49**, 2298–2306.

170 F. Yang, D. Wu, Z. Luo, B. Tan and Z. Xie, *Sens. Actuators B Chem.*, 2017, **249**, 486–492.

171 Z.-L. Xie, X. Huang and A. Taubert, *Adv. Funct. Mater.*, 2014, **24**, 2837–2843.

172 A. Kavanagh, R. Byrne, D. Diamond and A. Radu, *Analyst*, 2011, **136**, 348–353.

173 T. Ueki, Y. Nakamura, R. Usui, Y. Kitazawa, S. So, T. P. Lodge and M. Watanabe, *Angew. Chem. Int. Ed.*, 2015, **54**, 3018–3022.

174 M. Czugala, C. O'Connell, C. Blin, P. Fischer, K. J. Fraser, F. Benito-Lopez and D. Diamond, *Sens. Actuators B Chem.*, 2014, **194**, 105–113.

175 M. Tamada, T. Watanabe, K. Horie and H. Ohno, *Chem. Commun.*, 2007, 4050–4052.

176 C. Wang, W. Dong, P. Li, Y. Wang, H. Tu, S. Tan, Y. Wu and M. Watanabe, *ACS Appl.*

Mater. Interfaces, 2020, **12**, 42202–42209.

177 T. Ueki, R. Usui, Y. Kitazawa, T. P. Lodge and M. Watanabe, *Macromolecules*, 2015, **48**, 6750–6750.

178 W. Jiang, J. Hao and Z. Wu, *Langmuir*, 2008, **24**, 3150–3156.

179 Z.-L. Xie, A. Jeličić, F.-P. Wang, P. Rabu, A. Friedrich, S. Beuermann and A. Taubert, *J. Mater. Chem.*, 2010, **20**, 9543.

180 N. E. Hughes, A. G. Marangoni, A. J. Wright, M. A. Rogers and J. W. E. Rush, *Trends Food Sci. Technol.*, 2009, **20**, 470–480.

181 B. A. Voss, J. E. Bara, D. L. Gin and R. D. Noble, *Chem. Mater.*, 2009, **21**, 3027–3029.

182 H. Takeno, A. Maehara, M. Kuchiishi, K. Yoshiba, H. Takeshita, S. Kondo, T. Dobashi, M. Takenaka and H. Hasegawa, *Sen'i Gakkaishi*, 2012, **68**, 248–252.

183 H. Takeno and M. Kozuka, *Adv. Mater. Sci. Eng.*, 2017, **2017**, 1–8.

184 N. Matsumi, Y. Nakamura, K. Aoi, T. Watanabe, T. Mizumo and H. Ohno, *Polym. J.*, 2009, **41**, 437–441.

185 J. Vila, P. Ginés, J. M. Pico, C. Franjo, E. Jiménez, L. M. Varela and O. Cabeza, *Fluid Phase Equilibria*, 2006, **242**, 141–146.

186 D. S. Ashby, R. H. DeBlock, C.-H. Lai, C. S. Choi and B. S. Dunn, *Joule*, 2017, **1**, 344–358.

187 P. Terech and R. G. Weiss, *Chem. Rev.*, 1997, **97**, 3133–3160.

188 S. S. Babu, V. K. Praveen and A. Ajayaghosh, *Chem. Rev.*, 2014, **114**, 1973–2129.

189 P. Dastidar, *Chem. Soc. Rev.*, 2008, **37**, 2699–2715.

190 M. de Loos, B. L. Feringa and J. H. van Esch, *European J. Org. Chem.*, 2005, **2005**, 3615–3631.

191 N. Thakur, B. Sharma, S. Bishnoi, S. K. Mishra, D. Nayak, A. Kumar and T. K. Sarma, *ACS Sustainable Chem. Eng.*, 2018, **6**, 8659–8671.

192 Y. Nishida, A. Tanaka, S. Yamamoto, Y. Tominaga, N. Kunikata, M. Mizuhata and T.

Maruyama, *Angew. Chem. Int. Ed.*, 2017, **56**, 9410–9414.

193 H. Sawalha, R. den Adel, P. Venema, A. Bot, E. Flöter and E. van der Linden, *J. Agric. Food Chem.*, 2012, **60**, 3462–3470.

194 S. Ray, A. K. Das and A. Banerjee, *Chem. Mater.*, 2007, **19**, 1633–1639.

195 B. Adhikari, G. Palui and A. Banerjee, *Soft Matter*, 2009, **5**, 3452–3460.

196 M. O. Guler and S. I. Stupp, *J. Am. Chem. Soc.*, 2007, **129**, 12082–12083.

197 N. Singh, M. Tena-Solsona, J. F. Miravet and B. Escuder, *Isr. J. Chem.*, 2015, **55**, 711–723.

198 T. Tu, W. Assenmacher, H. Peterlik, R. Weisbarth, M. Nieger and K. H. Dötz, *Angew. Chem. Int. Ed.*, 2007, **46**, 6368–6371.

199 Z. Li, Y. Zhou, T. Li, J. Zhang and H. Tian, *VIEW*, 2021, 20200112.

200 K. J. Skilling, F. Citossi, T. D. Bradshaw, M. Ashford, B. Kellam and M. Marlow, *Soft Matter*, 2014, **10**, 237–256.

201 R. Ochi, T. Nishida, M. Ikeda and I. Hamachi, *J. Mater. Chem. B*, 2014, **2**, 1464–1469.

202 M. Ikeda, R. Ochi, Y.-S. Kurita, D. J. Pochan and I. Hamachi, *Chem. – Eur. J.*, 2012, **18**, 13091–13096.

203 S.-L. Zhou, S. Matsumoto, H.-D. Tian, H. Yamane, A. Ojida, S. Kiyonaka and I. Hamachi, *Chem. – Eur. J.*, 2005, **11**, 1130–1136.

204 Q. Chen, D. Zhang, G. Zhang and D. Zhu, *Langmuir*, 2009, **25**, 11436–11441.

205 Q. Chen, Y. Lv, D. Zhang, G. Zhang, C. Liu and D. Zhu, *Langmuir*, 2010, **26**, 3165–3168.

206 J. Gao, J. Zhan and Z. Yang, *Adv. Mater.*, 2020, **32**, 1805798.

207 H. He, W. Tan, J. Guo, M. Yi, A. N. Shy and B. Xu, *Chem. Rev.*, 2020, **120**, 9994–10078.

208 I. Tomatsu, K. Peng and A. Kros, *Adv. Drug Deliv. Rev.*, 2011, **63**, 1257–1266.

209 W. Fang, X. Liu, Z. Lu and T. Tu, *Chem. Commun.*, 2014, **50**, 3313–3316.

210 X. Zheng, Q. Miao, W. Wang and D.-H. Qu, *Chin. Chem. Lett.*, 2018, **29**, 1621–1624.

211 P. J. Jervis, L. Hilliou, R. B. Pereira, D. M. Pereira, J. A. Martins and P. M. T. Ferreira,

Nanomaterials, 2021, **11**, 704.

212 D. Koda, T. Maruyama, N. Minakuchi, K. Nakashima and M. Goto, *Chem. Commun.*, 2010, **46**, 979–981.

213 A. Tanaka, Y. Fukuoka, Y. Morimoto, T. Honjo, D. Koda, M. Goto and T. Maruyama, *J. Am. Chem. Soc.*, 2015, **137**, 770–775.

214 Z. Yang, G. Liang and B. Xu, *Acc. Chem. Res.*, 2008, **41**, 315–326.

215 Z. Yang, G. Liang, L. Wang and B. Xu, *J. Am. Chem. Soc.*, 2006, **128**, 3038–3043.

216 X. Liu, B. He, Z. Wang, H. Tang, T. Su and Q. Wang, *Sci. Rep.*, 2014, **4**, 6673.

217 H. Mizuno, K. Hashimoto, K. Shigenobu, H. Kokubo, K. Ueno and M. Watanabe, *Macromol. Rapid Commun.*, 2021, **42**, 2100091.

218 L. Wang, X. Ma, L. Wu, Y. Sha, B. Yu, X. Lan, Y. Luo, Y. Shi, Y. Wang and Z. Luo, *Eur. Polym. J.*, 2021, **144**, 110213.

219 R. Tamate, R. Usui, K. Hashimoto, Y. Kitazawa, H. Kokubo and M. Watanabe, *Soft Matter*, 2018, **14**, 9088–9095.

220 X. Ma, R. Usui, Y. Kitazawa, R. Tamate, H. Kokubo and M. Watanabe, *Macromolecules*, 2017, **50**, 6788–6795.

221 T. Komiyama, Y. Harada, T. Hase, S. Mori, S. Kimura, M. Yokoya and M. Yamanaka, *Chem. –Asian J.*, 2021, **16**, 1750–1755.

222 M. Yamanaka and N. Miyachi, WIPO, 2017/099232 Al, *Patent*.

223 F. Piana, D. H. Case, S. M. Ramalhete, G. Pileio, M. Facciotti, G. M. Day, Y. Z. Khimyak, J. Angulo, R. C. D. Brown and P. A. Gale, *Soft Matter*, 2016, **12**, 4034–4043.

224 T. Küppers, E. Bernhardt, H. Willner, H. W. Rohm and M. Köckerling, *Inorg. Chem.*, 2005, **44**, 1015–1022.

225 D. Zhao, Z. Fei, T. J. Geldbach, R. Scopelliti and P. J. Dyson, *J. Am. Chem. Soc.*, 2004, **126**, 15876–15882.

226 S. M. Mahurin, P. C. Hillesheim, J. S. Yeary, D.-E. Jiang and S. Dai, *RSC Adv.*, 2012, **2**,

11813–11819.

227 N. Amiri, H. Benyounes, Z. Lounis and W. Shen, *Chem. Eng. Res. Des.*, 2021, **169**, 239–249.

228 X. Zhang, X. Feng, H. Li, J. Peng, Y. Wu and X. Hu, *Ind. Eng. Chem. Res.*, 2016, **55**, 11012–11021.

229 D. Ghosh, M. T. Mulvee and K. K. Damodaran, *Molecules*, 2019, **24**, 3472.

230 M. Sun, H. Sun, Y. Wang, M. Sánchez-Soto and D. A. Schiraldi, *Gels*, 2018, **4**, 33.

231 O. Kuzmina, N. H. Hassan, L. Patel, C. Ashworth, E. Bakis, A. J. P. White, P. A. Hunt and T. Welton, *Dalton Trans.*, 2017, **46**, 12185–12200.

232 I. Ojima, A. T. Vu and D. Bonafoux, in *Science of Synthesis*, ed. M. Lautens, Thieme Verlag, 2001, pp. 531–616.

233 M. A. Garralda and L. A. Oro, *Transition Met. Chem.*, 1980, **5**, 65–73.

234 J. A. Osborn and R. R. Schrock, *J. Am. Chem. Soc.*, 1971, **93**, 3089–3091.

235 J. Emerson-King, R. C. Knighton, M. R. Gyton and A. B. Chaplin, *Dalton Trans.*, 2017, **46**, 11645–11655.

236 P. A. Wender and T. J. Williams, *Angew. Chem. Int. Ed.*, 2002, **41**, 4550–4553.

237 S. O. Kang, V. M. Lynch, V. W. Day and E. V. Anslyn, *Organometallics*, 2011, **30**, 6233–6240.

238 F. Toda, *Organic Solid State Reactions*, Springer, Berlin Heidelberg, 2005.

239 A. Togni and T. Hayashi, Eds., *Ferrocenes: Homogeneous Catalysis, Organic Synthesis, Materials Science*, Wiley-VCH Verlag, Weinheim, Germany, 1995.

240 P. Stepnicka, Ed., *Ferrocenes: Ligands, Materials and Biomolecules*, Wiley-Blackwell, Hoboken, NJ, 2008.

241 R. J. Webb, M. D. Lowery, Y. Shiomi, M. Sorai, R. J. Wittebort and D. N. Hendrickson, *Inorg. Chem.*, 1992, **31**, 5211–5219.

242 F. Grepioni, G. Cojazzi, S. M. Draper, N. Scully and D. Braga, *Organometallics*, 1998,

17, 296–307.

243 T. Mochida, M. Ishida, T. Tominaga, K. Takahashi, T. Sakurai and H. Ohta, *Phys. Chem. Chem. Phys.*, 2018, **20**, 3019–3028.

244 H. Kimata and T. Mochida, *Cryst. Growth Des.*, 2018, **18**, 7562–7569.

245 J. M. Pringle, *Phys. Chem. Chem. Phys.*, 2013, **15**, 1339–1351.

246 H. Ishida, T. Iwachido, N. Hayama, R. Ikeda, M. Terashima and D. Nakamura, *Z. Naturforsch., A*, 1989, **44**, 741–746.

247 K. Matsumoto, U. Harinaga, R. Tanaka, A. Koyama, R. Hagiwara and K. Tsunashima, *Phys. Chem. Chem. Phys.*, 2014, **16**, 23616–23626.

248 T. Enomoto, S. Kanematsu, K. Tsunashima, K. Matsumoto and R. Hagiwara, *Phys. Chem. Chem. Phys.*, 2011, **13**, 12536–12544.

249 Z.-B. Zhou and H. Matsumoto, *Electrochem. Commun.*, 2007, **9**, 1017–1022.

250 T. Hayasaki, S. Hirakawa and H. Honda, *Bull. Chem. Soc. Jpn.*, 2013, **86**, 993–1001.

251 R. Yunis, T. W. Newbegin, A. F. Hollenkamp and J. M. Pringle, *Mater. Chem. Front.*, 2018, **2**, 1207–1214.

252 D. R. MacFarlane, J. Huang and M. Forsyth, *Nature*, 1999, **402**, 792–794.

253 J. Harada, *APL Mater.*, 2021, **9**, 020901.

254 A. Basile, M. Hilder, F. Makhlooghiazad, C. Pozo-Gonzalo, D. R. MacFarlane, P. C. Howlett and M. Forsyth, *Adv. Energy Mater.*, 2018, **8**, 1703491.

255 H. Zhu, D. R. MacFarlane, J. M. Pringle and M. Forsyth, *Trends Chem.*, 2019, **1**, 126–140.

256 M. Yoshizawa-Fujita, M. Nakazawa, Y. Takeoka and M. Rikukawa, *J. Non-Crystalline Sol. X*, 2022, **13**, 100078.

257 Y. Su, G. Liu, B. Xie, D. Fu and D. Wang, *Acc. Chem. Res.*, 2014, **47**, 192–201.

258 T. Shimizu, S. Tanaka, N. Onoda-Yamamuro, S. Ishimaru and R. Ikeda, *J. Chem. Soc., Faraday Trans.*, 1997, **93**, 321–326.

259 J. M. Pringle, Y. Shekibi, D. R. MacFarlane and M. Forsyth, *Electrochim. Acta*, 2010, **55**, 8847–8854.

260 Y. Yamada, E. Kashimoto and H. Honda, *Bull. Chem. Soc. Jpn.*, 2019, **92**, 1289–1298.

261 M. Green and T. A. Kuc, *J. Chem. Soc., Dalton Trans.*, 1972, 832–839.

262 T. V. RajanBabu, T. A. Ayers, G. A. Halliday, K. K. You and J. C. Calabrese, *J. Org. Chem.*, 1997, **62**, 6012–6028.

263 G. Song, Y. Zhang, Y. Su, W. Deng, K. Han and X. Li, *Organometallics*, 2008, **27**, 6193–6201.

264 O. G. Sas, I. Domínguez, B. González and Á. Domínguez, *J. Environ. Manage.*, 2018, **228**, 475–482.

265 A. S. Weller, M. F. Mahon and J. W. Steed, *J. Organomet. Chem.*, 2000, **614–615**, 113–119.

266 Y. Tang and B. Yu, *Eur. J. Inorg. Chem.*, 2020, **2020**, 107–118.

267 O. G. Polyakov, S. M. Ivanova, C. M. Gaudinski, S. M. Miller, O. P. Anderson and S. H. Strauss, *Organometallics*, 1999, **18**, 3769–3771.

268 M. J. Begley, D. B. Sowerby, R. D. Verma and A. Vig, *J. Organomet. Chem.*, 1994, **481**, 243–246.

269 J. Xiao, Y. Cui, C. Li, H. Xu, Y. Zhai, X. Zhang and S. Ma, *Angew. Chem. Int. Ed.*, 2021, **60**, 25708–25713.

270 M. A. Bowring, R. G. Bergman and T. D. Tilley, *J. Am. Chem. Soc.*, 2013, **135**, 13121–13128.

271 A. C. Sievert and E. L. Muetterties, *Inorg. Chem.*, 1981, **20**, 489–501.

272 B. Guzel, M. A. Omary, J. P. Fackler and A. Akgerman, *Inorganica Chim. Acta*, 2001, **325**, 45–50.

273 M. Green, T. A. Kuc and S. H. Taylor, *J. Chem. Soc. A*, 1971, 2334–2337.

274 D. M. P. Mingos and A. L. Rohl, *J. Chem. Soc., Dalton Trans.*, 1991, 3419–3425.

275 P. Atkins and T. Overton, *Shriver and Atkins' Inorganic Chemistry*, Oxford University Press, New York, 2010.

276 L. Dahlenburg, N. Osthoff and F. W. Heinemann, *Acta Crystallogr. Sect. E*, 2001, **57**, 117–118.

277 N. C. Baenziger, E. A. Mottel and J. R. Doyle, *Acta Crystallogr. Sect. C*, 1991, **47**, 539–541.

278 Y. Kotani and H. Honda, *Bull. Chem. Soc. Jpn.*, 2019, **92**, 768–778.

279 D. M. Rice, R. J. Wittebort, R. G. Griffin, E. Meirovitch, E. R. Stimson, Y. C. Meinwald, J. H. Freed and H. A. Scheraga, *J. Am. Chem. Soc.*, 1981, **103**, 7707–7710.

280 J. W. Emsley, J. C. Lindon and J. Tabony, *Mol. Phys.*, 1973, **26**, 1499–1509.

281 H. Kimata, R. Sumitani and T. Mochida, *Chem. Lett.*, 2019, **48**, 859–862.

282 R. Sumitani and T. Mochida, *J. Mol. Liq.*, 2021, **344**, 117784.

283 B. de Bruin, J. A. Brands, J. J. J. M. Donners, M. P. J. Donners, R. de Gelder, J. M. M. Smits, A. W. Gal and A. L. Spek, *Chem. – Eur. J.*, 1999, **5**, 2921–2936.

284 B. de Bruin, M. J. Boerakker, J. J. J. M. Donners, B. E. C. Christiaans, P. P. J. Schlebos, R. de Gelder, J. M. M. Smits, A. L. Spek and A. W. Gal, *Angew. Chem. Int. Ed.*, 1997, **36**, 2064–2067.

285 D. Braga, L. Maini and F. Grepioni, *Chem. Soc. Rev.*, 2013, **42**, 7638–7648.

286 M. Green, T. A. Kuc and S. H. Taylor, *J. Chem. Soc., Dalton Trans.*, 1970, 1553–1554.

287 A. Tiripicchio, M. T. Camellini, C. Claver, A. Ruiz and L. A. Oro, *J. Organomet. Chem.*, 1983, **241**, 77–86.

288 R. Dorta, H. Rozenberg, L. J. W. Shimon and D. Milstein, *Chem. – Eur. J.*, 2003, **9**, 5237–5249.

289 J. W. Bats, A. Rivas Nass and A. S. K. Hashmi, *Acta Crystallogr. Sect. E*, 2003, **60**, 85–87.

290 T. G. Schenck, J. M. Downes, C. R. C. Milne, P. B. Mackenzie, T. G. Boucher, J. Whelan

and B. Bosnich, *Inorg. Chem.*, 1985, **24**, 2334–2337.

291 K. Shelly, D. C. Finster, Y. J. Lee, W. R. Scheidt and C. A. Reed, *J. Am. Chem. Soc.*, 1985, **107**, 5955–5959.

292 J. H. Davis, K. R. Jeffrey, M. Bloom, M. I. Valic and T. P. Higgs, *Chem. Phys. Lett.*, 1976, **42**, 390–394.

293 *APEX3*, v2015.52; Bruker AXS Inc.: Madison, WI, 2015.

294 C. F. Macrae, I. J. Bruno, J. A. Chisholm, P. R. Edgington, P. McCabe, E. Pidcock, L. Rodriguez-Monge, R. Taylor, J. van de Streek and P. A. Wood, *J. Appl. Crystallogr.*, 2008, **41**, 466–470.

295 Sheldrick, G. M. *TWINABS,* v2012/1; University of Göttingen: 2012.

296 *XPREP*, v2014/2; Bruker AXS Inc.: Madison, WI, 2014.

LIST OF PUBLICATIONS

1* "Reversible Control of Ionic Conductivity and Viscoelasticity of Organometallic Ionic Liquids by Application of Light and Heat"

R. Sumitani, H. Yoshikawa and T. Mochida, *Chem. Commun.* 2020, **56**, 6189–6192.

2* "Metal-Containing Poly(ionic liquid) Exhibiting Photogeneration of Coordination Network: Reversible Control of Viscoelasticity and Ionic Conductivity"

R. Sumitani and T. Mochida, *Macromolecules*, 2020, **53**, 6968–6974.

3* "Thermal Properties and Crystal Structures of Ruthenium-Containing Photoreactive Ionic Liquids with Short Substituents"

R. Sumitani, Y. Funasako and T. Mochida, *J. Mol. Liq.*, 2020, **318**, 114071.

4* "Reversible Formation of Soft Coordination Polymers from Liquid Mixtures of Photoreactive Organometallic Ionic Liquid and Bridging Molecules"

R. Sumitani and T. Mochida, *Soft Matter*, 2020, **16**, 9946–9954.

5* "Switchable Ionic Conductivity and Viscoelasticity of Ionogels Containing Photo- and Thermo-Responsive Organometallic Ionic Liquids"

R. Sumitani and T. Mochida, *J. Mol. Liq.*, 2021, **342**, 117510.

6* "Thermal Properties, Crystal Structures, and Photoreactivity of Ru-Containing Ionic Liquids with Sulfur-Containing Substituents"

R. Sumitani and T. Mochida, *J. Mol. Liq.*, 2021, **344**, 117784.

7* "On-demand Gelation of Ionic Liquids Using Photoresponsive Organometallic Gelators"

R. Sumitani, M. Yamanaka and T. Mochida, *Soft Matter*, 2022, **18**, 3479–3486.

8* "Structures, Thermal Properties, and Reactivities of Cationic Rh–cod Complexes in Solid State (cod = 1,5-cyclooctadiene)"

R. Sumitani, D. Kuwahara and T. Mochida, *Inorg. Chem.*, *in press*.

9 "Phase Transitions and Crystal Structures of Ionic Plastic Crystals Comprising Quaternary Ammonium Cations and Carborane Anion"

H. Kimata, R. Sumitani and T. Mochida, *Chem. Lett.*, 2019, **48**, 859–862.

10 "Synthesis, Crystal Structures, Electrochemical Properties, and Complexation of Ferrocene-based Compounds: 1,2-Bis(dimethyldithiocarbamate)ferrocene and 1,2-Bis(benzothiazol-2-ylthio)ferrocene"

R. Horikoshi, R. Sumitani and T. Mochida, *J. Organomet. Chem.*, 2019, **900**, 120928.

11 "Synthesis and Reactivity of Cyclopentadienyl Ruthenium(II) Complexes with Tris(alkylthio)benzenes: Transformation Between Dinuclear and Sandwich-Type Complexes"

R. Fan, R. Sumitani and T. Mochida, *ACS Omega*, 2020, **5**, 2034–2040.

12 "Thermal Properties, Crystal Structures, and Phase Diagrams of Ionic Plastic Crystals and Ionic Liquids Containing a Chiral Cationic Sandwich Complex"

T. Mochida, R. Sumitani and T. Yamazoe, *Phys. Chem. Chem. Phys.*, 2020, **22**, 25803–25810.

13 "Nitro-Nitrito Photoisomerization of Cationic Platinum(II) Complexes in the Solid State: Reactivity in Polymorphic Crystals and Glassy State"

I. Nakamura, R. Sumitani and T. Mochida, *Cryst. Growth Des.*, 2021, **21**, 1861–1868.

14 "Photoinduced and Thermal Linkage Isomerizations of an Organometallic Ionic Liquid Containing a Half-Sandwich Ruthenium Thiocyanate Complex"

T. Mochida, S. Maekawa and R. Sumitani, *Inorg. Chem.*, 2021, **60**, 12386–12391.

15 "Incongruent Melting and Vitrification Behaviors of Anionic Coordination Polymers Incorporating Ionic Liquid Cations"

T. Mochida, Y. Qiu, R. Sumitani, H. Kimata and Y. Furushima, *Inorg. Chem.*, 2022, **61**, 14368–14376.

16 "Synthesis and Electrochemical Properties of Mixed-Metal Triangular Complexes Based on Ferrocene-based Ligand and Dinuclear Arene Ruthenium Building Blocks"
R. Horikoshi, R. Sumitani, N. Shimooka and T. Mochida, *Eur. J. Inorg. Chem.*, 2022, e202200453.

*Main publications included in this dissertation.

ACKNOWLEDGMENTS

The present work was carried out under the supervision of Professor Tomoyuki Mochida. I wish to thank him for his critical discussions and continuous encouragement. I also thank Professor Takashi Uchino and Professor Kazuyuki Takahashi for extremely beneficial advice.

I thank Professor Hirofumi Yoshikawa for the XAFS measurements, Professor Masamichi Yamanaka for providing gelators, Professor Daisuke Kuwahara for the solid-state NMR spectroscopy measurements, and Dr. Yusuke Funasako for useful discussions. Thanks are also due to all members of the Solid-State Chemistry Laboratory for their help and friendship. In particular, I wish to thank Dr. Ryo Horikoshi for useful discussions and encouragements. Finally, I am sincerely grateful to my parents for their continuous support and encouragement.

January, 2023
Ryo Sumitani